

https://dspace.org/

High-pressure megacrysts and lower crustal contamination: probing a mantle source for Proterozoic massif-type anorthosites

Bybee, Grant Michael

2014-03-05
http://hdl.handle.net10539/14033

Downloaded from a DSpace repository. https://dspace.org/

HIGH-PRESSURE MEGACRYSTS AND LOWER CRUSTAL CONTAMINATION: PROBING A MANTLE SOURCE FOR PROTEROZOIC MASSIF-TYPE ANORTHOSITES

Grant Michael Bybee

A Thesis submitted to the Faculty of Science, University of the Witwatersrand, in fulfillment of the requirements for the degree of Doctor of Philosophy

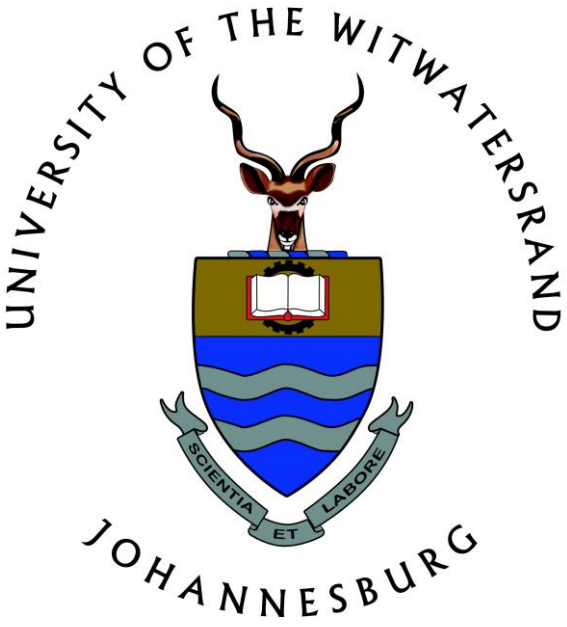

10 October 2013

Johannesburg, 2013

I declare that this thesis is my own, unaided work. It is being submitted for the Degree of Doctor of Philosophy at the University of the Witwatersrand, Johannesburg. It has not been submitted before for any degree or examination at any other University.

_____

Grant Michael Bybee

_____ day of _____ 2013 in _____

Abstract

Many aspects of Proterozoic massif-type anorthosite petrogenesis have been, and remain, controversial. Mafic lower crust and depleted mantle have both been proposed as mutually exclusive sources of these near-monomineralic, temporally restricted batholiths. The debate surrounding the magma source has also led to uncertainty regarding the tectonic setting of these massifs, with a range of possibilities including convergent, divergent and anorogenic settings. The dramatic geochemical effects of crustal contamination in these massifs are well known and strong crustal signatures are evident in most, if not all, Proterozoic anorthosite massifs. The source debate, in the simplest sense, reduces to whether the ubiquitous crustal signature is derived principally from melting of a lower crust or is an effect of crustal assimilation. The origin of this crustal signature, and whether it obscures the original isotopic composition of the magmas or not, has fuelled the debate surrounding the source of the anorthosites. Using major element, trace element and isotopic compositions, as well as energy-constrained assimilation-fractional-crystallisation (EC-AFC) modelling from samples representing various stages of the polybaric crystallisation history of the magmas, including high-pressure megacrysts, anorthosites and their internal mineral phases, I remove the obfuscating effects of possible crustal contamination and probe the source of the magmas. In order to assess the effects of crustal contamination, if any, anorthosites from three massifs – the Mealy Mountains Intrusive Suite, Nain Plutonic Suite (both in eastern Canada) and Rogaland Anorthosite Province (Norway), have been analysed – all of which intrude into crust of significantly different age and chemical character.

Sm-Nd geochronology of high-Al, high-pressure orthopyroxene megacrysts, as well as the comagmatic, host anorthosites, indicate that the magmatic system is long-lived, with an age difference between the megacrysts and hosts of ~110-130 million years. Isotopic compositions of primitive megacrysts qualitatively show that the magmas were derived from melting of the depleted mantle. Strong links between the isotopic offset from depleted mantle evolution and the age and composition of the surrounding crust confirm that the geochemical nature of the crustal contaminant plays a significant role in the petrogenesis of the anorthositic rocks. The geochronological indications of a long-lived magmatic system point to Proterozoic anorthosite formation in a continental magmatic arc – one of the only environments capable of supplying geographically-localised magma and heat to the base of the crust for over 100 million years. Proposed divergent or 'anorogenic' settings could not plausibly supply magma to the base of the crust for over 100 m.y. without initiating ocean formation or continental break-up. Anorthosite emplacement at mid-crustal levels may coincide with late- to post-orogenic events in several terranes, but evidence presented for a long-lived magmatic system is incongruent with this proposed setting. In this thesis, I propose that the petrogenesis of these intrusives must span both orogenic and post-orogenic periods. An overlap in megacryst crystallisation age with the onset of calc-alkaline orogenic magmatism in the Sveconorwegian Orogen, both occuring ~100 m.y. before anorthosite emplacement, confirms that initial magma and megacryst formation coincides with the main phase of magmatic and orogenic activity in a convergent magmatic arc. These geochronological constraints have implications for regional geodynamics in the Sveconorwegian Orogen (and the Labrador region) with the evidence providing corroboratory support for a long-lived accretionary orogen, as opposed to the widely-held view that the Sveconorwegian orogeny was predominantly collisional.

Compositions of high-pressure megacrysts, anorthosites and analysis of internal isotopic disequilibrium indicates that lower crustal contamination has a significant influence on the isotopic composition of the rocks, with relatively minor contributions from the mid- to upper crust. Energy-constrained AFC modelling confirms that significant lower crustal contamination occurs during ponding of magmas at the Moho and is able to reproduce the observed isochronous isotopic compositions of the megacrysts as well as the compositions of the host anorthosites. Evidence of varying degrees of internal isotopic disequilibrium reinforces the significant role that assimilation of crust of different age and chemical nature have on the compositions of Proterozoic anorthosites. Unexpected patterns of isotopic disequilibrium show that anorthosite petrogenesis is not a "simple" case of progressive crustal contamination during polybaric ascent of viscous, partially-molten

magma mushes, but is more likely to involve significant differentiation and solidification at lower crust depths, followed by ascent of high-crystallinity bodies (> 50 % crystallinity) to upper crustal levels.

Although the composition of the bulk continental crust is different to plagioclase-rich Proterozoic anorthosites, both are missing a mafic component. It is unclear how this missing mafic component was generated in the continental crust, because most of the evidence for these crustal differentiation processes is sequestered below or near the Moho. However, Proterozoic anorthosites, formed by viscous, plagioclase-rich mushes, entrain rare cumulate megacrysts from these depths and consequently preserve evidence of magmatic differentiation processes at the Moho. The evidence for the formation and sequestration of dense ultramafic cumulates in ponding magmas at the Moho can not only explain the missing mafic component in Proterozoic anorthosites, but also suggests that cumulate formation in crust-forming, arc environments is a significant process and should be taken into account in models dealing with evolution and differentiation of the continental crust.

Sampling and petrographic and geochemical analysis of five pegmatitic segregations, or "pods", from anorthosites of the Mealy Mountains Intrusive Suite reveal a diverse range of compositions from mafic, Fe-rich and Si-poor, to Fe-poor and Si-rich felsic compositions and from monzogranite through quartz-monzodiorite and monzodiorite to Fe-P-rich gabbronorite. Each pod shows a range of noteworthy graphic, myrmekitic and symplectic textures on a variety of scales, along with distinctive mineralogical assemblages and highly-enriched trace element compositions. Derivitive minerals (e.g. apatite and zircon), high concentrations of Fe, Ti, P (and in some cases SiO_2) and 10-1000 times chondrite enrichment suggest that many of the pods are highly fractionated. U-Pb zircon geochronology reveals that all the pods are the same age as the anorthositic hosts and confirms that the Mealy Mountains Intrusive Suite was emplaced between 1654 and 1628 Ma. Using the aforementioned evidence, I show that the pods represent the fluid-bearing, late-stage crystallisation products of a residual liquid in the massif anorthosite system and provide a window into the final stages of crystallisation in the anorthosite system. A range of rock types (monzonites, monzonorites, ferrodiorites and jotunites) observed in similar pod-like structures, as well as dykes and plutons, have also been documented in other Proterozoic anorthosite massifs. These have, at one time or another, controversially been interpreted as the residual liquids of anorthosite crystallisation. The observation of *in-situ* pods with similar compositions to all of the aforementioned rock types and displaying textures indicative of late-stage crystallisation support the notion that these associated lithologic units are comagmatic with, but residual to, the anorthosites and are not residual liquids of other crustally-derived rocks, immiscible liquids, parental magmas or cumulates. Isotopic compositions of these highly-fractionated, late-stage pods also overlap with those of anorthosites, lending further evidence to the case that upper crustal contamination plays only a minor role in developing the chemical signature of the anorthosites. With these results I propose that the nature/composition of the residual liquids of Proterozoic anorthosite magmas can vary dramatically, depending on geochemical differences in the original magma pulses and by mixing of mobilised, independently-evolved segregations of residual liquids. This process could explain why so many varied rock types associated with Proterozoic anorthosites have been suggested as residual liquids: these rocks all represent residual liquids resulting from varying degrees of differentiation, subsequent mobilisation, mixing and final solidification as plutons or dykes.

Proterozoic anorthosite petrogenesis is an inherently polybaric process and so by its very nature produces a range of complicated and contradictory features which have clouded interpretation of numerous aspects of the rocks formation. In analysing crystallisation products from numerous stages of the anorthosites polybaric history, I have been able to probe the magmatic processes operating at different stages of Proterozoic anorthosite petrogenesis. In doing so I show that the magmas are derived from melting of the depleted mantle in continental-arc-like settings – two controversial aspects of Proterozoic anorthosite petrogenesis. These constraints on the source and tectonic setting will allow renewed investigation into the ultimate question surrounding Proterozoic anorthosites: why are these rock types restricted to the Proterozoic and what clues does this temporal restriction offer about Earth's geodynamic evolution during this period? The assertion in this thesis that

Proterozoic anorthosites formed in arc environments dictates that subduction processes or geodynamic conditions during the Proterozoic favoured the production of voluminous masses of plagioclase, because modern-day magmatic arc terranes show no evidence of anorthosites with similar compositions. However, calcic anorthositic inclusions and xenoliths are observed in modern-day volcanic and continental arcs suggesting that anorthosites may be forming in these environments, but that conditions such as water content or style of subduction are different to the Proterozoic, producing less and compositionally different plagioclase and anorthosite. The results of this thesis shed new light on and refine the petrogenesis of Proterozoic anorthosites, but the focus of research must now shift to explaining the temporal restriction of these intrusions and the implications of this restriction for the geodynamic evolution on Earth during the Proterozoic.

Acknowledgements

Projects spanning three field areas and involving work performed in several different laboratories will always involve the contributions of many people and this project has been no different. C.F. Gower and B. Ryan provided invaluable field support in Labrador and access to a vast sample database at the Geological Survey: Newfoundland and Labrador. T.B. Andersen and F. Corfu endured many hours of megacryst hunting, supporting a sampling foray in the Rogaland region of southwestern Norway. A large proportion of the geochemical analyses in this thesis were completed in the Department of Terrestrial Magnetism (DTM) at the Carnegie Institute of Washington and I wish to thank all the staff and post-doctoral researchers for enriching my time spent in Washington D.C. as a Pre-Doctoral Fellow. During the eights months spent at the DTM, I obtained a wealth of knowledge, not only geochemically, but also scientifically. In particular, S. Shirey, M. Horan, T. Mock and R.W. Carlson facilitated, organised and oversaw my visits, ensuring I was able to complete the necessary analyses. Each of these individuals are fantastic mentors, from whom I have learnt vital geochemical and scientific skills. The School of Geosciences and Faculty of Science at Wits University must also be acknowledged for providing funding to visit the DTM for extended stays over a period of two years. R.L. Gibson and R.G. Cawthorn are acknowledged for the efforts they put into funding and facilitating this research and the thesis. Various other geochemical data were sourced from the Earth Lab at Wits University and the geochemistry laboratories at the University of Cape Town for which I thank A.H. Wilson, A.P. le Roux and P. le Roux. M. Hamilton performed precise U-Pb geochronology at the Jack Satterly Lab at the University of Toronto that is included in this thesis. To the many friends and colleagues in the School of Geosciences, thank you for the support and camaraderie throughout my time in the School. Finally, I am indebted to L.D. Ashwal, my advisor and the individual who wrote the book on anorthosites (literally). Throughout numerous stages of my undergraduate and postgraduate career, Lew has inspired, challenged and encouraged me to constantly delve deeper into geoscience and geochemistry, whilst always keeping science fun and exciting. This support, as well as guidance in the many spheres of the project, has been invaluable – it has been, and still is, a priviledge to work with such a dedicated and talented scientist and scientific mentor. To everyone involved in some way, large or small, thank you.

Contents

1 AN INTRODUCTION TO THE ANORTHOSITE PROBLEM 16

1.1 THE DEBATES RAGE ON 18

1.1.1 The Magma Source for Proterozoic Anorthosites 18

1.1.2 The Parental Melts and Emplacement Mechanisms 19

1.1.3 The Tectonic Setting of Proterozoic Anorthosites 21

1.2 THE SCOPE OF THIS WORK AND A HYPOTHESIS 23

1.3 GEOLOGIC SETTING OF A TRIO OF ANORTHOSITE INTRUSIONS 24

1.3.1 The Mealy Mountains Intrusive Suite 24

1.3.2 Nain Plutonic Suite 27

1.3.3 Rogaland Anorthosite Province 27

1.4 METHODS 30

1.4.1 Zircon Separation and Geochronology Methodology 30

1.5 ANORTHOSITE AND ORTHOPYROXENE MEGACRYST PETROGRAPHY 31

1.5.1 Anorthositic Lithologic Units 31

1.5.2 Orthopyroxene Megacrysts 37

1.6 A SUMMARY OF SCIENTIFIC CONTRIBUTIONS 37

2 GIANT PYROXENE MEGACRYSTS IN ANORTHOSITES: REVEALING CONTINENTAL CRUST FORMING PROCESSES AT MOHO DEPTHS 40

2.1 HIGH-AL MEGACRYST ISOCHRON GEOCHRONOLOGY 42

2.1.1 True Isochrons vs. Pseudochronous Mixing Lines? 45

2.2 THE TECTONIC SETTING AND SOURCE OF PROTEROZOIC ANORTHOSITES 49

2.3 GEODYNAMIC IMPLICATIONS OF THE HIGH-AL MEGACRYSTS 51

2.4 CONCLUSIONS 56

3 REGIONAL GEODYNAMIC IMPLICATIONS OF MEGACRYST GEOCHRONOLOGY IN THE SVECONORWEGIAN OROGEN AND EASTERN LABRADOR 58

3.1 GEOCHRONOLOGY OF THE ROGALAND ANORTHOSITE PROVINCE 60

3.2 IMPLICATIONS FOR THE SVECONORWEGIAN TECTONIC REGIME 60

3.3 REGIONAL IMPLICATIONS FOR ANORTHOSITE INTRUSIONS IN LABRADOR 64

3.3.1 Testing the Geodynamic Paradigm in Labrador using Megacryst Geochronology 64

3.4 CONCLUSIONS 68

4 PROBING THE MANTLE SOURCE OF PROTEROZOIC ANORTHOSITES: STRIPPING AWAY THE EFFECTS OF CRUSTAL CONTAMINATION 70

4.1 Crustal Contamination and Isotopic Equilibrium 70
4.2 Quantifying Internal Isotopic Equilibrium 71
4.3 Petrology and Trace Element Geochemistry 72
4.3.1 Noteworthy Petrographic Features 72
4.3.2 Trace Element Compositions 72
4.3.3 Internal mineral trace element concentrations 74
4.4 Isotope Geochemistry 75
4.4.1 Whole-Rock and Mineral Isotopic Compositions 75
4.4.2 Assessing Isotopic Disequilibrium 77
4.5 Discussion 83
4.5.1 Assimilation and Fractional Crystallisation (AFC) Modelling 88
4.5.2 Traditional Assimilation and Fractional Crystallisation (AFC) Modelling 88
4.5.3 Energy-Constrained Recharge, Assimilation and Fractional Crystallisation (EC-RAχFC) Modelling 92
4.6 Melting of the Depleted Mantle vs. Lower Crust? 101
4.7 Refining the Petrogenetic Model for Proterozoic Anorthosites Genesis 102
4.7.1 Assessing the Ascent and Crystallisation of Proterozoic Anorthosites in Light of Isotopic Disequilibrium 104
4.7.2 Implications of the Isotopic Composition of Leuconorite vs. Leucotroctolite 106
4.8 Conclusions 107

5 INSIGHTS INTO THE FINAL STAGES OF PROTEROZOIC ANORTHOSITE CRYSTALLISATION IN THE MEALY MOUNTAINS INTRUSIVE SUITE 109
5.1 Geologic Setting 110
5.2 Pod Petrography and Mineral Chemistry 111
5.2.1 Leuconorite-Hosted Pods 112
5.2.2 Pod Hosted by Olivine-Bearing Anorthosite 114
5.2.3 Replacement Features of the Pods 117
5.3 Pod Compositions 118
5.4 U-Pb Geochronology 121
5.5 Discussion 124
5.5.1 Graphic Intergrowths 124
5.5.2 Potassic Replacement of Plagioclase 125
5.6 Myrmekitic Intergrowths 126
5.7 Conclusions 130

6 A SUMMARY – PROBING THE PETROGENESIS OF PROTEROZOIC ANORTHOSITES.....131

7 REFERENCES.....136

APPENDICES.....148

List of Figures

Figure 1.1: The global distribution of major Proterozoic anorthosite massifs and associated layered intrusions. Anorthosites: HC - Horse Creek; HL - Harp Lake; Ko - Korosten; La - Laramie; Lbv - Labreville; Mi - Michikamau; MM - Mealy Mountains; N - Nain; Rog - Rogaland; Su - Suwałki. Associated layered mafic intrusions: Ki - Kiglapait; VB - Voisey`s Bay. 17

Figure 1.2: A typical anorthositic terrane in the northern hemisphere illustrating the vast extent of plagioclase and "massif" nature of the intrusion. This photo is taken in the Mealy Mountains Intrusive Suite. 17

Figure 1.3: a. The geological setting of the Nain Plutonic Suite (NPS) and Mealy Mountains Intrusive Suite (MMIS) in Labrador, easternmost province of Canada. b. The Rogaland Anorthosite Province is located on the southwestern coast of Norway and intrudes into rocks of the Sveconorwegian orogen. 25

Figure 1.4: Map illustrating the various terranes making up the Eastern Grenville Province (EGP) of the Grenville Province in North America (after Gower and Krogh 2002). The EGP is separated into the Exterior Thrust Belt and the Interior Magmatic Belt. The Mealy Mountains Terrane, which is part of the Exterior Thrust Belt, plays host to the 1650-1630 Ma Mealy Mountains Intrusive Suite (as indicated by the star).....26

Figure 1.5: The geologic framework of eastern Labrador showing the location of the Nain Plutonic Suite in relation to other Proterozoic anorthosite massifs (e.g. Harp Lake, Mistastin and Michikamau massifs), the Torngat Orogen and the Nain and Churchill Provinces (Ryan, 2000). 28

Figure 1.6: The geology of the Rogaland Anorthosite Province showing the three anorthositic intrusions (Egersund-Ogna, Håland-Helleren and the Åna-Sira intrusions) alongside the Bjerkreim-Sokndal layered intrusion (Charlier et al. 2006). Both the Tellness ilmenite deposit and Storgangen sheet are located in the Åna-Sira massif which is adjacent to two smaller leuconoritic bodies known as the Hidra and Garsanatt massofs. S: Storgangen; T: Tellnes "main dyke"; T': Tellnes ilmenite deposit. Numerous crosscutting dykes are not depicted in this map. 29

Figure 1.7: a. A simplified map of the Mealy Mountains Intrusive Suite (MMIS) located in the Eastern Grenville Province showing sampling locations and previously dated samples reported in Gower et al., 2008. b. A simplified map of the Nain Plutonic Suite (NPS) intruding along the Torngat Orogen which marks the suture between the Palaeoproterozoic Churchill and Archaean Nain Provinces (after Ryan 1990). Stars indicate generalised locations for several orthopyroxene megacryst sampling locations, simplified for clarity. c Geological map showing megacryst sampling localities in the Egersund-Ogna Massif of the Rogaland Anorthosite Province (RAP; after Charlier et al. 2010). 35

Figure 1.8: a. Typical leuconorites from the Etaugalet massif of the MMIS illustrating intercumulus orthopyroxene in addition to minor biotite and magnetite (CG09-17) set within euhedral, tabular plagioclase grains (ppl). b. When compared with a., this sample (CG09-26A) displays a different texture, perhaps due to recrystallisation with rounded orthopyroxene crystals set among both tabular and euhedral plagioclase crystals

(ppl). c. A typical leuconorite sampled from the NPS showing intercumulus orthopyroxene (with pervasive oxide rod-like inclusions), sub- to anhedral plagioclase (variably deformed) and minor clinopyroxene. 36
Figure 2.1: The field setting and microscopy of HAOMs. a. One large (~30 cm), euhedral HAOM crystal forming part of aggregate/pod from the MMIS. b. Equant and subhedral megacryst aggregation from the NPS (photo courtesy B. Ryan). c. Rounded HAOM aggregate from RAP d. Elongate (~40 cm) orthopyroxene megacryst from RAP possibly fractured during magma ascent/transport e. Two HAOMs from RAP showing interstitial relationships with plagioclase grains. f. Crossed-polarized photomicrographs of HAOM showing plagioclase exsolution lamellae (RAP). g. Plane polarized microphotographs of HOAMs (RAP). 41
Figure 2.2: a. Chondrite-normalised (Anders & Grevesse, 1989) REE element diagram comparing HAOMs and anorthosites from the three localities sampled in this study. Numbers adjacent to HAOMS from the MMIS represent Al_2O_3 contents (wt %). b. Al_2O_3 content vs. Eu anomaly in orthopyroxene megacrysts from the RAP, MMIS and NPS. Samples from the MMIS and NPS show no clear trends, but the highest Al suite of megacrysts from the RAP show variable Eu anomaly. With decreasing Al content in the megacrysts, a negative Eu anomaly develops.....43
Figure 2.3: a. $^{143}Nd/^{144}Nd$ vs. $^{147}Sm/^{144}Nd$ illustrating the isochronous relationships between high-Al megacrysts from three different Proterozoic anorthosite massifs. Each isochron defines an age approximately 110-130 m.y. older than the recognized age range of the anorthosite intrusions. 2σ errors are all smaller than the symbol size. The Churchill and Nain Province Gneisses cluster around the following isotopic compositions not shown on the graph: $^{143}Nd/^{144}Nd$: 0.511421-0.510451; $^{147}Sm/^{144}Nd$: 0.107025-0.085978 (Appendix C). MSWD: mean square of the weighted deviates. b. $^{206}Pb/^{204}Pb$ vs. $^{207}Pb/^{204}Pb$ showing that although Pb remobilisation during various orogenic events has partially reset some isotopic compositions, isochronous relationships are preserved in some datasets and are similar to the Sm-Nd age. 44
Figure 2.4: Four-point isochrons (including repeat analyses of whole-rock megacryst) between plagioclase lamellae, host orthopyroxene and whole-rock megacrysts indicating that the ascent of HAOMs in plagioclase-rich mushes to final emplacement levels in the upper crust requires significant lengths of time – similar to the age differences between HAOMs and the host anorthosites.....45
Figure 2.5: a-c. Time-integrated (930 Ma) $^{143}Nd/^{144}Nd$ vs. $^{147}Sm/^{144}Nd$ plots for various traditional AFC models between a magma represented by the most primitive megacryst composition in the RAP and the observed lower crustal compositions in the region (Othman et al. 1984). 48
Figure 2.6: a. A depleted mantle origin for HAOMs and Proterozoic anorthosites. εNd vs. time illustrating how emplacement of anorthositic mushes into terranes of different ages dramatically influences the isotopic composition of the anorthosites. In young terranes, where the effect of contamination is least dramatic, the initial megacrystic isotopic compositions (large triangles, derived from isochron regression) is consistently only slightly displaced from depleted mantle evolution, indicating magma derivation from depleted mantle. Linear fields indicate evolution of potential crustal contaminants (potential contaminants for the NPS include both Churchill and Nain Province gneisses, due to intrusion into the province-suturing Torngat Orogen). b. The initial assimilation of lower crust by a depleted-mantle-derived melt, subsequent crystallisation of high-pressure megacrysts, and later polybaric fractionation and upper crustal assimilation during anorthosite crystallisation is traceable in this εNd vs. $(^{208}Pb/^{204}Pb)_i$ plot. The highest-Al megacrysts record a limited pulse of lower-crustal contamination during ponding of depleted-mantle-derived melt. Later mid- to upper-crustal

polybaric contamination deflects the isotopic composition of the lower-pressure megacrysts and anorthosites (particularly noticeable in the RAP) to more upper-crustal values. The ^{232}Th-^{208}Pb system is chosen as a better tracer of contamination because of increased concentrations of Th in the continental crust. Depleted mantle composition determined from Rehkamper and Hofmann (1997) and the representative lower-crustal composition is taken from Othman et al. (1984).....52

Figure 2.7: Selected Harker diagams showing similarities between HAOMs and experimental, high pressure (2.1 GPa) basaltic compositions (Müntener & Kelemen 2001). Correlations between SiO_2 and Al_2O_3, particularly amongst the highest HAOMs from the RAP are indicative of equilibrium crystallisation and support the proposed model of magma ponding and crystallisation at the Moho. All HAOMs show lower Mg# for a given SiO_2 content than the experimental basaltic cumulates due to olivine fractionation prior to orthopyroxene megacryst crystallisation. 54

Figure 2.8: Extracted magma and cumulate densities from MELTS modeling of high-Al basalt crystallisation at Moho pressures. The starting composition is the same in each model permutation. a. Model fractionating solids at 1 GPa (10 kbars). b. Model not fractionating solids at 1 GPa (10 kbars). c. Model not fractionating solids at 1.5 GPa (15 kbars). d. Model fractionating solids at 1.5 GPa (kbars). 55

Figure 2.9: a. MgO vs. SiO2 illustrating the compositional discrepancy between single-stage melts (grey-shaded box) of peridotitic mantle [Process 1] in arc environments and the bulk continental crust (CC; Rudnick & Gao 2003 and references therein). Fractionation [Process 2] of these peridotitic melts at the Moho and associated sequestration of dense ultramafic cumulates (real megacryst compositions, experimental cumulates and modeled MELTS phases) below the Moho drives the composition of the residual magma, which goes on to form the continental crust, to more intermediate compositions, in line with observed bulk crustal compositions. Primitive mantle (PM) compositions are taken from (Palme & O'Neill 2003) and references therein. Yellow pentagon represents the proposed parental magma of Proterozoic anorthosites (Charlier et al. 2010). Density contrast ($\Delta\rho$) calculations between magma, mantle and cumulates derived from MELTS modelling. 57

Figure 3.1: a. Lithotectonic domains of the Sveconorwegian Orogen in SW Scandinavia (Vander Auwera et al. 2011). 59

Figure 3.2: ^{143}Nd/^{144}Nd – ^{147}Sm/^{144}Nd plot showing the isochronous relationship between the highest-Al megacrysts from the RAP, suggesting that the megacrysts crystalised under equilibrium conditions in a ponded magma at the Moho. This isochron yields an age of 1041 ± 17 Ma. b. ^{207}Pb/^{204}Pb – ^{206}Pb/^{204}Pb plot showing a close correspondence in age to the ^{147}Sm-^{143}Nd age in megacrysts with >8 wt% Al_2O_3. 61

Figure 3.3: Regional and megacryst geochronology illustrating the coincidence of high-pressure megacryst crystallisation at ~1040 Ma with the onset of calc-alkaline Sirdal magmatism. Although this period of calc-alkaline magmatism is followed by a 30 m.y. lull in magmatic activity, as is characteristic in many Cordilleran margins, continued supply of heat and magma at the base of the crust must have continued until ~950 Ma to produce anorthosite mushes and crustal anatexis as well as keep the anorthositic crystal-rich mushes mobile. HBG - hornblende and biotite-bearing granitoid suite (Vander Auwera et al. 2011). 62

Figure 3.4: Schematic geodynamic development in the eastern Labrador region (Gower and Krogh, 2002). 66

Figure 4.1: $^{143}Nd/^{144}Nd$ vs. $^{147}Sm/^{144}Nd$ plot illustrating the geometrical relationships describing the Delta (Δ) value - a measure of the deviation of an internal mineral isotopic composition from a reference isochron (for a given time, T) passing through the whole-rock isotopic composition. 71

Figure 4.2: Noteworthy field and petrographic features in the MMIS and NPS. a. Meter-scale block structure in the MMIS where a sub-rounded block of grey leuconorites (highlighted by dashed yellow line) is included within leuconorite with distinct maroon hues (probably caused by small heamatite inclusions in plagioclase). b. Subhedral orthopyroxene grain rimmed by a subsequent generation of orthopyroxene (CG09-17). c. A large subhedral orthopyroxene grain interpreted as a cumulus phase adjacent to intercumulus clinopyroxene and magnetite in CG09-32A. d. In the same sample as shown in c. (CG09-32A), intercumulus orthopyroxene is also observed. e. Orthopyroxene and clinopyroxene included within cumulus plagioclase grains. f. Peritectic reaction rim of orthopyroxene around olivine in the interstitial space between cumulus plagioclase grains (CG09-30). 73

Figure 4.3: a-c. Typical examples of plagioclase, orthopyroxene (CG-09-18A) and magnetite (CG-09-15) from the MMIS. d-e. Typical plagioclase and pyroxene from the NPS. f-g. Examples of slightly recrystallised plagioclase and orthopyroxene from the NPS causing discolouration in the grains. The width of each photo is 1.5 mm, except for a. which is 3 mm wide and c. and d. which are 0.75 mm wide. 75

Figure 4.4: a. εNd vs. time illustrating how emplacement of anorthositic mushes into terranes of different ages dramatically influences the isotopic composition of the anorthosites. In young terranes, where the effect of contamination is least dramatic, the initial megacrystic isotopic compositions (large triangles, derived from isochron regression) are consistently only slightly displaced from depleted mantle evolution, indicating magma derivation from depleted mantle. Linear fields indicate evolution of potential crustal contaminants (potential contaminants for the NPS include both Churchill and Nain Province gneisses, due to intrusion into the province-suturing Torngat Orogen). b. The initial assimilation of lower crust by a depleted-mantle-derived melt, subsequent crystallisation of high-pressure megacrysts, and later polybaric fractionation and further crustal assimilation during anorthosite crystallisation is traceable in this εNd vs. $(^{208}Pb/^{204}Pb)_i$ plot. ... 76

Figure 4.5: a. ε_{Nd}-I_{Sr} compositions for whole-rock anorthosites, high-pressure megacrysts, and internal mineral phases (orthopyroxene, magnetite, plagioclase) in the MMIS. b. Detailed view of whole rock leuconorite and leucotroctolite sample with internal plagioclase compositions from the MMIS. 78

Figure 4.6: ε_{Nd}-I_{Sr} compositions for whole rock and internal mineral phases from the NPS. 79

Figure 4.7: $\varepsilon_{Nd,T}$ vs. T illustrating mineral isotope compositions in relation to whole-rock compositions from the MMIS. All compositions are calculated to either 1.64 Ga or 1.765 Ga (high-Al megacryst crystallisation age), but are expanded for clarity. The large range in orthopyroxene compositions relative to the leuconorites and plagioclase compositions is noteworthy. 79

Figure 4.8: Comparitive Δ-values for the MMIS an NPS (a. ΔNd vs. ΔSr, b. ΔNd vs. ΔPb, c. ΔPb vs. ΔSr) calculated using methodology outlined in Section 4.1.2 and Figure 4.1. Dahsed lines indicate whole-rock equilibrium set-point. 82

Figure 4.9: a-b. $^{143}Nd/^{144}Nd$ – ^{147}Sm-^{144}Nd plot with reference isochrons and internal mineral compositions for several samples from the MMIS (a) and NPS (b). c. $^{87}Sr/^{86}Sr$ – $^{87}Rb/^{86}Sr$ plot showing reference isochrons and internal mineral compositions in the MMIS. Note how the basement compositions plot along the trend of the

reference isochron at higher Sr/Sr and Rb/Sr values. d. $^{207}Pb/^{204}Pb$ – $^{206}Pb/^{204}Pb$ compositions for internal mineralogy in relation to whole-rock reference isochrons. 83
Figure 4.10: a. Schematic Nicolayson diagram showing effects of progressive crustal contamination on initial whole-rock and mineral compositions. b. The time-integrated effect of progressive crustal contamination on the internal isotopic composition and the averaging effect of incorporation of these various compositions into a sample. 87
Figure 4.11: Traditional AFC model simulating assimilation and fractional crystallisation of a melt derived from depleted mantle (DM) with lower crustal material (or upper crustal material; see Table 4.4). *r* represents the non-dimensional ratio of mass assimilated vs. mass crystallised, and *F*, the degree of crystallisation/fraction liquid remaining. The models are able to reproduce the most primitive compositions in the anorthosite system (high-Al megacrysts) but only at unreasonably high *r*- (>0.5) and *F*-values (>80). 91
Figure 4.12: a. EC-RAχFC showing the evolution of depleted mantle-derived magma during assimilation of lower crust. b. Sensitivity tests illustrating how changing various parameters effects the modelled magma paths. 95
Figure 4.13: a. Two-stage EC-RAχFC model simulating "polybaric" AFC in the RAP. b. Mineral compositions calculated from the liquid evolution path in a. compared with actual megacryst and whole-rock compositions. 96
Figure 4.14: a. Two-stage EC-RAχFC model simulating "polybaric" AFC in the NPS using an intermediate crustal composition between Churchill and Nain Province compositions. b. Mineral compositions calculated from the liquid evolution path in a. compared with actual megacryst and whole-rock compositions. 98
Figure 4.15: A model attempting to simulate magma differentiation in both Nd (a) and Sr (b) isotopic space assuming that lower crust in the NPS has similar composition to observed upper crustal compositions. Using a pure average of crust compositions from the Churchill and Nain Provinces, the appropriate isotopic compositions cannot be recreated. 99
Figure 4.16: Two models illustrating the difficulty in modelling the MMIS isotopic compositions. Only when the isotopic composition and Nd concentrations in the assimilant and magma parameters are changed to extreme values can the compositions be obtained. 100
Figure 4.17: A revised petrogenetic model for the petrogenesis of Proterozoic massif-type anorthosites. 108
Figure 5.1: Geologic setting of the Mealy Mountains Intrusive Suite showing sampling location of pegmatitic pods (and one anorthosite; CG09-21). Ages indicated by small black circles show previous geochronological measurements performed on felsic members of the MMIS and reported in Gower et al. (2008). 111
Figure 5.2: (previous page): a-b. Irregular pods (CG09-027C) of pegmatitic (~15 cm) plagioclase crystals hosted by coarse-grained (~2-4 cm) anorthosite. Interstitial areas within the pods are filled with altered pyroxenes and pinkish albitic alteration material. This pod most resembles the host anorthosites. c-e. Pod CG0916A (hosted by leuconorite) consisting of large (20 cm) plagioclase crystals showing variable stages of alteration (fresh = grey, alteration = red/brown). In d, intergrowths of Fe-Ti oxide are observed intergrown with apatite (see also Fig 3d). f. Irregular pod (CG0918D) with large (~50 cm) plagioclase crystals and graphic intergrowth of quartz and K-feldspar forming an Fe-rich quartz-monzodiorite composition. g-h. Pod CG0933B, hosted by olivine-bearing anorthosite. Pod consists of large, dark, pyroxene crystals with interstitial altered feldspar and intergrowths of Fe-Ti oxide and apatite (h; see also Fig 6a). 114

Figure 5.3: a. Pinkish albitic alteration material interstitial to coare-grained, euhedral to subhedral plagioclase grains and minor magnetite from the most 'anorthositic' pod (CG09-027C). b. Cobaltinitrate-stained hand sample from pod CG09-018D showing the presence of K-bearing phases and large plagioclase crystals surrounded by symplectic intergrowths of quartz and K-feldspar. c. Extensive development of graphic quartz-K-feldspar intergrowths in pod CG09-026B. d. Fe-Ti oxide-apatite (light green colour) symplectites in the pod hosted by an olivine-bearing anorthosite (CG09-033B). e-f. Crossed-polarised (e) and plane-polarised (f) view of extensive symplectic intergrowths of K-feldspar (e) or plagioclase (f) and quartz in pods CG09-026B and CG09-016A, respectively.....115

Figure 5.4: Or-An-Ab ternary diagram illustrating feldspar compositions observed in the pods, determined using EMPA. Tie-lines join host orthoclase compositions and plagioclase exsolution lamellae observed in several pods. These exsolution lamellae are less than 4 um wide and are abundant in the feldspar, with an estimated ratio of 70:30 for host and lamellae, respectively (See Fig. 7d). Care was taken in ensuring that the orthoclase analyses were free of exsolution lamellae except for one point (black diamond falling on solvus). Data presented in Appendix F-1.....116

Figure 5.5: a. Apatite, zircon and Fe-Ti oxides in combination with a graphic quartz-orthoclase intergrowth in sample CG09-018D. b-c. Development of microscopic films and plumose structures of myrmekite at the interface between quartz and K-feldspar phases of a graphic intergrowth (CG0918D). d. Similar microscopic symplectites, in this case developed between plagioclase and clinopyroxene in pod CG09-027C. 117

Figure 5.6: Petrology and mineralogy of the only observed pod hosted by leucotroctolites. a. Intergrowths of apatite and Fe-Ti oxide adjacent to a large crystal of pyroxene (inverted pigeonite). b. Blebby and lamellar inverted pigeonite surrounding apatite crystal viewed under cross-polarised light. c. Microphotograph of a slightly thick thin-section of sample CG0933B in cross-polarised light showing apatite, Fe-Ti oxide, inverted pigeonite and plagioclase-orthopyroxene symplectites radiating from a corroded plagioclase grain, magnified in d. d. SEM image of plagioclase-orthopyroxene symplectites emanating from a perthite grain.....118

Figure 5.7: a. Crossed-polarised view of primary plagioclase (An_{15-25}) showing albite twinning, replaced by darker orthoclase later altered to albite (An_{0-5}). Black grain is Fe-Ti-oxide while white grains are quartz. b. A plagioclase grain (albite twinning) situated adjacent to an extinct quartz grain and surrounded by orthoclase (crossed-polars). c. An intergrowth of quartz, rimmed by plagioclase that is surrounded by albitised orthoclase. Remnant domains of plagioclase are observed indicating that orthoclase is a replacement phase after plagioclase. This orthoclase is subsequently altered to albite, potentially by late-stage magmatic fluids. d. SEM image of perthite (intergrown graphically with quartz) altering to albite. Lamellae of abundant ~4 um wide plagioclase visible in perthite.....119

Figure 5.8: Chondrite-normalised (Anders and Grevesse, 1989) rare earth element diagram comparing the composition of the pods and host anorthosites. A spectrum of REE enrichment is observed in the pods, from very similar to the host anorthosite, to 1000x chondrite enrichment, along with negative Eu anomalies in the most evolved pods. 121

Figure 5.9: When compared to the host anorthosites, the pegmatitic pods show the least radiogenic or lowest isotopic compositions ($\varepsilon_{Nd;\,T}$), slightly overlapping with the leuconoritic and leucotroctolitic lithologies of the MMIS. Isotopic compositions are all calculated at 1.65 Ga, but are expanded for clarity. A decrease in $\varepsilon_{Nd;\,T}$ with progressive increase in silica content is noted in the anorthosites, leucotroctolites and leuconorites.

Coeval granites of the MMIS plot at lower ε_{Nd} compositions and are not comparable with the late-stage pods which are geochemically most similar to the most contaminated host rocks. Isotopic data for pods and anorthosites are provided in Appendix C. 122
Figure 5.10: U-Pb zircon geochronology for the four pegmatitic pods and one anorthosite from the MMIS. Although extending the emplacement ages for the MMIS to between 1654 to 1628 Ma, the ages produced agree well with previous geochronological determinations from felsic members of the MMIS (Gower et al. 2008b). 123
Figure 5.11: Development of peritectic phase equilibria due to extreme differentiation in pod-like structures. With continued differentiation, alkali feldspar compositions move across the cotectic (Alk1 to Alk 2) and force the evolving liquid off the cotectic, causing instability in plagioclase phases and reaction with the K-rich liquid to form K-feldspar. 126
Figure 5.12: Chondrite-normalizsd REE (Anders and Grevesse, 1989) diagram showing the close similarity between modelled residual liquids of anorthositic magmas and the pegmatitic pod compositions. Two of the most mineralogically evolved pods show increased enrichment and display similar pattens with more prominent negative Eu anomalies. The $[La/Sm]_N$ in the pod hosted by leuconorite is noticeably different to the $[La/Sm]_N$ of the modelled residual liquid as well as the pod hosted by an olivine-bearing anorthosite. Light grey patterns with filled circles represent residual liquid concentrations calculated by mass-balance fractionation models in (McLelland et al. 1994). 128

List of Tables

Table 2.1: Ages differences between high-Al orthopyroxene megacrysts, host anorthosites and an exsolution event 42
Table 2.2: Parameters Used for Traditional AFC Modelling and Time Integration in three scenarios with different lower crustal compositions (AFC 1, 2, 3) using a starting composition defined by the most primitive megacryst analysed. 47
Table 4.1: Range and average Sr and Nd concentrations (ppm) for analysed plagioclase, orthopyroxene and magnetite phases from anorthosites in the MMIS and NPS 74
Table 4.2: Average Δ-values for internal mineral compositions in anorthosites from the MMIS and NPS. Δ-values measure the deviation of an internal mineral phase from a reference isochron passing through the whole-rock composition at time of emplacement. LN = leuconorites, LT = leucotroctolites. HAOM – high-Al orthopyroxene megacryst. 80
Table 4.3: Whole rock and mineral isotopic compositions (Opy: orthopyroxene; Mag: magnetite; Pl: plagioclase) for samples from the MMIS and NPS 81
Table 4.4: Thermal and chemical parameters used in AFC and EC-RAχFC models. Specific heat of magma and assimilant as well as heats of crystallisation and fusion are calculated using data provided in (Spera & W. Bohrson 2001) and the typical compositions for the materials. 90
Table 5.1: Normative mineral composition of five pods from the MMIS 120

1 An Introduction to the Anorthosite Problem

Proterozoic anorthosites, one of the Earth's most enigmatic cumulate, igneous rocks are found around the world, and were initially noted because of their areal extent (up to 15000 km^2), near-monomineralic plagioclase-rich compositions and impressive iridescence, but after decades of research many questions regarding the petrogenesis and temporal restriction of these rocks remain (Figure 1.1 and 1.2; Ashwal 1993; Duchesne 1984; Emslie 1985; Morse 1982). The allure of anorthosites now centres on understanding the petrogenesis, tectonic setting and temporal restriction of these massive plutonic igneous rocks and the insights they can offer about the secular evolution of magmatic processes on Earth. Anorthosites are not only restricted to the Proterozoic eon and have, in general, been classified into six broad categories, including: 1) Archaean anorthosites, 2) Proterozoic massif-type anorthosites, 3) anorthosites specific to layered mafic intrusions, 4) anorthosites found in oceanic settings, 5) anorthosite inclusions in other igneous rocks and 6) extra-terrestrial anorthosites (Ashwal 1993; Ashwal 2010). Although Proterozoic massif-type anorthosites are primarily associated with anorthosite *senso stricto*, samples with greater than 65 % plagioclase (typically between An_{45-65}) and subordinate amounts of mafic minerals such as orthopyroxene, clinopyroxene and olivine, as well as magnetite and/or ilmenite, are considered part of the anorthositic series (Streckeisen, 1976). It is the restriction of these rocks to a specific time interval in the Proterozoic eon (1800-900 Ma) that is most surprising and enigmatic, and may be a key to understanding part of the Earth's geodynamic evolution (Ashwal 2010).

These massifs display enriched rare earth element (REE) patterns with further enrichment in the light REE (LREE; 10 times chondrites) and variable isotopic signatures (e.g. ε_{Nd} and $[^{87}Sr/^{86}Sr]_i$) extending from depleted mantle values to regional crustal values (Ashwal & Seifert 1980; Maji et al. 2010). Associated with these plagioclase-rich intrusions are equally voluminous, typically younger, batholiths of granite and mangerite, smaller bodies of mafic cumulates, subsidiary amounts of Fe-rich ferrodiorites to monzonorites and Fe-Ti ores, which when considered in conjunction with the anorthosites, constitute the Proterozoic massif-type anorthosite suite, or what is otherwise known as anorthosite-mangerite-charnockite-granite (AMCG) complexes (Ashwal 1993; Emslie 1985; Morse 1982). It is generally acknowledged that the magmas forming the anorthosites have a significant crustal isotopic signature, but whether this signature is derived from crustal assimilation or melting of a lower crustal source is contentious (Ashwal 2004) and forms a major thrust of this thesis.

The Mealy Mountains Intrusive Suite (MMIS) and the Nain Plutonic Suite (NPS, Figure 1.3), both located in Labrador, Canada, as well as the Rogaland Anorthosite Province (RAP; Norway; see Section 1.3, Figure 1.3), are prime examples of Proterozoic massif-type anorthosites and form the focus of this dissertation, in which the effects of crustal contamination have been assessed using not only whole-rock radiogenic isotopic compositions (Sr, Nd and Pb), but also internal, mineral isotopic compositions. The purpose of these analyses and energy-constrained AFC modelling is to strip away the obfuscating effects of crustal contamination and scrutinise the source and petrogenesis of the magmas more closely. High pressure orthopyroxene megacrysts hosted by comagmatic anorthosites from the MMIS, NPS and the RAP have proven useful in accomplishing this and their isotopic signatures and geochronology have led to interpretations that shed new light on the source and tectonic

setting of Proterozoic massif-type anorthosites as well as the mechanisms involved in differentiation of the bulk continental crust.

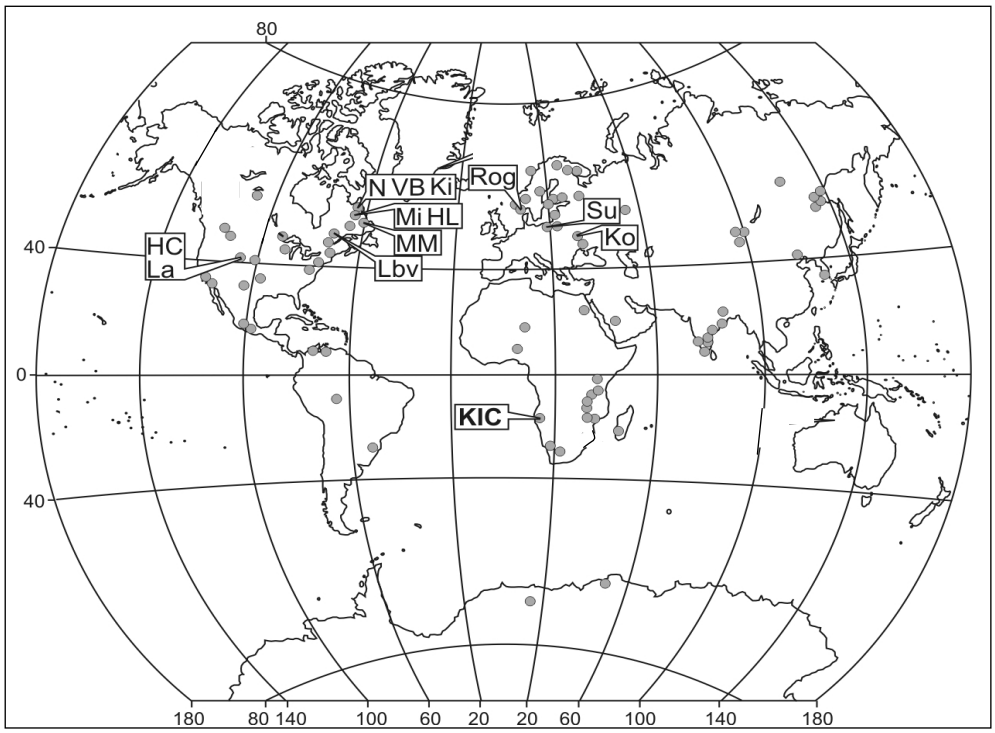

Figure 1.1 The global distribution of major Proterozoic anorthosite massifs and associated layered intrusions (after Gleiβner 2011). Anorthosites: HC - Horse Creek; HL - Harp Lake; Ko - Korosten; La - Laramie; Lbv - Labreville; Mi - Michikamau; MM - Mealy Mountains; N - Nain; Rog - Rogaland; Su - Suwałki. Associated layered mafic intrusions: Ki - Kiglapait; VB - Voisey`s Bay.



Figure 1.2 A typical anorthositic terrane in the northern hemisphere illustrating the vast extent of plagioclase and "massif" nature of the intrusion. This photo is taken in the Mealy Mountains Intrusive Suite.

1.1 The Debates Rage On

"Seldom can it be truly said that the puzzling feature of any object is its simplicity, yet of all the problems that the anorthosites present to us for solution, the most difficult is their simple mineralogical composition"

Norman L. Bowen (1917)

The words of Bowen regarding the petrogenesis Proterozoic anorthosites, in many respects, still ring true today, almost one hundred years after being published (Bowen 1917). Although the mechanisms by which the rocks develop nearly monomineralic status have been partially resolved (Section 1.1.2), many aspects of the petrogenesis of these massifs remain contentious. The tectonic setting, parental melt and residual liquid compositions, emplacement mechanisms, magma source and temporal restriction of these massifs are challenges currently at the forefront of anorthosite research.

1.1.1 The Magma Source for Proterozoic Anorthosites

Competing hypotheses describing the source of anorthosite-forming magmas in the Proterozoic have existed for decades (Berg, 1969; Morse, 1969; Philpotts, 1969) and in the simplest sense the two schools of thought argued that the melts were derived either from the mantle or the lower crust. Early ideas regarding a crustal origin suggested that anorthosites represented a residue after anatectic partial melting of albitic portions of paragneiss (Berg, 1969), but for several decades since, a mantle origin has been favoured.

Geochemical and petrologic studies investigating not only Proterozoic anorthosites, but also associated jotunites/monzonites and marginal basaltic/high-Al gabbroic rocks, pointed to several petrologic and geochemical lines of evidence indicating that the magmas were derived from the mantle (Emslie 1978; Mitchell et al. 1995; Mitchell et al. 1996; Morse 1982; Olson 1992; Wiebe 1990). The broadly tholeiitic chemistry of the anorthosites, related residua and fine-grained basalts is the main line of reasoning supporting the mantle derivation assertion (Morse 1982; Wiebe 1990). Different mantle sources for the magmas were acknowledged based on dramatic isotopic differences between massifs astride major crustal terrane boundaries such as the Grenville Front (Ashwal & Wooden 1983; Icenhower et al. 1998). Key to many of the mantle-derivation proposals is the recognition that crustal assimilation played a role in developing the petrologic and geochemical flavour of the magmas. Stable and radiogenic isotope geochemistry data support the proposals that the magmas are derived from melting of the depleted mantle combined with all-important crustal contamination (Emslie et al. 1994; Frost et al. 2010; Peck & Valley 2000; Peck et al. 2010). These ideas culminated in a model presented by Emslie et al. (1994) as follows: Basaltic magmatic activity derived from the mantle impinges on the base of the crust, causing lower-crustal anatexis and the ascent of granitic melts that form the characteristic silicic suites associated with anorthosites. The remaining, restitic lower crust would be depleted and reminiscent of plagioclase-pyroxene granulites. The assimilation of this hot, lower-crustal residue by the mantle-derived basaltic magma during eventual ascent from the Moho, combined with fractionation, produces the observed chemical and petrologic signatures.

One challenging aspect of the mantle-derived models has been the mechanism for generating hyper-feldspathic liquids capable of producing such plagioclase-rich rocks. Did the magma experience large degrees of fractionation of mafic material, or was the magma inherently hyper-feldspathic? Emslie's model negated the

requirement for original hyper-feldspathic magmas, as combined assimilation and fractional crystallisation (AFC) is able to keep plagioclase on the liquidus for protracted periods aiding in the development significant volumes of anorthositic magma (Emslie et al. 1994; Morse 1982; Wiebe 1990).

In recent years, the idea of derivation of melts from the lower crust has become popular, based on several experimental investigations, geochemical arguments and field/geophysical observations. One of the first serious proposals developed arguments that explained various geochemical and mineralogical features by anatexis of an aluminous lower crust (Taylor et al. 1984). This lower crust had in the Archaean experienced intra-crustal melting and granitic melt separation, 100-200 m.y. prior to anatexis (Taylor et al. 1984). Re-Os isotopic data purported to show that the magmas were derived from melting of a 1570 – 1236 Ma mafic lower crust in the Rogaland region, as anorthositic and internal isotopic compositions are not realistically compatible with a depleted mantle-derived melt, variably contaminated with lower crustal material (Schiellerup et al. 2000). Significance is attached to the upper end of the lower crustal age range, as this corresponds with the major crust-forming event in southwest Norway (Schiellerup et al. 2000). Variances on this model have recently been reported using Lu-Hf data in zircon separated from high-aluminium megacrysts from anorthosites in the RAP (949-920 Ma; Schärer et al. 1996; Sauer et al. 2013), in which three lower crustal components, with ages of ~1500 Ma, ~1260 Ma and 1050-1020 Ma were suggested as probable sources (Sauer et al. 2013). Emphasis was placed on the observation that a lower crust age of ~1500 Ma cannot be a major component of the source and that crust between 1050-1020 Ma is the most likely source of the anorthositic magmas (Sauer et al. 2013). Modelling of fractional crystallisation (and assimilation) and experimental investigations of the phase stability of potential parental magmas of anorthosites – high-Al basalts (Labrador) and jotunites (Rogaland) at 10-13 kbar – indicate that these parental compositions lie on a thermal maximum between plagioclase, orthopyroxene and clinopyroxene, that in combination with peritectic-like equilbria, cause mantle-derived liquids, through fractionation and assimilation, to become nepheline-normative (Longhi et al. 1999; Longhi 2005). These liquid compositions cannot therefore form the array of mineral assemblages observed in anorthosite massifs, and must instead be formed by the anatexis of mafic plagioclase-orthopyroxene-clinopyroxene-bearing rocks at depths of 40-50 km (Duchesne 2001; Longhi et al. 1999; Longhi 2005). The association of anorthosite provinces with crustal-scale weakness zones and terrane boundaries extending to Moho offsets (particularly in the Rogaland Province) and underthrust lower crustal material is viewed as evidence for the thrusting of lower crustal material into the mantle, subsequent heating and melt generation from these lower crustal "tongues" along these major crustal structures (Duchesne et al. 1999; Duchesne 2001).

Proponents of both the mantle- and crustal-derivation models would agree that anorthosites, and the associated suite of rocks, have a strong crustal signature manifest in the crustal isotopic components and unique petrology developed in these massifs. Whether this crustal signature is indicative of lower crustal melting or of significant assimilation of lower and/or upper crustal material is contentious and the ultimate barrier preventing consensus on the source of the anorthosites.

1.1.2 The Parental Melts and Emplacement Mechanisms

Both the parental melts and the emplacement mechanisms of the derivative magmas are contested issues amongst anorthositologists. Fine-grained marginal rock types associated with the anorthosites, experimental

petrology and geochemical modelling suggest that the parental melts were either high-Al basalts or jotunites (hypersthene monzodiorite; Bédard 2010; Charlier et al. 2010; Duchesne 1984; Longhi et al. 1999; Morse 1982; Vander Auwera et al. 1998). Fine-grained marginal rocks, commonly troctolitic, noritic, gabbroic (high-Al) or jotunites provide the best field evidence for the possible parental liquids of anorthosites. Experimental work has had limited success in demonstrating that high-Al basaltic magmas were the parental melts to Proterozoic anorthosites. Longhi et al. (1999) showed that fractionation of mantle-derived liquids could not produce the full-range of troctolitic, noritic and gabbroic compositions observed in the intrusions due to a thermal divide and peritectic equilibria that work to produce nepheline-normative magmas. Related experimental work illustrates that primitive jotunitic melts could produce the anorthosites (Vander Auwera et al. 1998). However, field observations, petrology, geochemistry and modelling also point to high-Al basalts as being primitive members of the anorthosite suite and likely candidates for the parental melts (Mitchell et al. 1995; Charlier et al. 2010). The understanding of the parental melt composition for Proterozoic anorthosites is complicated by the cumulate nature of the rocks and the fact that there are missing mafic components in these samples, but the suggestion has been made that a compositional continuum between high-Al basalts and primitive jotunites indicates a mutually-inclusive relationship between these two proposed parental liquids. High-Al basalts have recently been proposed as the parental melt in anorthosite massifs traditionally thought to be derived from primitive jotunites (e.g. RAP), indicating that the balance of evidence is shifting to parental melts of high-Al basaltic composition (Charlier et al. 2010).

A challenge related to the parental melt composition has been the mechanism/s by which super-saturation of plagioclase develops in the parental magmas – a problem that has been approached from two angles. Using a basaltic magma as a starting point, one can either appeal to concentration of plagioclase by mechanical means (floatation) and subsequent rise through the crust or to crystallisation of vast amounts of plagioclase from inherently hyper-feldspathic magmas (Morse 1982; Wiebe 1990). Several mechanisms for creating these hyper-feldspathic melts have been proposed and include: 1) the existence of anorthositic liquids (Buddington 1939), 2) Delayed nucleation of plagioclase in a basaltic melt (Morse, 1982), and 3) Supersaturation of plagioclase components by resorption or remelting of plagioclase in ponded magma (Wiebe 1990). Most researchers would agree that enrichment of plagioclase by mechanical means is a vital process in the petrogenesis of these rocks, but anorthositic liquids have been ruled out mainly due to the unrealistically high temperatures required for the existence of such a melt, and no clear evidence for delayed nucleation (Ashwal 1993). No decisive evidence, however, exists to explain whether delayed nucleation or resorption are important mechanisms that operate together with mechanical concentration. Given that the parental magmas of Proterozoic anorthosites are broadly basaltic, these hyper-feldspathic compositions imply that there is a missing mafic component to the anorthosites that is, as of yet, unaccounted (Dymek and Gromet 1984). At equilibrium, basaltic magmas can crystallise, at most, 50-60 % plagioclase (Müntener and Ulmer 2006), but on average Proterozoic anorthosites contain 80-90 % plagioclase and 10-20 % of mafic minerals. This indicates that approximately 20-40 % of the mafic phases are missing.

The mechanisms by which magmas rise from mantle or lower crustal sources is an important aspect in the petrogenesis of all igneous rocks, but is of special interest for the petrogenesis of Proterozoic anorthosite massifs due to the near-monomineralic compositions and related buoyancy considerations (Berg 1977; Simmons

1964). By assessing the field geometry of granitoid intrusions (roughly circular) and associated deformation in the country rocks, many studies have suggested that granitoid magmas ascend diapirically into or through the crust, as hot, buoyant crystal mushes (Cruden 1990; Ramsey 1989; Schmeling et al. 1988). This mechanism of magma emplacement has been proposed for several anorthosite bodies, including the Rogaland Anorthosite Province, and the validity of these models has been confirmed using finite element modelling (Duchesne et al. 1985; Martignole & Schrijver 1970). More recently, the role of conduit ascent and dyking as a mechanism to deliver magma to upper crustal or surficial levels has become popular (Clemens and Mawer 1992; Petford et al. 1993). A combination of detailed mapping of the marginal deformation to plutons in the Nain Plutonic Suite and calculations of settling rate of high-Al, high-pressure orthopyroxene megacrysts versus ascent rates of the magma suggest that diapirism is untenable (Royse & Park 2000). The unique high-pressure, primitive origin of the orthopyroxene megacrysts means that magma ascent rate must exceed the terminal setting velocity of these phases in order to be preserved in the final anorthosite. Using the appropriate set of parameters, including magma mush, crystal and crustal densities, viscosities, and crystal abundance and size, Royse and Park (2000) calculated that diapiric ascent velocities would be eight orders of magnitude slower than terminal setting velocities of the megacrysts (V_{ascent} = 7.5 x 10^{-8} cm/s vs. $V_{settling}$ = 4.99-8.19 cm/s). Megacrysts ascending in magmas rising diapirically would not be carried with the magma mush, but instead sink and not be exposed in the mid-crustal anorthosites. However, Royse & Park (2000) proposed that ascent velocities associated with conduit ascent via dykes are fast enough to carry megacrysts to the appropriate crustal levels (maximum ascent velocities = 7.56 cm/s for dyke widths of 18 m). The association of many Proterozoic anorthosites with crustal scale zones of weakness (e.g. Abloviak Shear Zone associated with the Torngat Orogeny for the NPS) may provide pathways for conduit-ascent and corroborate this model (Royse & Park 2000). Assessment of the input parameters in these calculations is essential to critically evaluating this important aspect of anorthosite petrogenesis and is discussed further during arguments in Section 4.7.

1.1.3 The Tectonic Setting of Proterozoic Anorthosites

Although hypotheses regarding the source of anorthositic magmas have become polarised, both schools of thought require a source of heat to melt either the mantle or lower crust. It is this uncertain source of heat and the associated tectonic regime, only producing typical anorthosite magmas during a restricted period of the Proterozoic eon (1.8-1.0 Ga), which has evaded a convincing line of reasoning for decades (Ashwal 2010). Early ideas proposed that an extensional rifting regime might have been the most likely environment to create anorthosite massifs, as crustal extension creates the necessary space to intrude voluminous magmas, supplies ample magma to the base of the crust and typical rift-related sequences are observed together with the anorthosites (Berg 1977; Bridgewater & Windley 1973). Evidence emerged from anorthositic terranes in North America that anorthositic magmatism occurred prior (~100 m.y.) to the production of typical bimodal rift-related lithologic units and led to a shift in consensus to an anorogenic setting for Proterozoic anorthosite production (Emslie 1978). No structural evidence for rifting during anorthosite production confirms this assertion. The lack of evidence for orogenesis is well documented in the NPS of northern Labrador, where granites as old as 2.3 Ga are undeformed, the youngest recrystallisation events are 2.7-2.4 Ga and the 1.8 Ga supracrustals are unmetamorphosed and undeformed, except by the intrusion of the NPS (Berg 1977; Morse 1982). Berg (1977) points out that metamorphosed anorthosites south of the Grenville Front contradict an anorogenic setting, but reasons that these southerly intrusions may have simply been accidental participants in

the younger Grenvillian orogeny and metamorphism. Implicit in the anorogenic hypothesis is the notion that magma is produced through hot spot or mantle plume activity and that the anorthosites may mark magmatism at failed intracontinental rifts (Morse 1982). Nevertheless, the issue of anorthosite temporality is still problematic for these hypotheses, and arguments stating why anorthosites are not observed in younger, failed rifts have not been forthcoming.

Suffering from the same temporality issues, proposals that anorthosites may represent part of the deep roots of Andean-arc systems were favoured because these settings could account for long, linear arrays of anorthosites (e.g. Grenville Province, Eastern Ghats Belt) and metamorphic overprinting during eventual Himalayan-style continent-continent collision (as observed in the Grenville Province; Ashwal 1993; Hamilton 1981). The foremost argument against Andean-arc genesis is that the coeval granitoid suites in Proterozoic anorthosites are anhydrous and show strong Fe-enrichment (Ashwal 1993). Andean plutonic suites are fundamentally different, being characterised by intermediate, hydrous rock types like quartz diorite and tonalite (and volcanic equivalents: rhyolite through andesite).

The issues of restricted temporality ultimately led to non-uniformitarian hypotheses being put forward, the first of which states that large mantle superswells, caused by the blanketing effects of a stationary supercontinent between 1.6 to 1.3 Ga, gave rise to voluminous anorogenic magmatism (Hoffman 1989). This model elegantly dealt with the restricted temporality by suggesting that prior to the mid-Proterozoic, crustal mass was insufficient to form supercontinents able to insulate the mantle sufficiently, while secular cooling of the mantle by the Phanerozoic eon prevented such superswells form forming (Hoffman 1989). Supercontinent assembly in the mid-Proterozoic, therefore, presented conditions ideal for the production of voluminous, apparently anorogenic, anorthositic magmatism. A more recent variant on the non-uniformitarian, supercontinental model suggested that the assembly of the Columbia supercontinent at ~1.7 Ga created numerous downflows of subduction-related material into the mantle (Vigneresse 2005). Although material was being returned to the mantle, heat (presumably in the form of melt) was still being transferred to the base of the crust in what is known as an “antiplume” scenario. This heat transfer produces high thermal gradients where energy delivery is essentially conductive. Melting of the lower crust to produce granitic magmatism and magma intrusion therefore takes place over long periods of time. Numerical modelling indicates that such antiplume scenarios are viable and, in addition to producing voluminous magmatism, would cause supercontinent-splitting tangential forces to develop, breaking the supercontinent apart (Vigneresse 2005).

Consensus on the tectonic setting for Proterozoic anorthosites has gradually shifted towards a late- to post-orogenic setting for the production of anorthosite magmas (Corrigan & Hanmer 1997; McLelland et al. 2010; Scoates & Chamberlain 1997). This proposal is based on detailed geochronological data and tectonic reconstructions, from several anorthosite-bearing terranes that place anorthosite production in the waning stages of orogenic activity (McLelland et al. 2010). Two pulses of anorthositic magmatic activity in the Grenville Province (Marcy, Morin, and Lac St. Jean Complexes, as well as smaller complexes), both following major crustal-thickening events under brief extensional regimes, suggest that these anorthosites were emplaced in extending crust in an overall compressional orogen. The Duchesne et al. (1999) model of lower crustal tongue melting also hinges on the post-collisional reactivation of lithospheric discontinuities. Other Grenvillian and Sveconorwegian anorthositic suites show evidence of emplacement through crustal sutures in environments of

late- to post-orogenic extension, transtension or both (Scoates & Chamberlain 1997; McLelland et al. 2010). Key to these models is the decompression and delivery of asthenosphere to Moho depths and subsequent high-pressure fractionation and continuous replenishment of gabbroic magma. Anatexis of the lower crust produces the characteristic silicic end-members of the suite and contemporaneous polybaric fractionation and ascent of the anorthositic magma produces typical AMCG suites. The mechanisms that deliver asthenosphere to the base of the crust in the waning stages of orogeny are less well-understood and several possibilities include: delamination of dense, thick lithosphere, flat slab subduction with or without delamination, extension in back arc basins and slab break-off (McLelland et al. 2010). There are however exceptions to this geodynamic hypothesis, exemplified by intrusions such as the Nain Plutonic Suite that intrudes into a crustal-scale lithospheric suture between the Nain and Churchill Provinces, known as the Torngat Orogen (Hamilton 2008). Magmatism in this region has been considered anorogenic and, in this vein, McLelland et al. (2010) relate the coincidence in timing of sinistral displacement and magmatism to decompression melting of mantle beneath a reactivated suture zone experiencing transtensional displacement. However, other workers view the Torngat suture as merely facilitating magma ascent from melting of asthenosphere and/or slab during a flat-slab subduction regime initiated during Pinwarian Orogeny (Gower & Krogh 2002).

1.2 The Scope of this Work and a Hypothesis

Crustal contamination has been recognised as a significant factor contributing to the differentiation and petrogenesis of mantle-derived magmas ever since the pioneering work of Bowen (1928). Nowhere is this more apparent than in Proterozoic anorthosite massifs, where the nature and age of the crust into which the magmas are emplaced dramatically affects and obscures the original isotopic geochemistry of the magmas (Ashwal et al. 1986; Heinonen et al. 2010; Frost et al. 2010; Scoates & Frost 1996; Wiebe 1990). These obfuscated isotopic signals have fuelled debate surrounding the source and tectonic setting of Proterozoic anorthosite massifs as described in Section 1.1. The Mealy Mountains Intrusive Suite (MMIS), Nain Plutonic Suite (NPS), and Rogaland Anorthosite Province (RAP) are classic examples of Proterozoic massif-type anorthosites and are intruded into crust with markedly different age and isotopic composition, allowing clear comparison of the effects of crustal contamination (see Section 1.3). Internal isotopic disequilibrium has been observed in a variety of igneous intrusions and has been ascribed to crustal contamination (Davidson et al. 2007a; Davidson et al. 2007b). This includes a brief contribution identifying internal disequilibrium in two anorthosite massifs intruded into old, evolved crust (Ashwal and Wiebe 1989).

The petrogenesis of Proterozoic anorthosites is a truly polybaric process with crystallisation beginning beneath the Moho (30 - 40 km) and ending with emplacement at upper crustal depths (< 20 km; Berg 1977; Emslie 1975a; Charlier et al. 2010; Fram & Longhi 1992; Longhi et al. 1993; Valley & O'Neil 1982;). By virtue of their ascent and emplacement as viscous crystal-rich magmas, the anorthosites transport comagmatic products of polybaric crystallisation, such as orthopyroxene megacrysts, from a range of pressures to final emplacement at upper crustal levels (Charlier et al. 2010). The isotopic compositions of the anorthosites, in combination with that of high-pressure, cogenetic megacrysts, reflect various stages of magmatic evolution, allowing assessment of the polybaric contamination history of the magma. The contrast in the nature and age of the potential contaminants of the three anorthosite massifs, along with the distinctive provenance of orthopyroxene

megacrysts, provides unique insight into the roles of contamination and polybaric petrogenesis in the formation of Proterozoic anorthosites.

In this thesis I test how the contamination of anorthositic magma with crust of different isotopic character and age affects the whole-rock and internal isotopic composition of the anorthosites. In addition, using the polybaric properties of these rocks, I assess the crustal levels at which this contamination occurs and the implications for the petrogenesis of anorthosites. I use Sr, Nd and Pb isotopic compositions of the anorthosites, their internal minerals, and the cogenetic, high-pressure pyroxene megacrysts from the aforementioned intrusions, as well as energy-constrained AFC modelling, to show that the parental magmas were not derived from anatexis of the lower crust, but rather from melting of the depleted mantle and experienced significant lower crustal contamination in addition to minor mid- to upper crustal contamination on their ascent to final emplacement at upper crustal levels. High-pressure megacryst geochronology and geochemistry is also used to illustrate that Proterozoic anorthosite formation occurred on a hundred-million-year time scale and must have therefore developed in Andean-arc environments – the only setting capable of supplying the required volumes of magma over these timescales. These observations and interpretations are used to provide new evidence supporting recent controversial findings regarding the regional tectonic setting of the Sveconorwegian Orogen in south-western Norway. Moreover, I show that the isotopic compositions of these megacrysts provide the first direct geochemical and petrologic evidence for ponding of, and cumulate formation in, mafic magma at the Moho. I also propose that these high-pressure, ultramafic cumulates are sequestered at or beneath the Moho and represent the missing mafic reservoir that is ubiquitous in both Proterozoic anorthosites as well as in the bulk continental crust.

1.3 Geologic Setting of a Trio of Anorthosite Intrusions

In light of the dramatic effects of crustal contamination on the isotopic composition of Proterozoic anorthosites, comparison of massifs from terranes of different age and nature is a necessity. In this study I examine anorthosites emplaced into pre- and early-Labradorian orthogneisses of the Grenville Province, Archaean ortho- and paragneisses from the Torngat Orogen (the suture between the North Atlantic and Churchill Provinces; Labrador, Canada) and assess a suite of high-pressure megacrysts from the Rogaland Anorthosite Province of the Sveconorwegian Orogen (Norway; Figure 1.3).

1.3.1 The Mealy Mountains Intrusive Suite

The Mealy Mountains Intrusive Suite (MMIS; Figure 1.3), which forms part of a deep-level, thrust-stacked block in the Exterior Thrust Belt of the Grenville Province, known as the Mealy Mountains Terrane, is the largest of several anorthosite massifs in the easternmost section of the Eastern Grenville Province (Figure 1.4; Emslie, 1976, Gower et al. 2008a; Gower et al. et al. 2008b). A multitude of definitions exist for the Grenville Province or the Grenville Orogen, as it also known (e.g. Gower & Krogh, 2002; McLelland et al. 1996; Moore and Thompson 1980; Rivers 1997), but the broadest designation refers to terranes that have been affected by orogenesis between 1.3 and 1.0 Ga (Tollo et al., 2004).

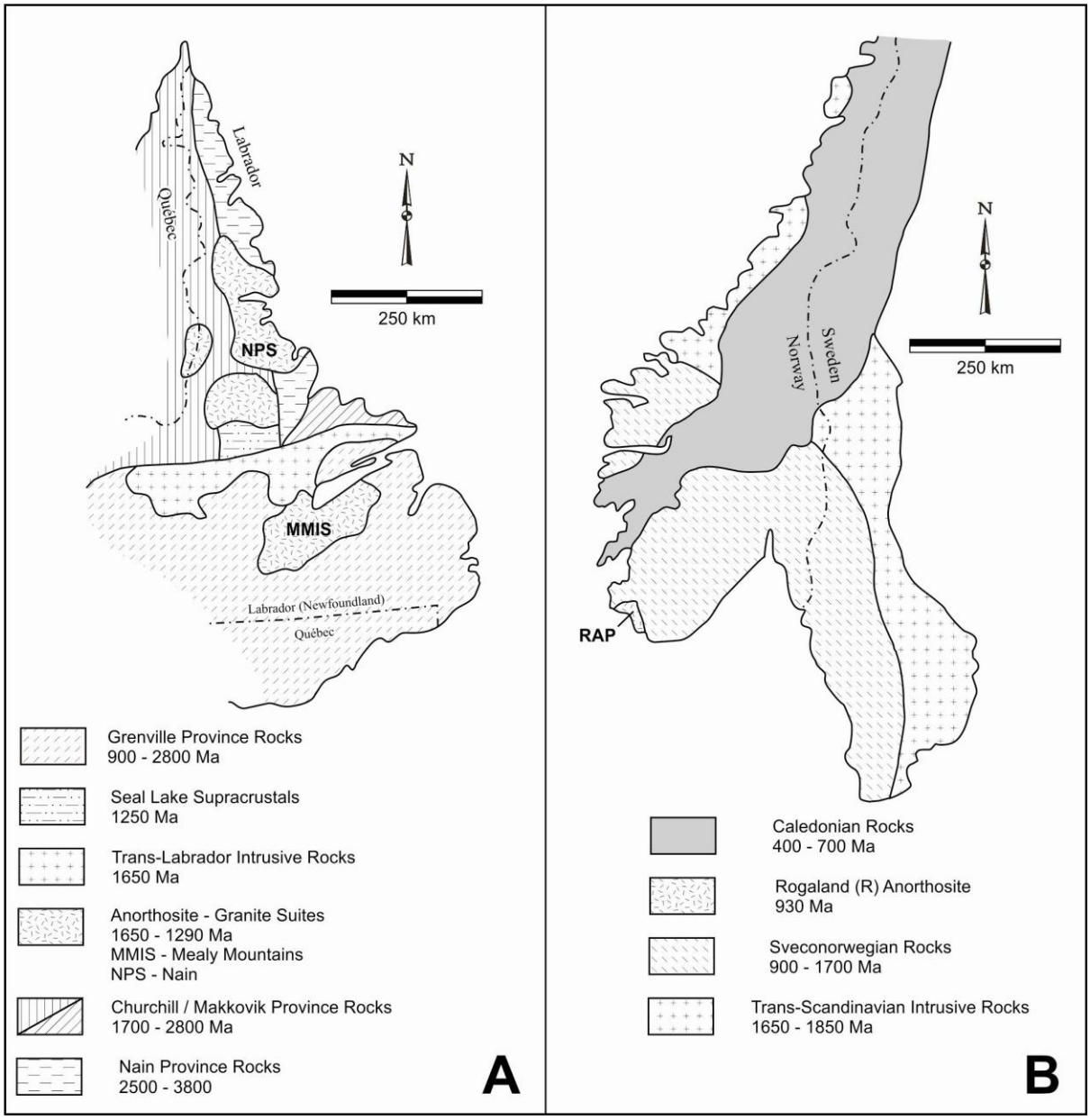

Figure 1.3 a. The geological setting of the Nain Plutonic Suite (NPS) and Mealy Mountains Intrusive Suite (MMIS) in Labrador, easternmost province of Canada. b. The Rogaland Anorthosite Province is located on the southwestern coast of Norway and intrudes into rocks of the Sveconorwegian orogen.

This definition encompasses a large number of terranes, and within North America alone the Grenville Province stretches through parts of Mexico, Texas, the Appalachians, the Adirondacks and along most of the south-eastern coast of Canada. The Grenville Province is considered a prime example of a terrane representing the deep roots of Himalayan-type collisional orogeny, although many of the igneous rocks emplaced into this province did not form during the Grenville Orogeny (1085-985 Ma). The Mealy Mountains Terrane represents an allocthonous, thrust-stacked unit of the Exterior Thrust Belt of the Eastern Grenville Province (Hegner et al. 2010). The Eastern Grenville Province (EGP); generally defined as the section of the Grenville Province east of the 68° W line of longitude, has been further divided (along the 60° W line of longitude) into western and eastern segments by Gower et al. (2008b) due to significantly different tectonic histories in each area. The

western and central terranes of the EGP display evidence of frontal ramp tectonics and collision, involving frontal thrusting and channel flow, analogous to the Himalayan-Tibetan-style orogenesis (Gower et al. 2008a). In contrast, orogenesis in the eastern-most EGP involved thrusting of the EGP over the pre-Grenvillian Laurentia in a dextral, lateral ramp regime (Gower et al. 2008a).

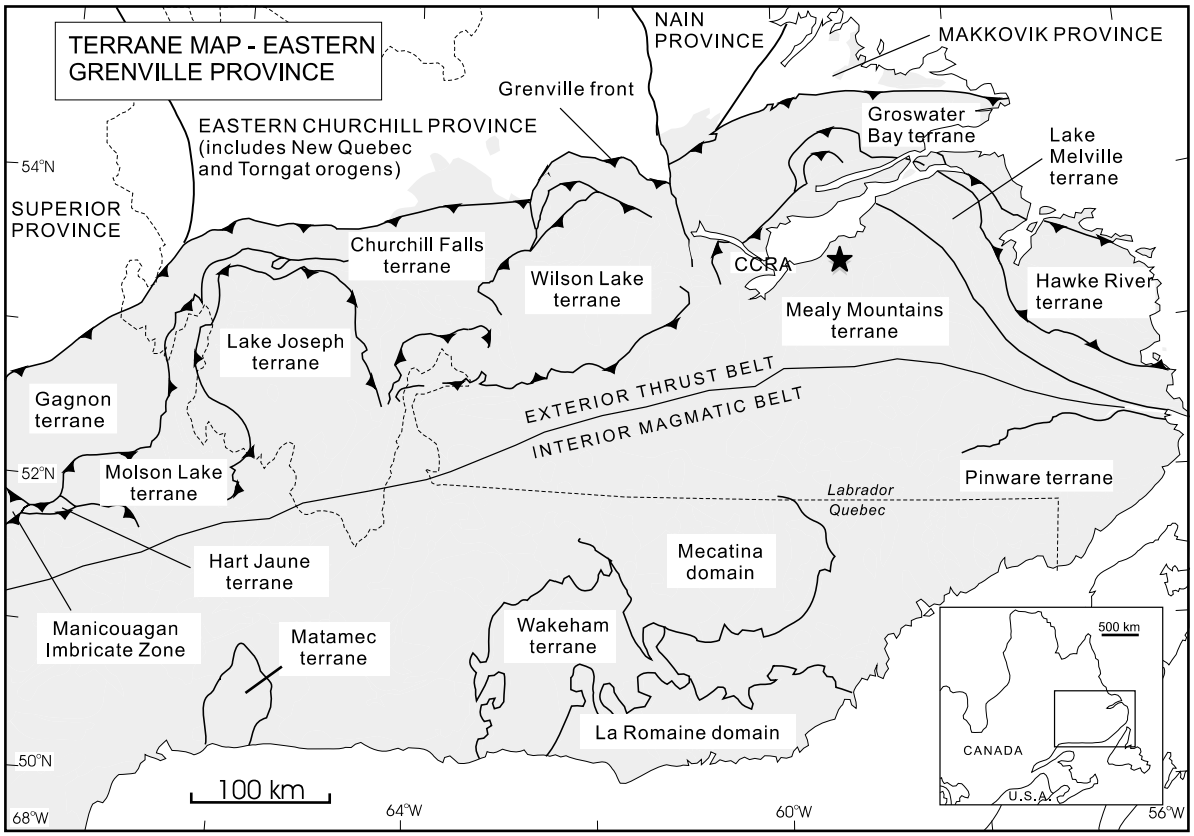

Figure 1.4 Map illustrating the various terranes making up the Eastern Grenville Province (EGP) of the Grenville Province in North America (after Gower and Krogh 2002). The EGP is separated into the Exterior Thrust Belt and the Interior Magmatic Belt. The Mealy Mountains Terrane, which is part of the Exterior Thrust Belt, plays host to the 1650-1630 Ma Mealy Mountains Intrusive Suite (as indicated by the star).

The MMIS (1650-1630 Ma; Gower et al. 2008 and references therein) lies approximately 200 km southeast of the Grenville Front and has been emplaced into relatively juvenile and immature, pre-Labradorian (1800-1770 Ma) and early-Labradorian (1710-1655 Ma) orthogneisses and paragneisses that make up a significant portion of the NE sector of the Grenville Province (Emslie & Hegner 1993; Gower et al. 2008b). Two distinct massifs make up the anorthositic member of the suite: leuconorites and pyroxene-bearing anorthosites of the Etagaulet massif and leucotroctolites and olivine-bearing anorthosites of the Kenemich massif (Emslie and Bonardi, 1979). Fe-Ti-rich rock types such as ferrodiorites (and monzodiorites) form more silicic parts of the suite along with the felsic, granitoid component, consisting primarily of mangerite (pyroxene monzonite), quartz monzonite and biotite-hornblende granite (Emslie and Bonardi 1979; Emslie et al., 1983; Hegner et al. 2010). The MMIS is also host to intriguing red-brown, pegmatitic pods, or segregations, described as graphic granites (Emslie, 1976). Geochemically, the pre-Labradorian and early-Labradorian gneisses of the Mealy Mountains Terrane, into which the anorthositic suite has intruded, are juvenile with $I_{Nd;\ 1640\ Ma}$ = 0.51040 to 0.51051 ($\varepsilon_{Nd;\ 1640\ Ma}$ = -2.27 to +0.59). Lower crustal compositions, from mafic granulite xenoliths interpreted as samples from the lower crust, range from $I_{Nd;\ 1640\ Ma}$ = 0.510522 to 0.510619 ($\varepsilon_{Nd;\ 1640\ Ma}$ = +0.10 to +2.01; Hegner et al. 2010).

1.3.2 Nain Plutonic Suite

A roughly north-south trending tectonic junction, known as the Torngat Orogen, not only plays host to the mid- to upper-crustal Mesoproterozoic Nain Plutonic Suite, but also marks a zone of oblique collision, transcurrent shear and subsequent uplift between the Archaean Nain Province and the Palaeoproterozoic Churchill/South Eastern Rae Province between 1860 and 1740 Ma (Figure 1.5; Ryan, 2000; Van Kranendonk, 1996). The NPS is part of a ~200 000 km^2 Elsonian magmatic province in Labrador and intruded during the younger of two magmatic episodes that characterise Elsonian magmatism at 1450-1420 Ma and 1330-1290 Ma (Emslie et al. 1994). The coalesced batholithic NPS assemblage of more than 12 anorthositic, granitic, troctolitic and gabbronoritic intrusions was emplaced in two distinct sequences spanning 1363-1289 Ma (Myers et al. 2008; Ryan 2000). The westernmost part and southern margin of the suite are composed of granitoids ranging in composition from quartz monzonite to granite (including syenite and monzonite) and spanning the entire age range of the NPS (Ryan 2000). The anorthosites, of which leuconorites and troctolites are dominant, separate the granitoids to the west and Archaean gneisses of the Nain Province to the east (Ryan 2000). The economically important Voiseys Bay Ni-Cu-Co deposit occurs in one of the oldest troctolitic plutons with the same name (1334 Ma; Amelin et al. 2000; Ryan 2000). A detailed analysis of the geochemistry of five major plutons in the NPS reveals significant geochemical diversity and suggests that different magmas were responsible for different individual plutons (Xue & Morse 1993). A fundamental difference in the chemistry of plutons is noted in the west and south versus the east, with workers suggesting that plutons in the east crystallised from troctolitic magma as opposed to parental noritic magmas for plutons in the west and south (Xue & Morse 1993). Small plutons, dykes and sheets of ferrodiorite are also common in the NPS, as are layered troctolitic intrusions (e.g. Kiglapait Layered Intrusion; Ryan 2000). The Torngat Orogen itself is made up of three lithotectonic components: 1) In the east, Archaean granulite- to ampibolite-grade tonalitic orthoneisses, migmatites, remnant ultramafic to anorthositic meta-igneous rocks and NW-SE- and NE-SW-trending Palaeoproterozoic diabase dykes that underlie two metamorphosed volcano-sedimentary successions, the Rama and Mugford Groups. 2) Reworked Archaean and Palaeoproterozoic gneisses of the Churchill/Rae Province form the western part of the orogen, in addition to shelf-type metasedimentary rocks and deformed Palaeoproterozoic dykes. 3) These two provinces are separated by a 50-km-long septum of quartzo-feldspathic garnet-biotite ± sillimanite paragneisses and migmatites known as the Tasiuyak Gneiss, the protolith of which is thought to be pelitic and arenitic turbidites laid down, either as an accretionary prism or on the continental margin of the eastern fringe of the Rae craton (Van Kranendonk, 1996). The Nain Plutonic Suite is generally considered a classic example of anorogenic Proterozoic magmatism based on the paucity of field evidence supporting orogenesis and because it is temporally removed, by ~ 400 m.y., from events of the Torngat Orogeny, which ended at 1.77 Ga (Bertrand et al., 1990; Emslie & Loveridge 1992).

1.3.3 Rogaland Anorthosite Province

The Sveconorwegian Orogen, host to the Rogaland Anorthosite Province, formed during Meso-Neoproterozoic times and is considered a Grenvillian correlative on the western margin of the Fennoscandian plate (Figure 1.6) within the larger Baltica or East European Craton (Bingen et al. 2008, Bogdanova et al. 2008, Rivers and Corrigan 2000). Three separate massifs, the Egersund-Ogna, Håland-Helleren and Anå-Sira bodies, make up the anorthositic end member of the RAP (Charlier et al. 2010). The Egersund-Ogna massif, from which the majority

of the megacrysts in this study are derived, is a mantled dome with margins consisting predominantly of undeformed leuconorites (Robins et al. 2008).

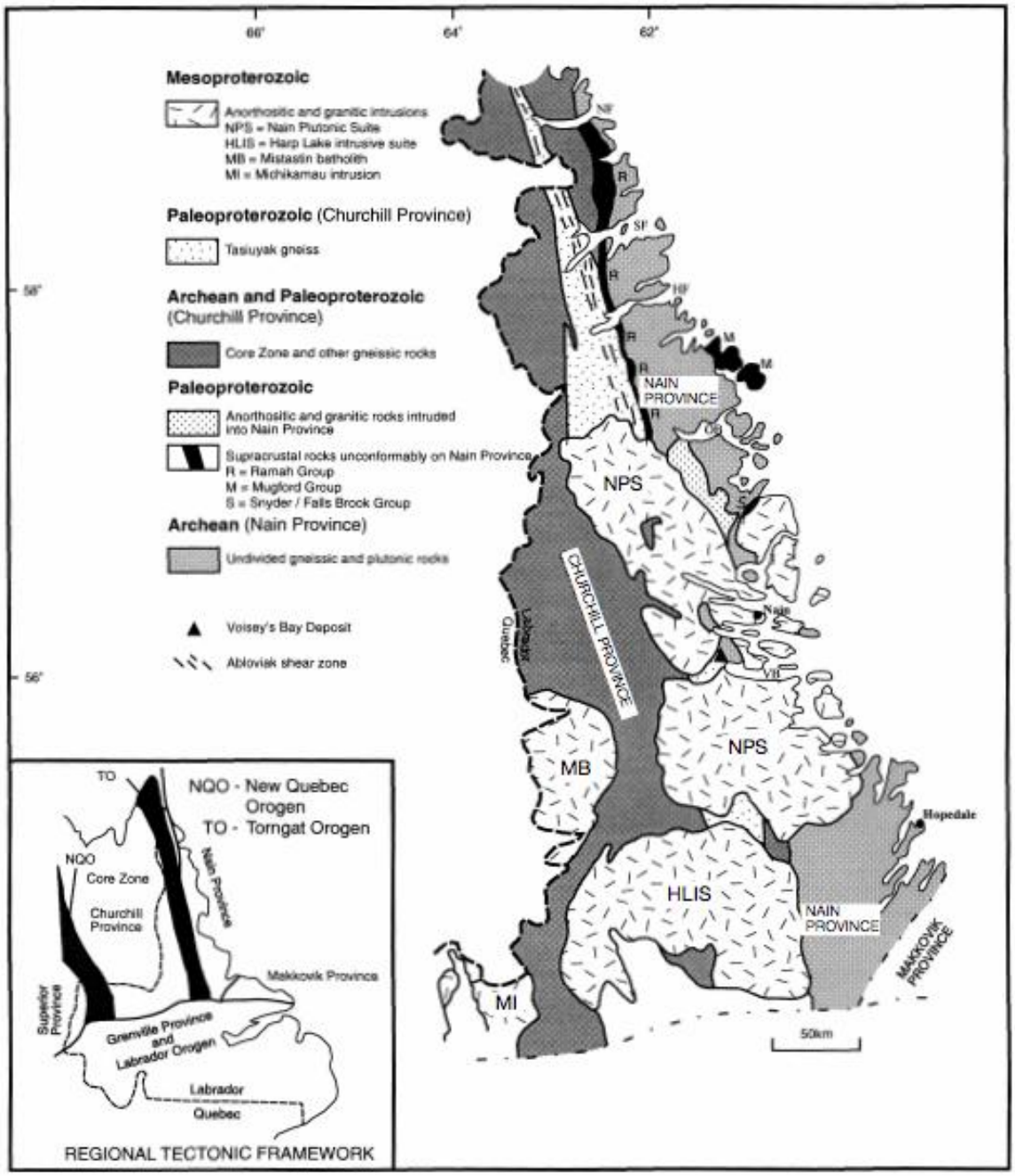

Figure 1.5 The geologic framework of eastern Labrador showing the location of the Nain Plutonic Suite in relation to other Proterozoic anorthosite massifs (e.g. Harp Lake, Mistastin and Michikamau massifs), the Torngat Orogen and the Nain and Churchill Provinces (Ryan, 2000).

The central regions of the body are composed of a leuconoritic-noritic facies known as the anorthositic-noritic complex that displays granulated, 1-3 cm plagioclase grains and hosts substantial concentrations of sub-ophitic pyroxene and plagioclase megacryst aggregates (Charlier et al. 2010). The megacrysts found in these aggregates display Al_2O_3 contents ranging from 8.66 to 2.85 wt. % and have been shown to have crystallised polybarically from 3 to 13 kbar (Charlier et al. 2010). Associated with these voluminous anorthositic bodies are a layered

intrusion, known as the Bjerkreim-Sokndal Intrusion, with rock types ranging from anorthosite to charnockite, and two leuconoritic bodies known as Hidra and Garsaknatt (Robins et al. 2008). The Anå-Sira Massif plays host to two large ilmenite ore deposits: the Storgangen sheet and Tellnes imenite-norite lens (Westphal, 2003). These rocks are emplaced into granulite facies, migmatitic gneisses that represent metamorphosed granitoids and volcanic rocks that formed at 1.5 Ga during one of the first recorded magmatic, crust-forming events in the Sveconorwegian Orogen (Bingen & Nordgulen 2008; Slagstad et al. 2012; Vander Auwera et al. 2011). These gneisses show similar juvenile characteristics to those in the Mealy Mountains Terrane with $I_{Nd;\ 930\ Ma}$ = 0.51127 – 0.51142 compositions ($\varepsilon_{Nd;\ 930\ Ma}$ = -3.28 to -0.35; Menuge 1988). Importantly, geochemical constraints on the lower crustal composition in southwestern Norway have been recorded by Othman et al. (1984), and show that the lower crust is also relatively juvenile, with a range in compositions from two samples of $I_{Nd;\ 930\ Ma}$ = 0.510521 to 0.511329 ($\varepsilon_{Nd;\ 930\ Ma}$ = -2.13 to -17.93), with no real constraints on the Sr isotopic composition.

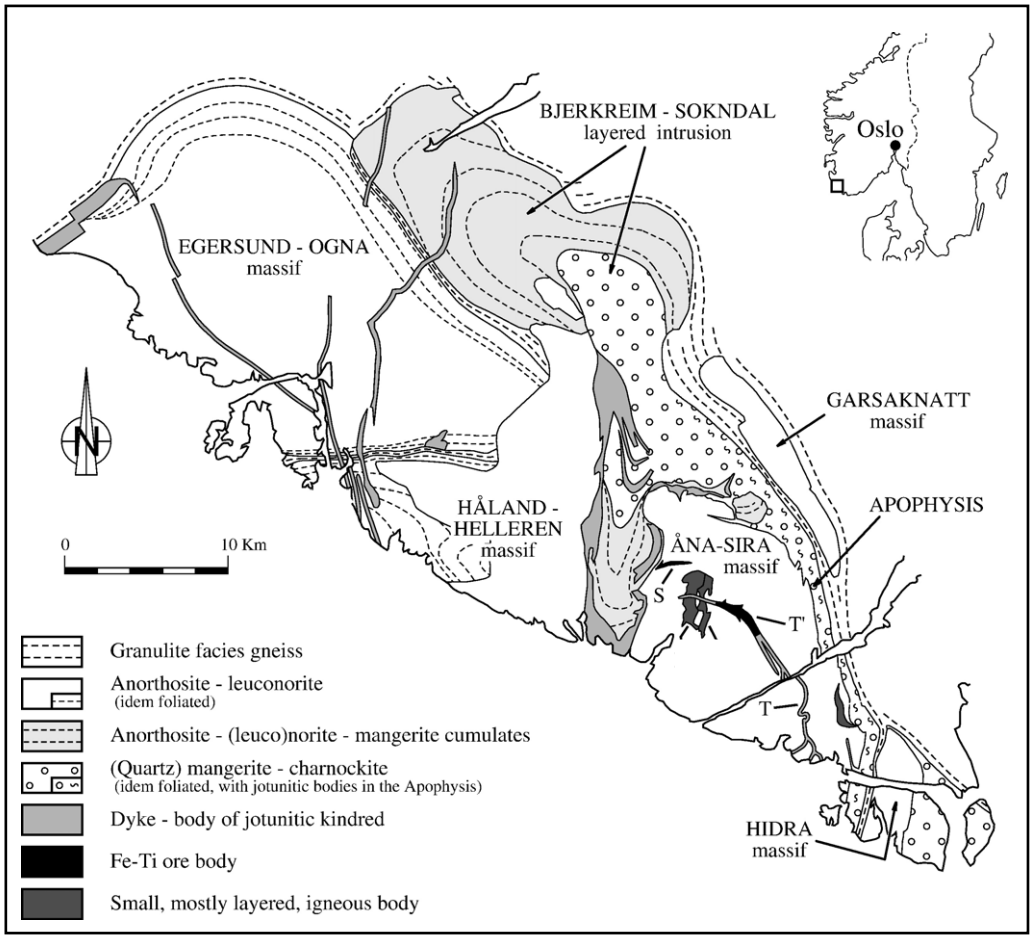

Figure 1.6 The geology of the Rogaland Anorthosite Province showing the three anorthositic intrusions (Egersund-Ogna, Håland-Helleren and the Åna-Sira intrusions) alongside the Bjerkreim-Sokndal layered intrusion (Charlier et al. 2006). Both the Tellness ilmenite deposit and Storgangen sheet are located in the Åna-Sira massif which is adjacent to two smaller leuconoritic bodies known as the Hidra and Garsanatt massofs. S: Storgangen; T: Tellnes "main dyke"; T': Tellnes ilmenite deposit. Numerous crosscutting dykes are not depicted in this map.

1.4 Methods

Anorthosites and orthopyroxene megacrysts from the MMIS and RAP were collected in 2009 and 2011, respectively, while the NPS samples were taken from the collections at the Geological Survey of Newfoundland and Labrador in 2009. The focus of sampling in the RAP was to collect high-alumina megacrysts with a wide range of Al_2O_3 contents representing crystallisation at a range of pressures. Samples were coarsely crushed using a carbide-steel jaw crusher and milled to a powder using a carbide-steel swing mill in the School of Geosciences (Univ. Witwatersrand). Mineral phases were separated from the rocks through sieving of coarsely milled samples to 180-250 μm, magnetic separation using a Frantz magnetic separator, hand picking to ensure purity and to eliminate any alteration and finally, rinsing with milliQ water before digestion for isotopic chemical procedures. Major element XRF data were obtained on a Panalytical PW2404 spectrometer in the Earth Lab at the University of the Witwatersrand, using procedures described in Wilson (2012). A full suite of trace elements were analysed at the Department of Geological Sciences at the University of Cape Town using a Perkin-Elmer ELAN 6000 ICPMS using methodology similar to that reported in Le Roux et al. (2001). Radiogenic isotopic abundances and concentration data, for Rb, Sr, Sm, Nd and Pb were analysed at the Department of Terrestrial Magnetism (DTM) of the Carnegie Institute of Washington using isotope dilution, ion-exchange chromatography and a combination of Thermal Ionisation Mass Spectrometry (TIMS for Sr and Nd) and Multi-Collector Inductively Coupled Mass Spectrometry (MC-ICPMS for Rb, Sm and Pb). Rb, Sr, Sm, Nd and Pb were separated using cation-exchange chemical separation using methods similar to those described in Carlson et al. (2006) and Heinonen et al. (2010). Sr and Nd were measured by TIMS using a Thermo-Fischer Triton instrument, while Rb, Sm and Pb were analysed using a Nu Plasma HR MC-ICPMS. A static measuring mode was used with double Re filaments during TIMS analyses. The data are reported relative to in-run averages of three JNdi standard measurements and were corrected for fractionation using $^{146}Nd/^{144}Nd = 0.7219$. Over a two year period, JNdi produced a running average of $^{143}Nd/^{144}Nd = 0.512113 \pm 0.000002$ (n = 27) compared to the accepted in-house value of $^{143}Nd/^{144}Nd = 0.512117$. Sm analyses were internally corrected for mass fractionation using $^{147}Sm/^{152}Sm = 0.56081$ and measurements were monitored for Gd and Nd interferences. The NBS-987 standard was used for reporting Sr isotopic analyses and produced a running average of $^{87}Sr/^{86}Sr = 0.710264$ (n = 24; over a two year period). Mass fractionation was monitored and corrected for during Pb analysis by comparing bracketing runs of NBS 981 standard values to values reported by Todt et al. (1996). NBS 981 running averages over a two-year period are $^{208}Pb/^{204}Pb = 38.0891$, $^{207}Pb/^{204}Pb = 15.8912$ and $^{206}Pb/^{204}Pb = 17.3479$. Blank measurements were consistently in-line with Department of Terrestrial Magnetism norms of Rb: 7 pg, Sr: 306 pg, Sm: 3 pg, Nd: 60 pg, Pb: 100 pg. All data are presented in Appendices A-F.

1.4.1 Zircon Separation and Geochronology Methodology

Pegmatitic pods in the MMIS, many with visible zircon in hand specimen, were selected for geochronological analysis. All samples from the Mealy Mountains Intrusive Suite selected for age dating initially underwent zircon separation in the Earth Lab in the School of Geosciences at the University of the Witwatersrand, followed by zircon selection and analysis in the Jack Satterly Geochronology Lab at the University of Toronto (JSGL). Conventional crushing and grinding techniques (using a carbide-steel jaw crusher and disc mill) were employed, followed by a shaking water (Wilfley) table procedure to obtain initial heavy mineral concentrates. Final first-order concentrations were achieved via standard Frantz magnetic separation techniques and with methylene

iodide heavy liquids. All of the pegmatitic pods yielded tens to hundreds of zircon grains except for pod CG09-27C, from which no zircons were found. Several anorthositic samples were also processed for geochronology, but only one sample, CG09-21, yielded a viable zircon fraction.

Hand-picking of highest-quality zircon grains was achieved under ethanol in a petri dish, using a binocular microscope. Selected grains were as free as possible of cracks, alteration, inclusions, and any optical evidence of cores. They were then digitally photographed and analyzed using conventional isotope dilution - thermal ionization mass spectrometry (ID-TIMS) methods at the JSGL. Zircons were pretreated with a chemical abrasion procedure (modified after Mattinson, 2005) which involved annealing at 1000°C for approximately 48 hrs followed by leaching in a dilute mixture of HF:HNO_3 for 6 hrs at 200°C. Final weight estimates were made from a digital measurement of grain dimensions and mineral density. Final zircon grains selected for analysis were washed on parafilm with nitric acid, rinsed with ultraclean water, and loaded into Teflon bombs with concentrated HF along with a mixed ^{205}Pb - ^{235}U isotopic tracer solution (Krogh, 1973). Dissolution occurred over four days at 195°C, after which fractions were dried down with phosphoric acid and loaded with silica gel directly onto outgassed rhenium filaments.

The isotopic compositions of Pb and U were measured using a single Daly collector with a pulse counting detector on a solid source VG354 mass spectrometer. A detector mass discrimination of 0.053% per atomic mass unit (AMU) and dead times of 20 nsec were employed for Daly detector measurements. A thermal source mass discrimination correction of 0.1% per atomic mass unit was applied for both Pb and U. The assigned laboratory blank for U was 0.2 pg, while that for Pb is routinely measured below 1 pg. Error estimates were calculated by propagating known sources of analytical uncertainty for each analysis including within-run ratio variability, uncertainty in the fractionation correction, and uncertainties in the isotopic composition of laboratory blank. Uncertainties for the ID-TIMS data are given at the 95% (2σ) confidence level. Initial corrections were made using an in-house data reduction program (UTILAGE). Decay constants used in age calculations are those of Jaffey et al. (1971). Graphical data presentation and quoted ages were generated using the Microsoft Excel Add-in Isoplot/Ex v. 3.00 of Ludwig (2003).

1.5 Anorthosite and Orthopyroxene Megacryst Petrography

Anorthosites from all three intrusions under consideration typify the dominant rock types in Proterozoic anorthosites in general and range in composition from anorthosites (*sensu stricto*) to leuconorites, leucotroctolites and leucogabbros. The following sections detail the petrography and sampling locations of anorthosites from the MMIS (Figure 1.7a), NPS (Figure 1.7b) and RAP (Figure 1.7c) while summarising the body of knowledge relating to the anorthosite petrography (Figure 1.8).

1.5.1 Anorthositic Lithologic Units

The MMIS is characterised by a sub-equal distribution of anorthosite, leuconorite and leucotroctolite with anorthosite occurring in both the Etaugalet and Kenemich massifs, while leucotroctolite is restricted to the Kenemich massif and leuconorites to the Etaugalet massif. As this nomenclature suggests, the sampled anorthosites from the MMIS (Figure 1.7a) contain varying proportions of orthopyroxene, minor clinopyroxene, olivine, Fe-Ti-oxide and biotite (Figure 1.8 a-c). Plagioclase of the anorthosites is generally sub- to euhedral

with wide variation in size from a few millimetres to several tens of centimetres in length (Figure 1.8 a and c). Plagioclase, where euhedral in the MMIS and anorthosite massifs in general, tends to be tabular and commonly carries very fine inclusions of Fe-Ti oxide. These inclusions, thought to be exsolution products within plagioclase (Anderson 1966), produce colour variations depending on the composition, ranging from black, bluish-grey to shades of red/pink/purple in plagioclase crystals on a macroscopic level (Ashwal & Wooden 1989; Buddington 1939; Emslie 1975b). Annealing and adcumulate overgrowth commonly obscures primary lath-like plagioclase structure in several samples from the MMIS. Minor sericitisation is observed in some samples (Figure 1.8a). True anorthosites sampled in the MMIS show annealed textures with very minor amounts of orthopyroxene and clinopyroxene in the small interstices of triple-point boundaries or on the boundaries between plagioclase grains. Orthopyroxene in the leuconorites is commonly intercumulus, although examples of subhedral, cumulate grains are observed in several samples (Figure 1.8b). Flecks and elongate laths of iron oxide characterise the orthopyroxene in all of the anorthosites. In some cases, both cumulus and intercumulus grains are observed in the same samples. Olivine occurs as both a cumulus and intercumulus phase in the leucotroctolites and is commonly fractured and altered to serpentine. In these rocks, clinopyroxene and orthopyroxene are observed discontinuously rimming olivine in what may be a peritectic reaction relationship – a feature that has also been observed in the Harp Lake massif, although suggestion has been made that these rims may also be post-cumulus in origin (Emslie, 1980). In the MMIS, orthopyroxene commonly forms the first rim, followed by clinopyroxene. Although within any given anorthosite massif many rock types will display pristine igneous textures, Longhi and Ashwal (1985) note that granular textures are also common, where two-thirds of the grains are anhedral, deformation twinning is observed and plagioclase-plagioclase boundaries appear ragged. These two contrasting textures are commonly noted in different samples from the same complex (e.g. Harp Lake; Longhi & Ashwal 1985) and have also been observed in this study in the MMIS and NPS (Figure 1.8a and b).

All of the samples from the NPS (Figure 1.7b) are leuconoritic (Figure 1.8c), but as described above, the NPS contains a diverse range of rock types from troctolite, anorthosite, diorite and granite. Typical leuconorites from the NPS present intercumulus orthopyroxene in addition to cumulus plagioclase and minor Fe-Ti oxides as well as clinopyroxene. Adcumulate and annealed/polygonal textures are common, but euhedral plagioclase laths also characterise several samples. Although orthopyroxene is the predominant pyroxene in Proterozoic anorthosites, several samples obtained from the NPS display inverted pigeonite with course, blebby exsolution lamellae – a texture also observed in other anorthosite massifs (Ashwal 1982; Ashwal 1993; Bohlen & Essene 1978). These pyroxene compositions and textures are more rarely observed in the MMIS. A spectrum of recrystallisation is observed in the NPS. Many samples are pristine, but others show signs of variable recrystallisation and sericitic alteration, including the development of bulbous, wart-like myrmekitic textures on the plagioclase grain boundaries. Similar calcic myrmekites, developed predominantly on plagioclase boundaries, described by Dymek & Schiffries (1987) in the Saint-Urbain massif were ascribed to a corrosive reaction, known as steam corrosion, between cumulate plagioclase grains and high-temperature, aqueous fluid.

The RAP is composed predominantly of anorthosite and leuconorite with a notable absence of leucotroctolites. Sampling in the RAP focused on high-Al megacrysts and consequently very few leuconorites samples have

been analysed in this intrusion. The map in Fig 1.7c shows sample locations of orthopyroxene megacrysts in the predominantly leuconoritic Egersund-Ogna massif of the Rogaland Anorthosite Province (Figure 1.7c).

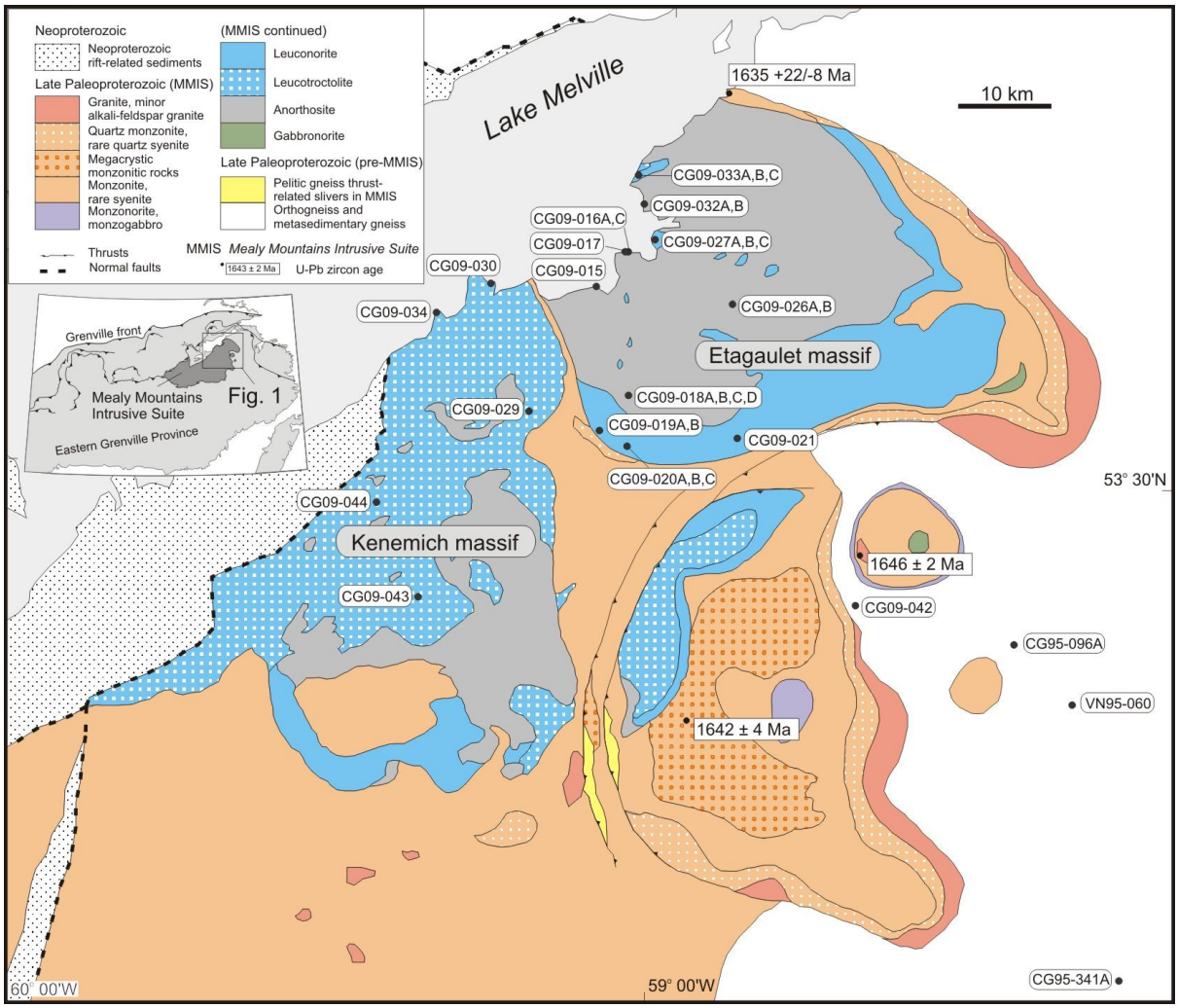

Figure 1.7a A simplified map of the Mealy Mountains Intrusive Suite (MMIS) located in the Eastern Grenville Province showing sampling locations and previously dated samples reported in Gower et al. (2008).

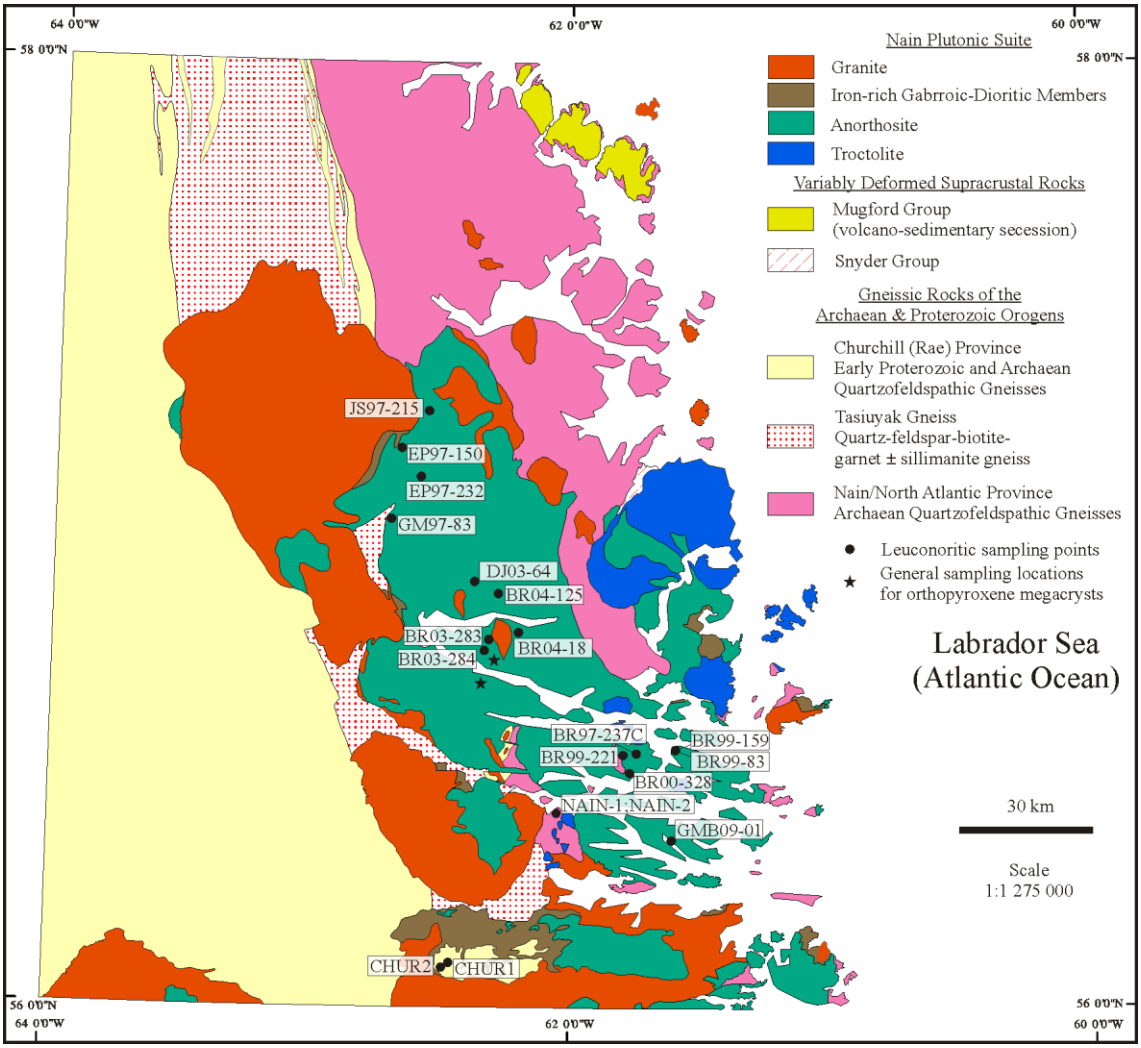

Figure 1.7b A simplified map of the Nain Plutonic Suite (NPS) intruding along the Torngat Orogen which marks the suture between the Palaeoproterozoic Churchill and Archaean Nain Provinces (after Ryan 1990). Stars indicate generalised locations for several orthopyroxene megacryst sampling locations, simplified for clarity.

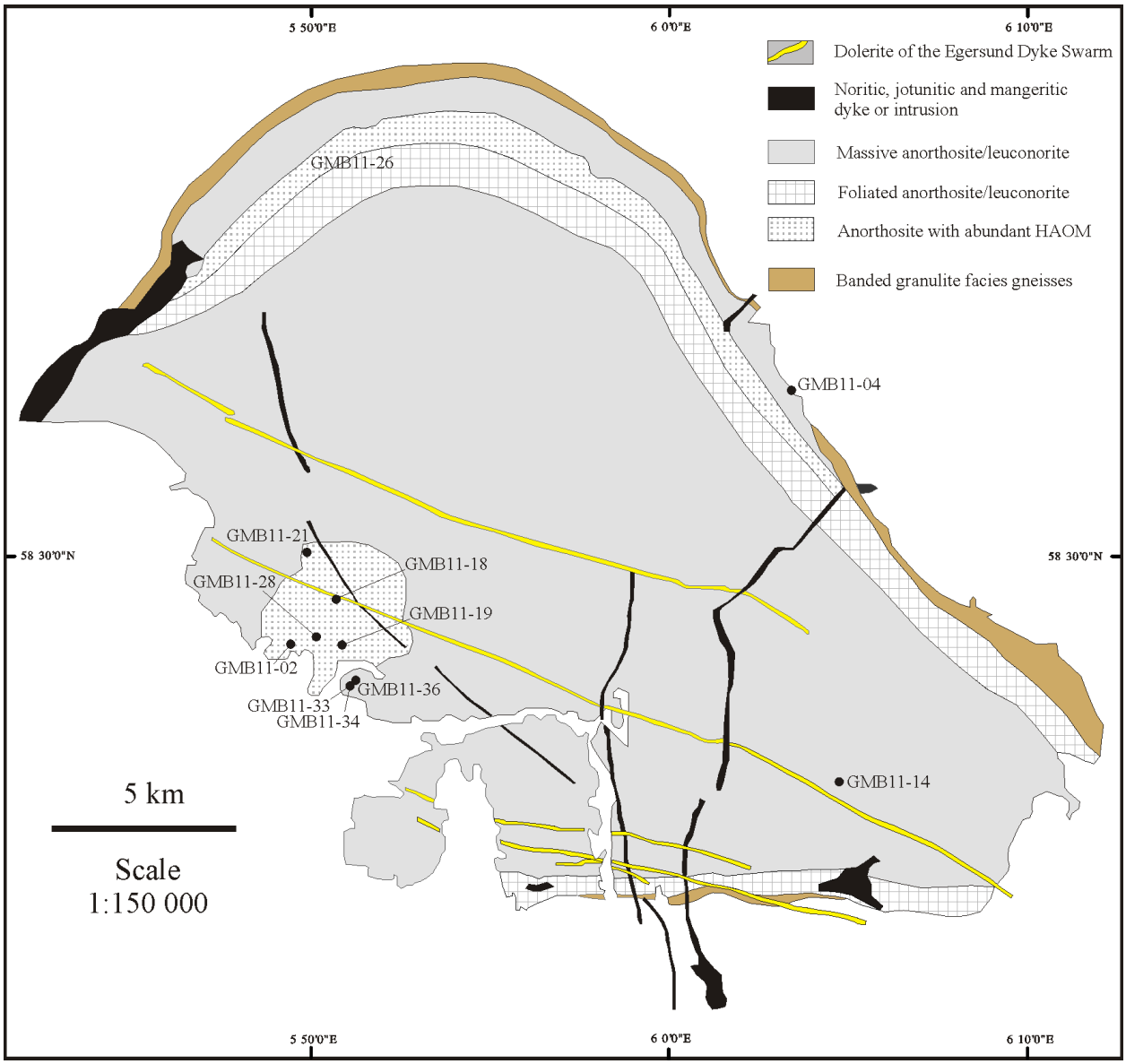

Figure 1.7 c Geological map showing megacryst sampling localities in the Egersund-Ogna Massif of the Rogaland Anorthosite Province (RAP; after Charlier et al. 2010).

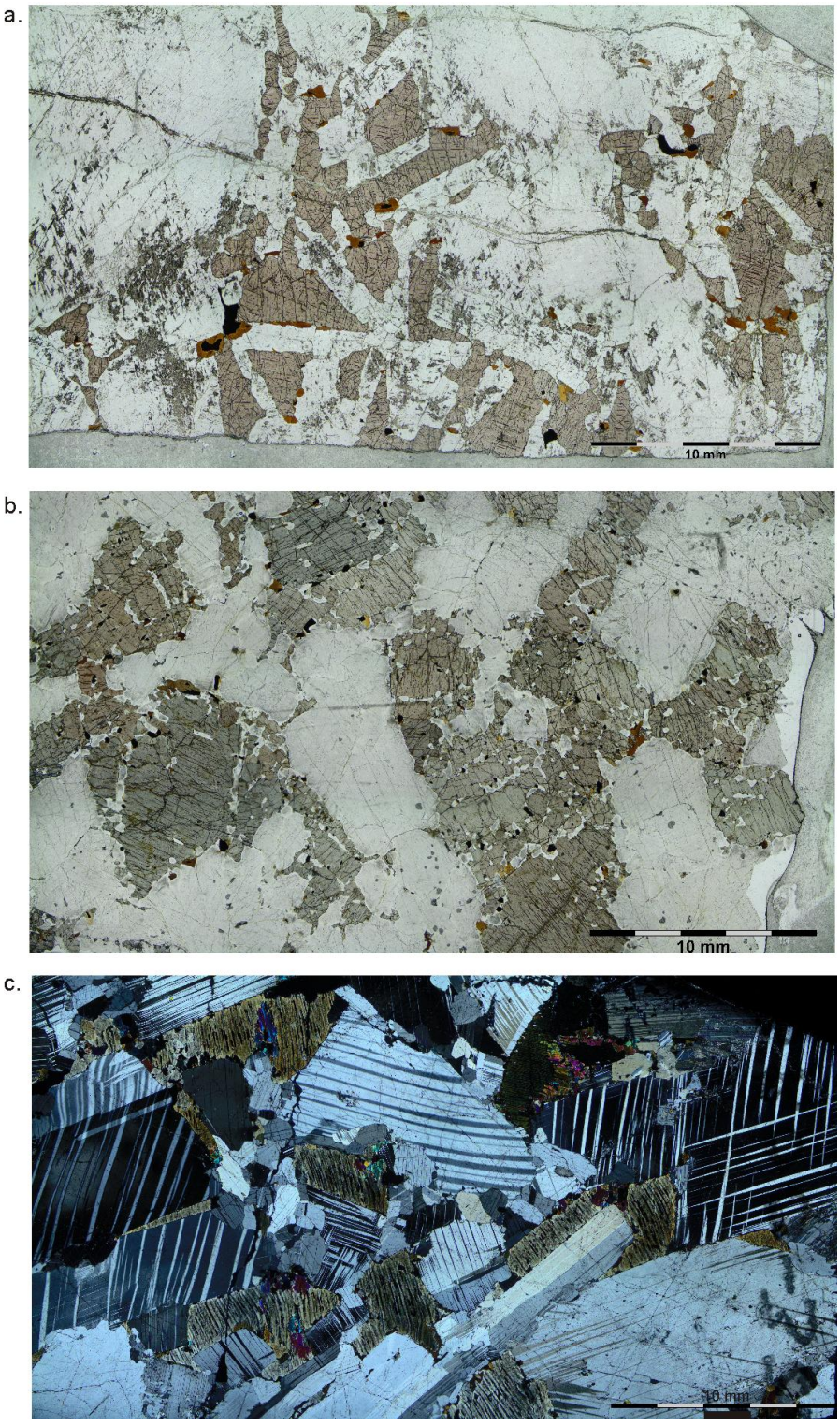

Figure 1.8 a. Typical leuconorites from the Etaugalet massif of the MMIS illustrating intercumulus orthopyroxene in addition to minor biotite and magnetite (CG09-17) set within euhedral, tabular plagioclase grains (ppl). b. When compared with a., this sample (CG09-26A) displays a different texture, perhaps due to recrystallisation with rounded orthopyroxene crystals set among both tabular and euhedral plagioclase crystals (ppl). c. A typical leuconorite sampled from the NPS showing intercumulus orthopyroxene (with pervasive oxide rod-like inclusions), sub- to anhedral plagioclase (variably deformed) and minor clinopyroxene.

1.5.2 Orthopyroxene Megacrysts

Orthopyroxene megacrysts are ubiquitous in Proterozoic massif-type anorthosites and the orthopyroxene megacrysts studied in this contribution show the typical features such as plagioclase exsolution lamellae and pervasive inclusions of Fe-oxide minerals. In both the MMIS and RAP, these megacrysts either occur as single, euhedral to subhedral crystals or form part of aggregates of several subhedral megacrysts. Megacryst habit in the NPS is more varied and in addition to occurring as single, curved crystals or giant aggregate pods, these phases also occur as single, angular pyroxene crystals with an intercumulus relationship to surrounding plagioclase (Morse 1976). In the MMIS, field observations, in addition to collations of previous field workers' observations, shows that the orthopyroxene megacrysts are restricted to leuconorite-bearing rock types and appear to be absent in the olivine-bearing Kenemich massif. Similar correlations between orthopyroxene-bearing rock types and presence of megacrysts are also noted in the leuconoritic RAP, where the vast number of megacrysts is impressive (Charlier et al. 2010). More detailed megacryst petrography is discussed in Chapter 2.

Megacrysts from the MMIS are undeformed and pristine and while the outer margins of the RAP do preserve deformed and recrystallised megacrysts, the only samples collected from the RAP were pristine and showed no signs of post-intrusion alteration. On the other hand, many of the samples from the NPS show signs of recrystallisation and some samples show kink-banding caused by deformation.

1.6 A Summary of Scientific Contributions

The subsequent chapters in this thesis are extended versions of four research papers that are currently in various stages of assessment (from in preparation to in press) at different international geoscience journals including *Earth and Planetary Science Letters* (Chapter 2), *Terra Nova* (Chapter 3), *Journal of Petrology* (Chapter 4) *and Contributions to Mineralogy and Petrology* (Chapter 5).

The first contribution in this thesis (Chapter 2) uses new geochemical information from high-Al megacrysts and host anorthosites in the MMIS, NPS and RAP intrusions to investigate broad issues related to the anorthosite petrogenesis, such as magma source and tectonic setting. This contribution presents the first comprehensive Nd and Pb isotopic analyses on suites of orthopyroxene megacrysts in the literature and reveals that the megacrysts in three different massifs crystallised ~100 m.y. before final anorthosite crystallisation at upper crustal levels. This result is surprising and significant as it indicates that the anorthosite system is long-lived and is only likely to remain active for this length of time in an Andean-arc margin. This is the only plausible regime that can supply heat and material to a restricted area at the base of the crust over such timescales. In addition to refining the tectonic setting for Proterozoic anorthosites, the megacrysts, which track depleted mantle evolution in the terranes where crust is juvenile, suggest that the magmas were derived from this reservoir and subsequently interacted with the crust before crystallising these high-pressure phases. On a global geodynamic scale, the observation of isochronous suites of megacrysts, 100-130 m.y. older than the comagmatic hosts, indicates that the magmas ponded at the Moho for significant periods. Finally, the bulk continental crust, like Proterozoic anorthosite massifs, is missing a significant mafic component. The observation of dense, ultramafic cumulate formation below the Moho provides evidence for a mechanism explaining, at least in part, how the origin of the missing mafic crustal component – a mechanism that must be considered in future studies on the evolution and differentiation of the continental crust. These mafic cumulates are either sequestered beneath the Moho, or sink

deeper into the mantle and may then contribute chemically to other chemical reservoirs within the Earth, such as EM1.

Chapter 3 discusses recent controversies regarding the tectonic setting of the Sveconorwegian orogen in light of the results and interpretations presented in Chapter 2. The Sveconorwegian orogeny in southwestern Norway has long been considered a typical, Himalayan-type, continent-continent collisional orogeny with associated crustal melting and metamorphic characteristics. Based on the model that Proterozoic anorthosites are derived from lower crustal melting in the waning stages of orogeny, the location of the RAP has been used as evidence for a collisional orogeny. New evidence for anorthosite formation from depleted mantle in long-lived, Andean arcs, presented in Chapter 2, contradicts these arguments and directly supports a recent assertion that the Sveconorwegian Orogeny was accretionary, as opposed to collisional for much of its history. In this research I also address the U-Pb and Lu-Hf zircon-in-megacryst geochronology that was used to date the RAP and support its derivation from lower crustal sources. Exsolution geochronology of the megacrysts shows that timing of plagioclase exsolution coincides with the zircon ages, suggesting that zircons recovered from the megacrysts are not dating crystallisation of the megacrysts, but rather timing of exsolution. Finally, I assess whether the megacryst geochronology and resulting interpretations discussed in Chapter 2 and 3 can be reconciled with regional field relations and tectonic settings in southern and northern Labrador.

The focus of Chapter 4 shifts predominantly to the MMIS and NPS where I assess the degree of isotopic disequilibrium between internal mineral phases, whole-rock compositions and high–pressure megacrysts. The degree of disequilibrium is found to depend on the age and nature of the surrounding crust, with significantly higher degrees of disequilibrium observed in the NPS. Orthopyroxene and plagioclase in the MMIS do also indicate disequilibrium with the whole-rocks, but to a lower degree than in the NPS. The polarity of disequilibrium is unexpected; intercumulus orthopyroxene is generally isotopically primitive compared to the reference value/isochron, while plagioclase is in equilibrium or slightly more evolved. High-pressure orthopyroxene megacrysts also show significant disequilibrium, but are also the most primitive. These unexpected disequilibrium polarities are partly attributed to an averaging effect during mineral separation and solution TIMS analyses, but also indicate that a large proportion of the chemical ‘flavour’ of anorthosites is imparted during lower-crustal contamination, with a relatively small contribution from the mid- to upper crust. Energy-constrained AFC modelling (EC-RAχFC) shows that it is possible to produce the observed isotopic compositions of megacrysts, whole-rocks and minerals with predominantly lower-crustal contamination. The strong influence of lower crustal assimilation together with the unique disequilibrium geometries observed in the anorthosites indicates that a large proportion of the crystallisation took place at lower crustal depths, suggesting the these diapirs rose into the mid-crust with high degrees of crystallinity (> 50 %).

The final chapter deals with the final stages of anorthosite crystallisation by discussing the petrology and geochemistry of highly evolved, pegmatitic, graphic pods found in the MMIS. Age dating on zircons from these pods was undertaken by M.A. Hamilton at the Jack Satterly Lab at the University of Toronto and confirms that the MMIS was emplaced between 1654-1628 Ma. Based on unique textures, including resorption relationships, reactive myrmekites, graphic and symplectic intergrowths and pegmatitic grain size, in addition to evolved chemistry, I interpret these pods as the residual liquids of anorthosites, preserved *in situ*. Although the observation of *in situ* residual liquids is not particularly new, the mineralogical and chemical diversity observed

in five of these rare pods is noteworthy. The compositions of these pods range from essentially anorthosite and gabbronorite, through monzodiorite and quartz monzodiorite to monzogranite. This range spans all of the compositions that have been suggested as potential residual liquids and illustrates that the final stages of anorthosite crystallisation can be expected to produce a wide range of rock types. Observation of a pod with Fe-enrichment in an olivine-bearing anorthosite, in contrast with the other pods that show clear Si-enrichment in orthopyroxene-bearing rock types, suggests that the fundamental composition of magmas and the amount of crustal contamination may have a significant role to play in the nature of the residual liquid of Proterozoic anorthosites.

2 Giant Pyroxene Megacrysts in Anorthosites: Revealing Continental Crust Forming Processes at Moho Depths

The mismatch between bulk, intermediate compositions (SiO_2 > 60 %) of the continental crust and predicted basaltic compositions (SiO_2 < 50 %) of mantle-derived melts in crust-forming environments poses a major problem in models of crustal evolution and requires that a mafic component be physically separated from felsic end-members (Jagoutz et al. 2011; Jagoutz & Schmidt 2012; Rudnick 1995; Rudnick & Gao 2003; Tatsumi 2005). Although information from the crust-mantle interface, where these poorly understood crustal differentiation processes are likely to occur, is rare, I explore possible constraints on these processes as revealed by Proterozoic anorthosite massifs. These temporally-restricted plagioclase-rich intrusions that, like the continental crust, suffer mafic mass balance problems, were emplaced as crystal-laden magmas carrying with them giant (up to 1 m in length), cogenetic, high pressure, high-Al orthopyroxene megacrysts (HAOMs; 3-9 wt% Al_2O_3; Fig. 2.1; Appendix A; Ashwal 1993).

Four independent studies using general petrography/geochemistry (Wiebe 1986), Al-in-orthopyroxene geobarometry (Emslie 1975a), experimental work (Longhi et al. 1993; Fram & Longhi 1992) and major element geochemical modelling (Charlier et al. 2010), show that HAOMs crystallised from fractionating magmas, beginning at pressures of 10-15 kbar (30-40 km). These crystallisation depths are at, or near, the Moho, a depth seldom sampled by other geological processes, and are far deeper than the emplacement depths of the host anorthosites (<10-20 km; Berg 1977; Valley & O'Neil 1982). Although Al-content in many mafic systems is not always the sole indicator of depth of crystallisation, detailed calibration and studies on pyroxenes from the anorthositic system show that Al-content is a well-calibrated geobarometer. Dymek & Gromet (1984) and Morse (1975) have refuted this by suggesting that these megacrysts were products of rapid *in-situ* crystallisation due to an increased incorporation of Al_2O_3 into orthopyroxene at the liquid-crystal interface as a result of sluggish diffusion of Al_2O_3 into the liquid. Had this been the case, the Cr_2O_3 content of the megacrysts would have been depleted. This, however, does not occur, and a natural, positive correlation of Cr_2O_3 and Al_2O_3 is observed (Longhi et al. 1993). Thus HAOMs provide a rare window into magmatic processes at the crust-mantle interface and provide insight into crustal-mantle differentiation processes, since high-viscosity anorthositic magma mushes fortuitously trap this high-pressure ultramafic material and transport it to mid-crustal levels. The Nd- and Pb-isotopic compositions of these giant HAOMs, from the Mealy Mountains Intrusive Suite (MMIS), Nain Plutonic Suite (NPS, both in Labrador, Canada) and Rogaland Anorthosite Province (RAP, Norway; Figure 1.3 and 1.7), provide direct evidence that ponding of upwelling magmas and dense cumulate formation in these magmas occurs at the Moho.

Igneous relationships between HAOMs and surrounding megacrystic plagioclase (Emslie 1975) and geochemical modelling (Charlier et al. 2010) indicate a cogenetic relationship between them and their host anorthosites (Figure 2.1). Microscopically, these HAOMs are unzoned crystals of orthopyroxene with abundant, thin, planar, calcic plagioclase exsolution lamellae (average An_{80}) occasionally showing inclusions of olivine, ilmenite and biotite (Emslie 1975a).

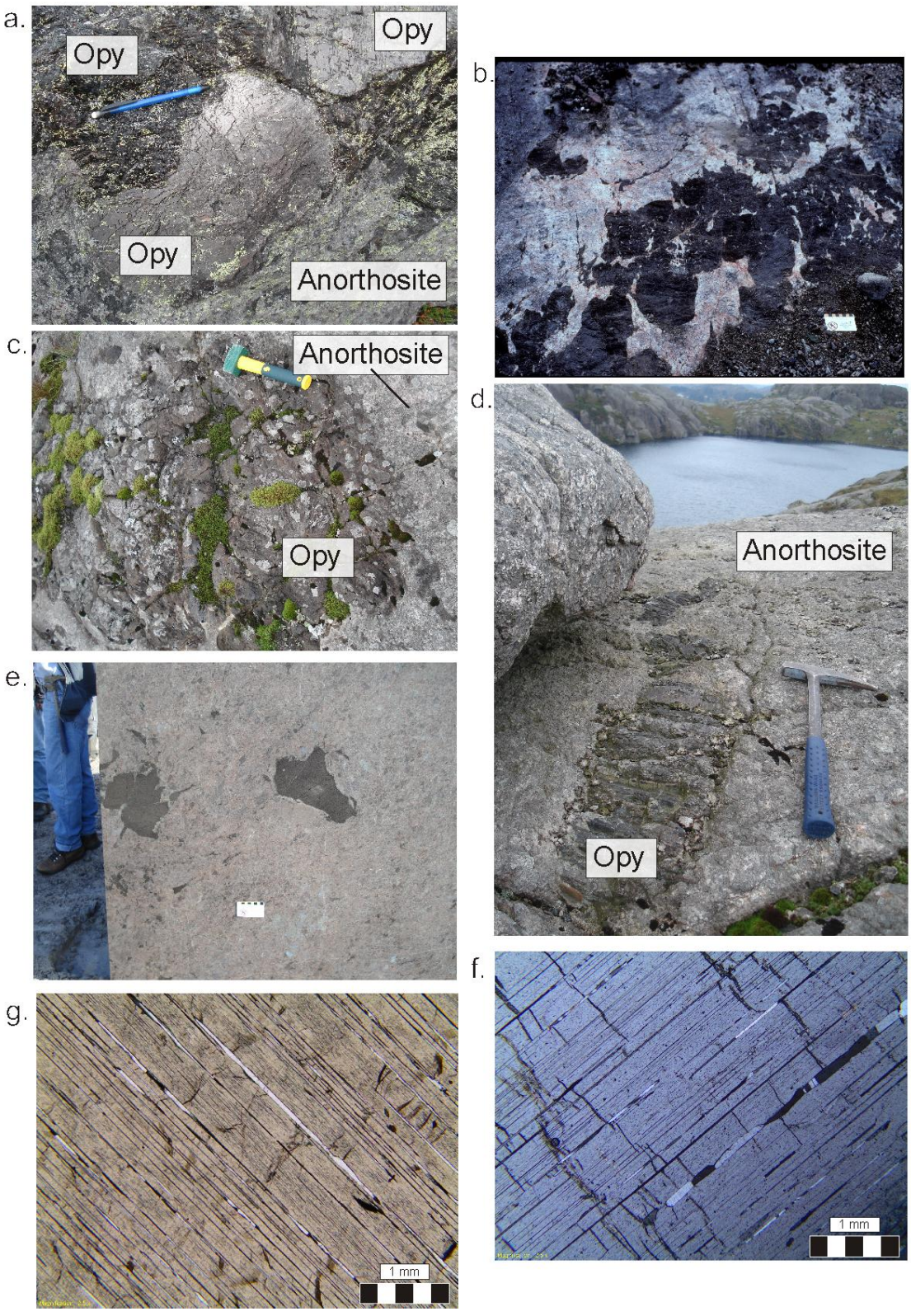

Figure 2.1 The field setting and microscopy of HAOMs. a. One large (~30 cm), euhedral HAOM crystal forming part of aggregate/pod from the MMIS. b. Equant and subhedral megacryst aggregation from the NPS (photo courtesy B. Ryan). c. Rounded HAOM aggregate from RAP d. Elongate (~40 cm) orthopyroxene megacryst from RAP possibly fractured during magma ascent/transport e. Two HAOMs from RAP showing interstitial relationships with plagioclase grains. f. Crossed-polarized photomicrographs of HAOM showing plagioclase exsolution lamellae (RAP). g. Plane polarized microphotographs of HOAMs (RAP).

Light rare earth element enrichment (LREE) and Eu anomalies vary substantially within and between sample sets with the highest-Al, most LREE-depleted samples showing no or small Eu anomalies, while more LREE enriched samples display prominent negative Eu anomalies (Figure 2.2a and b; Appendix B). In an effort to confirm that these megacrysts are not lower crustal xenoliths, I note that the rare earth element (REE) composition of mafic xenoliths, thought to be typical of the lower crust, are significantly more isotopically enriched relative to HAOMs (Downes & Dupuy 1990). This indicates that the HAOMs cannot be lower crustal xenocrysts and must therefore have crystallised from the host magmas.

2.1 High-Al Megacryst Isochron Geochronology

Isochronous relationships among high-Al megacrysts in the Sm-Nd system (Figure 2.3; Table 2.1; Appendix C) demonstrate that the highest-pressure HAOMs in each suite are 110-130 m.y. older than the comagmatic anorthosites that host them (Figure 2.3a; Table 2.1). U-Pb geochronology and detailed field studies reveal that these comagmatic, coalesced anorthosite massifs were emplaced over at least a 12-80 m.y. period (Table 2.1; Gower et al. 2008b; Myers et al. 2008; Schärer et al. 1996). HAOMs from RAP with lower Al_2O_3 contents, as well as intercumulus orthopyroxene, display various degrees of isotopic disequilibrium with the highest-Al megacrysts (Figure 2.3a). Recrystallisation has affected, and is unavoidable in many of the samples from the Nain Plutonic Suite, creating a larger age error for this suite. However, the close correspondence in megacryst-anorthosite age difference between all three suites suggests that the age derived from the NPS data is reasonable and reliable. Minimum age differences, inclusive of 2 sigma error, between megacryst crystallisation and anorthosite emplacement, range from 103 m.y. (MMIS), 65 m.y. (RAP) and effectively 0 m.y. (NPS; caused by significant recrystallisation in megacrysts and consequent large age error on the isochron). However, consistent ~100 m.y. differences between megacryst crystallisation and anorthosite emplacement ages suggest that the isochron ages are reliable. Several additional arguments to support the reliability of the isochrons and ages are presented in Section 2.1.1. Age data from Pb-Pb isochrons are of poorer quality, perhaps due to the ease with which Pb remobilisation occurs. In one case (RAP), however, data trends are preserved in the U-Pb system, and although not a true isochron, this data array produces a comparable age to those produced in the Sm-Nd system (Figure 2.3b).

Table 2.1 Ages differences between high-Al orthopyroxene megacrysts, host anorthosites and an exsolution event

Intrusion	MMIS	NPS	RAP (>8 wt % Al_2O_3)
Megacryst Isochron Age (Ma)	1765 ± 12 (n=6 this study)	1444 ± 100 (n=9., this study)	1041 ± 17 (n=5; >8 wt% Al_2O_3, this study)
Megacryst Exsolution Age (Ma; see Figure 2.4)	-	1346.9 ± 5.9 (n=4, this study)	968 ± 43 (n=4, this study)
Anorthosite Emplacement Age (Ma)	1650-1630[1]	1363-1289[2]	949-920[3]

[1]U-Pb zircon/baddeleyite ages from anorthosites and granitoids (Gower et al. 2008b; Emslie 1990)

[2]U-Pb zircon/baddeleyite/apatite, Ar-Ar ages from multiple sources summarised in (Myers et al. 2008)

[3]U-Pb zircon/baddeleyite in high-Al megacrysts (Sauer et al. 2013; Schärer et al. 1996) and Storgangen orebody of the RAP (Andersen & Griffin 2004)

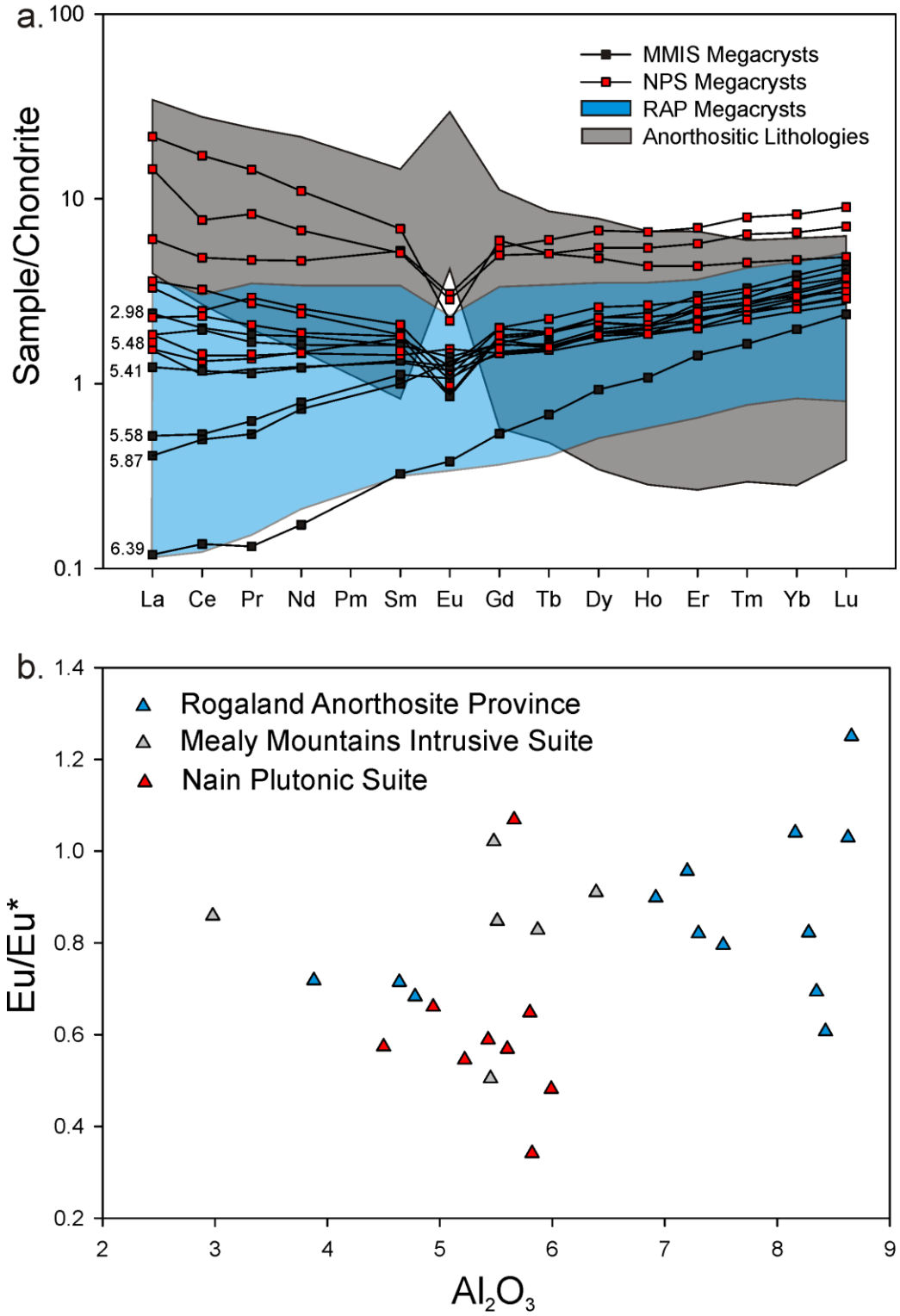

Figure 2.2 a. Chondrite-normalised (Anders & Grevesse, 1989) REE element diagram comparing HAOMs and anorthosites from the three localities sampled in this study. Numbers adjacent to HAOMS from the MMIS represent Al_2O_3 contents (wt %). b. Al_2O_3 content vs. Eu anomaly in orthopyroxene megacrysts from the RAP, MMIS and NPS. Samples from the MMIS and NPS show no clear trends, but the highest Al suite of megacrysts from the RAP show variable Eu anomaly. With decreasing Al content in the megacrysts, a negative Eu anomaly develops.

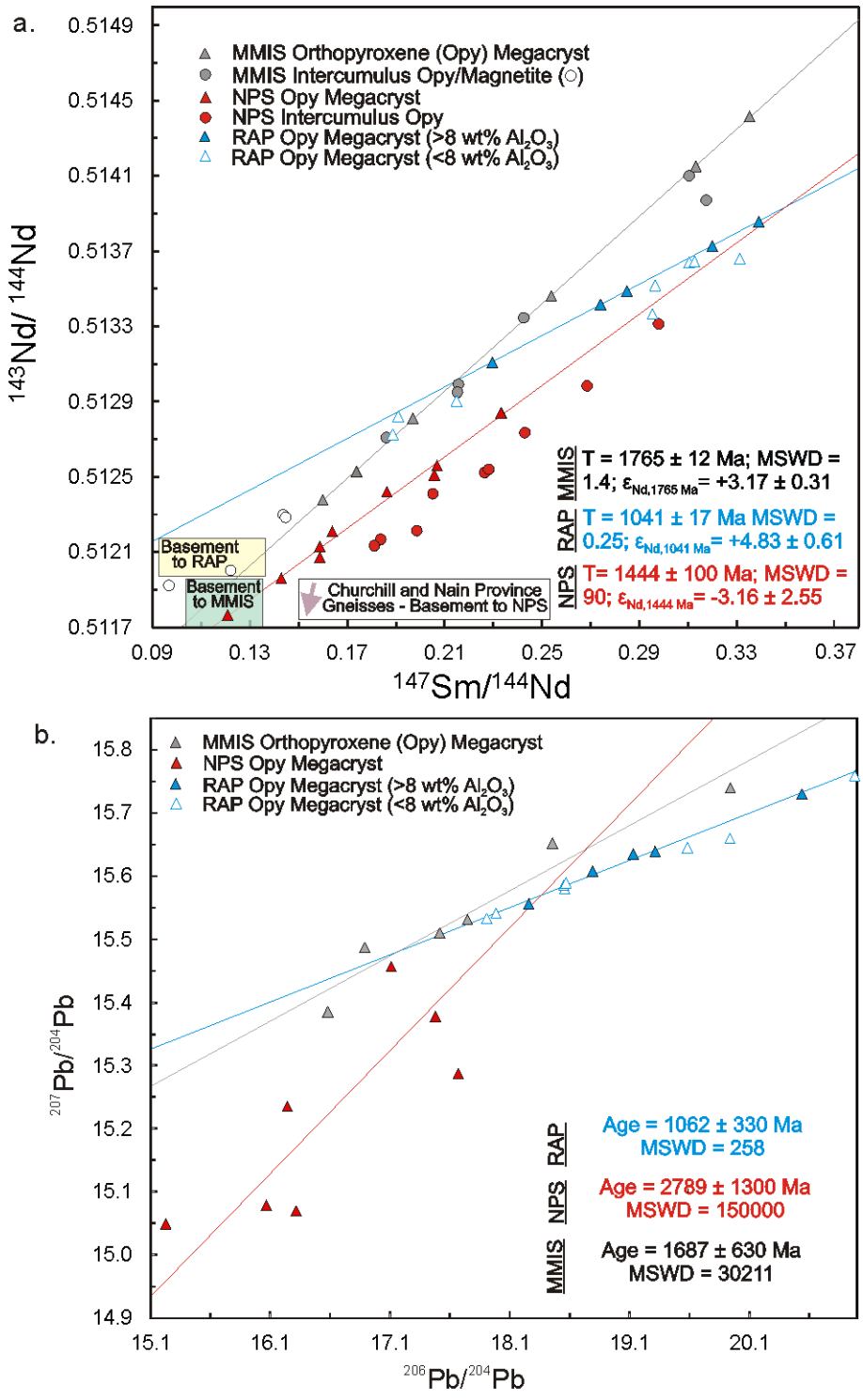

Figure 2.3 a. $^{143}Nd/^{144}Nd$ vs. $^{147}Sm/^{144}Nd$ illustrating the isochronous relationships between high-Al megacrysts from three different Proterozoic anorthosite massifs. Each isochron defines an age approximately 110-130 m.y. older than the recognized age range of the anorthosite intrusions. 2σ errors are all smaller than the symbol size. The Churchill and Nain Province Gneisses cluster around the following isotopic compositions not shown on the graph: $^{143}Nd/^{144}Nd$: 0.511421-0.510451; $^{147}Sm/^{144}Nd$: 0.107025-0.085978 (Appendix C & E). MSWD: mean square of the weighted deviates. b. $^{206}Pb/^{204}Pb$ vs. $^{207}Pb/^{204}Pb$ showing that although Pb remobilisation during various orogenic events has partially reset some isotopic compositions, one data array is preserved in the U-Pb system, and although not a true isochron, this data array produces a comparable age to those produced in the Sm-Nd system.

Four-point Sm-Nd isochrons between plagioclase lamellae, host orthopyroxene and whole-rock HAOM compositions from two high-Al megacrysts in the NPS and RAP (Table 2.1, Figure 2.4) show that decompression exsolution occurred at 1346.9 ± 5.9 Ma and 968 ± 43 Ma, respectively – ages that correspond (within error) with anorthosite crystallisation age ranges in both massifs. Plagioclase exsolved from these megacrysts 70-100 m.y. after crystallisation, and although the exact depth of exsolution in unknown, this finding suggests that significant timescales are required for the 20-30 km ascent from crystallisation depth to plagioclase exsolution depth. Furthermore, the low Al_2O_3 contents (less than 3 wt%) and lack of plagioclase exsolution lamellae in intercumulus orthopyroxene of the host anorthosites indicate that these samples must have crystallised at shallow, upper-crustal depths (Berg 1977; Valley & O'Neil 1982) over the time spans indicated above, and 110-130 m.y. after megacryst formation.

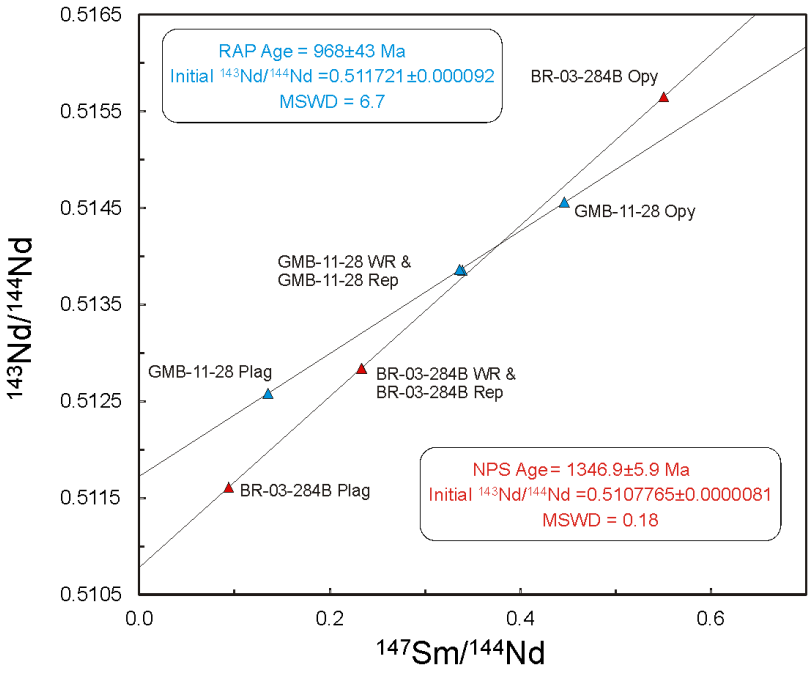

Figure 2.4 Four-point isochrons (including repeat analyses of whole-rock megacrysts) between plagioclase lamellae, host orthopyroxene and whole-rock megacrysts indicating that the ascent of HAOMs in plagioclase-rich mushes to final emplacement levels in the upper crust requires significant lengths of time – similar to the age differences between HAOMs and the host anorthosites.

2.1.1 True Isochrons vs. Pseudochronous Mixing Lines?

At first glance, the isotopic arrays created by the high-pressure megacrysts in all three of the anorthosite intrusions may be interpreted as time-integrated mixing lines, created due to either mixing during crystallisation or assimilation-fractional-crystallisation (AFC) of a magma with crustal material. This initial differentiation creates variations in I_{Nd} compositions, which when time-integrated, produce linear arrays with different ages that are at odds with the true age of the body. This variation in initial isotopic composition due to magmatic differentiation has been shown, through modelling and natural examples, to produce pseudochrons older than the true age of the intrusion (Davidson et al. 2005a; DePaolo 1981). Although this interpretation is convenient,

several lines of evidence disprove the "mixing" hypothesis and indicate that these arrays are true isochrons, ~ 100 m.y. older than the host anorthosites:

- Isotopic disequilibrium in lower-Al_2O_3 megacrysts and in intercumulus orthopyroxene: In the RAP, megacrysts with Al_2O_3 content >8 wt% form a ~ 1041 Ma isochron, but lower Al_2O_3 megacrysts (3 - 7 wt %) are in disequilibrium with this isochron and are displaced to lower Nd isotopic compositions (Figure 2.3a). Isotopic disequilibrium between these compositions suggests that magmatic differentiation processes, like AFC, affected only the lower-Al megacrysts. Had AFC processes affected all the megacrysts, it would be expected that they all plot on a mixing line. If these isochrons were formed by I_{Nd} variations due to AFC processes, all the megacrysts would be expected to fall on one isochron.

- Coincidence in Pb-Pb isochron age: Although much of the Pb-Pb isotopic data appear reset, due perhaps to later orogenic activity (e.g. Grenvillian orogenesis in the MMIS) or secondary effects (e.g. recrystallisation events in the NPS), high-Al megacrysts from the RAP form a linear array on a ^{207}Pb-^{206}Pb plot with an age of 1062 ± 330 Ma (MSWD = 258; c.f. Sm-Nd age = 1041 ± 17 Ma; Figure 2.3b). Although not strictly an isochron, perhaps due to Pb remobilisation, the age produced provides a useful comparison to the Sm-Nd isochrons (Figure 2.3a). Given the differences in fractionation behaviours and half-lives between the Sm-Nd and U-Pb isotope systems, it is highly unlikely that similar age differences between the megacrysts and host anorthosites would result from initial crustal mixing or assimilation (Davidson et al. 2005a). The close correspondence between Sm-Nd and Pb-Pb isochron ages, in at least one intrusion, argue against the hypothesis that the isochrons could result from variation in the initial isotopic ratio of the magma.

- AFC/Mixing Models: Using megacrysts from the RAP, where a range of Al_2O_3 contents are preserved in the megacrysts and reasonable constraints on the isotopic composition of the lower continental crust exist (Othman et al. 1984), I model the effect of variations in I_{Nd} ratio due to mixing or assimilation on aged isotope data. Traditional AFC models described by (DePaolo 1981; Ersoy & Helvacı 2010) were used for these models. If, given reasonable chemical constraints, the differentiated arrays produce isochrons with appropriately older ages than the U-Pb zircon emplacement ages (100-200 m.y.), the hypothesis that these arrays represent mixing lines is acceptable. If not then the null hypothesis, that the isochrons portray the true age of the megacryst suites, remains viable.

  End-member compositions and modelling parameters for the AFC models illustrated in Figure 2.5 are provided in Table 2.2. The AFC models shown below focus on lower crustal assimilation as high-pressure orthopyroxene megacrysts are known to crystallise at lower crustal depths. Of the reported lower crustal values in the Rogaland region (Othman et al. 1984), three compositions were used for comparative AFC modelling; an average of two compositions and the two end-member compositions. The most depleted end-member has a Nd isotopic composition higher than typical mid-crustal samples reported (Menuge 1988) and so covers the effects of mid- to upper-crustal assimilation.

Starting compositions are represented by the most primitive megacryst analysed in the RAP (GMB-11-28; $I_{Nd;\ 930\ Ma}$ = 0.511788).

Table 2.2 Parameters used for traditional AFC modelling and time integration in three scenarios with different lower crustal compositions (AFC 1, 2, 3) using a starting composition defined by the most primitive megacryst analysed.

			$I_{Nd;\ 930\ Ma}$	$\varepsilon_{Nd;\ 930\ Ma}$	$Sm/Nd_{i;930Ma}$	Sm (ppm)	Nd (ppm)
Starting Compositions	Primitive Megacryst Starting Comp.		0.511788	6.84	0.33909	0.1168	0.1996
	Assimilant	Model:					
		AFC1	0.510925	-10.3	0.102320	6.78	39.7
		AFC2	0.510521	-17.9	0.108759	8.66	48.43
		AFC3	0.511329	-2.3	0.095881	4.90	31.12

Figure 2.5a-c presents geochemical paths for a range of *r*-values (fraction of crust assimilated vs. crystals formed) and *F*-values (fraction of liquid remaining). High degrees of fractionation (F → 0) produce a much larger range of isotopic compositions (0.513 - 0.511) than observed in the isochronous megacryst suite (0.51384 - 0.5131) and Figure 2.5a-c only consider lower degrees of fractionation, which reproduce the range of isotopic compositions observed in the megacrysts. Using a simple average of the two possible lower crustal values in the Rogaland region in model AFC1, lower degrees of fractionation (F: 1 - 0.99) and r-values of 0.1 and 0.5, this produces the required range of isotopic compositions, but form 2568 and 1883 Ma arrays (Figure 2.5a). A binary mixing model using the same chemical parameters also produces an unreasonably large age discrepancy with an isochron age of 1481 Ma. Use of the evolved lower crustal end member composition ($I_{Nd;\ 930\ Ma}$ = 0.510521; AFC2) produces arrays of older ages (3232, 2239, 1761 Ma; F: 1 - 0.99, r: 0.1, 0.5 and 0 i.e. mixing, respectively; Figure 2.5b). Model AFC3 (Figure 2.5c) uses the most depleted end-member observed as a potential contaminant to the RAP ($I_{Nd;\ 930\ Ma}$ = 0.511329). Only in a simulation where no fractionation occurs (r = 1), representing pure mixing, do array ages approach those of the actual megacryst isochrons (1215 Ma c.f. 1041 Ma; Figure 2.5c). A scenario involving pure mixing is highly unlikely (DePaolo 1981) and not applicable in the case of the RAP as variations in Eu anomaly between the isochronous megacrysts (>8 wt% Al_2O_3; Figure 2.2a and b) indicate that plagioclase entered the fractionating assemblage during high-pressure megacryst crystallisation. All of the "isochron" ages produced by AFC and pure mixing using constraints appropriate to the RAP are between 285 m.y. and over a billion years older than the anorthosite, illustrating that it is not possible to create isochrons only ~ 100 m.y. older than the anorthosites.

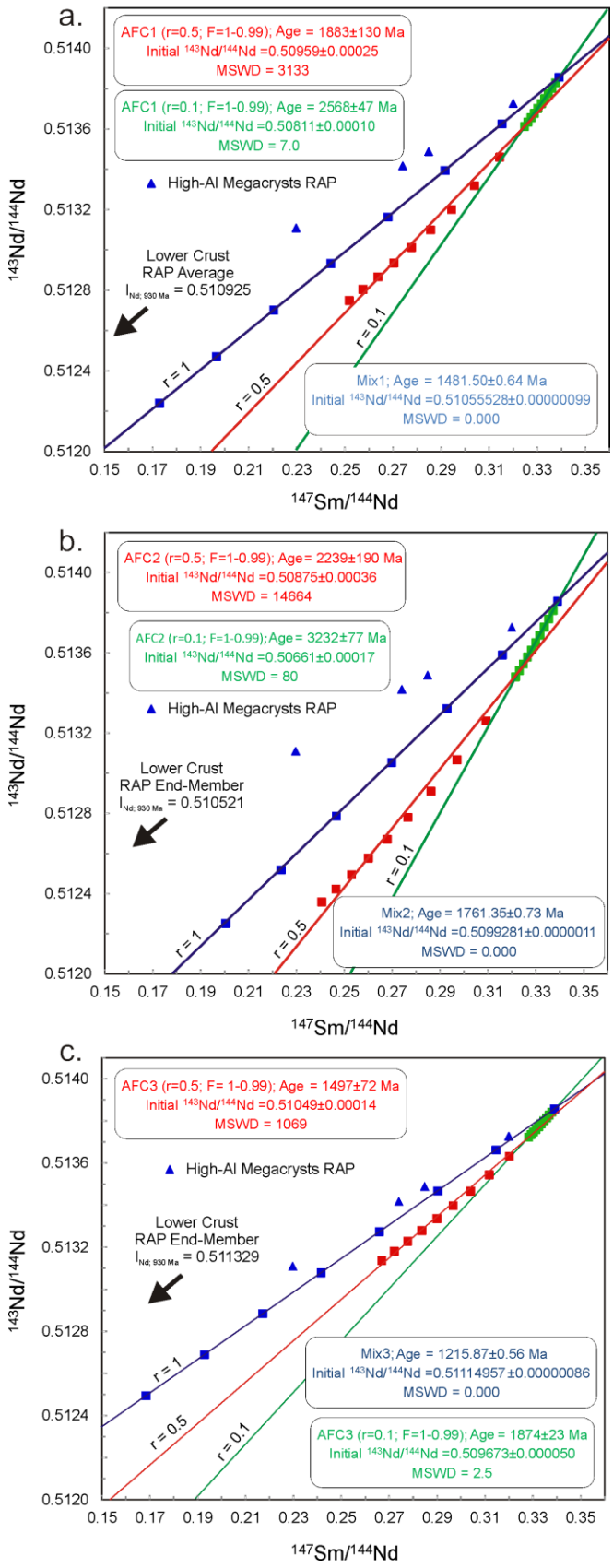

Figure 2.5 a-c. Time-integrated (930 Ma) $^{143}Nd/^{144}Nd$ vs. $^{147}Sm/^{144}Nd$ plots for various traditional AFC models between a magma represented by the most primitive megacryst composition in the RAP and the observed lower crustal compositions in the region (Othman et al. 1984).

Use of highly depleted crustal values could conceivably produce the isochron ages, but only for unrealistically high degrees of assimilation (0.5 and greater). DePaolo (1981) illustrates that *r*-values over 0.3 are unlikely, lending further credence to the suggestions that these are true isochrons. Lower crustal constraints in the MMIS and NPS regions are less well known and so have not been modelled here, but are as unlikely to support the hypothesis that consistent ages differences between anorthosites and megacrysts are the result of AFC or mixing processes.

- Anorthosite isochrons and the U-Pb ages: Sm-Nd isotopic arrays for anorthosite whole-rock compositions from the MMIS, although not isochronous, produce an age equivalent to the U-Pb zircon/baddeleyite ages determined for these intrusions (1653 ± 150 Ma vs. 1650-1630 Ma, respectively). If initial contamination had affected the magmas and produced old isochrons in the megacrysts, one would expect the anorthosites, which crystallise from the same, if not more contaminated magma, to display similarly old ages relative to the U-Pb ages. This is not the case, providing further evidence against the megacryst arrays representing pseudochrons. Anorthosites from the NPS do not form arrays with any meaningful age and so no comparison can be made in this case.

  Consistent isochron ages between intrusions: Finally, the RAP, MMIS and NPS intrusions are each of significantly different age (~ 930 Ma, 1650-1630 Ma, 1363-1289 Ma, respectively; see Table 2.1) and intrude into crust with significantly different isotopic compositions and age. If the arrays do represent mixing or AFC trends between melt and a crustal assimilant, the diversity of age and crustal compositions would be highly unlikely to produce the observed, self-consistent age differences between the megacrysts and the comagmatic host anorthosites (100-144 m.y., Table 2.1).

These various and diverse lines of evidence all argue against the hypothesis that the isochronous Sm-Nd data arrays could be produced by time-integrated initial I_{Nd} variations due to mixing or AFC processes in a magma chamber. Section 2.3 details a more likely scenario for the creation of isochronous data arrays in all three anorthosite-hosted megacryst suites.

2.2 The Tectonic Setting and Source of Proterozoic Anorthosites

A variety of tectonic settings have been proposed for Proterozoic anorthosites (see Section 1.1.3), with opinion divided between intraplate, divergent, anorogenic and convergent plate tectonic settings (see review in Ashwal 1993; McLelland et al. 2010). Anorthositic magma production, in terranes such as the Grenville-Labrador region (at over 1600 km long), spans about 500 m.y. and it is difficult to envisage even the largest continental rifts supplying magma to a region for this length of time without initiating continental break-up (Ashwal 1993). In recent years, the balance of evidence relating to the tectonic setting of Proterozoic anorthosites has, based on burgeoning precise geochronological data, shifted to a late- to post-orogenic setting, although there are notable exceptions to this hypothesis in important anorthositic terranes like the Nain Plutonic Suite (Martignole et al. 1993; McLelland et al. 2010). The observation of anorthosite emplacement at mid- to upper-crustal levels during the waning stages of orogeny in the Grenville and Sveconorwegian Orogenies precipitated this proposal, however, the mechanisms producing this magmatism are poorly understood. Potential mechanisms include delamination of over-thickened lithosphere, extension in back-arcs or flat-slab subduction with/without delamination (McLelland et al. 2010).

Although anorthosite emplacement is generally observed during the waning stages of orogeny, megacryst geochronology from three anorthosite massifs of different ages, emplaced into different terranes, indicates that magmatism began ~100 m.y. prior to this. These age relationships are corroborated by plagioclase exsolution ages in high-Al megacrysts that overlap with emplacement age of the anorthosites (determined by U-Pb zircon/baddeleyite dating in anorthosites and megacrysts, see Chapter 3). Given this long-lived magmatic system and the ~100 m.y. age gap, between what may be considered the beginning of magmatism and final anorthosite emplacement, anorthosite petrogenesis can no longer be considered restricted to late- or post-orogenic settings. The petrogenesis of these intrusives must therefore span both orogenic and post-orogenic periods. Arguments may be made that the late- to post-orogenic periods in these cases were simply protracted, but an overlap in megacryst crystallisation age and the onset of calc-alkaline, orogenic magmatism forming the Sirdal Magmatic Belt in the Sveconorwegian Orogen, both ~100 m.y. before RAP anorthosite emplacement, show that megacryst formation coincides with the main phase of magmatic, orogenic activity (see Chapter 3; Slagstad et al. 2012).

I therefore suggest that the only geodynamic setting capable of delivering sufficient, geographically-focused quantities of magma (and heat) to the base of the crust for more than 100 m.y. is a convergent arc setting. Well-known convergent arc systems such as the Californian Arc were in operation for >150 m.y., and produced surface and shallow-crustal magmatism in only two short episodes (10-20 m.y. in duration; Ducea 2001). Subduction-related plutonic magmatism is also recorded for a period of over 150 m.y. in Late Jurrasic to Neogene granitoids making up the South Patagonian Batholith (Hervé et al. 2007). Given the proposal that Proterozoic anorthosites formed in Andean-type arc environments, a logical question to ask is whether massif-type anorthosites are observed in similar Phanerozoic arc terranes? Although large, batholithic bodies of massif-type anorthosite have not yet been found in Phanerozoic or modern-day arc-related terranes, calcic, anorthositic bodies have been reported as xenoliths or cognate inclusions in both island and continental arc volcanics from various magmatic arcs (see Ashwal, 1993 for review). The plagioclase composition in these inclusions/bodies is significantly more calcic (An_{70-100}) compared to that of Proterozoic anorthosites (An_{45-60}), but the occurrence of anorthosite fragments in these arc environments may indicate that larger bodies exist at greater depths. These two types of anorthosites are petrographically similar, but variation in plagioclase chemistry may suggest operation of non-uniformitarian processes in Proterozoic versus more recent subduction styles. For instance, higher water content in Phanerozoic arcs would suppress plagioclase crystallisation, leading presumably to smaller anorthosite bodies, while increasing the anorthite content of the plagioclase. The comparison of these two occurrences is deserving of further study as new light may be shed on the formation, tectonic setting and temporal restriction of Proterozoic anorthosites. Further research is also needed to assess why anorthosite petrogenesis in arc settings was so protracted. The necessity of creating large amounts of buoyant plagioclase to allow mush ascent to upper crustal levels may require relatively lengthy periods of magma fractionation and recharge in ponded magmas at the Moho. In the model presented here, megacrysts form 100 m.y. before anorthosite emplacement in the upper crust, but I do not envisiage these crystals remaining at the Moho for 100 m.y., and I suggest that part of this time period was spent in a convecting magma at the Moho with the remainder of the period involving the ascent of the magma mush to mid-crustal levels. However, the exact length of time spent at these various levels suffers from a degree of untestability, and imaginative methodologies need to be considered in order to assess this aspect of the model. Furthermore, the ascent of

magmas, sufficiently saturated with plagioclase to be positively buoyant, may take significant lengths of time – longer than predicted for less-viscous basaltic magmas (Kushiro 1980). Finally, anorthosite emplacement in the mid- to upper crust may be facilitated by extensional regimes common to post-orogenic settings by, for instance, weakening the crust through orogenic collapse, or warming the collapsed crust to near-solidus temperatures thereby facilitating ascent of viscous magmas.

Magmas forming Proterozoic anorthosites and their cogenetic megacrysts are controversially considered to be derived from melting of either the depleted mantle (Emslie et al. 1994) or the lower crust (Schiellerup et al. 2000). Data in this study supports previous workers' conclusions (Ashwal et al. 1986) that the age and nature of the continental crust into which anorthositic magma intrudes dramatically affects its isotopic composition, changing the convecting or depleted mantle isotopic signature of these rocks (Figure. 2.6a,b). The NPS, which intrudes into old, isotopically evolved crust of the Nain and Churchill Provinces (Archaean-Palaeoproterozoic) has Nd isotopic compositions up to 10 ε-units lower than the MMIS and RAP, which intrude into lithosphere of the Palaeoproterozoic Grenvillian and Mesoproterozoic Sveconorwegian provinces (Ashwal 1993; Ashwal et al. 1986). In these younger terranes, the initial isotopic compositions of the magmas from which the highest-pressure megacrysts crystallised has only been slightly displaced from depleted mantle, indicating that the parental magmas forming both the megacrysts and anorthosites were derived from melting of the depleted mantle. Melting of the lower crust alone to produce the necessary mafic melts requires unreasonably high degrees of melting and an external source of heat from upwelling magmas (for which the concomitant mantle-derived magmatism is not observed; Morse 1991). I therefore suggest that Proterozoic anorthosites formed from melting of the depleted mantle in long-lived continental-arc environments.

2.3 Geodynamic Implications of the High-Al Megacrysts

Broadly basaltic melts, thought to be the parental magmas of Proterozoic anorthosites, initially crystallise olivine and clinopyroxene while rising towards the base of the crust (Müntener & Kelemen 2001; Müntener & Ulmer 2006). Interactions between this magma and partial melts of the mafic lower crust would induce a limited pulse of more silicic lower crustal contamination, not only inducing orthopyroxene crystallisation due to peritectic olivine reaction (Müntener & Kelemen 2001), but lowering and shifting the Nd and Pb isotopic composition of the high-Al orthopyroxene cumulates, as I observe (Figure 2.6a,b). Although most Proterozoic anorthosite massifs commonly preserve orthopyroxene megacrysts, rare examples of the occurrence of high-Al orthopyroxene and clinopyroxene megacrysts have been noted in the Labrieville and Grenville Township massifs (Quebec; Ashwal 1993; Owens & Dymek 1995; Philpotts 1966). These observations illustrate that most clinopyroxene (and olivine) is likely to have crystallised before, and in rare cases, together with orthopyroxene and plagioclase at high pressures. The paucity of clinopyroxene (and olivine) megacrysts in anorthosite massifs suggests that these phases formed (and perhaps sank in the magma chamber) before sufficient, buoyant plagioclase mush had formed – a vital ingredient for delivering some high-Al orthopyroxene megacrysts to upper crustal depths with the anorthosite.

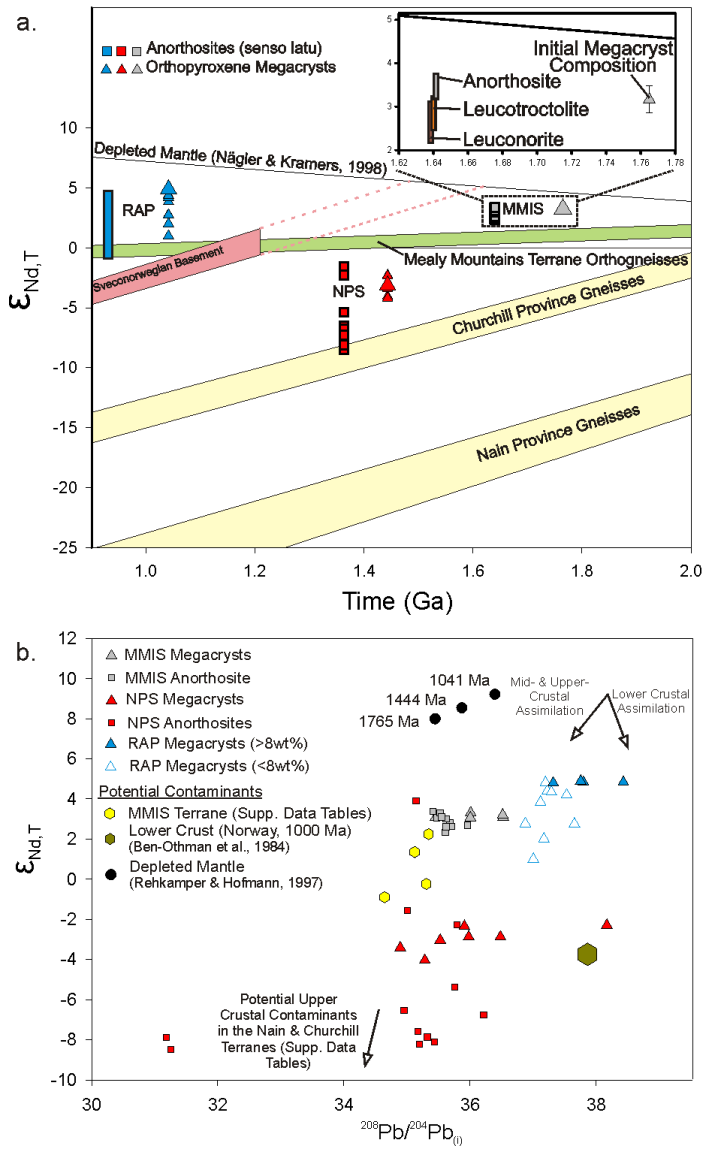

Figure 2.6 a. A depleted mantle origin for HAOMs and Proterozoic anorthosites. εNd vs. time illustrating how emplacement of anorthositic mushes into terranes of different ages dramatically influences the isotopic composition of the anorthosites. In young terranes, where the effect of contamination is least dramatic, the initial megacrystic isotopic compositions (large triangles, derived from isochron regression) is consistently only slightly displaced from depleted mantle evolution, indicating magma derivation from depleted mantle. Linear fields indicate evolution of potential crustal contaminants (potential contaminants for the NPS include both Churchill and Nain Province gneisses, due to intrusion into the province-suturing Torngat Orogen). b. The initial assimilation of lower crust by a depleted-mantle-derived melt, subsequent crystallisation of high-pressure megacrysts, and later polybaric fractionation and upper crustal assimilation during anorthosite crystallisation is traceable in this εNd vs. ($^{208}Pb/^{204}Pb)_i$ plot. The highest-Al megacrysts record a limited pulse of lower-crustal contamination during ponding of depleted-mantle-derived melt. Later mid- to upper-crustal polybaric contamination deflects the isotopic composition of the lower-pressure megacrysts and anorthosites (particularly noticeable in the RAP) to more upper-crustal values. The ^{232}Th-^{208}Pb system is chosen as a better tracer of contamination because of increased concentrations of Th in the continental crust. Depleted mantle composition determined from Rehkamper and Hofmann (1997) and the representative lower-crustal composition is taken from Othman et al. (1984).

The isochronous isotopic composition of the highest-Al megacrysts (Figure 2.3a) indicates that they were in equilibrium with a fractionating magma that received minor lower crustal contamination and/or little compositionally-distinct magmatic recharge or contamination at upper-mantle or lower-crustal pressures. Modelling presented in Section 2.1.1 shows that these arrays could not be produced by time-integrated I_{Nd} variations caused by mixing or assimilation in an evolving magma chamber. Ponding and subsequent crystallisation of a rising basaltic magma at a suitable interface in the lithosphere allows creation of such a locus for crystallisation in which a magma chamber receives isotopically indistinct recharge and little, no or indistinct assimilation. The Moho provides the required rheological contrast to stall an upwelling mafic magma at the calculated depths of HAOM crystallisation on modern-day Earth (Artemieva 2011). Ponding of magma at the Moho is a commonly-proposed, but poorly-documented phenomenon when describing magma ascent from source to surface through the continental lithosphere. Our new data for HAOMs, however, provide the first direct, geochemical and petrological evidence for these processes at the Moho. This new finding supports recent seismic refraction studies by Richards et al. (2013) which image large ultramafic bodies (V_p ~ 7.4-8.0 km/s) at or above the Moho, below relatively old oceanic hotspots, formed beneath thick oceanic lithosphere. These findings, together with the isotopic compositions of the high-pressure megacrysts, illustrate the importance of cumulate formation in magmas that pond at the Moho – an observation that has implcations for continental crust evolution as discussed in the following section.

The scarcity of negative Eu anomalies in some of the highest-Al megacrysts, in addition to their high-Al contents, suggest that plagioclase was not yet part of the crystallising assemblage at these pressures (Figure 2.2). Positive-buoyancy instabilities develop once sufficient plagioclase has formed, allowing plagioclase-rich mushes (defined as magmas with volume fraction crystallinity of 0.25 – 0.55) to begin rising through the crust (Kushiro & Fuji 1977). Crucial in this model is the formation of plagioclase mushes which trap and facilitate the transport of these megacrysts to mid-crustal levels, without which these dense phases would simply sink. The large size of these high-Al megacrysts could be due to slow crystallisation at high temperature and pressures as well as the long timescales over which the magmatic system evolves. Both lower-Al megacrysts (displaying prominent negative Eu anomalies) and intercumulus orthopyroxene in the host leuconorites are in isotopic disequilibrium with the highest-pressure megacrysts (plotting off the isochrons; Figure 2.3a), indicating that polybaric assimilation and fractional crystallisation characterise the remainder of the ascent of these buoyant plagioclase mushes to their final level of emplacement (Figure 2.3a).

Recent work has shown that equilibrium crystallisation of basaltic magmas produces, at most, 50 – 60 % of plagioclase (Müntener & Ulmer 2006) in the crystallising assemblage. Based on maximum estimates, any given anorthositic massif contains 10-15 % of mafic phases (olivine, orthopyroxene, clinopyroxene & magnetite/ilmenite), suggesting that 35-40 % of the mafic minerals are unaccounted for. Considering the evidence presented here for cumulate formation at the Moho, I propose that ultramafic crystallisation and sequestration in ponded magmas at these depths could represent the missing component in Proterozoic anorthosites. Calculations show that, in arc environments, ~21 % ultramafic cumulate formation from primitive mantle-derived magmas occurs below the Moho (Conrad & Kay 1984) and the observation of high-pressure ultramafic xenoliths in lavas from the Aleutian arc (Conrad & Kay 1984) and the Nógrád-Gömör Volcanic Field in northern Hungary (Zajacz et al. 2007) provide corroboratory evidence that upper mantle cumulates do form in

other environs, but are rarely brought to the surface. HAOM compositions also compare favourably with fields of experimentally determined, high-pressure (12 kbar) basaltic arc cumulates (Figure 2.7; Müntener & Kelemen 2001). HAOMs are slightly more evolved than these experimental cumulates, suggesting that olivine fractionation did occur prior to HAOM crystallisation. These lines of evidence point to similar ultramafic cumulates forming in major continental crust-generation zones where basaltic magmas pond at the Moho. HAOMs, therefore, are not peculiarities restricted to Proterozoic anorthosites, but instead are vestiges of ubiquitous and significant magmatic processes operating at the Moho, fortuitously brought to the surface as a result of high-viscosity plagioclase-rich mushes which form Proterozoic anorthosites.

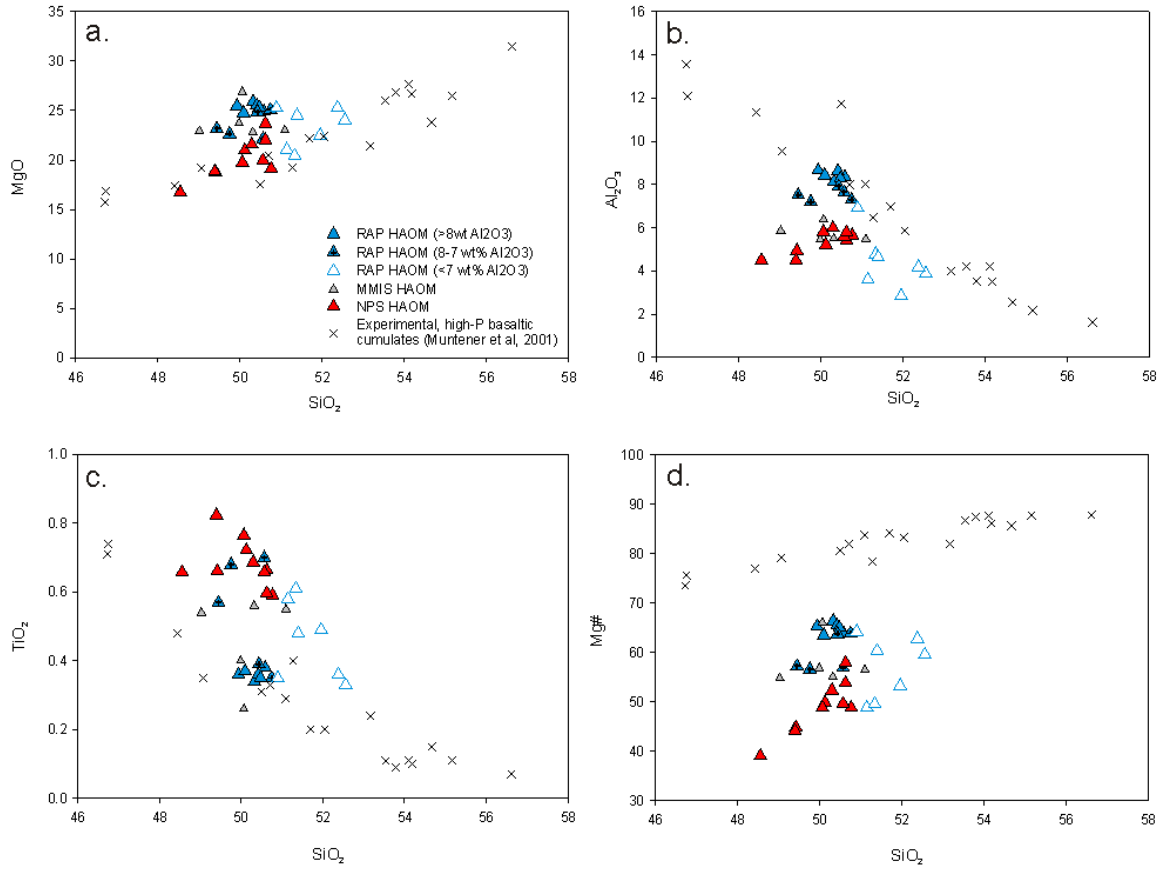

Figure 2.7 Selected Harker diagams showing similarities between HAOMs and experimental, high pressure (2.1 GPa) basaltic compositions (Müntener & Kelemen 2001). All HAOMs show lower Mg# for a given SiO_2 content than the experimental basaltic cumulates due to olivine fractionation prior to orthopyroxene megacryst crystallisation.

The fate of these ultramafic cumulates is an important consideration that has implications for mechanisms of crustal differentiation (Kay & Kay 1993; Kay & Kay 1991). Arndt and Goldstein (1989), working on the assumption that mafic magmas pond, crystallise and assimilate lower crust at the Moho (as I have demonstrated), show that olivine and pyroxene cumulates would sink back into the mantle due to negative density contrasts with the surrounding mantle. MELTS (Ghiorso & Sack 1995) modelling was performed to quantify the density contrasts between cumulates, magmas and the mantle at the Moho using starting conditions expected for Proterozoic anorthosite formation. An experimentally-produced high-Al basalt was used as the parental magma (Fram & Longhi 1992), with close similarities to natural samples found in various anorthositic

massifs and reported in Charlier et al. (2010). Models were run under equilibrium and fractional crystallisation scenarios at 10 and 15 kbar. This shows that pyroxenes formed between 10 and 15 kbar will be denser than both the crystallising magma and the surrounding mantle (e.g. $\Delta\rho_{\text{magma-pyroxene [10 kbar]}}$= -0.62 g.cm^{-3}; $\Delta\rho_{\text{PREMmantle-pyroxene [10kbar]}}$= -0.07 g.cm^{-3}) and will sink, not only in the ponded magma, but also into the mantle (Figure 2.8).

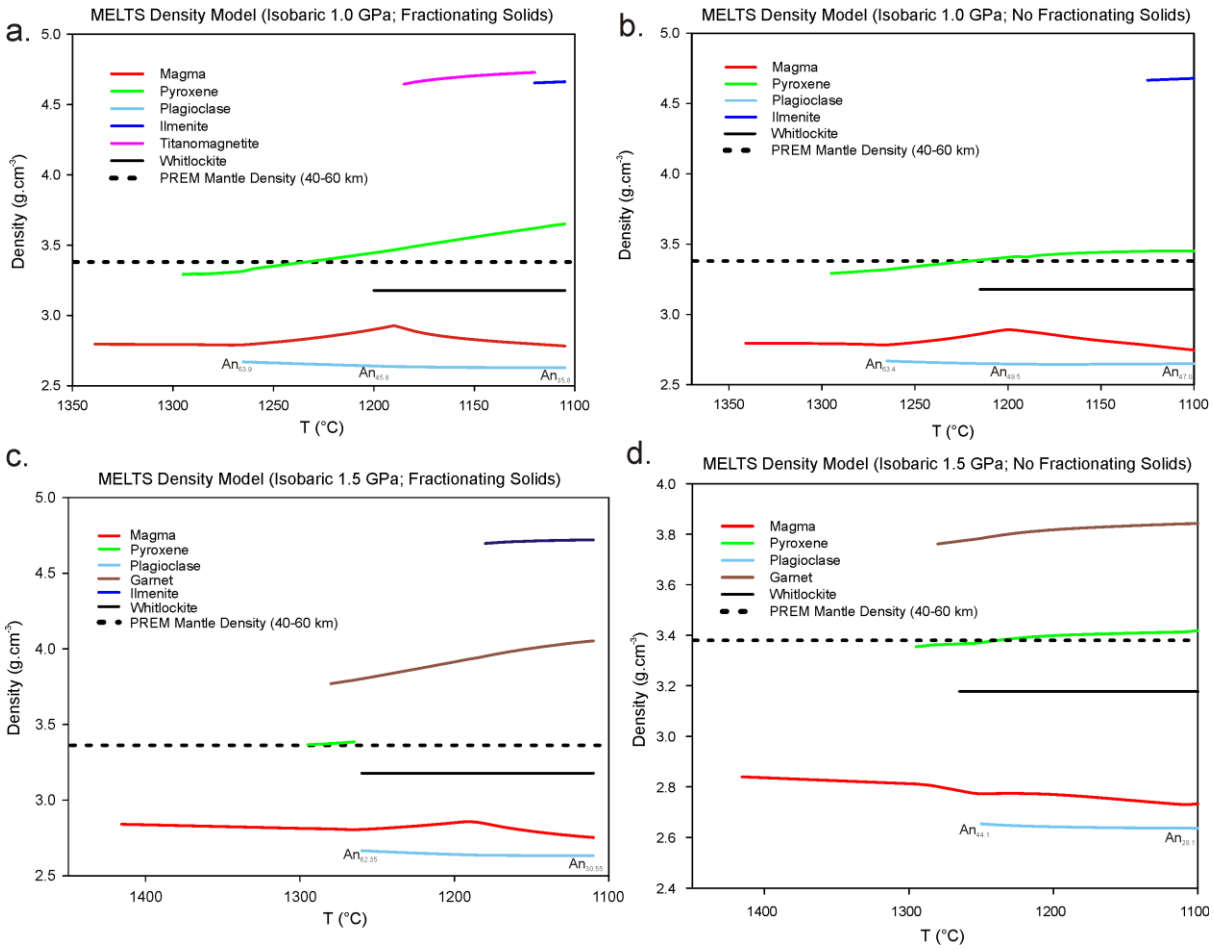

Figure 2.8 Extracted magma and cumulate densities from MELTS modeling of high-Al basalt crystallisation at Moho pressures. The starting composition is the same in each model permutation. a. Model fractionating solids at 1 GPa (10 kbars). b. Model not fractionating solids at 1 GPa (10 kbars). c. Model fractionating solids at 1.5 GPa (kbars). d. Model not fractionating solids at 1.5 GPa (15 kbars).

The density contrasts between the cumulate pyroxene and mantle are less pronounced at 15 kbar, although there are still relatively large density contrasts with the magma. The small negative density contrast between pyroxene cumulates and the surrounding mantle at both pressures will be exacerbated as the cumulates transition to eclogite facies. These results demonstrate that ultramafic material formed at the Moho, under conditions and using chemistries likely to crystallise anorthosites, would be denser than the magmas and the surrounding mantle and would consequently sink into the mantle, or at least be sequestered beneath the Moho. These MELTS models (particularly at 10 kb) also produce positively-buoyant plagioclase (with geologically reasonable An contents) that will accumulate at the top of a ponded magma and eventually rise diapirically through the crust, as predicted in models of anorthosite petrogenesis. Jull and Keleman (2001) modelled and quantified density contrasts between cumulates/lower crust at the Moho, using various methods, and

demonstrated that ultramafic material (olivine clinopyroxenites) present at Moho conditions (on arc-type geotherms) would have density contrasts with the mantle between 0.05 - 0.1 $g.cm^{-3}$ and would sink into the mantle on timescales of 10 million years, supporting the MELTS models created in this study.

As is the case with Proterozoic anorthosites, a missing mafic component is required to balance the intermediate/evolved composition of bulk continental crust with single-stage mantle-derived melts created by melting of a peridotitic mantle (Process 1, Figure 2.9). I use Proterozoic anorthosites as a proxy for bulk continental crust, as both are missing a mafic component. These dense ultramafic-mafic cumulates, whether they are sequestered as seismically indistinct bodies in the mantle lithosphere or lost to the deeper mantle through crustal delamination, provide a complementary chemical reservoir to the observed, intermediate composition of the continental crust. Although it is not known whether crustal delamination occurs by sinking of mantle-derived cumulates, or foundering of lower crustal material into the mantle (Kay & Kay 1993; Kay & Kay 1991; Lee et al. 2006), these results indicate that cumulate formation and foundering is a plausible mechanism of crustal delamination, especially in active continental crust-generation zones. In these zones, fractionation and cumulate formation beneath the Moho in ponded magmas (Figure 2.9; Process 2) allows physical separation of a mafic component and drives the bulk composition of the continental crust to more intermediate/silicic compositions (SiO_2 > 60 wt %). Similar processes of cumulate formation and delamination are inferred to have occurred in arc environments from studies in exposed arc sections (e.g. Kohistan Arc, northern Pakistan) and represent analogs to the processes inferred in Proterozoic anorthosites (Jagoutz et al. 2006; Jagoutz & Schmidt 2012). The ultimate fate of these cumulates may be remelting and creation of chemical heterogeneities elsewhere in the convecting mantle, followed by subsequent recycling into the sources of MORB and OIB (Tatsumi 2000).

2.4 Conclusions

Nd and Pb isotopic geochronology and geochemistry of Proterozoic anorthosites and ubiquitous, cogenetic high-pressure orthopyroxene megacrysts suggests that these intrusions are derived from melting of the depleted mantle in long-lived Andean-arc systems. The ~100 m.y. time differences between megacryst crystallisation and anorthosite emplacement, as well as isochronous high-pressure megacryst compositions are evidence for crystallisation in magmas that ponded at the Moho. Proterozoic anorthosites, which suffer similar mass balance problems, are viscous magmas that entrain evidence from the crust-mantle boundary in the form of these megacrysts, thereby providing an accessible proxy for crustal differentiation. Our results indicate that crustal differentiation by cumulate formation and sequestration at the Moho is a valid and significant mechanism that can create observed intermediate crust compositions and that should be taken into account in future studies on the evolution of the crust.

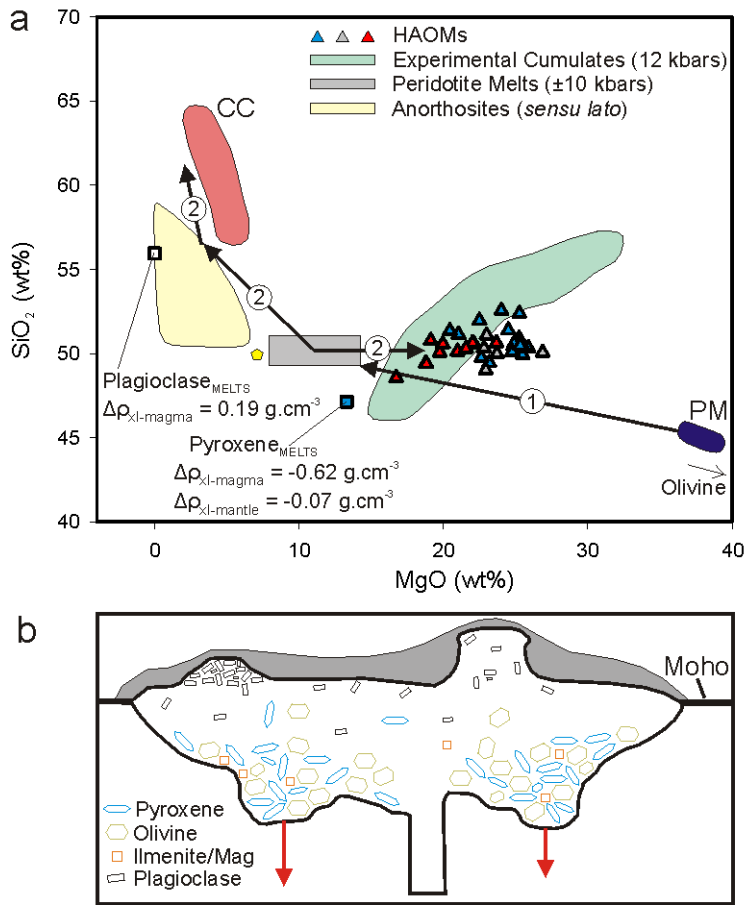

Figure 2.9 a. MgO vs. SiO2 illustrating the compositional discrepancy between single-stage melts (grey-shaded box) of peridotitic mantle [Process 1] in arc environments and the bulk continental crust (CC; Rudnick & Gao 2003 and references therein). Fractionation [Process 2] of these peridotitic melts at the Moho and associated sequestration of dense ultramafic cumulates (real megacryst compositions, experimental cumulates and modeled MELTS phases) below the Moho drives the composition of the residual magma, which goes on to form the continental crust, to more intermediate compositions, in line with observed bulk crustal compositions. Primitive mantle (PM) compositions are taken from (Palme & O'Neill 2003) and references therein. Yellow pentagon represents the proposed parental magma of Proterozoic anorthosites (Charlier et al. 2010). Density contrast (Δρ) calculations between magma, mantle and cumulates derived from MELTS modelling. The grey field represents anatectic melts of the lower crust. b. Ultramafic cumulates formed in fractionating magmas ponded at the Moho are denser than the melt and the surrounding mantle and may founder into the deeper mantle, leaving the residual melts to drive the bulk composition of the continental crust to the observed intermediate compositions.

3 Regional Geodynamic Implications of Megacryst Geochronology in the Sveconorwegian Orogen and Eastern Labrador

The geodynamic setting of the Sveconorwegian Orogenic Belt in Scandinavia (Figure 3.1a), considered an extension of the Grenvillian Orogenic Belt, has come under scrutiny recently with debate centering on whether orogenesis took the form of a Himalayan-type orogeny (as is the conventional view) or a non-collisional, accretionary, Andean-arc-type orogeny (Slagstad et al. 2012; Möller et al. 2013; Slagstad et al. 2013). Arguments supporting the alternative Andean-type orogeny hinge on recent geochemical and geochronological work suggesting that more voluminous, juvenile, calc-alkaline magmatism occurred over a longer time period than previously recognised in the western Rogaland-Vest-Agder sector of the Sveconorwegian Orogen (Figure 3.1b). Metamorphic constraints show that the area experienced P-T conditions (>800-900 °C; 6-7 kbar) too high for a collisional orogen (Drueppel et al. 2008 & Elsaesser et al. 2008 in Slagstad et al. 2012). Detractors of this model argue that an accretionary setting cannot be applied across the entire orogen, especially in the eastern region, where evidence of collisional tectonics has been described (Möller et al. 2013). Key to each argument are the characteristics that define a collisional versus accretionary orogen. As Slagstad et al. (2013) state, many of the metamorphic and deformational processes in collisional and accretionary orogens produce similar features in the geological record, whereas the magmatic products of different styles of orogensis are chemically distinguishable. The Neoproterozoic Rogaland Anorthosite Province (RAP; Figure 3.1c) forms an important magmatic feature of the Sveconorwegian Orogenic Belt and has been considered an example of magmatism occurring in the waning stages of orogeny due to post-collisional collapse and associated melting processes in the lower crust (Duchesne et al. 1999; Schiellerup et al. 2000; Vander Auwera et al. 2011). The controversial hypotheses that Proterozoic anorthosites are derived from melting of the lower crust in late- to post-orogenic settings (see Section 1.1) have, in part, been used support models of collisional orogenesis in the Sveconorwegian orogeny (Bingen et al. 2005; Vander Auwera et al. 2011). Using new geochronological and geochemical data from anorthosite-hosted, comagmatic, high-pressure orthopyroxene megacrysts in the RAP, I show that the magmas forming Proterozoic anorthosites are not formed during a post-collisional phase from melting of the lower crust and I provide evidence supporting the notion that the Sveconorwegian orogenic belt represents a long-lived, accretionary, Andean-type orogeny. As a test of these ideas, I apply similar data and evidence to geodynamic evolution of the eastern Labrador region and find that an accretionary, magmatic arc setting can also explain magmatic and tectonic features observed in this region.

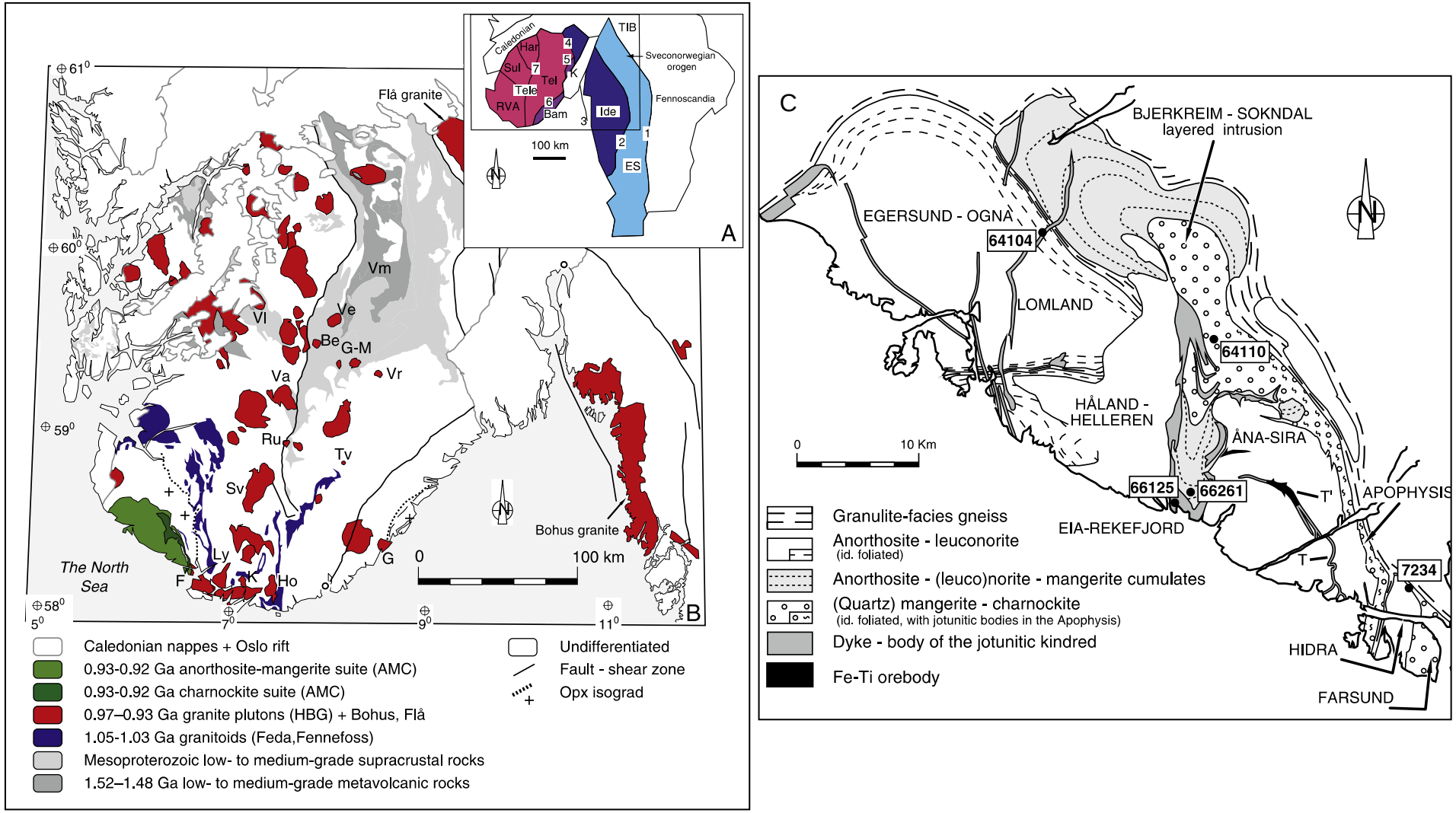

Figure 3.1 a. Lithotectonic domains of the Sveconorwegian Orogen in SW Scandinavia (Vander Auwera et al. 2011). b. The southwestern region of the Sveconorwegian Orogen incorporating several terranes including Rogaland-Vest-Agder Sector in which various felsic intrusive suites are highlighted. c. The Neoproterozoic Rogaland Anorthosite Province and associated mafic magmatic products (after Charlier et al. 2006).

3.1 Geochronology of the Rogaland Anorthosite Province

Central to this argument is the age of the Rogaland Anorthosite Province (RAP) and the ubiquitous high-Al orthopyroxene megacrysts that are hosted by the anorthosites. Three large massifs, the Egersund-Ogna, Håland-Helleren and Åna-Sira massifs, comprise the strictly anorthositic members of the Rogaland Anorthosite Province, but a layered intrusion (Bjerkreim-Sokndal) and two leuconortitic bodies (Hidra and Garsaknatt) also form part of the mafic series of the province (Figure 3.1c; Robins et al. 2008; Schärer et al. 1996).

The crystallisation age of the RAP has been constrained between 935 and 927 Ma, primarily by U-Pb dating of zircon and baddeleyite derived from orthopyroxene megacrysts in the Egersund-Ogna, Åna-Sira and Helleren massifs (Schärer et al. 1996). Recent U-Pb zircon geochronology on a megacryst from the Egersund-Ogna massif returned an age of 948 ± 3 Ma (Sauer et al. 2013). Associated magmatic entities such as the Storgangen noritic, ilmenite-rich orebody (949 ± 7 Ma; Andersen & Griffin 2004), jotunitic dykes (931 ± 5 Ma) and the Tellnes orebody (920 ± 3 Ma; Schärer et al. 1996) provide additional and independent age constraints for the RAP and extend the Rogaland magmatic event from 956 - 917 Ma (inclusive of 2 sigma error).

New Sm-Nd age information from this study, reported in Chapter 2 (and summarised in Figure 3.2, Appendix C), for three anorthosite massifs including the Rogaland Anorthosite Province, suggests that the high-Al megacrysts are ~ 100 million years older than the oldest ages reported for megacrysts, and by inference, the anorthosite itself. Sm-Nd isochron ages for a suite of high-Al (>8 wt% Al_2O_3) megacrysts of the RAP produce true isochron ages of 1041 ± 17 Ma (MSWD = 0.25). Pb-Pb isochron ages on the same suite of samples, although partially reset, confirm that this age is a true age (Figure 3.2b; Appendix C). Time-integrated AFC modelling documented in Chapter 2 shows that variation in the initial isotopic composition of the magma, due to either assimilation and fractional crystallisation or simple mixing, cannot be the cause of the isotopic arrays – in these models no comparable ages are produced.

3.2 Implications for the Sveconorwegian Tectonic Regime

High-Al megacrysts illustrate that crystallisation in anorthosite systems began at Moho pressures, but several lines of evidence also indicate that Proterozoic anorthosites were finally emplaced as crystal-rich magmas at shallow crustal levels (~10 km; Berg 1977; Valley & O'Neil 1982). In the context of the new megacryst age data, the process of magma ponding and crystallisation of high-Al megacrysts at the Moho, plagioclase accumulation and subsequent plagioclase-rich magma ascent through the crust is a long-lived process (~100 m.y.) requiring a constant supply of energy and heat to prevent complete magma crystallisation. There is little doubt that high-Al megacrysts are comagmatic with their anorthositic hosts (Charlier et al. 2010; Emslie 1975; Fram & Longhi 1992; Longhi et al. 1993), and therefore the observation of a ~100 m.y. difference in megacryst crystallisation age and anorthosite emplacement age indicates that these rock types are produced in long-lived magmatic systems.

The only geodynamic setting capable of providing sufficient heat and magma over these timescales is a convergent, Andean-arc-type setting. In areas where the plutonic products of well-known Andean-arc systems are preserved, such as the Sierra Nevada or Patagonian batholiths, detailed geochronology shows that magmatism occurred, at varying intensities, over >150 m.y. periods (Ducea 2001; Hervé et al. 2007). Stationary,

sub-continental plumes, back-arc rifting and lithospheric delamination is unlikely to produce such geographically-restricted magmatism over such long periods (McLelland et al., 2010). Over the timescales indicated, both plume and rifting environments would initiate continental breakup or the opening of ocean basins, respectively.

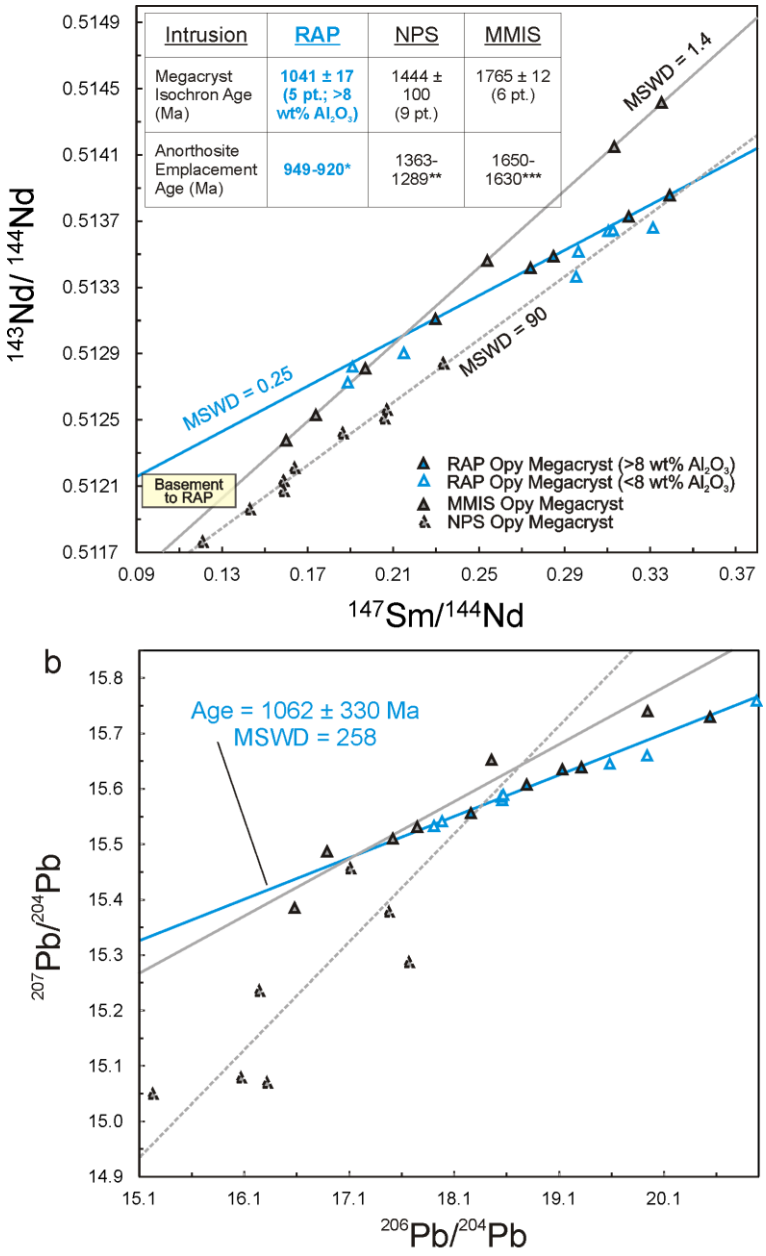

Figure 3.2 $^{143}Nd/^{144}Nd$ – $^{147}Sm/^{144}Nd$ plot showing the isochronous relationship between the highest-Al megacrysts from the RAP, suggesting that the megacrysts crystalised in a ponded magma at the Moho receiving isotopically indistinct recharge and little, no or indistinct assimilation. This isochron yields an age of 1041 ± 17 Ma. b. $^{207}Pb/^{204}Pb$ – $^{206}Pb/^{204}Pb$ plot showing a close correspondence in age to the ^{147}Sm-^{143}Nd age in megacrysts with >8 wt% Al_2O_3. Anorthosite emplacement geochronology: * - U-Pb zircon/baddeleyite in high-Al megacrysts (Schärer et al. 1996; Sauer et al. 2013) and Storgangen orebody of the RAP (Andersen & Griffin 2004), ** - U-Pb zircon/baddeleyite/apatite, Ar-Ar ages from multiple sources summarised in (Myers et al. 2008), * - U-Pb zircon/baddeleyite ages from anorthosites and granitoids (Emslie 1990; Gower et al. 2008a).**

The mechanisms and short timescales calculated for lithospheric delamination suggest that magmatism would be short-lived (Jull & Keleman 2001). High-Al megacrysts represent some of the most primitive material in the anorthositic system, and based on the initial isotopic composition of these megacrysts, I argue that the magmas that crystallised both the anorthosites and the megacrysts were derived from melting of depleted mantle (Chapter 2). In terranes where evolved crustal compositions have not dramatically affected the compositions of the magmas through contamination, the initial isotopic composition of the megacrysts track depleted mantle evolution (Chapter 2).

For the RAP, the crystallisation age of the highest-Al megacrysts, in what I argue is an accretionary Andean-arc environment, coincides with the onset of calc-alkaline magmatism producing the Sirdal Magmatic Belt (Figure 3.3; SMB; 1050-1020 Ma; Slagstad et al. 2012). Megacryst production in long-lived magmatic arc systems supports the interpretation by Slagstad *et al.* (2012) that accretionary, subduction-related magmatism occurred during this period. Moreover, the recognition of the 100 m.y. history of the megacrysts and associated anorthosites in Rogaland requires that the same heat and magma source producing the highest-Al megacrysts (and calc-alkaline magmas) at ~1040 Ma, must have operated during the entire period between 1040 and 930 Ma to allow polybaric anorthosite production and intrusion in the mid-crust. If the operation of a magmatic heat source ceased at any point during this period, either insufficient plagioclase would have accumulated to form the voluminous plagioclase-rich anorthosites or the rising crystal-rich magmas would have frozen at deeper crustal levels.

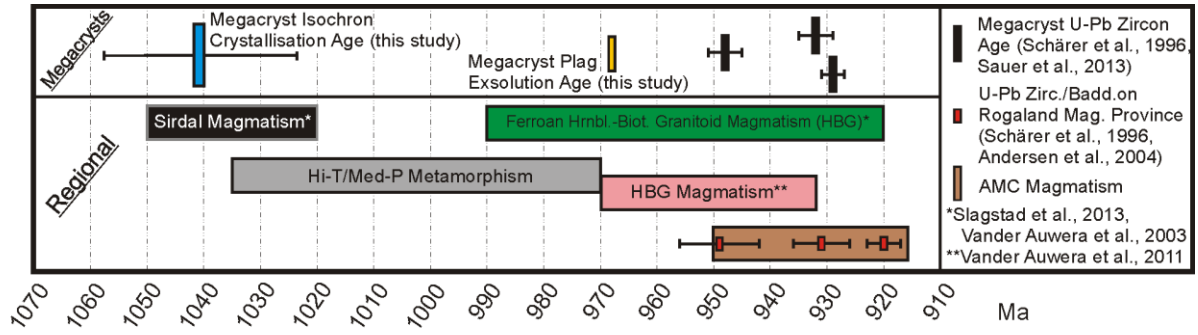

Figure 3.3 Regional and megacryst geochronology illustrating the coincidence of high-pressure megacryst crystallisation at ~1040 Ma with the onset of calc-alkaline Sirdal magmatism. Although this period of calc-alkaline magmatism is followed by a 30 m.y. lull in magmatic activity, as is characteristic in many Cordilleran margins, continued supply of heat and magma at the base of the crust must have continued until ~950 Ma to produce anorthosite mushes and crustal anatexis as well as keep the anorthositic crystal-rich mushes mobile. HBG - hornblende and biotite-bearing granitoid suite (Vander Auwera et al. 2011).

The similarity in age between the highest-Al megacrysts and the onset of calc-alkaline magmatism in the region is very unlikely to be coincidental. This close age relationship and long-lived magmatic system, observed not only in the RAP, but also the MMIS, is more likely to hint at specific processes operating in the genesis of these arc-related, Proterozoic anorthosites. Several scenarios may promote a long-lived magmatic system. For instance, the necessity of creating large amounts of buoyant plagioclase to allow mush ascent to upper crustal levels may require lengthy periods of magma fractionation and recharge (e.g. tens of millions of years) in ponded magmas at the Moho. Furthermore, the ascent of magmas, sufficiently saturated with plagioclase to be

positively buoyant, may take long periods of time – longer than predicted for less viscous basaltic magmas (Kushiro, 1980). Finally, different crustal strength regimes during this period of Earth's history may hinder the rapid ascent of these magmas.

Like many accretionary orogens, high-volume subduction-related magmatism does not necessarily need to characterise the entire accretionary period, and an oscillation between periods of intense magmatic activity has been observed juxtaposed with periods of low-level activity (DeCelles et al. 2009). Periods of low-level activity are not necessarily indicative of wholesale geodynamic changes (i.e. accretion to collision), but may rather reflect specific periods in an accretionary orogenic cycle. This Cordilleran orogenic cyclicity may explain the 30 m.y. gap in regional magmatic activity in the Sveconorwegian belt that is characterised by high-temperature/medium pressure (>800-900 °C; 6-7 kbar) peak metamorphism (Figure 3.3). Magmatic lulls of similar duration have been noted in well-known Cordilleran margins like the Andes and Sierra Nevada batholith (DeCelles et al. 2009).

Detractors of these accretionary models for the Sveconorwegian orogen will argue that Proterozoic anorthosites and their comagmatic megacrysts represent cumulate products of lower-crustal melts formed as tongues of lower crustal material are thrust into the mantle, and thus do not require subduction-related magmatism (Duchesne et al. 1999; Duchesne 2001; Schiellerup et al. 2000; Vander Auwera et al. 2011). While arguments for lower-crustal anorthosite derivation appear convincing, previously published (Ashwal 1993; Emslie et al. 1994) and new evidence (Chapter 2) show that the megacrysts and anorthosites are derived from melting of the depleted mantle. Basic petrologic principles provide reason to reject the hypothesis of lower crustal derivation: to produce broadly basaltic melts (the proposed parental magmas of Proterozoic anorthosites), proponents of lower crustal derivation would have to appeal to unreasonably high degrees of partial melting of lower crust (Morse 1991). In addition, the energy required to produce this anatexis would have to be derived from upwelling mantle, which itself should begin to melt, producing equally, if not more, voluminous mantle-derived magmatism alongside the products of lower crustal anatexis - features that are simply not observed. Our demonstration that both the megacrysts and anorthosites are derived from the mantle as opposed to the crust reaffirms the assertion that the entire period discussed in Slagstad et al. (2012) and Möller et al. (2013) was dominated by mantle-derived, subduction-related magmatism. The voluminous HBG (hornblende and biotite-bearing granitoid suite) magmatism that coincides with the anorthosite magmatism is likely to represent the products of crustal anatexis as the parental magma to the anorthosites impinges on and ascends through the crust.

The close correspondence between the megacryst exsolution age (968 ± 43; see Figure 2.4) and the most recent U-Pb zircon ages calculated from a high-Al megacryst in the Egersund-Ogna massif (948-930 Ma) requires a closer analysis of what these zircon-in-megacryst ages actually represent. The published U-Pb data on these megacrysts (Andersen & Griffin 2004; Schärer et al. 1996) offer no indication of where the zircon phases are located within the megacryst, but based on the close correspondence between the plagioclase exsolution ages (see Figure 2.4) and zircon ages, I suggest that the zircon may form part of the exsolution assemblage in these megacrysts and is therefore dating an exsolution event/s, as opposed to the true crystallisation age of the megacrysts, which according to my dating, precedes the exsolution and final anorthosite emplacement and

crystallisation by ~80-100 m.y. Detailed petrographic and electron microprobe analysis is required to confirm that the zircon phases are located in the exsolution lamellae of the megacrysts.

Recent controversy surrounding the style of orogenesis in the Sveconorwegian orogen is underpinned by the suggestions that accretionary orogenesis extended over an approximately 100 m.y. period (1050-920 Ma), as opposed to the widely accepted model where the period was dominated by protracted collisional orogenesis. Our geochronological evidence from high-pressure megacrysts and Rogaland anorthosites shows that the region experienced subduction-related magmatism between 1041-920 Ma, confirming the proposals of Slagstad et al. (2012) that the Sveconorwegian orogeny is best characterised by an accretionary, Andean-type orogeny.

3.3 Regional Implications for Anorthosite Intrusions in Labrador

Evidence that Proterozoic anorthosites formed in long-lived magmatic arc environments has important implications for the geodynamic setting of the terranes into which the rocks are emplaced, as demonstrated in the Rogaland Anorthosite Province where the megacryst and anorthosite geochronology can be reconciled with long-lived subduction dynamics and magmatic activity in an accretionary Sveconorwegian orogen between 1050 and 920 Ma. These geochronological constraints can also be applied to the geodynamic history of Labrador during a period in which several Proterozoic anorthosites, so common to the eastern coast of Canada, formed (1650 – 1250 Ma).

3.3.1 Testing the Geodynamic Paradigm in Labrador using Megacryst Geochronology

The evolution of, and activity on, the southern margin of Laurentia between 1800 and 1650 Ma provides the backdrop to discussions regarding the geodynamic setting of the Mealy Mountains Intrusive (MMIS) and Nain Plutonic Suites (NPS). Figure 3.4 illustrates the geodynamic evolution of the eastern Labrador region and places the following discussions in context. In this and the previous chapter I assert that Proterozoic anorthosites are the products of arc magmatism.

Megacryst geochronology provides strong evidence supporting this hypothesis. However, as described for the RAP and Sveconorwegian Orogen, the controversial source and tectonic setting of ubiquitous Proterozoic anorthosites results in misleading conclusions relating to the geodynamic setting of the region (Duchesne et al. 1999; Vander Auwera et al. 2011). The view that the RAP was emplaced, after melting of the lower crust, in a late- to post-orogenic setting during the waning stages of an orogeny was used as strong supporting evidence for a predominantly collisional Sveconorwegian orogeny. The interpretation that Proterozoic anorthosites form in long-lived, accretionary, magmatic arcs and are only emplaced or reach their final, mid-crustal location during the waning stages of orogeny, as I propose, challenges not only much of the current thinking on anorthosite petrogenesis, but also requires that geodynamic models for these terranes be rethought. In a similar vein to the RAP, petrogenesis of the MMIS, one of the oldest anorthositic members of the Grenville Province, is ascribed to melting of mafic lower crust as it is thrust into the mantle in what has been referred to as crustal tongues (see Section 1.1.1; Duchesne et al. 1999; Gower & Krogh 2002; Schiellerup et al. 2000; Vander Auwera et al. 2011). Magmatism is thought to occur in a late- to post-orogenic setting as lower crust delaminated or was underthrust, perhaps during orogenic collapse along lithospheric discontinuities into the mantle. The period preceding anorthosite emplacement in the Sveconorwegian Orogen is marked by calc-alkaline magmatic activity (in the

form of the SMB, Section 3.1) and in a similar vein, calc-alkaline activity (1680-1655 Ma) above a northwards-dipping subduction zone, precedes MMIS emplacement in the eastern Grenville Province (Gower at al. 2002, Gower et al. 1992).

The overlap in megacryst crystallisation age and calc-alkaline magmatism in the Sveconorwegian Orogen alludes to the initiation of convergent margin magmatism approximately 100 m.y. before anorthosite emplacement at mid-crustal levels. Do similar relationships exist between megacryst and anorthosite formation and calc-alkaline activity in eastern Labrador?

The first event recognised in the Mealy Mountains region is a pre-Labradorian (1800-1770 Ma) crust-forming event in which granitoids are intruded into earlier supracrustal assemblages that themselves were deposited after ±1800 Ma from immature, local sources (Gower at al. 2008a; Gower & Krogh 2003). The Mealy Mountains terrane plays host to these pre-Labradorian orthogneisses that range in age between 1782 and 1712 Ma, as well as minor paragneisses (Gower & Krogh 2002). It is into these young, and geochemically juvenile and immature rocks that the MMIS has intruded (Emslie & Hegner 1993). Other pre-Labradorian lithological groupings, occurring elsewhere in the Grenville Province, include a northern fringe of parautochthonous rocks and widespread, high grade metasedimentary gneisses such as pelitic-semipelitic rock types and minor quartzite, calc-silicate rocks and amphibolite. An early-Labradorian crust-forming event (1710-1655 Ma; Figure 3.4a), thought to be related to the formation of an island arc above southward-subducting oceanic crust, has been recognised in deformed and metamorphosed gneisses (e.g. nebulitic granodiorite; 1709 Ma) as well as strongly foliated calc-alkaline granitoids (1680-1650 Ma) in the region (Gower & Krogh 2002; Gower & Krogh 2003; Gower et al. 2008a). This calc-alkaline magmatism and island arc formation were outboard of pre-Labradorian Laurentia. A well-constrained period of deformation and metamorphism between 1665 and 1655 Ma requires a radical shift in tectonic conditions and may mark the actual accretion of this outboard arc to the Laurentian continent (Figure 3.4b).

Collision of an outboard arc with Laurentia between 1665-1655 Ma is thought to have initiated what has been referred to as Trans-Labradorian magmatism (Figure 3.4c and d; Gower & Krogh 2002; Gower & Krogh 2003). Magmatism in this mid-Labradorian period manifests itself as three distinct, but intimately linked, suites that include the Trans-Labrador batholith (1654-1646 Ma), coeval supracrustal units and trimodal anorthositic, mafic and monzogranitic magmatism (1650-1625 Ma). Tectonic thickening and the subsequent crustal melting is proposed to have produced the Trans-Labrador batholith (Figure 3.4c): a linear, chemically calk-alkaline to alkali-calcic granitoid belt (600 km in length by <100 km in width), running at an oblique angle to the Grenville Front. The northern fringe of the Trans-Labrador batholith is occupied by the supracrustal, back-arc sequence of felsic and minor mafic volcanics as well as related sediments that have been interpreted as the extrusive carapace of the Trans-Labrador batholith (Gower & Krogh 2003; James & Connelly 1995). The trimodal magmatism overlaps temporally with the Trans-Labrador batholith and has been bracketed between 1650 and 1625 Ma (Figure 3.4d). The mafic component of this trio consists predominantly of layered intrusions and tends to be found in the highest-grade country rocks and, by inference, the deepest crustal levels (Gower & Krogh 2003).

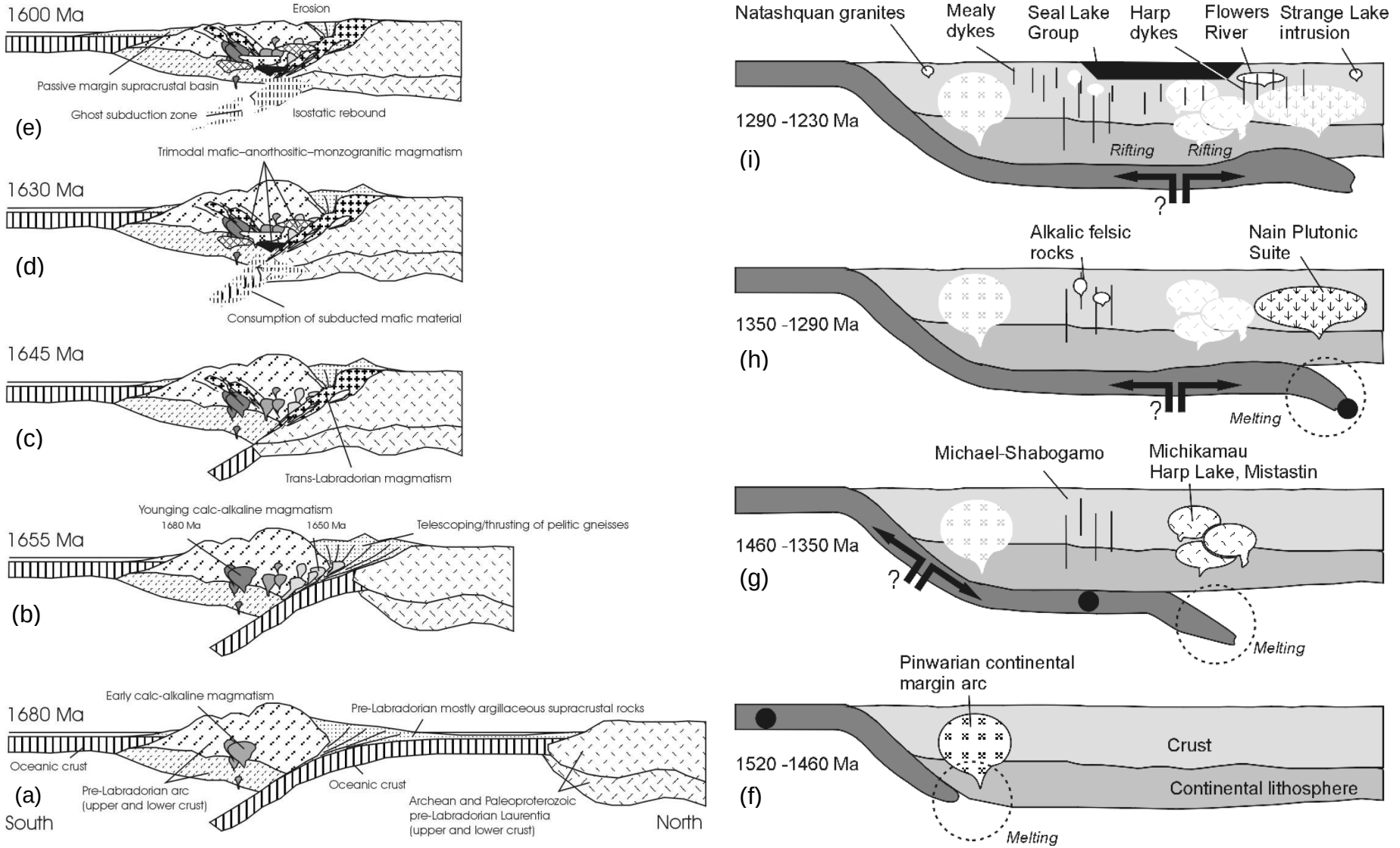

Figure 3.4 Schematic geodynamic development in the eastern Labrador region (Gower & Krogh 2002).

Monzogranitic magmatism is commonly, but not always, associated with the aforementioned mafic magmatism, and consists of a compositional spectrum of rock types from granite to, the dominant lithologic unit, monzonite (Gower & Krogh 2002). Anorthositic magmatism is generally separate from the monzogranitic magmatism and includes not only the Mealy Mountains Intrusive Suite (1650-1630 Ma; Gower *et al.* 2008a), but also the Northwest River Anorthosite and the Alexis River Anorthosite. The Northwest River Anorthosite (1625 ± 6 Ma) forms part of the Cape Caribou River allochthon and is regarded as part of the Mealy Mountains Intrusive Suite (Bussy et al. 1995; Gower & Krogh 2003).

Calc-alkaline magmatism in the Eastern Grenville Province (EGP), and in particular the Mealy Mountains Terrane, occurs in early-Labradorian times (1710-1655). However, crystallisation of MMIS megacrysts, determined by Sm-Nd isochron, predates this calc-alkaline magmatism, but coincides with granitoid magmatism in the region (1782-1754 Ma; Philippe et al. 1993). Evidence of granitoid magmatism is restricted to the Mealy Mountains Terrane, east of the Mealy Mountains and in the region of Goose Bay, and although geochemical data for these felsic intrusives is scarce, the data which exist suggest a calc-alkaline affinity (pers. comm. C.F. Gower, 2013). The temporal relationship between megacryst crystallisation and granitoid magmatism, 100 m.y. before calc-alkaline magmatism serves to confirm that although anorthosite magmatism/emplacement may only be apparent in the waning stages of orogeny, magmatism eventually resulting in anorthosite formation was initiated earlier in the tectonic regime, during subduction and calc-alkaline magmatism.

Based solely on the field and geodynamic evidence presented in the preceding paragraph, it is reasonable to conclude, as have most workers in the region, that anorthosite formation coincides with the waning stages of orogeny, after collisional thickening. Megacryst geochronology argues otherwise and the long-lived timing of this system suggests that magmatism was initiated during orogenic times, but that the anorthosites were only finally emplaced ~ 100 m.y. later in post- to late-orogenic times.

The final stages of the Labradorian orogenesis (1620-1600 Ma) are marked by deformation, metamorphism and a gradual dwindling of magmatic activity, represented by small plutons, stocks and minor granitic intrusions, as a passive, sediment-accumulating margin developed on the newly extended southern margin of Laurentia (Figure 3.4e; Gower & Krogh 2002, 2003; Gower 1996). Quiescence in the region (and the associated paucity of geochronological evidence for tectonic activity), as a result of this passive margin development, is sustained until the Pinwarian orogenesis begins at ~ 1520 Ma.

The Pinwarian orogeny (1520-1470 Ma) is distinguished by voluminous granitic magmatism (*sensu stricto*) and tends to be restricted to the southern part of the Eastern Grenville Province (EGP; Figure 3.4f). Deformation and metamorphism throughout this period is also evident in geochronological data, with the highest-grade metamorphic event occurring between 1470 and 1460 Ma (Gower & Krogh 2002). Geodynamic models explaining this predominantly felsic magmatism and metamorphism/deformation have settled on a continental arc environment, whereas older ideas proposed activity related to a within-plate tectonic setting (Gower & Krogh 2002). The next major event in the geodynamic evolution of eastern Labrador is the Elsonian Orogeny, extending from 1460 - 1230 Ma (Figure 3.4g-i). North of the Grenville Front, but linked to events within the Grenville Province, early Elsonian magmatism is characterised by the production of AMCG suites such as the Michikamau (1460 Ma), Harp Lake (1448-1426 Ma) and Mistastin (1420 Ma) Complexes that decrease in age

northwards (Figure 3.4g; Gower & Krogh 2002). In the Grenville Province, close to the Grenville Front, magmatism in this period manifests itself in the form of sheet-like, 700-km-long, ENE-trending, gabbroic bodies; the Michael and Shabogamo Suites. A period of tectonic quiescence (with exception of the gabbronoritic Matamec Complex) is noted in the region between 1420 and 1350 Ma (Gower & Krogh 2002). During mid-Elsonian times (1350-1290 Ma), AMCG magmatism continued to extend northwards with the formation of the Nain Plutonic Suite (NPS; Figure 3.4h). In the same period in the Grenville Province, extrusive and intrusive magmatism was of a predominantly felsic nature.

This anorthositic magmatism north of the Grenville Front (in particularly in the Nain Plutonic Suite) is challenging to explain, as a rough northward progression in anorthosite age needs to be accounted for, in addition to geographic and temporal isolation of magmatism from any active margins (300-500 km) and local magmatic events (by ca 400 m.y.). Magmatism in the NPS, and other anorthositic massifs north of the Grenville Front (Michikamau, Harp Lake and Mistastin) have traditionally been considered examples of anorogenic magmatism, given the geographic isolation from any reconstructed plate margins or sources of orogenic activity. A mantle plume, failed intercontinental rifting and back-arc settings have all been suggested as possible geodynamic environments for this period, but based on the immediately preceding period of continental arc magmatism, Gower and Krogh (2002) have suggested that the subduction of a spreading-ridge/oceanic plateau may caused evolution of the subduction architecture to that of more flat subduction. This model would account for the decrease in age of magmatic products in a northerly direction several hundred kilometers north of the Grenville Front. The slab would be 'funneled' between the Superior and North Atlantic Cratons.

The period directly preceding the emplacement of the aforementioned anorthosite suites saw widespread felsic magmatism associated with typical orogenic metamorphism and deformation in the EGP, leading workers to suggest that the Pinwarian magmatism and orogeny was caused by a northward-dipping subduction zone (Gower & Krogh 2002). Our evidence for anorthosite petrogenesis in an Andean-type arc would fit well with this model for Pinwarian magmatism, but must incorporate a mechanism for generating anorthositic magmatism up to several hundred kilometers north of the Grenville Front. Geodynamic modeling has shown that melting in arc environments need not only be generated by steeply-dipping slabs, but can also be caused by melting of wedges of asthenosphere and the actual slab, caught up at the slab-crust interface in flat-slab subduction (Gutscher et al. 2000). This model of magmatism has been used to support the northward progression of Elsonian ages for Proterozoic anorthosites and elegantly explains how magmatism can seemingly be produced without any local orogenic processes.

3.4 Conclusions

Although current field and geochronological evidence from Proterozoic anorthosites suggests that they were emplaced at the late- to post-orogenic stage, the overlap in pyroxene megacryst and regional calc-alkaline magmatic activity in both the RAP and MMIS, approximately 100 million years prior to observed anorthosite emplacement at mid-crustal levels, convincingly argues that anorthosite magmatism was long-lived and related to magmatic arc systems. Without knowledge of the megacryst geochronology, the available evidence points to anorthosite formation in the waning stages of orogeny, which in turn influences interpretation of regional geodynamic environments. Based on this new evidence, I show that anorthosite magmatism originated during

stages of accretionary orogenesis and arc magmatism, but that the anorthosites were only finally emplaced at mid-crustal levels during post-collisional periods of the orogenic cycle. These new results show that the Sveconorwegian Orogeny was predominantly accretionary, rather than collisional, and support models indicating that anorthosite production in Labrador was a result of various geometries of subduction-related activity on the margin of Laurentia during Labradorian and Elsonian times.

4 Probing the Mantle Source of Proterozoic Anorthosites: Stripping Away the Effects of Crustal Contamination

For nearly a century many aspects of the origin and petrogenesis of Proterozoic anorthosites have been contentious. In particular, considerable debate exists regarding the source of the magmas. Were the magmas derived from melting of the mantle, be it depleted or enriched, or did the anatexis of the lower crust provide the necessary voluminous magmas? This is particularly important because without a firm understanding of the source of the magmas, discussions relating to other controversies such as the tectonic setting and temporal restriction of Proterozoic anorthosites are moot (Section 1.1). In this chapter, I re-emphasize the dramatic affect that crustal contamination has on the whole-rock isotopic compositions of anorthosites, as several workers have demonstrated in the past (Ashwal et al. 1986; Frost et al. 2010; Heinonen et al. 2010; Scoates & Frost 1996). It is this influence of crustal contamination that obscures the original isotopic signals of the magma and fuels debate around the source of this temporally-restricted rock type. In this chapter I assess geochemical data from internal mineral phases in the anorthosites (orthopyroxene, plagioclase and magnetite) as well as high-pressure orthopyroxene megacrysts, in the framework of the polybaric crystallisation processes emphasised in Chapter 2.

4.1 Crustal Contamination and Isotopic Equilibrium

The addition of a crustal contaminant into an evolving magmatic system has effects upon, not only the whole-rock isotopic composition, but also the mineral compositions and may be the cause of isotopic disequilibrium if minerals form in a progressively contaminated magma. The isotopic signature of contamination is influenced by the age and nature of the crust through which the magmas passes.

Internal isotopic disequilibrium has been described from volcanic settings by several authors including Davidson *et al.* (2005b), Davidson and Tepley (1997) and Ramos *et al.* (2005). The Columbia River Basalt Group (northwestern United States), for example, shows Sr isotopic disequilibrium between plagioclase phenocrysts and the surrounding groundmass, which has been attributed to open-system processes in the crust, such as crustal contamination (Ramos *et al.* 2005). An important realisation of this study is that these lavas only attain their final geochemical characteristics shortly before or during eruption (Ramos *et al.* 2005). Mineral disequilibrium has also been identified in the Merensky Reef of the Bushveld Complex using Sm-Nd systematics (Prevec *et al.* 2005). The results of this study indicate that plagioclase, which is deemed to predate orthopyroxene on the basis of petrographic relationships, is isotopically depleted and hence less crustally contaminated than orthopyroxene (Prevec *et al.* 2005). This observation has been ascribed to progressive crustal contamination and mixing of early, less contaminated plagioclase with later-formed, more contaminated orthopyroxene in density-driven processes such as crystal settling (Prevec *et al.* 2005). Other recent discoveries of Sr isotopic disequilibrium on a range of scales (core to rim, core vs. core, layers) in the Upper Critical Zone of the Bushveld Complex ascribe the disequilbrium to accumulation of plagioclase from different magma sources, followed by plagioclase overgrowth in an evolving residual magma (Yang et al. 2013). Ashwal & Wiebe (1989) report Sm-Nd and Rb-Sr isotopic disequilibrium in Proterozoic anorthosites that have been

intruded into old and evolved crust such as Allard Lake (Quebec) and the Nain Complex (Labrador). Here plagioclase is isotopically primitive when compared to other phases such as orthopyroxene. These authors suggest that minerals crystallising at different times were progressively contaminated during the formation of these suites and therefore developed isotopic disequilibrium (Ashwal & Wiebe 1989).

4.2 Quantifying Internal Isotopic Equilibrium

Internal isotopic disequilibrium is defined as the deviation of the isotopic composition of a mineral from a reference isochron, set at the crystallisation age and passing through the whole-rock composition. While visually discernable, quantitative interpretation of disequilibrium is difficult on a typical isochron diagram and calculation of the deviation is necessary. I define a geometrical measure of the deviation of an internal phase from a whole-rock reference isochron as delta (Δ). Figure 4.1 illustrates the geometrical relationships and the equations used to calculate delta (Δ).

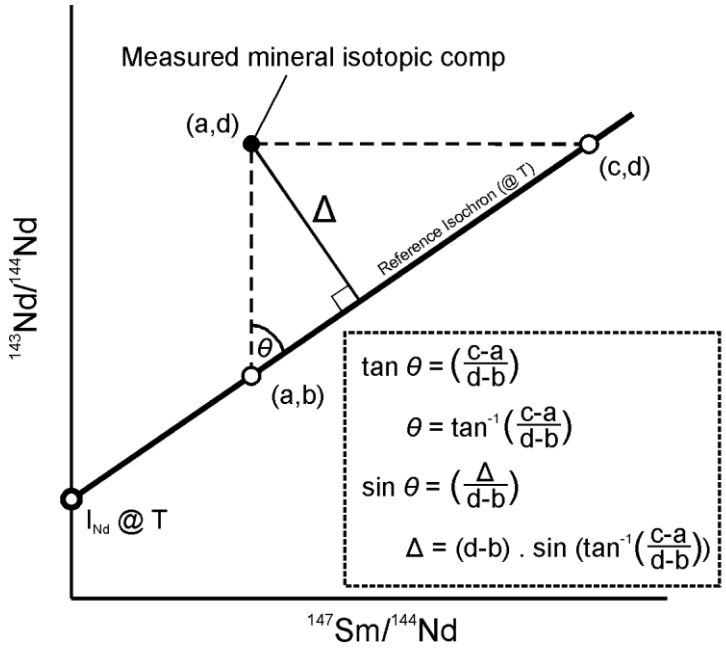

Figure 4.1 $^{143}Nd/^{144}Nd$ vs. $^{147}Sm/^{144}Nd$ plot illustrating the geometrical relationships describing the Delta (Δ) value - a measure of the deviation of an internal mineral isotopic composition from a reference isochron (for a given time, T) passing through the whole-rock isotopic composition.

A reference isochron (for a whole-rock composition) is calculated using the isotopic composition of the whole-rock, age of the sample and initial whole-rock isotopic composition at that age. The isotopic composition of the internal mineral phase, if in disequilibrium with the whole-rock, will then lie a given distance (Δ) from the reference isochron. Δ can either be positive, if the mineral composition lies above the reference isochron, or negative, if the composition plots below the reference isochron. To solve for Δ, unknown values of *b* and *c* are calculated using the straight-line equation of the reference isochron and the known values of *a* and *d*. Δ is then determined trigonometrically as shown in Figure 4.1. Although disequilibrium could also be assessed using the difference in intitial isotope ratios of the whole-rock and internal phases, this trigonometric calculation determines the minimum amount of disequilibrium. The ages of the samples analysed are crucial in determining the intercept and gradient of the reference isochrons and therefore could introduce error in the Δ value if the age

of the sample is not well constrained. Although the overall emplacement age range of the NPS is quite large (1393-1285 Ma), the ages of plutons from which samples were taken in the NPS are well constrained in the literature (Myers et al. 2008). No direct ages are reported for anorthositic samples in this study, but the reported age range for the MMIS is between 1650-1630 Ma. A 20 m.y. age uncertainty, such as observed in the MMIS, produces ~ 20% uncertainty in both Sr and Nd Δ calculations. This percentage error only becomes significant when minerals have low degrees of disequilibrium. External 2-sigma errors on the Δ-value, calculated using 2-sigma values for the whole rock isochron and the internal mineral phases, have on average of 15 % uncertainty, less than the error introduced by the age uncertainty of the massifs. All reference isochrons for the samples from the MMIS are plotted at age of 1640 Ma, while samples from the NPS use ages of plutons reported in the literature (Myers et al. 2008). Although U and Th concentrations were not analysed using isotope dilution, the relationship between $^{207}Pb/^{206}Pb$ and the fixed $^{235}U/^{238}U$ ratio (1/137.88) with time, allowed calculation of a reference isochron and quantification of disequilibrium for the Pb system (Faure and Mensing 2005).

4.3 Petrology and Trace Element Geochemistry

The general petrology of the anorthosites and orthopyroxene megacrysts has been summarised in the introductory chapters, but features pertinent to the discussions in this chapter are described in more detail here along with the trace element geochemistry of the anorthosites.

4.3.1 Noteworthy Petrographic Features

A striking field observation in Proterozoic anorthosites terranes is the complexity at a variety of scales. On a regional scale, many suites, like the NPS, Harp Lake Complex (Labrador) and Kunene Complex (Angola) for instance, are composed of many coalesced plutons with complex intrusive relations (Ashwal & Twist, 1993; Emslie, 1980). A block structure is also a common feature on a local scale, where blocks of anorthosite are hosted by a, presumably younger, anorthosite commonly with slightly higher mafic compositions (Figure 4.2a; Buddington, 1939).

Although marked by relatively simple mineralogy (described in Section 1.5.1), several interesting textures are noted in samples from the NPS and MMIS: 1) Ortho- and clinopyroxene generally form intercumulus phases (Figure 1.8a,c), but examples of cumulus-textured orthopyroxene are observed in several samples where the same phase is also an intercumulus phase (Figure 4.2b). Inclusions of orthopyroxene and clinopyroxene in cumulus plagioclase are also noted (Figure 4.2c, d), 2) Clinopyroxene and orthopyroxene are observed to rim pre-existing orthopyroxene grains (Figure 4.2e), 3) Peritectic reaction relationship is observed between olivine and orthopyroxene (Figure 4.2f; also noted in Harp Lake Complex, Emslie 1980). 4) Observations of 1-5 cm rims of orthopyroxene surrounding high-Al orthopyroxene megacrysts have been noted by Emslie (1976) in the MMIS.

4.3.2 Trace Element Compositions

The sampled anorthosites from both the Nain Plutonic Suite and the Mealy Mountains Intrusive Suite are typical of Proterozoic anorthosites worldwide and present characteristic positive Eu anomalies ($[Eu/Eu^*]_N = 3.6 – 5.1$), enriched LREE profiles ($[La/Sm]_N \sim 3.5$) and flat to slightly concave-upward HREE profiles (Figure 2.2).

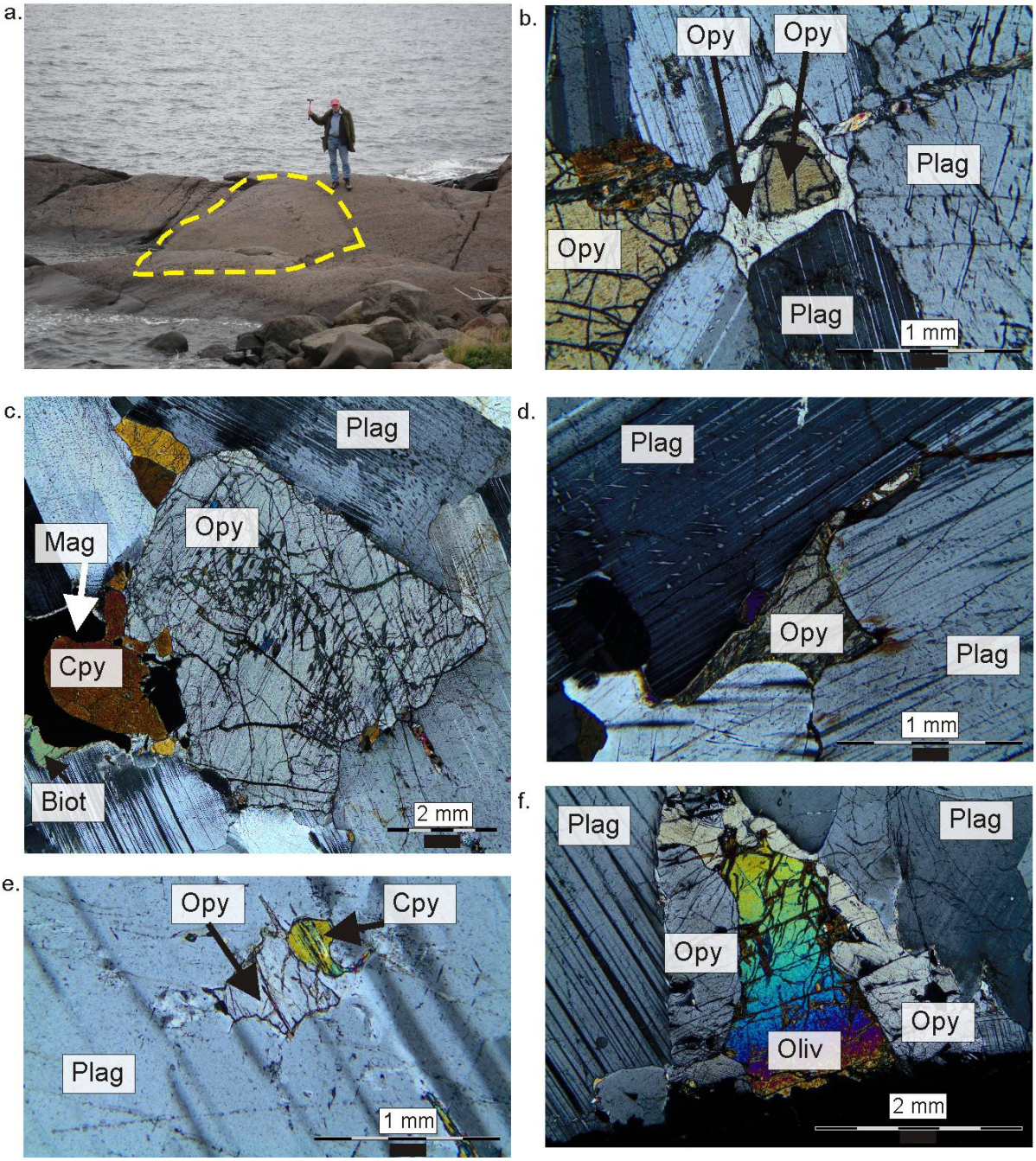

Figure 4.2 Noteworthy field and petrographic features in the MMIS and NPS. a. Meter-scale block structure in the MMIS where a sub-rounded block of grey leuconorites (highlighted by dashed yellow line) is included within leuconorite with distinct maroon hues (probably caused by small heamatite inclusions in plagioclase). b. Subhedral orthopyroxene grain rimmed by a subsequent generation of orthopyroxene (CG09-17). c. A large subhedral orthopyroxene grain interpreted as a cumulus phase adjacent to intercumulus clinopyroxene and magnetite in CG09-32A. d. In the same sample as shown in c. (CG09-32A), intercumulus orthopyroxene is also observed. e. Orthopyroxene and clinopyroxene included within cumulus plagioclase grains. f. Peritectic reaction rim of orthopyroxene around olivine in the interstitial space between cumulus plagioclase grains (CG09-30).

Orthopyroxene megacrysts from the aforementioned suites, as well as the megacryst-rich Rogaland Anorthosite Province, show significantly more variable REE patterns with broad correlations to Al_2O_3 content (a proxy for pressure of megacryst crystallisation; Figure 2.2). In both the MMIS and RAP, the highest-pressure (highest Al_2O_3) megacrysts show the most LREE-depleted patterns ($[La/Sm]_N$ = 0.05-0.37) and no, or very minor Eu anomalies ($[Eu/Eu^*]_N$ = 0.9-1.2). The lowest Al_2O_3 megacrysts, on the other hand, show slight LREE enrichment ($[La/Sm]_N$ = ≤ 1.5) and negative Eu anomalies ($[Eu/Eu^*]_N \leq 1.2$). Megacrysts from the NPS are far more uniform, with clustered Al_2O_3 contents (4-6 wt%), LREE enrichment ($[La/Sm]_N$ = 0.87-3.15) and negative Eu anomalies ($[Eu/Eu^*]_N \sim 0.6$). All data in this chapter can be found in Appendices A-E.

4.3.3 Internal mineral trace element concentrations

Table 4.1 documents the range and average Sr and Nd concentrations of the minerals phases analysed in this study.

Table 4.1 Range and average Sr and Nd concentrations (ppm) for analysed plagioclase, orthopyroxene and magnetite phases from anorthosites in the MMIS and NPS.

		Sr (ppm)		Nd (ppm)		Pb (ppm)	
		Range	Average	Range	Average	Range	Average
MMIS	Plagioclase	776.55-1209.47	991.09	2.05-4.90	2.95	1.14-5.94	2.44
	Orthopyroxene	3.03-10.09	7.94	0.58-14.90	1.06	0.06-2.21	0.89
	Magnetite	8.15-29.85	20.58	0.22-0.35	0.27	0.05-0.28	0.12
NPS	Plagioclase	623.80-911.70	732.01	1.9-12.10	4.61	0.91-3.54	2.06
	Orthopyroxene	2.16-13.40	5.29	0.52-7.4	2.40	0.06-0.29	0.13

Figure 4.3 shows a selection of mineral phases separated from the anorthosite, leuconorites and leucotroctolites exemplifying the type of material that was analysed. Figures 4.3a and b show typical plagioclase and orthopyroxene phases from leuconorites in the MMIS (CG-09-18A). To obtain estimates of disequilibrium in leucotroctolites, plagioclase and magnetite were separated because olivine contains prohibitively low concentrations of Sr and Nd. An example of typical magnetite is shown in Figure 4.3c. In samples from the NPS, very little magnetite is present, but Figures 4.3d and e show examples of plagioclase and pyroxene from this suite (GMB09-01). Figures 4.3f and g show examples of discoloured plagioclase and orthopyroxene. This discolouration is due to minor recrystallisation in the samples, and although attempts were made to avoid these samples, to obtain samples from a wide spectrum of massifs in the NPS, complete avoidance was not possible.

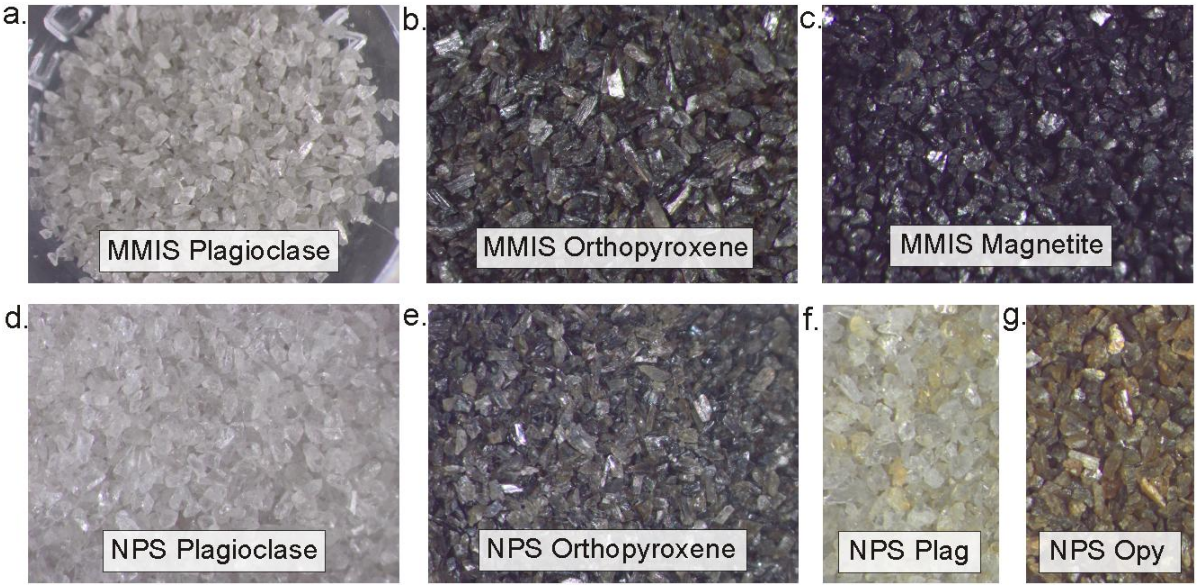

Figure 4.3 a-c. Typical examples of plagioclase, orthopyroxene (CG09-18A) and magnetite (CG09-15) from the MMIS. d-e. Typical plagioclase and pyroxene from the NPS (GMB09-01). f-g. Examples of slightly recrystallised plagioclase and orthopyroxene from the NPS causing discolouration in the grains. The width of each photo is 1.5 mm, except for a. which is 3 mm wide and c. and d. which are 0.75 mm wide.

4.4 Isotope Geochemistry

4.4.1 Whole-Rock and Mineral Isotopic Compositions

On a whole-rock scale, the distribution of isotopic compositions between the different suites is an important first order observation. The MMIS, NPS and RAP display remarkably different isotopic compositions with the MMIS and RAP, showing positive $\varepsilon_{Nd,T}$ compositions ($\varepsilon_{Nd,1640Ma}$ = 2.33-3.62 and $\varepsilon_{Nd,930Ma}$ = 2.2-4.4, respectively; RAP values from Menuge 1988), while the NPS presents a range of negative values ($\varepsilon_{Nd,1363Ma}$ = 1.57 to -8.49; Figure 4.4a). High-Al orthopyroxene megacrysts from each of these terranes have been shown to crystallise under isochemical/equilibrium conditions (i.e. crystallisation with isotopically indistinct recharge and assimilation), forming isochrons ~100 m.y. older than the emplacement ages of the comagmatic host anorthosites (Chapter 2). The initial isotopic compositions for each of these suites of isochronous megacrysts plot at, and overlap with, the upper, most radiogenic end of the whole-rock anorthosite spectrum. In the RAP, the highest-Al_2O_3, isochronous megacrysts produce an initial $\varepsilon_{Nd,1041\ Ma}$ composition of 4.83 ± 0.61. Megacrysts with Al_2O_3 < 8 wt % cover a range of $\varepsilon_{Nd,T}$ from 4.20 to 1.00, which coincides with the range of anorthositic compositions in the RAP. The precision of the isotopic analyses in the MMIS allows one to differentiate different rock types isotopically (Figure 4.4a inset, Figure 4.5a and b). The anorthosites (*sensu stricto*) have the highest $\varepsilon_{Nd,T}$ compositions, followed by leucotroctolites and then leuconorites (although the compositional ranges of the leuconorites and leucotroctolites overlap substantially when plotted with 2 sigma errors).

In ε_{Nd}-^{208}Pb space, suites of megacrysts that crystallised under isochemical conditions, and form true Sm-Nd isochrons have approximately constant ε_{Nd} compositions, but show variations in ^{208}Pb (Figure 4.4b). In the RAP, lower-Al megacrysts are displaced, in varying degrees, to lower ε_{Nd} and ^{208}Pb compositions on a vector trending towards upper-crustal compositions.

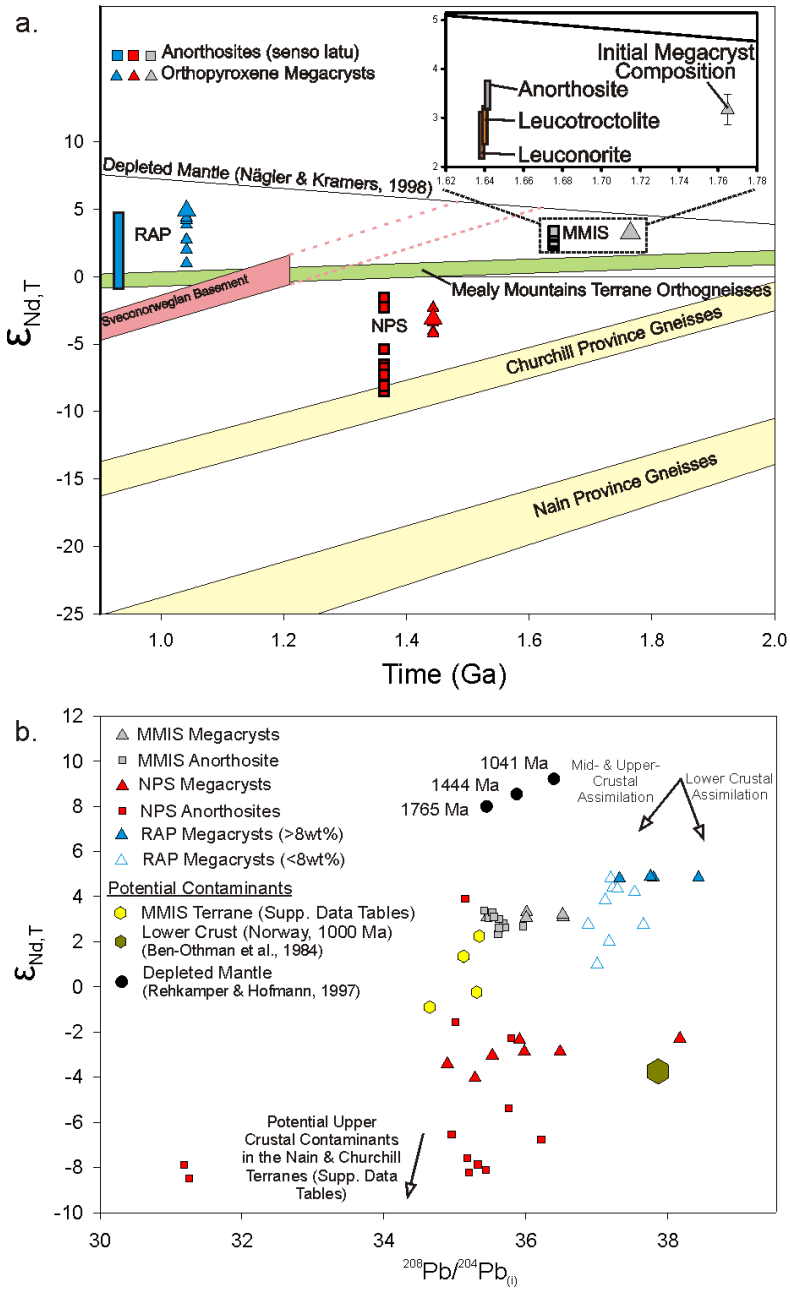

Figure 4.4 a. εNd vs. time illustrating how emplacement of anorthositic mushes into terranes of different ages dramatically influences the isotopic composition of the anorthosites. In young terranes, where the effect of contamination is least dramatic, the initial megacrystic isotopic compositions (large triangles, derived from isochron regression) are consistently only slightly displaced from depleted mantle evolution, indicating magma derivation from depleted mantle. Linear fields indicate evolution of potential crustal contaminants (potential contaminants for the NPS include both Churchill and Nain Province gneisses, due to intrusion into the province-suturing Torngat Orogen). b. The initial assimilation of lower crust by a depleted-mantle-derived melt, subsequent crystallisation of high-pressure megacrysts, and later polybaric fractionation and further crustal assimilation during anorthosite crystallisation is traceable in this εNd vs. ($^{208}Pb/^{204}Pb)_i$ plot.

Anorthosites from the MMIS are displaced to slightly lower ε_{Nd} than the megacrysts, although compositions do overlap. Megacrysts from the NPS have been displaced to much lower ε_{Nd} and slightly lower ^{208}Pb compositions than the other megacryst suites, while the host anorthosites show similar ^{208}Pb but lower ε_{Nd} compositions.

ε_{Nd}-I_{Sr} compositions for anorthosites as well as the internal minerals in the MMIS and NPS are shown in Figure 4.5a, b and 4.6a, b. In the case of the MMIS, orthopyroxene megacrysts show constant ε_{Nd} compositions, as expected given the isochronous nature of these samples. A clustering of whole-rock compositions and associated internal mineral compositions is observed with leuconorites presenting slightly more unradiogenic compositions compared to leucotroctolites (although a few leuconorites overlap in composition with leucotroctolites). In general, plagioclase compositions are grouped together with the respective whole-rock compositions. Orthopyroxene compositions are in disequilibrium with whole-rock anorthosite compositions and show variable ε_{Nd} values spanning the entire range of anorthositic whole-rock compositions, but shifted on the whole to more evolved I_{Sr} compositions. Anomalous magnetite compositions from the MMIS span a range of compositions overlapping with whole-rock anorthosite compositions, but extending to evolved I_{Sr} and depleted ε_{Nd} compositions. Plagioclase megacryst compositions overlap broadly with whole-rock anorthositic compositions. In the NPS, megacryst compositions are least evolved in terms of ε_{Nd} but show variable I_{Sr} values. All of the rock types sampled in the NPS are leuconoritic and so no clear distinctions are noted.

Leuconorites from both the MMIS and NPS show different degrees of disequilibrium in both plagioclase and orthopyroxene phases. Compositional ranges for leuconoritic plagioclase are shifted to slightly lower $\varepsilon_{Nd,T}$ isotopic compositions in both the NPS and MMIS (Figure 4.7)

4.4.2 Assessing Isotopic Disequilibrium

The assessment of internal isotopic disequilibrium provides crucial insight into the process of contamination and its effect on the geochemical composition of the anorthosites at various stages of their petrogenesis. In this contribution, isotopic disequilibrium is assessed either by using a calculated value (Δ, see Section 4.2, Figure 4.8) or visually on a Nicolayson diagram (Figure 4.9), both of which measure the variation in isotopic composition of an internal mineral phase (orthopyroxene, plagioclase or magnetite) from a reference isochron passing through the whole-rock isotopic composition at the time of crystallisation. Visual determination of disequilibrium is difficult for Sr and Nd isotopes (Figure 4.9) due to small differences in composition and hence the calculated disequilrium value is preferred. Average Δ values for the MMIS and NPS in Table 4.2 and Table 4.3 details whole rock and mineral isotopic compositions as well as Δ values for all samples from the NPS and MMIS.

Figure 4.8 summarises Sr, Nd and Pb Δ values for the internal phases of anorthosites in the MMIS and NPS, which are documented in Table 4.2 and 4.3. Both the NPS and MMIS show variable ΔNd and ΔPb values for orthopyroxene with this phase in the MMIS showing both positive and negative ΔNd and ΔPb, but an average ΔNd = 0.127 and ΔPb = 14.4. Orthopyroxene in the NPS does not show any negative ΔNd and ΔPb, but clearly has higher degrees of disequilibrium than the MMIS with ΔNd = 0.626 and ΔPb = 299.8. ΔSr compositions of orthopyroxene in the two intrusions are also variable with both intrusions showing positive and negative Δ geometries. ΔSr has only marginally higher degrees of disequilibrium in orthopyroxene in the NPS compard with the MMIS. The disequilibrium observed in plagioclase in markedly different. Both ΔSr and ΔNd for plagioclase in the NPS and MMIS are tightly constrained very close to ΔSr and ΔNd = 0. Plagioclase from leucotroctolites and leuconorites in the MMIS displays different polarities of isotopic disequilibrium (for Nd), with leuconoritic plagioclase showing ΔNd = -0.072, while leucotroctolitic plagioclase displays ΔNd = 0.103.

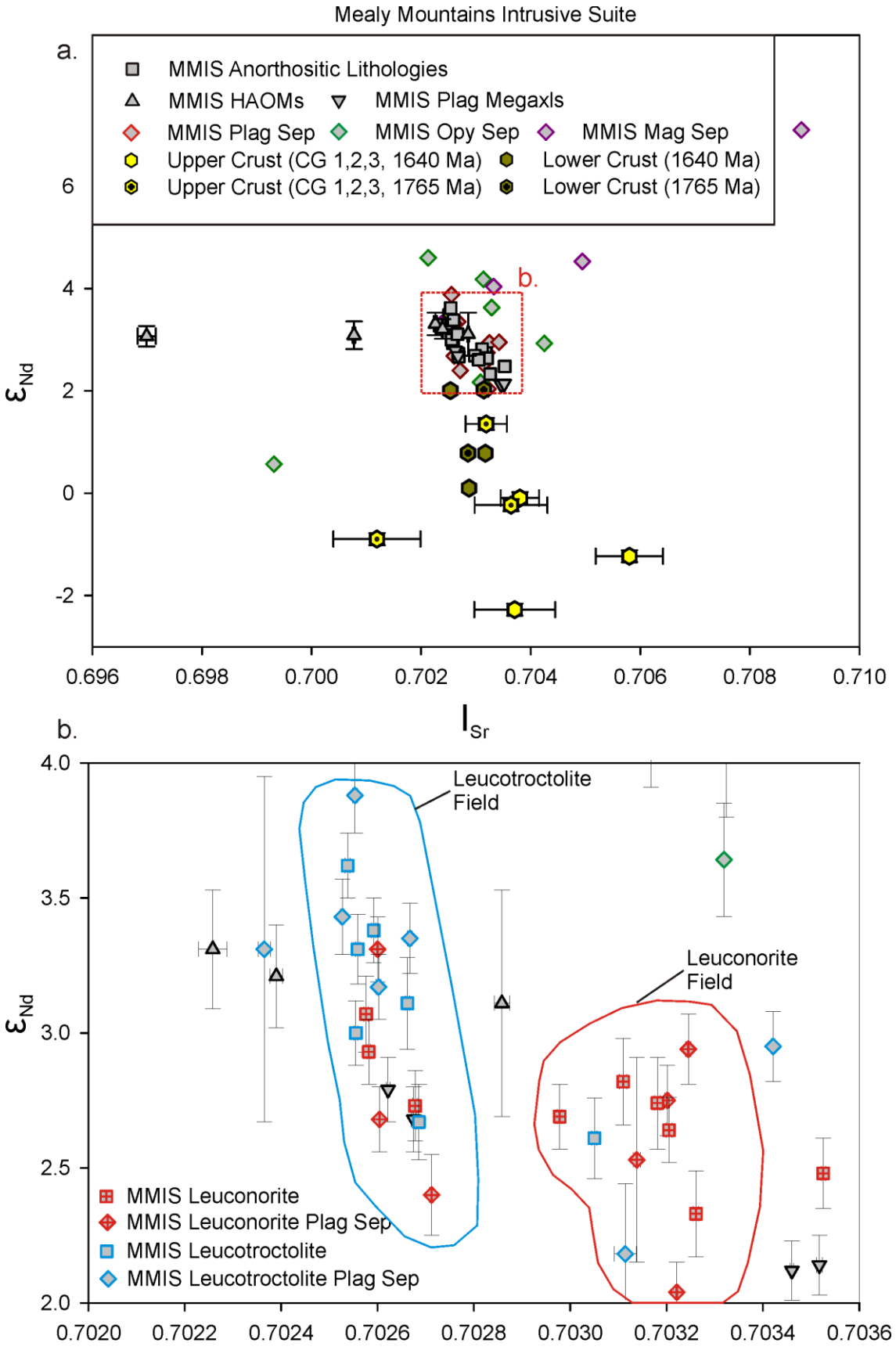

Figure 4.5 a. ε_{Nd}-I_{Sr} compositions for whole-rock anorthosites, high-pressure megacrysts, and internal mineral phases (orthopyroxene, magnetite, plagioclase) in the MMIS. b. Detailed view of whole rock leuconorite and leucotroctolite sample with internal plagioclase compositions from the MMIS. All compositions are plotted at 1640 Ma.

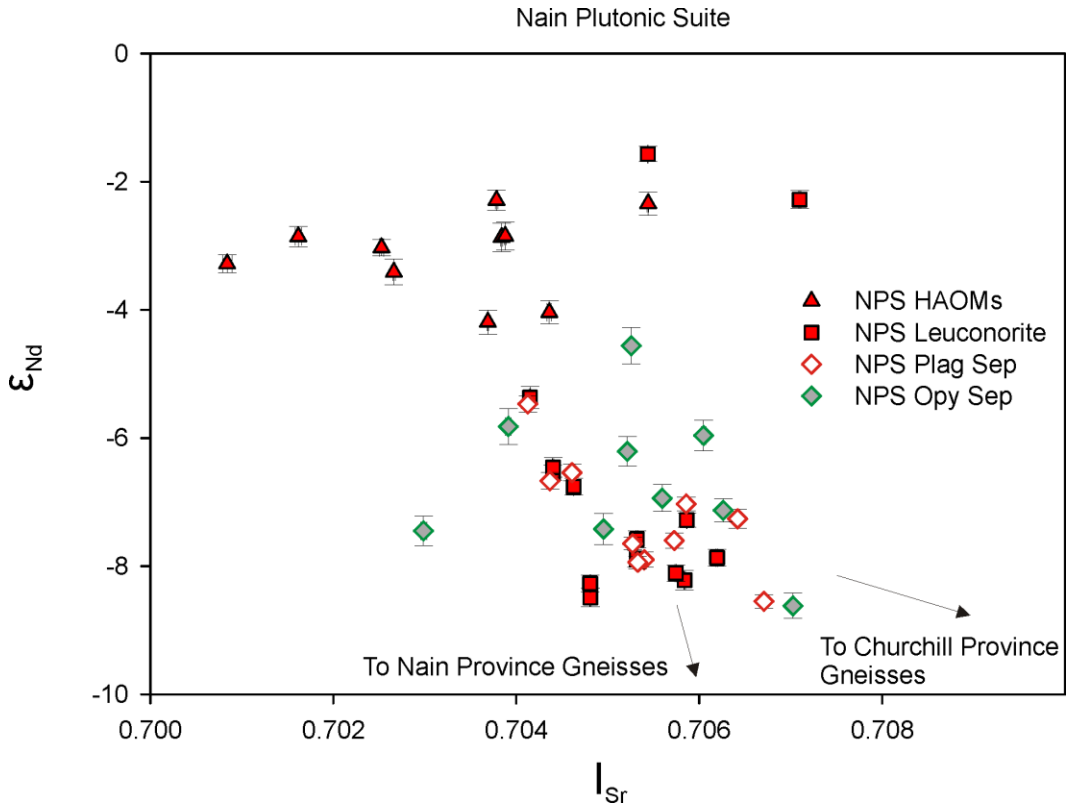

Figure 4.6 ε_{Nd}-I_{Sr} compositions for whole rock and internal mineral phases from the NPS plotted at 1311 Ma.

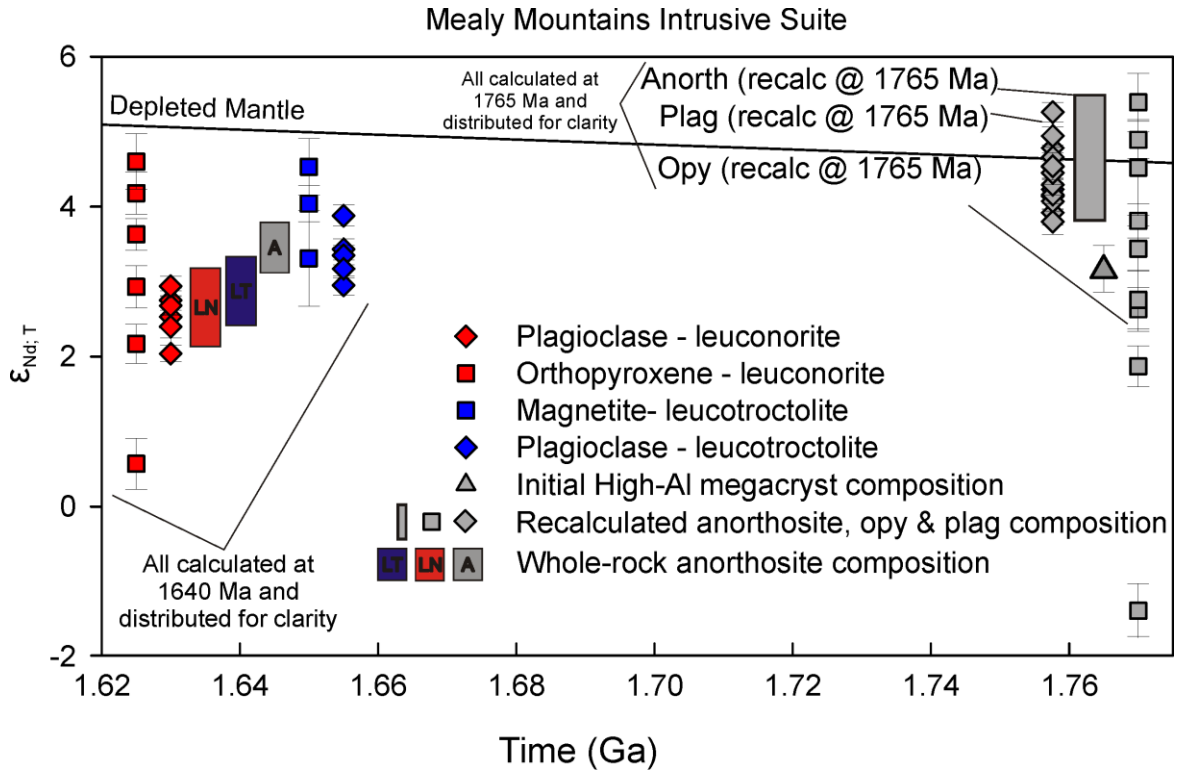

Figure 4.7 $\varepsilon_{Nd,T}$ vs. T illustrating mineral isotope compositions in relation to whole-rock compositions from the MMIS. All compositions are calculated to either 1.64 Ga or 1.765 Ga (high-Al megacryst crystallisation age), but are expanded for clarity. The large range in orthopyroxene compositions relative to the leuconorites and plagioclase compositions is noteworthy.

Table 4.2 Average Δ-values for internal mineral compositions in anorthosites from the MMIS and NPS. Δ-values measure the deviation of an internal mineral phase from a reference isochron passing through the whole-rock composition at time of emplacement. LN = leuconorites, LT = leucotroctolites. HAOM – high-Al orthopyroxene megacryst.

	ΔSr			ΔNd				ΔPb			
	Opy	Plag	HAOM	Opy	Mag	Plag	HAOM	Opy	Mag	Plag	HAOM
MMIS	-2.828	0.081	-3.077	0.127	0.302	Avg=-0.002 LT=0.1033 LN=-0.072	0.395	14.442	-63.184	-13.589	41.123
NPS	3.286	-0.057	-	0.626	-	-0.011	-	299.820	-	-202.451	-

ΔPb in plagioclase is variable, spanning both positive and negative geometries for the MMIS, while only showing negative geometries in the NPS (ΔPb = -202.5).

Once again, plagioclase in the NPS shows much greater degrees of disequilibrium than plagioclase in the MMIS. Magnetite in the MMIS shows relatively more disequilibrium than orthopyroxene and very variable values – perhaps to extensive alteration/oxidation in magnetite separates that was difficult to avoid during separation. High-Al orthopyroxene megacrysts in the MMIS are in isotopic disequilibrium with the anorthosites that host these phases. Interestingly, high-Al orthopyroxene megacrysts show the same disequilibrium polarity as their lower-Al, intercumulus orthopyroxene counterparts, but different megacrysts show either more or less disequilibrium than the intercumulus orthopyroxene in the anorthosite that hosts the megacryst. Finally, it is interesting to note that plagioclase from leucotroctolites and leuconorites in the MMIS displays different polarities of isotopic disequilibrium (Figure 4.8). There are some exceptions to the general trends outlined above: for instance CG09-26A shows anomalous disequilibrium geometries for both Sr and Nd in orthopyroxene. CG09-32A and BR04-125 also show anomalous orthopyroxene disequilibrium for Nd and Sr, respectively.

Table 4.3 Whole rock and mineral isotopic compositions (Opy: orthopyroxene; Mag: magnetite; Pl: plagioclase) for samples from the MMIS and NPS.

MMIS	$^{147}Sm/^{144}Nd$	$^{143}Nd/^{144}Nd$	$I_{(Nd;1640)}$	ΔNd	$^{87}Rb/^{86}Sr$	$^{87}Sr/^{86}Sr$	$I_{(Sr;1640)}$	ΔSr	$^{206}Pb/^{204}Pb$	$^{207}Pb/^{204}Pb$	$I_{Pb(1640)}$	ΔPb
CG-09-15	0.110159	0.511845	**0.510657**		0.022340	0.703697	**0.70318052**		16.3440	15.3604	13.71	
CG-09-15 Opy	0.242494	0.513345		**0.63**	0.235480	0.708585		**-0.27**	23.3582	16.0411	13.69	**-45.64**
CG-09-15 Mag	0.096766	0.511923		**1.89**	-	-		**-**	21.5701	15.7691	13.59	**-201.96**
CG-09-15 Pl	0.066972	0.511380		**0.01**	0.012602	0.703493		**0.12**	16.1031	15.3349	13.71	**-2.16**
CG-09-17	0.098936	0.511703	**0.510636**		0.010644	0.703507	**0.70326081**		16.1586	15.3486	13.72	
CG-09-17 Opy	0.215662	0.512992		**0.26**	0.100369	0.706569		**5.94**	17.0249	15.3934	13.68	**-72.63**
CG-09-17 Pl	0.076655	0.511448		**-0.13**	0.006054	0.703361		**-0.24**	15.0763	15.2147	13.69	**-42.12**
CG-09-18A	0.136576	0.512134	**0.510661**		0.040136	0.704038	**0.70310957**		16.5889	15.3891	13.72	
CG-09-18A Opy	0.186090	0.512709		**0.35**	0.036353	0.704128		**1.07**	17.2250	15.5218	13.78	**116.77**
CG-09-18A Pl	0.070701	0.511408		**-0.13**	0.035789	0.703967		**0.17**	15.3087	15.2714	13.73	**19.51**
CG-09-18B	0.196940	0.512810		**0.21**	0.251460	0.708527		**-2.42**	17.5160	15.510227	13.74	**47.07**
CG-09-20A	0.106657	0.511824	**0.510674**		0.007235	0.702743	**0.70257587**		16.1521	15.3216	13.69	
CG-09-20A Opy	0.310434	0.514099		**0.66**	0.111213	0.704703		**-2.69**	24.4981	16.1970	13.73	**57.32**
CG-09-20A Pl	0.090550	0.511630		**-0.17**	0.001846	0.702647		**0.17**	16.0134	15.2927	13.68	**-25.52**
CG-09-20B	0.2539472	0.5134603		**0.41**	0.185299	0.705393		**-8.86**	16.5806	15.3853	13.71	**34.84**
CG-09-26A	0.103878	0.511776	**0.510656**		0.011313	0.702940	**0.70267784**		-	-	0.00	
CG-09-26A Opy	0.317490	0.513970		**-0.94**	0.525014	0.711462		**-20.26**	20.5473	15.7277	13.66	**-63.38**
CG-09-26A Pl	0.091524	0.511626		**-0.14**	0.006007	0.702851		**0.20**	14.9611	15.1877	13.68	**-23.52**
CG-09-26C	0.313160	0.514149		**0.98**	0.089927	0.705099		**2.05**	16.8905	15.4868	13.78	**-**
CG-09-30	0.105850	0.511827	**0.510686**		0.005768	0.702693	**0.70255950**		16.0933	15.3209	13.70	
CG-09-30 Mag	0.143703	0.512298		**0.53**				**-**	17.4753	15.4981	13.74	**64.51**
CG-09-30 Pl	0.110704	0.511909		**0.25**	0.004471	0.702657		**-0.04**	16.5194	15.3462	13.68	**-30.24**
CG-09-32A	0.102746	0.511760	**0.510652**		0.022747	0.703732	**0.70320535**		16.4544	15.376660	13.72	
CG-09-32A Opy	0.215281	0.512949		**-0.20**	0.174915	0.707129		**-0.75**	17.3333	15.5083	13.76	**73.30**
CG-09-32A Pl	0.071650	0.511440		**0.13**	0.016235	0.703621		**0.24**	16.2561	15.3591	13.72	**4.17**
CG-09-33A	0.082943	0.511544	**0.510650**		0.018450	0.703477	**0.70305027**		16.163248	15.349918	13.72	
CG-09-33A Opy	-	-		**-**					-	-	0.00	**-**
CG-09-33A Pl	0.072950	0.511454		**0.15**					16.3454	15.3864	13.74	**30.89**
CG-09-33C	0.160025	0.512376		**0.00**					17.7471	15.5314	13.74	**41.45**
CG-09-43	0.108426	0.511845	**0.510676**		0.010044	0.702894	**0.70266154**		16.232637	15.339778	13.70	
CG-09-43 Mag	0.122066	0.512002		**0.09**	0.035156	0.703179		**-1.79**	18.6996	15.5552	13.67	**-56.99**
CG-09-43 Pl	0.078928	0.511539		**0.11**	0.005875	0.702803		**0.03**	15.9348	15.2834	13.68	**-44.89**
CG-09-44	0.100408	0.511772	**0.510690**		0.006158	0.702735	**0.70259229**		16.061606	15.304892	13.68	
CG-09-44 Mag	0.144706	0.512284		**0.29**				**0.06**	19.2070	15.6201	13.68	**-3.47**
CG-09-44 Pl	0.075347	0.511491		**-0.09**	0.005507	0.702730		**-**	15.9043	15.2735	13.67	**-26.49**

NPS	$^{147}Sm/^{144}Nd$	$^{143}Nd/^{144}Nd$	$I_{(Nd;T)}$	ΔNd	$^{87}Rb/^{86}Sr$	$^{87}Sr/^{86}Sr$	$I_{(Sr;1640)}$	ΔSr	$^{206}Pb/^{204}Pb$	$^{207}Pb/^{204}Pb$	$I_{Pb(1640)}$	ΔPb
GMB-09-01	0.105942	0.511491	**0.5105792**		0.004002	0.704478	**0.70440405**		14.9915	14.8814	**13.610138**	
GMB-09-01 Opy	0.205196	0.512410	***T=1311***	**0.569979**	0.087440	0.708073	***T=1311***	**14.12171**	17.8917	15.4143	***T=1311***	**578.3887**
GMB-09-01 Pl	0.078562	0.511239		**-0.14708**	0.003841	0.704458		**-0.11743**	14.3258	14.6382		**-376.4973**
BR-04-18	0.114232	0.511819	**0.5108328**		0.015421	0.705736	**0.70545011**		15.1629	14.9965	**13.707961**	
BR-04-18 Opy	0.183796	0.512168	***T=1315***	**-2.26168**	0.092331	0.707735	***T=1315***	**3.946227**	17.4058	15.3637	***T=1315***	**355.439**
BR-04-18 Pl	0.074981	0.511144		**-3.0114**	0.011959	0.705677		**0.034384**	14.9026	14.9426		**-63.80337**
BR-99-83	0.117325	0.511582	**0.5105655**		0.012274	0.704864	**0.70463567**		16.335684	15.2194	**13.828381**	
BR-99-83 Opy	0.268535	0.512984	***T=1319***	**0.823035**	0.283965	0.710485	***T=1319***	**3.946317**	18.2906	15.5579	***T=1319***	**345.3623**
BR-99-83 Pl	0.073375	0.511200		**-0.01485**	0.003850	0.704701		**-0.04129**	14.8910	14.8233		**-548.409**
BR-04-125	0.092064	0.511298	**0.510503**		0.003924	0.705391	**0.70531826**		15.410774	15.0938	**13.784235**	
BR-04-125 Opy	0.226417	0.512523	***T=1315***	**0.580603**	0.193008	0.707454	***T=1315***	**-9.86041**	17.6198	15.4320	***T=1315***	**302.6845**
BR-04-125 Pl	0.063484	0.511040		**-0.10385**	0.002810	0.705394		**0.163752**	14.8597	14.9214		**-252.5495**
EP-97-150	0.104608	0.511411	**0.510503**		0.018234	0.706547	**0.70620752**		15.517484	15.0693	**13.745873**	
EP-97-150 Opy	-	-	***T=1322***	**-**	-	-	***T=1322***	**-**	18.7782	15.4031	***T=1322***	**111.6939**
EP-97-150 Pl	0.099681	0.511398		**0.266957**	-	-		**-**	15.3811	15.0403		**-34.70873**
BR-99-159	0.113718	0.511621	**0.5106354**		0.010357	0.704351	**0.70415826**		15.850160	15.1645	**13.814831**	
BR-99-159 Opy	0.297933	0.513312	***T=1319***	**0.851183**	0.109386	0.707790	***T=1319***	**10.95853**	17.9604	15.5082	***T=1319***	**329.2302**
BR-99-159 Pl	0.085702	0.511365		**-0.11921**	0.003885	0.704217		**-0.09521**	15.1260	14.9637		**-279.4409**
BR-99-221	0.114198	0.511512	**0.5105258**		0.013810	0.705586	**0.7053307**		15.344641	15.0327	**13.728817**	
BR-99-221 Opy	0.181105	0.512134	***T=1315***	**0.393068**	0.119712	0.709033	***T=1315***	**10.19246**	18.7466	15.4760	***T=1315***	**310.2235**
BR-99-221 Pl	0.060095	0.511024		**-0.18462**	0.007343	0.705443		**-0.16188**	14.8480	14.8820		**-218.4249**
EP-97-232	0.105006	0.511445	**0.5105379**		0.006001	0.705979	**0.70586835**		15.892293	15.2026	**13.852148**	
EP-97-232 Opy	0.242941	0.512735	***T=1315***	**0.885418**	0.109142	0.707740	***T=1315***	**-1.01844**	18.0491	15.5074	***T=1315***	**244.4935**
EP-97-232 Pl	0.076147	0.511199		**0.032788**	0.003585	0.705942		**0.050854**	15.3885	15.1034		**-113.4763**
BR-97-237C	0.115086	0.511493	**0.5104987**		0.006252	0.705865	**0.70574916**		15.456300	15.0960	**13.782579**	
BR-97-237C Opy	0.228125	0.512540	***T=1315***	**0.63779**	0.135936	0.708101	***T=1315***	**-1.13023**	18.7083	15.5182	***T=1315***	**293.4806**
BR-97-237C Pl	0.095432	0.511343		**0.180327**	0.003365	0.705807		**-0.02812**	15.2718	15.0392		**-82.78277**

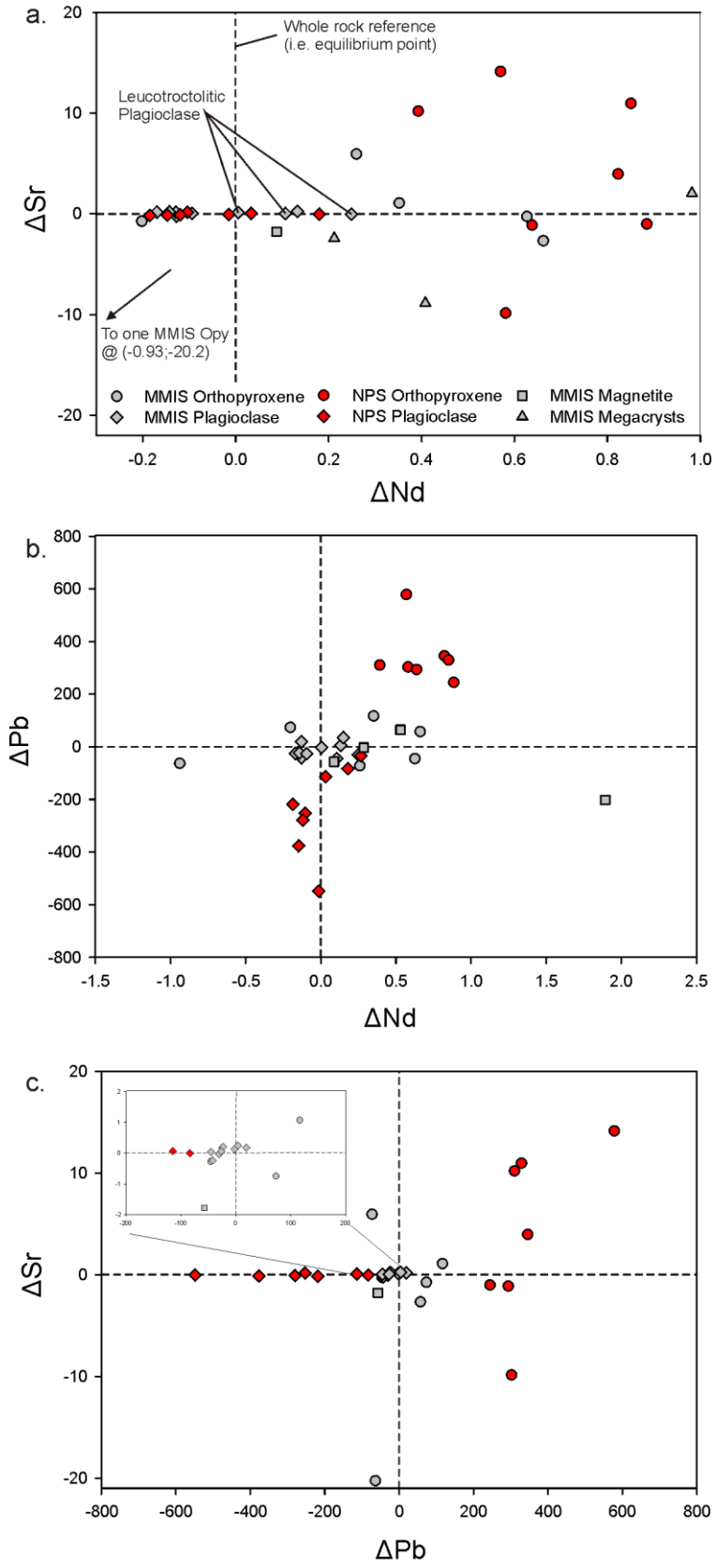

Figure 4.8 Comparitive Δ-values for the MMIS an NPS (a. ΔNd vs. ΔSr, b. ΔNd vs. ΔPb, c. ΔPb vs. ΔSr) calculated using methodology outlined in Section 4.1.2 and Figure 4.1. Dahsed lines indicate whole-rock equilibrium set-point. All reference isochrons and Δ-values for the samples from the MMIS are plotted at age of 1640 Ma, while samples from the NPS use ages of plutons reported in the literature (Myers et al. 2008).

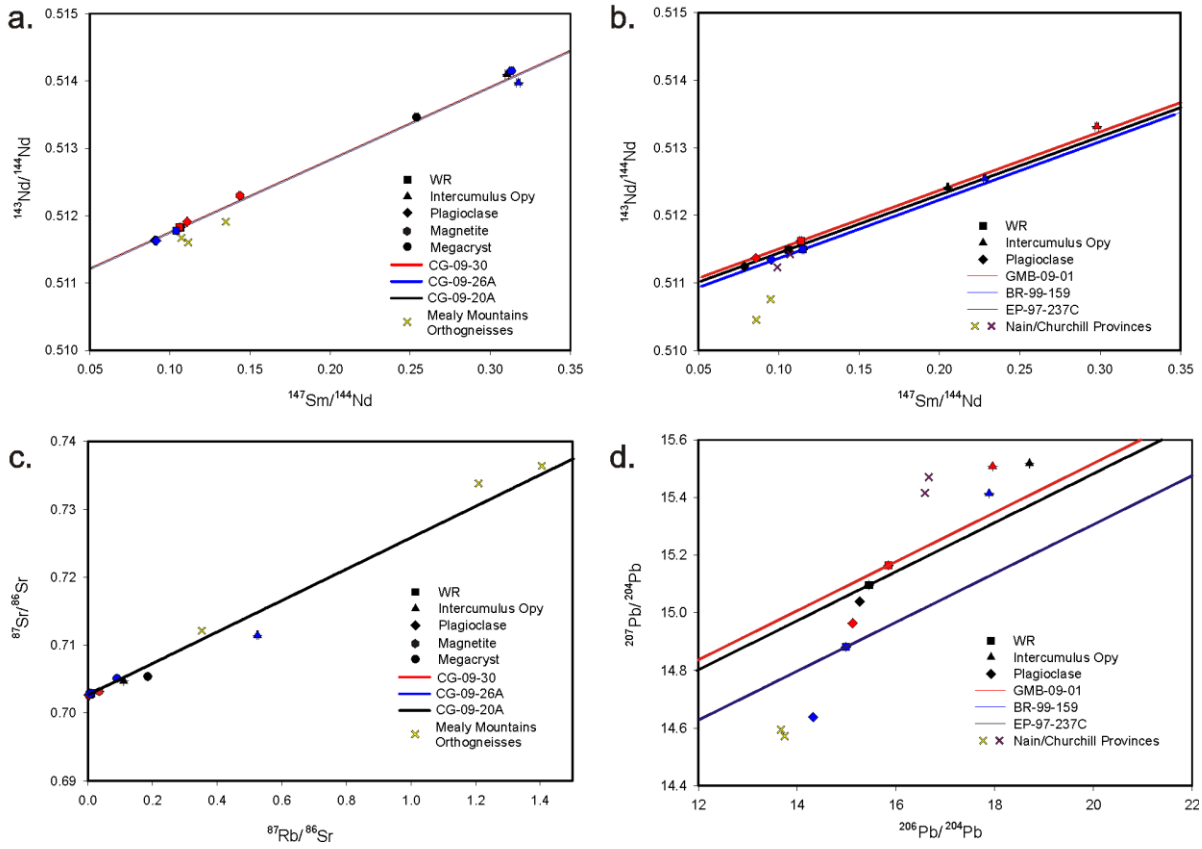

Figure 4.9 a-b. $^{143}Nd/^{144}Nd$ – ^{147}Sm-^{144}Nd plot with reference isochrons and internal mineral compositions for several samples from the MMIS (a) and NPS (b). c. $^{87}Sr/^{86}Sr$ – $^{87}Rb/^{86}Sr$ plot showing reference isochrons and internal mineral compositions in the MMIS. Note how the basement compositions plot along the trend of the reference isochron at higher Sr/Sr and Rb/Sr values. d. $^{207}Pb/^{204}Pb$ – $^{206}Pb/^{204}Pb$ compositions for the internal minerals in relation to whole-rock reference isochrons.

4.5 Discussion

It is well established that Proterozoic anorthosite petrogenesis is a polybaric process beginning at mantle/lower crustal depths (Ashwal 1993; Emslie 1975a; Emslie et al. 1994) and that the first products of this polybaric crystallisation are high-alumina, high-pressure orthopyroxene megacrysts (Charlier et al. 2010; Emslie et al. 1994; Longhi et al. 1993). The absence of negative Eu anomalies in some of the highest-Al megacrysts (Figure 2.2) indicate that plagioclase was not initially a liquidus phase during this crystallisation period and that orthopyroxene was one of the first phases to crystallise, along with clinopyroxene and/or olivine given the proposed basaltic composition of the parental melts (although evidence for the high pressure crystallisation of the latter of the two phases is lacking in the three intrusions studied). Clinopyroxene megacrysts have been found, together with high-Al orthopyroxene megacrysts, in other intrusions such as the Labrieville and Grenville Township massifs (Quebec; Ashwal 1993; Owens & Dymek 1995; Philpotts 1966), suggesting that other phases were on the liquidus before and/or together with orthopyroxene. Presumably these additional mafic phases sunk, with the majority of the orthopyroxene megacrysts, leaving very little to no evidence of olivine or clinopyroxene megacrysts in most anorthosite massifs. Even though these phases are arguably the most primitive products of this magmatic system, the highest-pressure megacrysts from different crustal terranes consistently plot at, and overlap slightly with, the most depleted, radiogenic compositions of the anorthosite

isotopic spectrum, still preserving the dramatic differences in isotopic geochemistry that characterise the anorthositic suites from different crustal terranes (Figure 4.4-4.6). The isotopic overlap in primitive megacryst compositions (which crystallise at the mantle-lower crust interface) with the some cogenetic anorthosite compositions indicates that lower-crustal assimilation in the anorthositic magmas plays a fundamental role in developing the isotopic signature of the magmas that initially crystallise the megacrysts, but that also go on to crystallise the anorthosites. A range of more evolved isotopic compositions in anorthosites and lower pressure megacrysts suggests that subsequent assimilation of compositionally distinct crust (be it lower or middle-crust) must play a role in developing the isotopic composition observed. Chapter 5 highlights the isotopic compositions of highly-differentiated pods in the MMIS, containing the *in situ* residual liquids after anorthosite crystallisation. These pods have isotopic compositions comparable to the most evolved end members of the anorthositic suite, only 1-2 ε-units lower than the megacrysts, confirming that mid- to upper crustal contamination, even after final emplacement and crystallisation of the anorthosites, plays a relatively minor role in developing the isotopic composition of the magmas. Models for Proterozoic anorthosite petrogenesis have suggested that magmatic interaction with the lower crust through assimilation and fractional crystallisation may have been important in the petrogenesis of these suites, although no convincing evidence has, until now, been produced (Emslie et al. 1994; Wiebe 1990). The close geochemical correspondence between primitive high-pressure megacrysts, that crystallise at lower crustal depths, and the more primitive, depleted members of anorthosite compositions provide evidence that lower crustal contamination plays a dominant role in developing the isotopic composition of the massifs.

To preserve the primitive, dense megacrysts (that based on MELTS modelling are negatively buoyant; Chapter 2) in magmas that eventually intrude mid- to upper-crustal levels, positively buoyant, viscous, plagioclase-rich crystal mushes need to develop. Due to the polybaric nature of crystallisation in the anorthositic system, observations of internal isotopic compositions and isotopic equilibrium, between cumulus vs. intercumulus phases for instance, provide clues revealing the petrogenesis of Proterozoic anorthosites. For both the Nd and Pb systems, differing degrees of isotopic disequilibrium are observed in both plagioclase and orthopyroxene (and magnetite where analysed) in the MMIS and NPS. Plagioclase and orthopyroxene from the NPS show a greater degree of disequilibrium for all isotopic systems compared with similar phases in the MMIS (Figure 4.8 and 4.9). I ascribe the differences in degree of disequilibrium to the significant geochemical differences in the nature and age of the lower crust (and to a limited extent, mid-crust) through which the anorthositic crystal-rich magmas have passed, given the propensity of these contaminants to affect the isotopic composition of the magma. These geochemical differences are particularly noticeable when analysing disequilibrium for Nd and Pb isotopes (Figure 4.8 a-c). Potential contaminants in the MMIS have juvenile isotopic compositions similar to that of the mantle-derived anorthositic magma, while in the NPS, potential contaminants (in particular the Archaean Nain Province gneisses; ~ 3 Ga) have significantly more evolved Nd isotopic compositions (Figure 4.4-4.6) and therefore a greater propensity to change the isotopic composition of the evolving magmas. Where the crust is younger and juvenile, the shift in whole-rock and internal isotopic compositions is less extreme, producing less disequilibrium and lower Nd- and Pb-Δ values (Figure 4.8b). In contrast, where the crust is older and more evolved crust (e.g. of the Nain Province) the internal isotopic (and whole rock) compositions are shifted to much larger ΔNd and ΔPb values. The effects of contamination are less obvious when analysing ΔSr as Figure 4.8a and c illustrate with ΔSr compositions that cluster around zero. Average ΔSr compositions for the

NPS and MMIS (Table 4.2) appear contradictory with, for example, positive ΔSr for orthopyroxene in the NPS, but negative ΔSr for orthopyroxene in the MMIS. These ΔSr disquilibrium geometries are also at odds with ΔNd and ΔPb geometries in the NPS and MMIS. This discrepancy highlights the important effects that the crustal assimilant composition plays in the development of isotopic signatures in Proterozoic anorthosites. In both cases, the Sr isotopic compositions of the potential contaminants lie at higher $^{87}Sr/^{86}Sr$ and $^{87}Rb/^{86}Sr$ compositions (MMIS: $^{87}Rb/^{86}Sr$=0.34-1.4; $^{87}Sr/^{86}Sr$=0.711790-0.736298, NPS: $^{87}Rb/^{86}Sr$=0.14-3.5 $^{87}Sr/^{86}Sr$=0.709172-0.803361), along the whole-rock reference line (Figure 4.9c). Contamination of magma with crust of these compositions will not discernably shift the isotopic composition of the crystallising phases above or below the reference isochron. Instead, the effect of this contamination would shift compositions along the reference isochron and, depending on the degree of assimilation and fractional crystallisation, could produce either positive or negative disequilibrium. In contrast, in Nd and Pb space, the contaminants do not lie along the whole-rock reference isochron (Figure 4.9a, b and d), but are offset, by varying degrees (depending on the age) from the isochron providing a greater propensity to shift isotopic compositions away from the reference isochron during crustal assimilation.

Although the age and nature of the crust in the respective terranes affects the degree of disequilibrium, a petrogenetic model describing how the disequilibrium is created is crucial to understanding the formation of the massifs. The observation that both intercumulus pyroxene and cumulus plagioclase show some degree of disequilibrium in all isotopic systems emphasises the importance of crustal contamination in the magmas. However, the polarity of disequilibrium for both Nd and Pb isotopic compositions (orthopyroxene - positive Δ, plagioclase - negative Δ) is unexpected and hints at a hidden complexity in the petrogenesis of Proterozoic anorthosites. These geometries are difficult to explain in a simple scenario where fractionation and ascent of isotopically primitive plagioclase is followed by mid- to upper-crustal contamination and evolved, intercumulus orthopyroxene formation. In this simple case, plagioclase should be isotopically primitive and show positive Δ values (if any disequilibrium at all), while intercumulus orthopyroxene that crystallised at shallower levels from a more contaminated magma might be displaced to lower isotopic values and present negative Δ values. These 'disequilibrium geometries' are not observed and the geometries observed are in fact reversed, with plagioclase showing small, but negative ΔNd and ΔPb values and orthopyroxene showing positive ΔNd and ΔPb values. A different model is therefore required to explain the observed compositions.

The megacryst-anorthosite chemistry and chronology highlighted in this chapter and Chapter 2 indicate that lower crustal assimilation affects the magmas during ponding at the base of the crust. At this level, first olivine and/or clinopyroxene and orthopyroxene are crystallising. Following this plagioclase + orthopyroxene/olivine/clinopyroxene join the crystallising phases. Logically, plagioclase and orthopyroxene must crystallise from this deep level until emplacement at ~ 10 km depth to firstly develop buoyant crystal-rich magmas, and secondly to form voluminous massifs in the mid crust. The schematic diagram for the Nd system (Figure 4.10) shows how the observed disequilibrium geometries may develop due to polybaric assimilation of the ascending magma and the effect of averaging variably contaminated mineral compositions in the final rock.

The isotopic composition of a primitive magma ($I_{Nd;0}$, red line), interacting with and assimilating crustal material polybarically, will be lowered progressively. Initial isotopic compositions of the fractionating phases (in this case, plagioclase and pyroxene) will reflect this progressive change in magma composition and in an

oversimplified scenario will be dragged towards the crustal composition (Figure 4.10a). The time integrated composition of these phases is shown in Figure 4.10b and depending on the proportions of each phase (a, b, c), the final rock will have a composition located in the blue quadrilateral. A reference isochron drawn through this composite composition at the time of anorthosite emplacement (which is ~ 100 m.y. after initial megacryst crystallisation, Chapter 2) will lead to certain phase compositions being in positive (a, a`, b`) and negative (b, c, c`) disequilibrium with the whole-rock composition. By separating orthopyroxene and plagioclase from the whole-rock for solution analysis using precise TIMS (as in this study), one would in effect be averaging these compositions. Depending on the proportions of isotopically primitive or evolved components of a particular mineral present in the rock, the mineral separate may either show positive or negative Δ. A sample will have higher positive Δ values if it contains a higher proportion of the more primitive end-members of any given phase and will, in contrast, show negative disequilibrium if the more isotopically evolved end-members are in the majority.

This explanation for the disequilibrium geometries observed in the MMIS and NPS suites suggests that there should be substantial variability in Δ values in different samples, depending on the proportion of early, primitive vs. later, more evolved mineral phases in the rock. This variability can be masked by the averging effect of mineral separation. Significant isotopic variability is, in fact, observed when one looks at the suite of samples (Figure 4.5-4.8). For instance, whereas most samples show positive Δ values for Nd and Pb in orthopyroxene, samples CG-09-26A and 32A show variable, and in the former case, very negative Δ values. Similar variability and polarity changes are observed in plagioclase compositions. Of course, this mechanism requires that any given anorthosite incorporate variably-contaminated phases. This incorporation need not happen polybarically and could take place in a magma chamber that is fractionating and progressively assimilating wall rock, although petrographic evidence and modelling (subsequent section) indicate the polybaric incorporation of progressively contaminated components is likely.

Blocks of anorthosite included in anorthosite (known as block structure; Buddington 1939; Wiebe 1978), cumulus vs. intercumulus pyroxenes, rims of orthopyroxene on orthopyroxene and clinopyroxene and successive generations of mafic phases (Section 4.3.1) all indicate that successive generations of material have formed on a variety of scales, and could introduce complexity/heterogeneity into the isotopic composition of these rocks. In reality, as the modelling in the subsequent section indicates, contamination of these rising magmas may be more complicated, with multiple assimilants at different crustal levels and curved chemical evolution paths due to the combined affect of fractionation and assimilation. A detailed, comprehensive study of *in situ* isotopic and trace element compositions of cumulus and intercumulus phases is required to unravel the surprising disequilibrium geometries observed in this study and test if a particular internal phase (like orthopyroxene) has a variable isotopic composition in a particular sample.

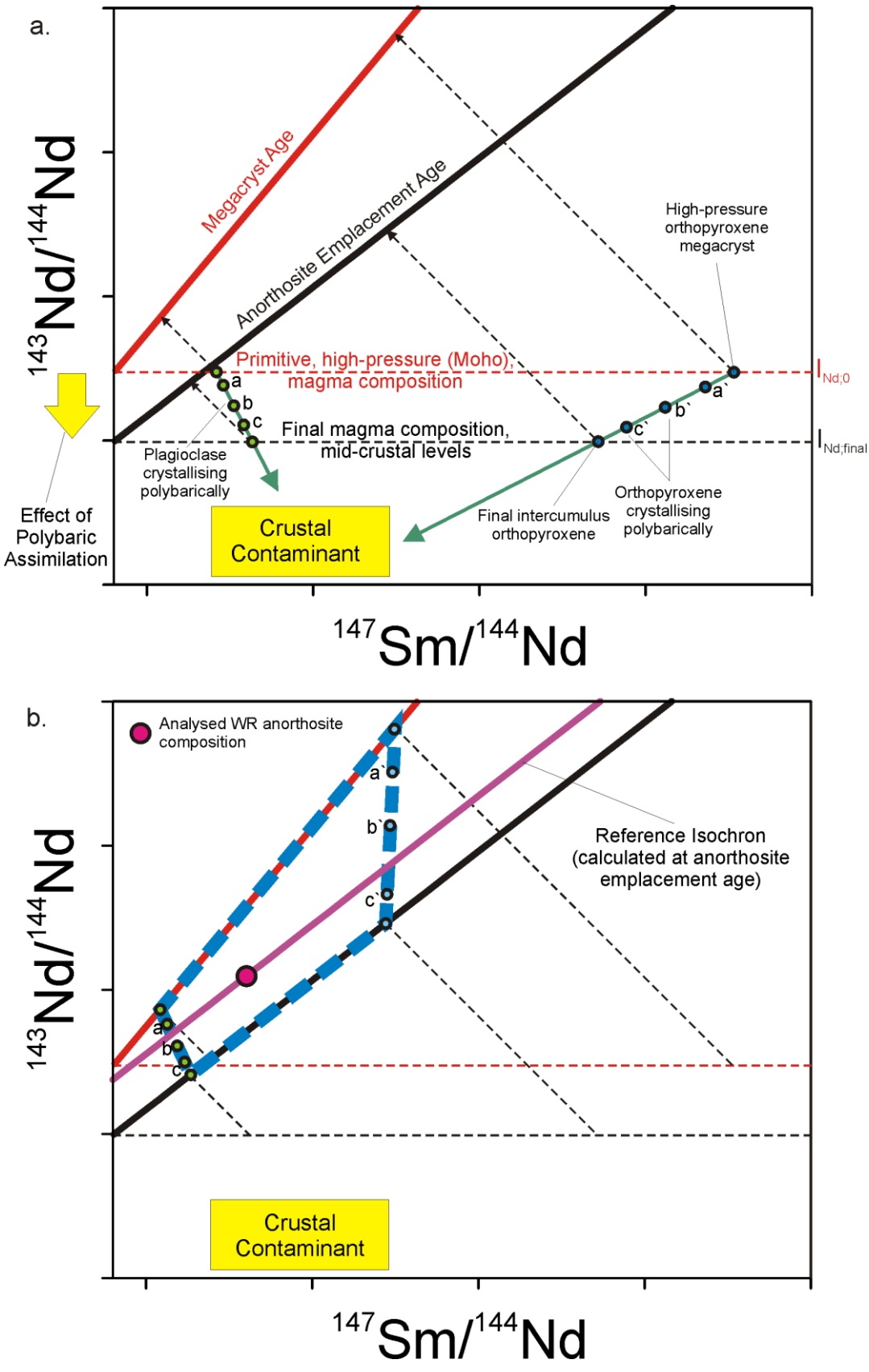

Figure 4.10 a. Schematic Nicolaysen diagram showing effects of progressive crustal contamination on initial whole-rock and mineral compositions. b. The time-integrated effect of progressive crustal contamination on the internal isotopic composition and the averaging effect of incorporation of these various compositions into a sample.

4.5.1 Assimilation and Fractional Crystallisation (AFC) Modelling

The foregoing results and discussions assert that lower crustal contamination plays an important role in developing the geochemical signature of the anorthosites. Several workers have shown that contamination, and particularly the nature and age of the contaminant, has a dramatic effect on the isotopic composition of the anorthosites (Ashwal et al. 1986; Frost et al. 2010; Gleißner et al. 2011; Heinonen et al. 2010; Scoates & Frost 1996). However, these models do not specify at what crustal level the contamination occurs. Although models suggest that lower crustal contamination is important in anorthosite petrogenesis (Emslie et al. 1994), no clear evidence exists to support this hypothesis. Through the isotopic analyses of high-pressure megacrysts and the minerals internal to the anorthosite, I provide evidence asserting that significant contamination of the magma occurs at the base of the crust as the magma ponds at the Moho. As the plagioclase-rich magma mushes develop gravitational instabilities and rise to mid- or upper-crustal levels (<10 km), minor polybaric contamination shifts the isotopic composition to values observed in the anorthosites. Skeptics may argue that a mafic lower crust does not have the propensity to shift the isotopic composition as observed and will argue that contamination occurs predominantly at mid- to upper-crustal levels or that the magmas are in fact derived from melting of the lower crust with minor upper crustal assimilation. Therefore, in the following sections I develop a polybaric AFC model confirming that the observed isotopic compositions of Proterozoic anorthosites can be simulated with reasonable assimilation of lower crustal material by mantle derived melts at Moho depths, in addition to minor mid- to upper-crustal contamination of the evolving magma mush. These models do not distinguish between bulk assimilation of lower crust or contamination by partial melts of lower crustal material.

Mathematical models dealing with AFC processes have, for more than two decades, only dealt with the conservation of mass between the melt and wall rock. In reality, the conservation of thermal energy, together with mass balance between a cooling magma and a warming, melting wall rock, are fundamental constraints for any model dealing with assimilation and fractional crystallisation. In recent years, Spera and Bohrson have developed increasingly detailed models based on coupled non-linear ordinary differential equations that simulate the geochemical path a magma follows as thermal equilibrium between the wall rock and magma is approached during fractional crystallisation, assimilation and recharge (Bohrson & Spera 2001; Spera & Bohrson 2001; Bohrson & Spera 2003; Spera & Bohrson 2002; Spera & Bohrson 2004). By virtue of the conservation of energy and mass, these models, referred to as EC-RAχFC models (energy constrained, recharge, assimilation and fractional crystallisation models), require thermal (as well as chemical) parameters for the magma and crust to be specified. Table 4.4 below defines and specifies these parameters for the three cases discussed in this thesis: the RAP, NPS and MMIS.

4.5.2 Traditional Assimilation and Fractional Crystallisation (AFC) Modelling

The proponents of anorthosite derivation from melting of the lower crust present various arguments detailing why a depleted mantle derivation is implausible (Schiellerup et al. 2000; Duchesne 2001). One such argument purports that traditional assimilation and fractional crystallisation (AFC) modelling of trace element and isotopic compositions typical of a depleted mantle melt cannot account for the observed isotopic compositions in anorthosites. In this section, I agree with this point of view and show that traditional AFC models, developed originally by DePaolo (1981), cannot adequately explain the geochemistry of Proterozoic anorthosites. This is, however, not because anorthosites are derived from melting of the lower crust, but instead that traditional AFC

models inadequately handle the quintessentially polybaric petrogenesis of an anorthositic magma (as shown in this chapter and Chapter 2) involving, as in any magma, the transfer of mass and thermal energy between magma and wall-rock of various compositions.

Using chemical constraints outlined in Table 4.4, Figure 4.11 shows that traditional AFC models for depleted mantle melts impinging on, and assimilating lower crust (or upper crust), fail to produce the primitive isotopic compositions (represented by high pressure orthopyroxene megacrysts and some anorthosites) observed in any of the three anorthosite systems under consideration. Othman et al. (1984) analysed compositions of lower crustal xenoliths from several terranes including lower crustal samples from the Rogaland region (only Nd compositions) and consequently the AFC model run for the RAP (Figure 4.11a) is able to assess the effects of lower crustal contamination (Table 4.4; Othman et al. 1984). There are no clear constraints on the isotopic composition of the lower crust in the MMIS and NPS, therefore the traditional AFC models for these intrusions rely on upper crustal compositions (Figure 4.11b and c).

Two parameters, *r* (the non-dimensional ratio of mass assimilated vs. mass crystallised) and *F* (fraction liquid remaining) aid in identifying whether a given model is plausible or not. Although the models do, under certain circumstances, reach primitive compositions of the anorthosite system (i.e. high-Al megacryst composition; Figure 4.11), the models fail on two accounts. Firstly, when the required isotopic composition is reached at realistic *r*-values (0.4-0.5; RAP and NPS; Figure 4.11a and b), the degree of fractionation required (i.e. fraction of liquid remaining) is extreme (F = 0.1-0). This scenario is unlikely as a magma with only 10 % liquid remaining at the Moho will not be mobile (Miller et al. 2011). Given that this isotopic composition must be achieved at Moho depths (based on geobarometry of orthopyroxene megacrysts), these plutons would never be able to move through the mantle-lower crust interface. At higher F-values (0.7-0.5 %), where magmas may still be able to ascend, the ratio of assimilant mass vs. mass crystallised (r) is unacceptably high, between 0.6 and 0.8 (Figure 4.11a). Calculations suggest that an 1150 °C magma intruding into 150 °C wall rock would, at equilibrium, only be able to assimilate a maximum of 30 % of the crust (Taylor, 1980). Although hotter wall-rock would facilitate more assimilation, r values of 0.6-0.8 are thought to be extreme and unlikely (Taylor, 1980; DePaolo 1981). Traditional AFC models show that untenable degrees of fraction and assimilation are rewuired to reproduce the primitive compositions of the MMIS (Figure 4.11c)

Of course, the fact that traditional mass-balancing AFC models for a depleted mantle melt (using both lower and mid-crustal assimilants; Figure 4.11) fail to produce the required isotopic and element compositions observed in anorthosites should not be reason to suggest that the mantle-derived model for anorthosite genesis is invalid as suggested by Schiellerup et al. (2000) and Duchesne (2001). A more plausible explanation is that these models fail to account for the complexities involved in Proterozoic anorthosite petrogenesis, such as polybaric AFC through crustal materials with varying compositions as well as magma ponding, recharge and assimilation at the Moho over significant timescales (>100 m.y., Chapter 2). To this end, modelling taking into account equilibration of thermal energy and chemical species is presented in the following section.

Table 4.4 Thermal and chemical parameters used in AFC and EC-RAχFC models. Specific heat of magma and assimilant as well as heats of crystallisation and fusion are calculated using data provided in (Spera & W. Bohrson 2001) and the typical compositions for the materials.

				Thermal Parameters				Chemical Parameters			
				C_{pm} (J/kg.K)	H_{cry} (J/kg)	C_{pa} (J/kg.K)	H_{fus} (J/kg)	Nd (ppm)	$(^{143}Nd/^{144}Nd)_i$	Sr (ppm)	$(^{87}Sr/^{86}Sr)_i$
Depleted Mantle Starting Composition used in Model		DM - RAP		1461.78	405115	-	-	**12.9** [1]	**0.512989** [2]	**210** [1]	**0.701854** [3]
		DM - NPS						**12.9** [1]	**0.512856** [2]	**210** [1]	**0.701266** [3]
		DM - MMIS						12.9 [1]	**0.512914** [2]	210 [1]	0.701527 [3]
AFC	Lower Crustal Assimilant	RAP	LC	N/A				31-48 [4]	0.510521-0.511329 [4]	Not modelled as no constraints on lower crust composition	
		NPS	UC					39.9 [5]	0.510100 [5]		
		MMIS	UC					50 [5]	0.501400 [5]		
EC-RAχFC	Assimilant Parameters Reported in Literature	RAP	LC	N/A				31.1-48.4 [4]	0.510442-0.511259 [4]	-	-
			UC					24.5-51.8 [6]	0.511184-0.511352 [6]	-	-
		NPS	LC					-	-	-	-
			UC					50-55.8 [5]	0.509635-0.510405 [5]	43.25-128 [5]	0.706293-0.740558 [5]
		MMIS	LC					-	-	-	-
			UC					21.3-31.7 [6]	0.510309-0.510423 [6]	28.99	0.702673
	Optimised Assimilant Parameters Used in Model	RAP	LC	-	-	1480.21	409794.7	34.7	0.511050	-	-
			UC	-	-	1417.41	316650.7	69	0.511214	-	-
		NPS	LC	-	-	Same as above		-	-	-	-
			UC	-	-			39	0.510100		
		MMIS	LC	-	-	Same as above		-	-	-	-
			UC	-	-			70	0.510394		

Where bold, model parameters are equivalent to those reported in literature, calculated or analysed.

C_{pm} &C_{pa}: isobaric heat capacity of the melt (m) and assimilant (a) based on melt and assimilant composition and oxide heat capacities provided in Spera and Bohrson (2001). General upper and lower crustal compositions used in calculations was taken from Rudnick and Gao (2003)

H_{cry} & H_{fus} : latent heat of crystallisation (melt) and fusion (for assimilant) calculated from latent heat of of crystallisation and fusion of silicate and oxide phases reported in Spera and Bohrson (2001).

[1] Emslie (1980), Charlier et al. (2010).

[2] DM calculated using Nägler and Kramers (1998).

[3] DM calculated using DePaolo and Wasserburg (1976).

[4] Ben-Othman et al. (1984)

[5] Analysed in unpublished work and this study (see Appendix E)

[6] Menuge (1988)

[7] Hegner et al. (2010)

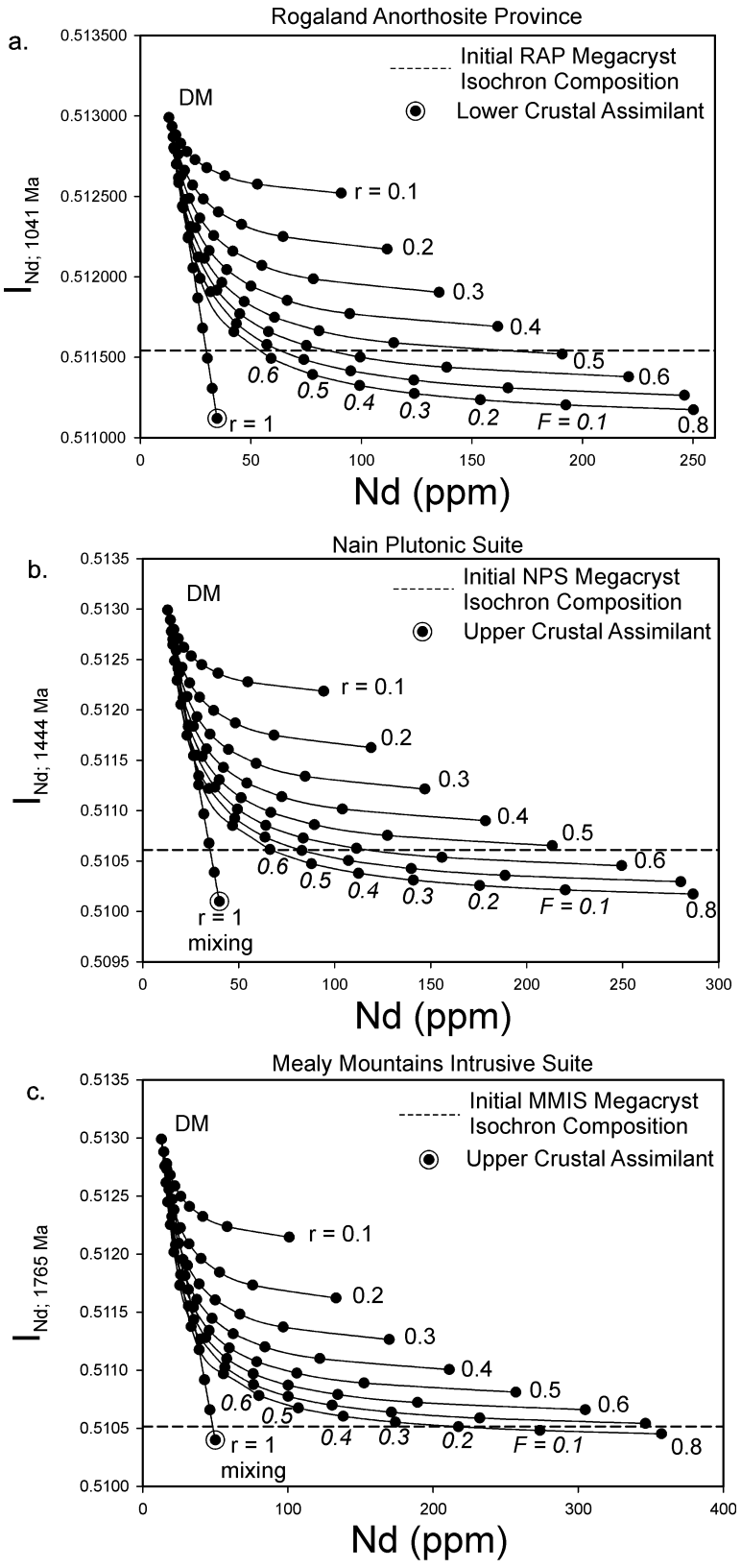

Figure 4.11 Traditional AFC model simulating assimilation and fractional crystallisation of a melt derived from depleted mantle (DM) with lower crustal material (or upper crustal material; see Table 4.4). *r* represents the non-dimensional ratio of mass assimilated vs. mass crystallised, and *F*, the fraction liquid remaining. The models are able to reproduce the most primitive compositions in the anorthosite system (high-Al megacrysts) but only at unreasonably high *r*- (>0.5) and *F*-values (>0.2).

4.5.3 Energy-Constrained Recharge, Assimilation and Fractional Crystallisation (EC-RAχFC) Modelling

The aims of this more realistic modelling regime are two-fold: 1. To illustrate that contamination of a depleted mantle-derived melt with lower crustal material (be it solid, bulk assimilation or liquid, anatectic melt) during a ponding event can result in the initial isotopic composition observed in high-pressure orthopyroxene megacrysts and some anorthosites. Subsequent assimilation of more evolved mid-crustal lithologic units, presumably during ascent of anorthositic mushes, can produce the range of isotopic compositions observed in the anorthositic members of these suites. 2. To show, more importantly for Proterozoic anorthosite petrogenesis, that it is possible to produce the observed geochemical signatures from a depleted mantle melt as opposed to a scenario involving lower crustal anatexis.

EC-RAχFC models allow the user to input the initial thermal and compositional parameters for the original magma, any recharge magma and the wall-rock/assimilant, partition coefficients for both the magma and wall-rock, heats of fusion and crystallisation and isobaric specific heat capacities of the system's constituents. Solution of a set of differential equations, with magma temperature (T_m) as an independent variable, produce values for the average temperature of the wall-rock (T_a), fraction of melt within the magma body (f_a), mass of both cumulates (M_c) formed and wall-rock involved, mass of anatectic melt assimilated and the concentration of trace elements as well as isotopic compositions of the evolving magma. Chi (χ) denotes a function in the model that allows varying proportions of melted wall-rock to be assimilated by the magma as well as simulating pure fractional crystallisation (when $\chi = 0$). The calculations run to a user-defined equilibration temperature (T_{eq}) that represents the point at which the magma and wall-rock temperatures are equivalent (an equilibrium condition) and require inputs relating to the initial magma temperature (T_{m0}), initial assimilant temperature (T_{a0}), initial isotopic compositions (IC_0) and bulk partition coefficients for the magma and assimlant (D_m and D_a). The initial mass of magma (M_m) used in the calculations is assigned a non-dimensional value of 1. Model outputs such as mass of cumulates formed (M_c), mass of magma recharge (M_r) and mass of crust assimilated (M_a), for example, are reported relative to this initial, non-dimensional magma mass of 1. For instance, M_r of 2 indicates that twice as much magma has entered the chamber as was initially present, while M_c of 1.5 indicates that a relative mass of cumulates, 1.5x the mass of the initial magma mass has formed.

In the three field areas under consideration, input parameters for the RAP scenario are well defined with good constraints, most importantly, on the composition of the lower crust in the region (Othman et al. 1984). As the foregoing description mentions, the final models represent "polybaric" models, although only two-stages are used to simulate this pressure change. The first simulations presented below deal initially only with assimilation of lower crustal material in the Rogaland anorthosite, as the chemical parameters are well constrained in this region. Using these chemical parameters, the models successfully reproduce observed isotopic and elemental compositions in the suite with a set of calculated and determined thermal parameters. These chemical and thermal parameters, successful in the Rogaland scenario, are then applied to the lower crustal assimilation stage in the other regions, before a second stage of assimilation involving mid-crustal assimilants (i.e. lower pressure) is run.

4.5.3.1 Setting the Scene with Simulations of Lower Crustal Assimilation in the Rogaland Region:

The predominant aim of this modelling iteration is to reproduce the initial Nd composition and isochronous character of the suite of high-Al orthopyroxene megacrysts from the RAP (I_{Nd}=0.511541±31, Chapter 2) using a depleted mantle melt as an initial starting point. As a general principle, models adhering to the predetermined thermal and chemical parameters and constraints are used. If these parameters do not reproduce the observed geochemistry, models using optimised constraints (also shown in Table 4.4) are run as long as the parameter changes can be justified.

Using the thermal and chemical constraints shown in Table 4.4, a depleted mantle derived melt, assimilating average lower crustal compositions (I_{Nd}=0.511050) in the Rogaland region, does not produce the observed isotopic compositions of the most primitive megacrysts. A range of isotopic compositions are, however, noted as possible lower crustal compositions in the region (Othman et al. 1984). If, therefore, a slightly more evolved composition is used (I_{Nd}=0.51105), the initial composition produced at a T_{eq} of 1030 °C is in line with that observed in the high-Al megacryst suite of RAP (Figure 4.12a). It is at the equilibration temperature that the model is optimised. At this particular equilibration temperature, the fraction of anatectic melt produced is 0.44. Mass of recharge (M_r) is optimised at 1.5 and consequently produces nearly double the mass of cumulates (M_c) relative to the original magma (M_0) – a feature crucial to any model dealing with anorthosite petrogenesis as vast quantities of buoyant plagioclase must be generated. A noteworthy feature of this model is the decrease or reversal in Nd concentrations in the evolving magma at T_m = ~1050 °C and stabilisation of the isotopic compositions in the magma as the T_{eq} is approached (Figure 4.12a). This feature is produced due to incompatibility of Nd in the assimilant and consequent dilutional effects during progressive assimilation. With progressive crustal anatexis, Nd is released into the differentiating mantle-derived magma increasing the concentration in the magma, in addition to lowering the isotopic composition. At a given point, incompatible Nd is exhausted in the assimilant, but the crust is still melting and being assimilated into the magma. At this stage, additional assimilation serves to only dilute and consequently lower the Nd concentration of the magma, causing the observed Nd concentration reversal and isotope ratio stabilisation in the magma. This stabilisation/flattening of isotopic compositions provides the necessary conditions to produce an isochronous series of megacrysts where the magma appears to be receiving little, no or isotopically indistinct recharge and assimilation, but in fact represents the consequence of continued RAFC at lower crustal depths. The extent of the reversal is largely dependent on the bulk partition coefficient of the assimilant (D_a), which is set a 0.25 in this simulation, based on the values described for impingement of a basaltic melt on/in a mafic lower crust in (Spera & Bohrson 2001). The reversal is large enough and extreme enough, using D_a = 0.25, to envisage a series of isochronous megacrysts forming over a small temperature range. If, however, a lower D_a = 0.15 is used in the simulations, the likelihood of forming a series of megacrysts with essentially constant I_{Nd} increases. Distribution coefficients for magmas and assimilants in the lower crust are variable and the values used above may not represent reality, but this simulation illustrates that it is possible to create the appropriate conditions for formation of isochronous megacrysts in a ponding magma at the Moho. As highlighted in the sensitivity tests below, a similar situation could be created by simple fractional crystallisation (χ set to 0) at these depths, but as Figure 4.12b shows, this scenario would not reproduce the I_{Nd} = 0.511541 isotopic compositions of the megacrysts and anorthosites. Using the distribution coefficients developed for Proterozoic anorthositic systems (Bédard 2001), the liquids produced in the EC models would crystallise orthopyroxene and plagioclase, and consequently anorthosite, of

appropriate Nd composition. At the 1030 °C equilibration temperature, ~ 40 % melt would still remain. This aspect is crucial and provides a check on the suitability of the model as the anorthositic mush, after reaching the desired isotopic composition, must still be mobile enough to rise to higher crustal levels. With 40 % liquid remaining, the mush may be mobile, but may also rise to mid-crustal levels in a quasi-solid state. Sensitivity tests for this model are shown in Figure 4.12b by adjusting several of the crucial parameters.

Thus far, the simulations have dealt with the initial stage of anorthosite genesis in an effort to reproduce the isochronous megacryst compositions and, by inference, the initial compositions of the entire RAP suite. Can a secondary iteration in the model account for the isotopic composition of the lower-Al megacrysts and anorthosites? Figure 4.13a shows continuation of the first iteration into a second stage, representing magma evolution at lower pressures. This pressure change is simulated in the models by a change in crustal/assimilant chemistry (mid/upper crustal compositions). Although pressure is known to have an effect on distribution coefficients, this is not the case for Nd in basaltic melts as indicated by (Spera & Bohrson 2001). Lower-Al contents of megacrysts in isotopic disequilibrium with the isochronous series of very high-Al megacrysts point to a pressure change associated with an isotopic change. Important assumptions in this iteration are the initial assimilant/country temperature (T_{a0}), which has been set at 875 °C, 155 °C below the T_{eq} of the initial iteration and 50 °C below the assimilant solidus. Changing the initial temperature of the assimilant has very little effect on the geochemical path as shown in Figure 4.13a. This temperature is justified as magma impingement at the Moho, and potential silicic melt (observed coevally with Proterozoic anorthosites) ascent through higher crustal levels, would increase the ambient temperatures. The chemical evolution is significantly different in this iteration as magma temperature, and consequently the fraction of anatectic melt produced, is lower. Isotopic and elemental Nd compositions of lower-pressure megacrysts and anorthosite are reproduced in this iteration except for the very unradiogenic end-members of the suite reported in Menuge (1988). It may be argued that the isochronous array of high-pressure megacrysts could be created in this second iteration during the first tens of degrees temperature drop. A flat isotopic path can be created in this second iteration with low χ-values (Figure 4.12b). The use of this parameter does not, however, reproduce the range of anorthosite and lower-pressure megacrysts observed in the RAP and therefore cannot be considered. This indicates that it is more likely for isochronous high-Al megacryst arrays to be created during an initial ponding stage, than on ascent of the mushes into shallower crust. This assertion is supported by the lack of negative Eu anomalies in the actual highest-pressure megacrysts, indicating crystallisation in magma before plagioclase crystallisation and with, consequently, no buoyancy potential to rise to shallower levels in the crust. A T_{eq} of 965 °C optimises the model.

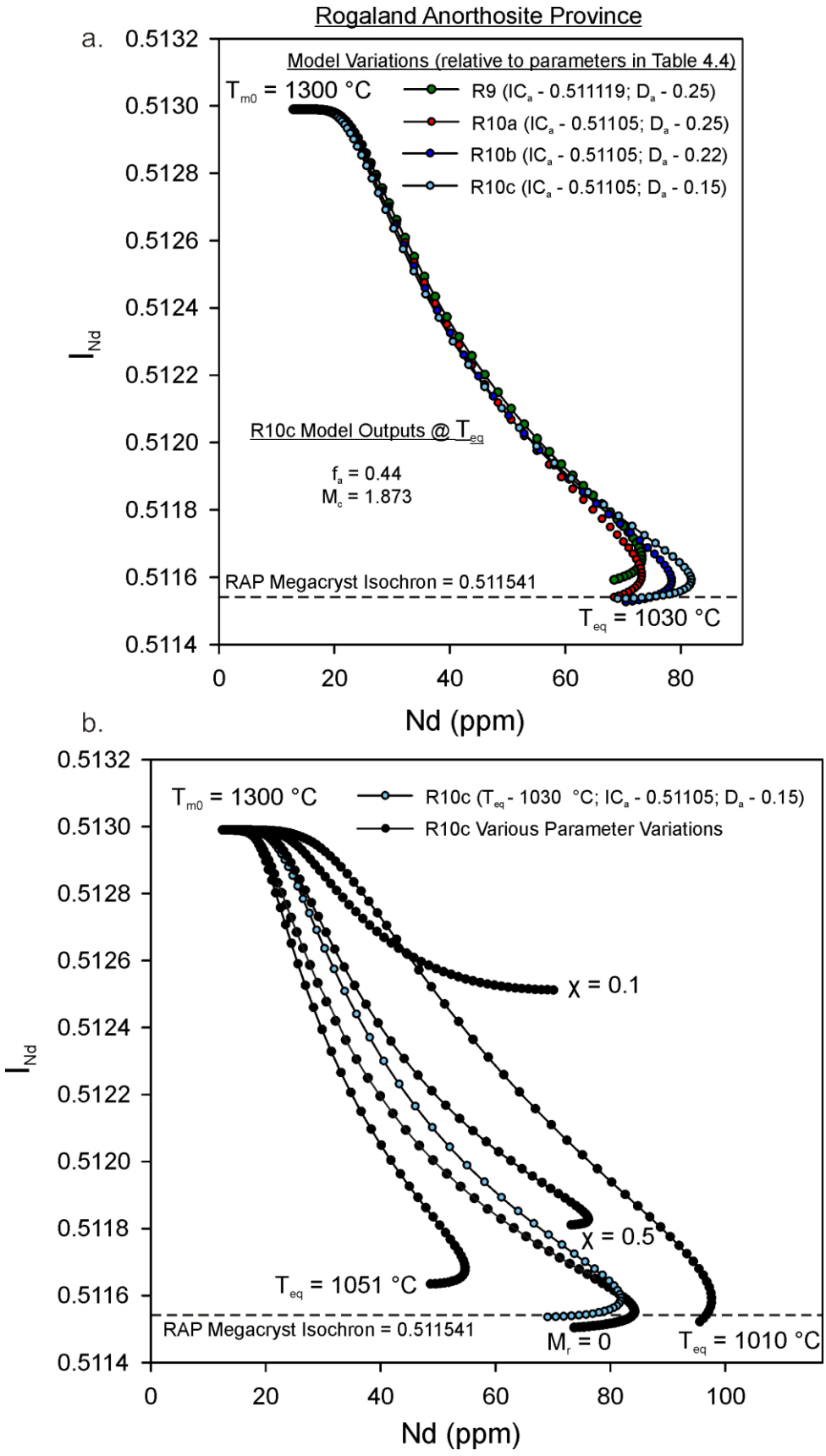

Figure 4.12 a. EC-RAχFC showing the evolution of depleted mantle-derived magma during assimilation of lower crust. b. Sensitivity tests illustrating how changing various parameters effects the modelled magma paths.

Using the distribution coefficients developed for Proterozoic anorthositic systems (Bédard 2001), the liquids produced in the EC models would crystallise orthopyroxene and plagioclase, and consequently anorthosite, of appropriate Nd composition.

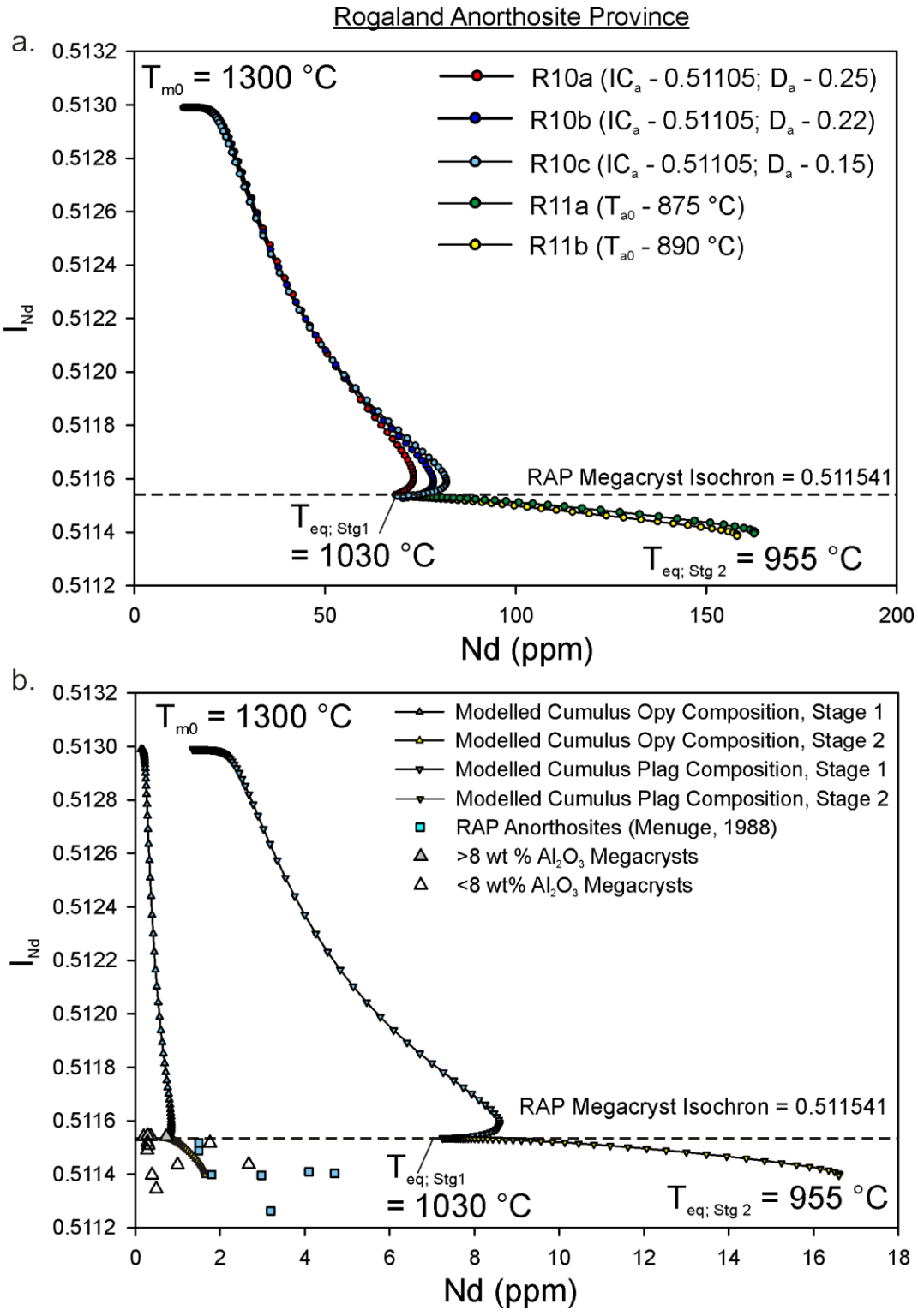

Figure 4.13 a. Two-stage EC-RAχFC model simulating "polybaric" AFC in the RAP. b. Mineral compositions calculated from the liquid evolution path in a. compared with actual megacryst and whole-rock compositions.

4.5.3.2 Simulations of Anorthosite Petrogenesis in the Isotopically-Evolved Nain Plutonic Suite

In contrast to the depleted isotopic compositions observed in the RAP and MMIS, the NPS presents extremely unradiogenic Nd isotopic compositions, given the premise that they are derived from melting of the depleted mantle. Would EC-RAFC models support derivation of the NPS magmas from a depleted mantle source given the observed unradiogenic compositions? Using the set of thermal parameters developed for the RAP scenario, the EC model can be applied to the NPS using chemical constraints from this region (Table 4.4).

The situation in the NPS is unique in that the anorthositic plutons are emplaced along a major crustal scale suture zone – the Torngat Orogen – between the Nain or North Atlantic Province and the Churchill Province. Typical rock types from each province (analysed in this work and previous studies) show that both terranes have unradiogenic rock types (Churchill Province $\varepsilon_{Nd;\ 1444\ Ma}$ = -7.2 to -9.5), but that the Nain Province preserves extreme isotopic enrichment (Nain Province $\varepsilon_{Nd;\ 1444\ Ma}$ = -17.9 to -22.2). Besides altering the composition of the assimilant in the NPS simulations, the same chemical and thermal constraints were used as in the RAP models. An intermediate composition between Nain and Churchill Province gneisses was used as a starting value for the assimilant composition. Note that these compositions represent mid- to upper-crustal compositions exposed alongside the anorthosites and in this model I assume that the lower crust has similar compositions, as lower crustal compositions are not known in the area. With an identical T_{eq} of 1030 °C, the isotopic composition of the megacrysts is reproduced (Figure 4.14a and b). Once again, a flat isotopic evolution path is produced at the lower end of the temperature range and is accentuated when D_a = 0.15 is used. The first stage of this model confirms that magmas derived from the depleted mantle at the time of NPS formation could develop extremely evolved compositions through interaction with an evolved lower crust of Archaean to Palaeoproterozoic age. Implementation of the second stage of the model in the NPS proceeds in a similar manner to that of the RAP and produces reasonable cumulate compostions (Figure 4.14b).

Although upper-crustal compositions are used as lower-crustal assimilants in the above forward models for the NPS (because of the paucity of lower-crustal samples in the Labrador region), these models do reproduce the high-pressure megacryst and anorthosite compositions. This suggests that the lower crust in the region may be of similar composition. Difficulty in reproducing the data is encountered however, when integrating the Sr and Nd modelling and assuming the lower crust and upper crust have similar compositions. Figure 4.15 illustrates how using a pure average of isotopic compositions from upper crustal gneisses of the Nain and Churchill Provinces (exposed alongside anorthosites) produces magma isotopic compositions that do not match those of the primitive megacrysts or anorthosites. These results suggest that a higher proportion of older and more evolved Nain Province gneisses may have been assimilated in order to produce the relatively evolved NPS anorthosites. Using an assimilant composition of 100 % Nain Province gneisses reproduces Nd compositions, but forces Sr compositions to too high values. Reducing M_r to 0, χ = 0.8 and increasing the T_{eq} to 1040 °C produces reasonable isotopic compositions for the megacryst suite analysed from the NPS. Sr isotopic compositions are at the high the end of the range, but the fraction of anatectic melt is too large at 0.54. Large variations in Sr composition in these megacrysts, probably due to recrystallisation, make accurately reproducing the observed compositions challenging and introduce large uncertainties. This, together with assumptions that the lower crust has similar compositions to the upper crust, introduces unacceptably high uncertainties into the models.

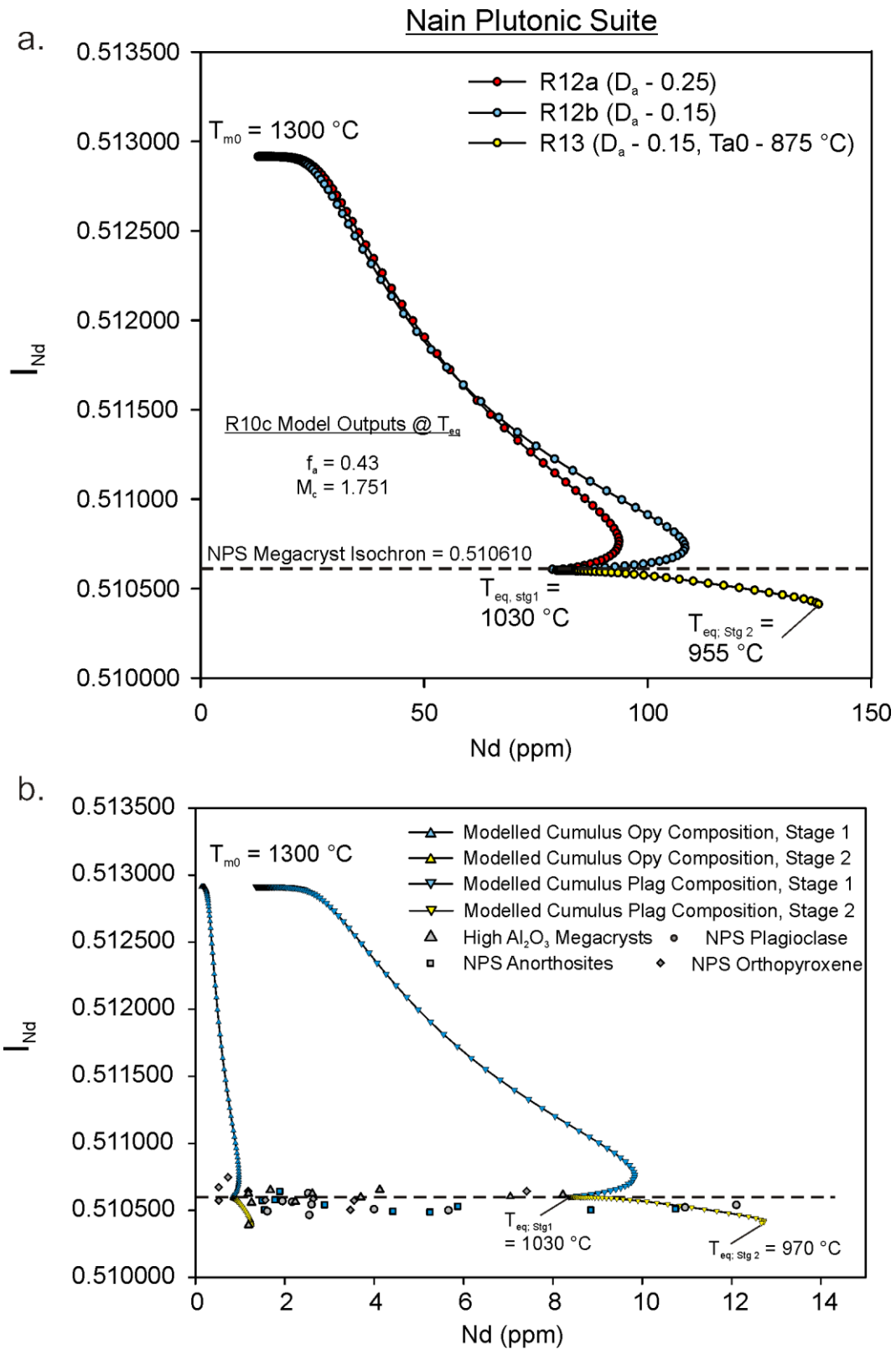

Figure 4.14 a. Two-stage EC-RAχFC model simulating "polybaric" AFC in the NPS using an intermediate crustal composition between Churchill and Nain Province compositions. b. Mineral compositions calculated from the liquid evolution path in a. compared with actual megacryst and whole-rock compositions.

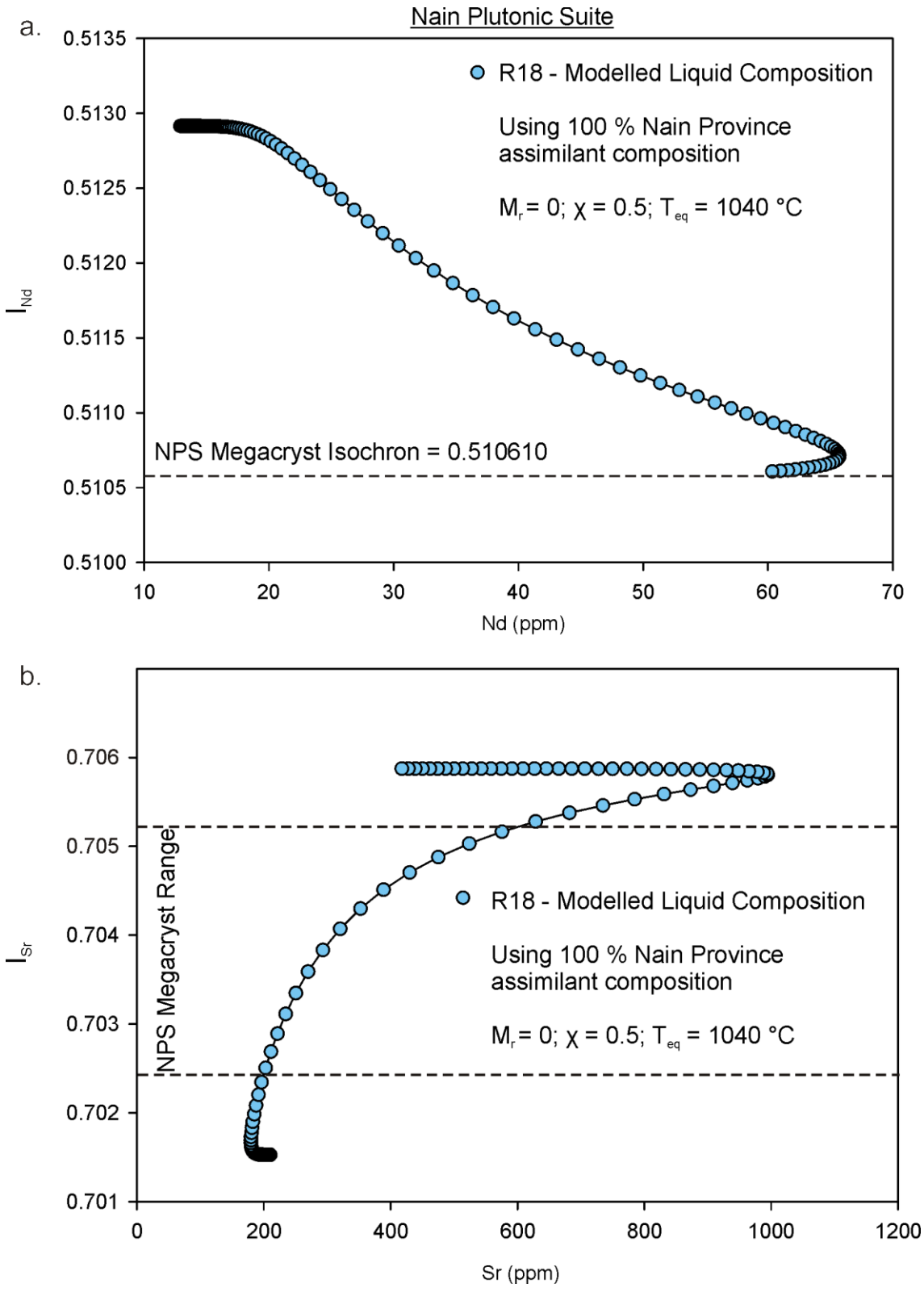

Figure 4.15 A model attempting to simulate magma differentiation in both Nd (a) and Sr (b) isotopic space assuming that lower crust in the NPS has similar composition to observed upper crustal compositions. Using a pure average of crust compositions from the Churchill and Nain Provinces, the appropriate isotopic compositions cannot be recreated.

4.5.3.3 EC-AFC Modelling in the MMIS

As observed in the simple, traditional AFC models (Figure 4.11), the isotopic compositions of the megacrysts in the MMIS are difficult to reproduce under reasonable conditions and in these models can only be simulated with very high degrees of fractionation and unreasonably high proportions of assimilation. A similar problem is encountered in the EC-RAχFC models applied to the MMIS. Estimates of possible lower crustal composition surrounding the MMIS exist, as reported in Table 4.3 (Hegner et al. 2010), but cannot reproduce the isotopic compositions of the high-pressure megacrysts in the MMIS (Figure 4.16). Shifting the assimilant composition to higher Nd concentrations (70 ppm) and lowering of the assimilant isotope ratio (I_{Nd}=0.51039) enables reproduction of the isotopic composition (Figure 4.16). Reproduction of the initial isotopic composition of the megacrysts requires C_{m0} (initial magma composition) to be changed to 8 ppm and C_{a0} (initial assimilant composition) to 75 ppm. In addition, a T_{eq} of 1010 °C is used in the optimised model to reproduce the data. Although the optimised parameters still fall within the range of observed sample compositions, the chosen values are derived from different samples. The magma evolution path is significantly different to the previous models primarily because of the higher Nd concentration of the assimilant. As no real constraints exist for the lower crustal composition in the MMIS, there is no way of assessing the reliability of the modified assimilant compositions used. This modelling approach therefore fails to reliably reproduce compositions observed in the MMIS.

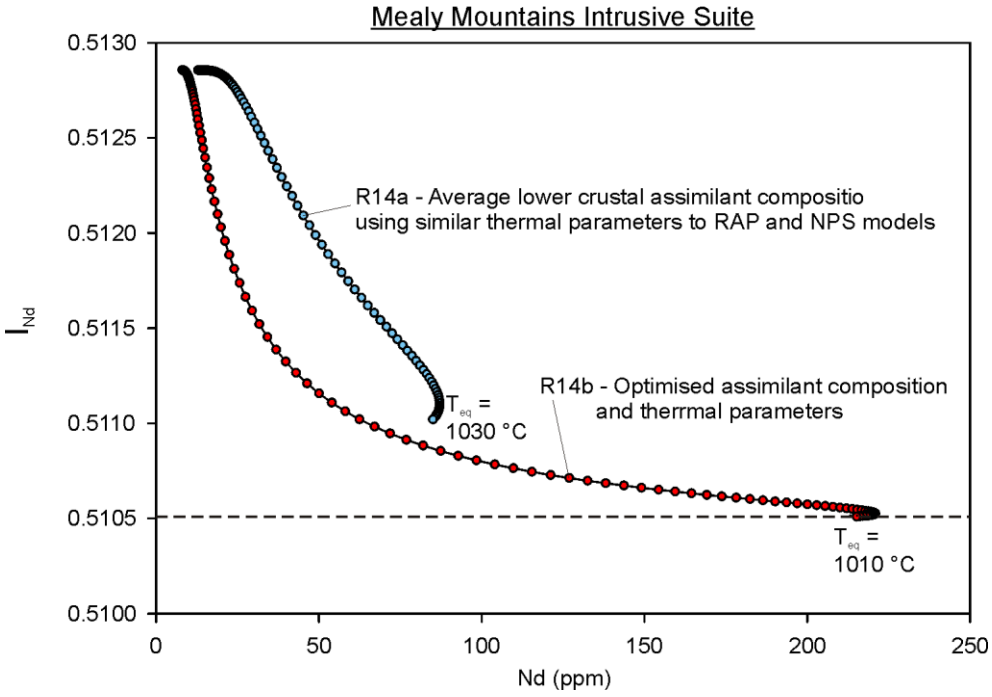

Figure 4.16 Two models illustrating the difficulty in modelling the MMIS isotopic compositions. Only when the isotopic composition and Nd concentrations in the assimilant and magma parameters are changed to extreme values can the compositions be obtained.

4.5.3.4 A Conclusion on Modelling

The modelling of magmas ascending from the Moho, taking into account both thermal and mass balance, will inherently involve many assumptions. In the case of the Rogaland Anorthosite Province, where constraints on the lower and mid-crustal Nd compositions were available, this modelling reproduced the isotopic and Nd

concentrations of the high-pressure megacrysts (this study) and anorthosites (literature). However Sr concentrations for the lower crust in the RAP are not available in the literature and future Sr analyses on these lower crustal compositions would help constrain and test the Nd EC-RAχFC models that appear successful. Constraints on lower-crustal compositions from Labrador are non-existent, and although using the assumption that lower crustal compositions are similar to mid-crustal compositions reproduces Nd composition of the NPS, integration of Sr data into the models results in the use of untenable crust compositions and fractions of anatectic melt (~50 %). A similar scenario occurs in the MMIS, primarily because lower-crustal compositions are poorly constrained. Although EC-RAχFC modelling offers a more realistic approach to the modelling of magma differentiation, the polybaric petrogenesis of Proterozoic anorthosites invokes numerous parameters that are generally poorly defined or unknown (e.g. lower crustal compositions, K_D at lower crustal pressures) for many regions. Of the models generated in the aforementioned sections, only those where reported lower crustal compositions are used, reproduce the compositions of the actual material with reasonable results. This serves to confirm that Proterozoic anorthosites can be generated from melting of the depleted mantle, but successful models require that lower crustal compositions be reasonably constrained.

4.6 Melting of the Depleted Mantle vs. Lower Crust?

The contentious source debate for Proterozoic anorthosites has fractured and slowed efforts to understand the tectonic setting and consequently the geodynamic reasons for the temporal restriction of these coalesced batholithic intrusions. High-pressure megacryst isotopic compositions from terranes of different age and chemical composition qualitatively show that magmas were derived from the depleted mantle as they track, but are offset from depleted mantle evolution (in terranes like the MMIS and RAP, where crustal assimilation has not dramatically lowered the isotopic compositions; Chapter 2). The failure of traditional, simple AFC modelling to quantitatively illustrate that melting of the mantle and subsequent crustal assimilation can produce the observed isotopic compositions of the anorthosites has led to many workers favouring a lower crustal derivation of the magmas (Duchesne et al. 1999; Longhi et al. 1999; Schiellerup et al. 2000). As outlined in Chapter 2, melting of the lower crust to produce magmas that ultimately form Proterozoic anorthosites, is petrologically and thermodynamically challenging, especially given the mechanisms proposed to cause the melting (lower crustal delamination/thrusting lower crustal tongues into the mantle; Duchesne et al. 1999; Duchesne 2001). Unreasonably high degrees of melting of mafic, aluminous lower crust would be required to produce the required high-Al parental basalts, necessitating a heat source from the mantle. Megacryst and anorthosite geochronology (Chapter 2) indicates that the magmatic systems were long-lived and would have to provide magma and heat to the base of the crust for tens of millions of years. Lower crustal delamination or crustal-tongue tectonics are generally considered relatively short-lived events (Duchesne et al. 1999; Duchesne 2001; Jull & Keleman 2001) and so are unlikely to supply magma to the Moho for the required lengths of time.

These thermodynamic restrictions allude to the fact that traditional AFC models, which do not consider conservational of thermal energy, may be inadequate in simulating the complex, polybaric, long-lived petrogenesis of Proterozoic anorthosites. EC-RAχFC forward models, as described and presented in Sections 4.5.3, quantitatively confirm that melting of the depleted mantle and interaction of this magma with lower crust in ponding magmas at the Moho can explain the isotopic compositions of the RAP and NPS (partly), but not the MMIS. These model failures are likely due to no constraints on lower crustal compositions as well as the

increased number of assumptions required for the more realistic EC-RAχFC models. In the scenarios where lower crustal compositions in the region are well-constrained (RAP), the fraction of anatectic melt produced is reasonable (~40 %) and a scenario can be simulated where high-Al megacrysts will crystallise from a magma with unchanging isotopic composition, while still assimilating lower crust. The models are optimised with a mass of recharge 1.5 times that of the initial magma mass and produce over 1.5 times the mass of cumulates – a necessary parameter given the large volumes of plagioclase-rich intrusives observed. These models therefore confirm that Proterozoic anorthosites can be derived from melting of the depleted mantle.

4.7 Refining the Petrogenetic Model for Proterozoic Anorthosites Genesis

Qualitative arguments in Chapter 2 support melt derivation from the depleted mantle by detailing how, in terranes where the magmas are not contaminated by old, evolved crust (i.e. MMIS and RAP), high-pressure primitive megacrysts track depleted mantle evolution. This assertion has been tested using EC-RAχFC models of depleted mantle melting and in the case where constraints on the lower crust exist (RAP), interaction between the mantle melt and lower crust is able to reasonably reproduce the observed compositions of the primitive megacrysts and most anorthosites. Minor mid-crustal contamination is required to simulate the remainder of the anorthositic compositions. In addition, the thermal constraints on assimilation in these models predict that isotopic composition would remain constant over a small temperature range, confirming that production of isochronous megacrysts suites under these conditions is plausible. Subsequent magma ascent and continued assimilation recreate the majority of isotopic compositions observed in the anorthositic suites.

Broadly basaltic, depleted-mantle-derived melts initially crystallise olivine and clinopyroxene while rising towards the base of the crust. Proterozoic anorthosites are proposed to crystallise from high-Al basaltic tholeiites, and this, together with the rare observation of clinopyroxene megacrysts in these suites, suggests that clinopyroxene (and olivine) may have existed together with, and before, orthopyroxene, as primary liquidus phases. The absence of Eu anomalies in the highest-pressure megacrysts indicates that orthopyroxene (as well as olivine and clinopyroxene) may also have been liquidus minerals before plagioclase entered the crystallising assemblage. Interactions between this magma and melts of the mafic lower crust would induce silicic lower crustal contamination, not only inducing orthopyroxene crystallisation due to peritectic olivine reaction (a texture preserved in some samples, Figure 4.2f), but also lowering and shifting the Nd and Pb isotopic composition of the orthopyroxene cumulates, as observed. EC-RAχFC modelling (where chemical constraints exist on the lower crust) indicates that lower crustal contamination of a magma, experiencing continual recharge, reproduces the isotopic compositions of the primitive, high-pressure megacrysts and anorthosites, and in addition creates the appropriate conditions to produce isochronous suites of megacrysts over certain temperature ranges. Ponding and subsequent crystallisation of a rising basaltic magma at a suitable interface in the lithosphere, such as the Moho, allows creation of a scenario where a magma chamber continually being supplied with new, hotter magma is able to assimilate a relatively large amount of crust or partial melt of the crust (~ 40 %). Initially assimilation lowers the isotopic composition and increases the incompatible trace element concentrations of the evolving magmas. These conditions allow anatexis to deplete the crust in incompatible elements, and with progressive assimilation, effectively dilutes the magma in incompatible elements like Nd, while the isotopic composition of the evolving magma remains relatively constant. Variations in $[Sm/Nd]_N$ and Eu anomaly (Figure 2.2b) among the highest pressure, isochronous megacrysts indicate that

these ponded magmas were not only assimilating lower crust, but also fractionating, during which time plagioclase entered the fractionating assemblage. MELTS density modelling for proposed anorthositic parental melts presented in Chapter 2 indicates that clinopyroxene and orthopyroxene phases would be denser than the magma and even the surrounding mantle at Moho pressures, and would consequently sink at these depths. The beginning of plagioclase crystallisation and mush formation would provide a mechanism facilitating transport of the dense megacrysts to upper crustal levels. Given the mafic mass balance problems in Proterozoic anorthosite massifs, a large proportion of these megacrysts presumably formed before sufficient plagioclase development and consequently sank into the magma and perhaps deeper into the mantle.

Lower-Al, and therefore, lower pressure orthopyroxene megacrysts as well as orthopyroxene mineral separates from host anorthosites are in isotopic disequilibrium with the highest-pressure, isochronous suites of megacrysts, suggesting that after an initial stage of ponding and sufficient plagioclase formation, magma mushes move to higher crustal levels and continue to assimilate surrounding crustal material. At this stage, analysis of isotopic disequilibrium provides two insights into the polybaric evolution of the magma:

1. As expected, the nature of the crustal contaminant not only affects the whole-rock isotopic composition, but also affects the internal disequilibrium of the mineral phases. The degree of disequilibrium is influenced by the age and chemical nature of the potential contaminants, with largest degree of disequilibrium observed in the NPS where the potential contaminants, in the form of the Archaean and Palaeoproterozoic Nain and Churchill Province gneisses, are significantly older and more evolved (between ~ ε_{Nd} = -7 to -20) than the anorthosite. Contrary to initial predictions that the MMIS would show no or very minimal internal disequilibrium, due to the juvenile nature of the surrounding crust, I find that certain phases (orthopyroxene, magnetite) do show measurable disequilibrium, although this is less than that observed in the NPS, as expected. This indicates that anorthosite intrusions emplaced into juvenile and relatively young crust are still chemically affected by assimilation, albeit to a lesser degree.

2. The geometry of internal mineral disequilibrium is somewhat unexpected in both the NPS and MMIS (Figur 4.8). On average, orthopyroxene in most samples from both the NPS and MMIS (in Nd and Pb space) is more primitive than the reference isochron. If orthopyroxene formed purely as an intercumulus phase from a polybarically and progressively contaminated magma, one would expect orthopyroxene to be more evolved than the reference whole-rock composition – this, for the majority of samples, is not the case. There are, however, samples where orthopyroxene is in fact more evolved than the reference isochron (e.g. CG09-026A, 032A). Figure 4.8 also illustrates and confirms that many orthopyroxene separates are more depleted than the plagioclase phases and consequently the whole-rock. Figure 4.10 attempts to explain how these disequilibrium geometries may develop based on a range of isotopic compositions for orthopyroxene (and plagioclase) in one sample and the averaging affect inherent in mineral separation and solution geochemistry. To produce the range in isotopic compositions as shown in Figure 4.8 and 4.10, individual samples would have to incorporate primitive orthopyroxene as well as more evolved, intercumulus orthopyroxene. The degree of disequilibrium would then be determined by the relative amounts of primitive, early-crystallised vs. evolved, late, intercumulus orthopyroxene. A similar relationship would hold for plagioclase, although absolute variation in disequilibrium is likely to be lower due to the similarity in parent-daughter ratios between whole-rock anorthosite and plagioclase. The implication is that a large proportion of orthopyroxene (and by inference, mafic phases)

developed early in the formation of the mush and assimilation history of the magma. Although orthopyroxene and other mafic phases are generally considered to be intercumulus minerals in Proterozoic anorthosites (Ashwal 1993), I document evidence for different generations of orthopyroxene development in the anorthosites (Section 4.3.1). These textures highlighted in Section 4.3.1 indicate that some mafic phases formed early in the chemical evolution of the magma in order to create the observed disequilibrium geometries. Observation of high-pressure megacrysts and cumulus-textured olivine in leucotroctolites also suggests that mafic phases did crystallise at various stages throughout magma petrogenesis. These disequilibrium geometries require that a significant amount of the orthopyroxene be formed early in the assimilation history of the magma, as isotopically depleted cumulate phases. This requirement is contrasted by prevalence of intercumulus orthopyroxene petrographically. These apparently contradictory isotopic and petrographic observations raise serious questions regarding the crystallisation history of the magmas. Did most crystallisation occur at Moho/lower crustal depths, followed by crystallisation of the remaining interstitial, more isotopically evolved liquid to form minor intercumulus orthopyroxene once the system had experienced increased contamination from shallower crustal reservoirs?

4.7.1 Assessing the Ascent and Crystallisation of Proterozoic Anorthosites in Light of Isotopic Disequilibrium

A fundamental aspect in the ascent of Proterozoic anorthosite to mid-crustal levels, and in the general production of these plagioclase-rich intrusives, is related to the buoyancy of plagioclase with regard to the parental magma. Kushiro (1980) showed that at depth, basaltic liquids have higher compressibility than plagioclase phases. These results indicate that typical plagioclase in Proterozoic anorthosites (An_{45-60}) would float in a basaltic magma at depths greater than 1-2 kbars. The significance of these results for Proterozoic anorthosite petrogenesis is two-fold. Firstly, the floatation and accumulation of plagioclase in a deep magma chamber/s, accompanied by the fractionation and sinking of dense mafic phases, like pyroxene and olivine, provides a mechanism by which a magma can develop large quantities of plagioclase without appealing to more complex mechanisms to produce these hyperfeldspathic magmas (Wiebe 1990). The missing mafic component in Proterozoic anorthosites and observations of volumetrically minor high-pressure mafic cumulates supports the assertion that these magmas are mechanically enriched in plagioclase through cotectic crystallisation of mafic and felsic phases and subsequent gravitational fractionation. Secondly, the accumulation of positively buoyant plagioclase is fundamental to the ascent of these massifs. Had plagioclase not been buoyant at these depths, it is unlikely that these massifs would have ever been exposed on the surface.

At this juncture a crucial question arises: what is the critical mass of buoyant plagioclase required to allow ascent of these crystal mushes? This relates to the aforementioned isotopic disequilibrium discussion because isotopic evidence suggests that a large proportion of crystallisation (of mafic and felsic phases) took place at mantle-lower crustal depths, before the magma/crystal mush could be contaminated by more isotopically evolved, and presumably, shallower crustal material. Based on this evidence I propose that a large proportion of the anorthosite seen at surface, crystallised in magmas ponded at the Moho or which had just begun to ascend through the lower crust, and had consequently only assimilated lower crustal material. This assertion becomes immediately controversial, as crystal mushes are thought to be essentially immobile when the proportion of crystals rises to between 40-60 % (Marsh 1981; Miller et al. 2011). Although impossible to quantify using

standard TIMS solution analyses, the geometry of isotopic disequilibrium suggests that at least 50 % of the phases must have crystallised before assimilation of more evolved crustal material occurred (Figure 4.10). By way of this argument, I therefore propose that anorthosite ascent occurred as extremely viscous, barely mobile, diapiric ascent (Miller et al. 2011; Weinberg & Podladchikov 1995). However, on intrusion into the mid-crust, intercumulus liquid must have still existed and subsequently crystallised, as zircons recovered from the anorthosite produce ages 100 m.y. younger than the high-pressure megacryst ages, but comparable to the plagioclase decompression-exsolution and zircon-in-megacryst (presumably exsolution) ages (Chapter 2).

The rise of a positively buoyant, "extremely crystal-rich magma" has been assessed, modelled numerically and compared to the types of structures and fabrics commonly observed in diapirs and wall-rocks. Although the rise of magma diapirs is assumed to end once a magma reaches a certain degree of crystallinity (40 – 50 %) or becomes completely solid, research suggests that this need not be the case; a solid-state diapir will continue to rise through a medium if the material remains buoyant (Weinberg & Podladchikov 1994; Weinberg & Podladchikov 1995). The types of fabrics and structures observed in these simulations, in both the surrounding crust and intrusion, are dependent on whether the materials involved act as power-law or Newtonian fluids as well as the regional strain-rate at the time of emplacement (Weinberg & Podladchikov 1995). Although within-pluton and country rock deformation in Proterozoic anorthosite massifs is fairly variable, both between regions and on a massif-scale, the fabrics simulated during ascent of a solid-state diapir match many of the structures seen in and around Proterozoic anorthosite massifs. The clearest example of this is found in the Rogaland Anorthosite Province (Figure 1.6), where the core of the Egersund-Ogna massif is undeformed and shows low-strain rate, whilst the rim of the intrusion displays high-strain rate and has accommodated significant deformation (Weinberg & Podladchikov 1995). If the materials behave as power-law fluids the intrusion may or may not appear deformed and in the former case, should a show a gradation of deformation in the pluton from core to rim – a feature observed in the RAP. Variation in the type of deformation in both materials occurs if the pluton is emplaced in a pre-, syn- or post-tectonic setting (Weinberg and Podladchikov, 1995). In the RAP, structural features are most consistent with the fabrics described in a post-tectonic setting (Charlier et al. 2010; Royse & Park, 2000). Petrographically, the granular texture common to many massifs supports the notion that the crystal-rich masses rose in a high-crystallinity state (> 50 % crystallinity), destroying primary igneous textures (Longhi & Ashwal 1985). Corroboratory evidence for diapiric rise of magma mushes in arc environments has recently taken the form of gravity data indicating diapiric rise of felsic magmas through the crust above the Altiplano-Puna Magma Body in the Central Andes (del Potro et al. 2013).

Evidence for diapiric rise of extremely crystal-rich magmas in this thesis is contrasted by evidence from Royse and Park (2000) in which it is argued that only magmas ascending via conduit ascent, with less than < 50 % crystallinity, would be able to counter-act the terminal settling velocities of the dense, high-pressure megacrysts and consequently deliver these phases to mid-crustal levels. However, calculations performed by Royse and Park (2000) assume magma crystallinity below 50 %. The results presented in this chapter indicate that the anorthositic magmatic system probably achieved over 50 % crystallinity at lower crustal depths and therefore is unlikely to have risen via conduit-ascent. Increasing viscosity of the magma (through higher degrees of crystallinity) may allow megacrysts to be carried with the crystal-rich magmas regardless of the slower ascent rates associated with diapiric ascent.

Although a detailed assessment of the mechanics of anorthositic ascent is beyond the scope of this work, a useful test of the ideas mentioned above, is to calculate the critical mass of plagioclase needed to initiate buoyant ascent of a magma-mush through the overlying crust. If a very small mass of plagioclase is needed (i.e. the crystal-rich magma is still mobile), the high-crystallinity hypothesis fails and another mechanism of generating the isotopic disequilibrium should be sought. Longhi and Ashwal (1985) performed calculations describing the near-solid-state ascent of anorthosite diapirs in situations where the viscosity of the diapirs approximates to that of the surrounding medium, and giving the system 50-100 m.y. to accumulate plagioclase and rise to final levels of emplacement (based on lunar evolution models). The results indicate that for solid-state diapirs to grow and ascend in the given timescale (similar to that which I observe in Proterozoic anorthosites) would require plagioclase-rich layers on the order of 1 km in thickness. More detailed calculations are required to understand the dynamics in situations where the viscosity of the diapir is much less than the surrounding medium i.e. in the case of a crystal-rich mush.

4.7.2 Implications of the Isotopic Composition of Leuconorite vs. Leucotroctolite

Differences in the isotopic composition of olivine- and pyroxene-bearing anorthosites (leucotroctolites and leuconorites) in the MMIS (where both rock types were sampled) allude to another interesting aspect of Proterozoic anorthosite massif development. Figures 2.6a and 4.4-4.6 indicate that leuconorites are more evolved than the olivine-bearing counterparts. These whole-rock chemical relationships are well known from other Proterozoic anorthosite massifs (e.g. Kunene, Ahvenisto, Laramie Complexes; Gleißner et al. 2011, Heinonen et al. 2010, Frost et al. 2010), but similar differences are also noticeable in the degree and polarity of plagioclase disequilibrium (Δ = 0.1032 for leucotroctolites vs. Δ = -0.072 for leuconorites). Differences in whole-rock isotopic compositions could either be ascribed to chemical variations in pulses of parental magma or to variations in contamination between different pulses of magma. Discussions in Chapter 2 highlighted how pulses of magma, ponding at regions of the Moho that have already experienced ponding and anatexis during earlier pulses of magma ascent, may experience significantly less lower-crustal contamination, as the crust would be preconditioned, refractory and essentially sealed to further anatexis. This process of preconditioning of magma pathways or interfaces has been described in shallower magma systems (Schmidt & Grunder, 2010). Fundamental, but small, differences in parental magma composition could also explain the whole-rock differences, although mechanisms for generating isotopic source differences would be required. However, changes in internal plagioclase isotopic disequilibrium between leuconoritic and leucotroctolitic samples could not be caused by variations in parental magma composition. The differing isotopic disequilibrium geometries indicate the affects of variable degrees of assimilation in different pulses of magma. Plagioclase in leucotroctolitic massifs crystallised from magma that had experienced less crustal assimilation, leaving a more primitive, more depleted composition, in positive isotopic disequilibrium with the whole-rock. These particular geometries support the aforementioned model wherein “leuconoritic magmas” experience extensive interaction and assimilation of crustal material, while magmas that subsequently interact with this preconditioned, ‘sealed’ crust experience less contamination and go on to form more depleted rock types i.e. leucotroctolitic intrusions. This variation in degree of contamination in one massif, affecting isotopic compositions and presumably the oxygen and silica fugacity (Frost et al. 2010), is therefore manifest in the fundamental mineral composition of the intrusions. This process also explains why orthopyroxene megacrysts appear to be restricted to leuconorites. The buoyancy of plagioclase is a crucial ingredient in allowing these hyperfeldspathic rocks to reach mid-crustal

levels. In turn, a critical mass of plagioclase is required to allow buoyant ascent as described in Section 4.7.1. The observation of varying degrees of disequilibrium in plagioclase from olivine- vs. orthopyroxene-bearing rocks suggests that this contamination occurs before the critical mass of buoyant plagioclase is reached, affirming the suggestion in this thesis that lower-crustal contamination, as opposed to upper-crustal contamination, is a dominant process operating in these magmas. In assessing the silica and oxygen fugacity of three anorthosite massifs from the Laramie Complex in relation to radiogenic isotopic compositions, Frost et al. (2010) confirm that crustal contamination has a demonstrable affect on mineral compositions of Proterozoic anorthosites. As the work in this chapter emphasises, the correlations observed by Frost et al. (2010) between silica, oxygen fugacity and Sr and Nd compositions highlight the importance of lower crustal contamination of common mantle-derived melts in the petrogenesis of Proterozoic anorthosites.

The preceding discussions highlight the importance of lower crustal contamination in the petrogenesis of Proterozoic anorthosites, but the exact mechanisms introducing the contaminants into the magma are largely unknown and suffer from a degree of untestability. Possible mechanisms include bulk assimilation of wall rock (that is then assimilated by the magma) or mixing of anatectic melts into the magma. Given that a large proportion of assimilation must occur at Moho/lower crustal depths as indicated in this thesis, novel and imaginative tests are required to determine the mechanism/s of contamination.

Based on the body of evidence presented in Chapter 2, 3 and 4, Figure 4.17 presents a revised schematic model for the decidedly polybaric petrogenesis of Proterozoic anorthosites.

4.8 Conclusions

The existing models describing Proterozoic anorthosite petrogenesis (Ashwal 1993; Duchesne 1999; Emslie et al. 1994) all emphasize the importance of crustal contamination in development of the isotopic and mineralogical composition of Proterozoic anorthosites. Of these models, those advocating a mantle derivation for the melts suggest that magmatic interactions in the lower crust may be important (e.g. Emslie et al. 1994), although no decisive evidence has existed, up until now, to support this assertion. By analysing individual constituents of the Proterozoic anorthosite system, namely high-pressure orthopyroxene megacrysts, anorthosites, and internal mineral phases, isotopic analyses provide a window into processes operating at different stages of the polybaric evolution of these massifs. Comparable isotopic compositions between high-pressure megacrysts (that crystallised at upper mantle to lower crustal depths) and comagmatic, host anorthosites indicate that significant lower crustal contamination occurred in ponding magmas at the Moho. In scenarios where constraints on lower and upper crustal compositions are published, EC-AFC modelling is able to reproduce the compositions of anorthosites and megacrysts within a reasonable thermal framework. The modelling is of course complicated by an already-complex, polybaric petrogenesis, and in cases where crustal composition are less well-known, model optimisation requires undesirable, and sometimes, untenable input parameters. The unexpected geometries of isotopic disequilibrium suggest that, in addition to receiving predominantly lower crustal contamination, the magmas may have experienced significant crystallisation at Moho/lower crustal depths, before rising as extremely crystal-rich magmas (> 50 % crystallinity) to the final level of emplacement in the mid-crust.

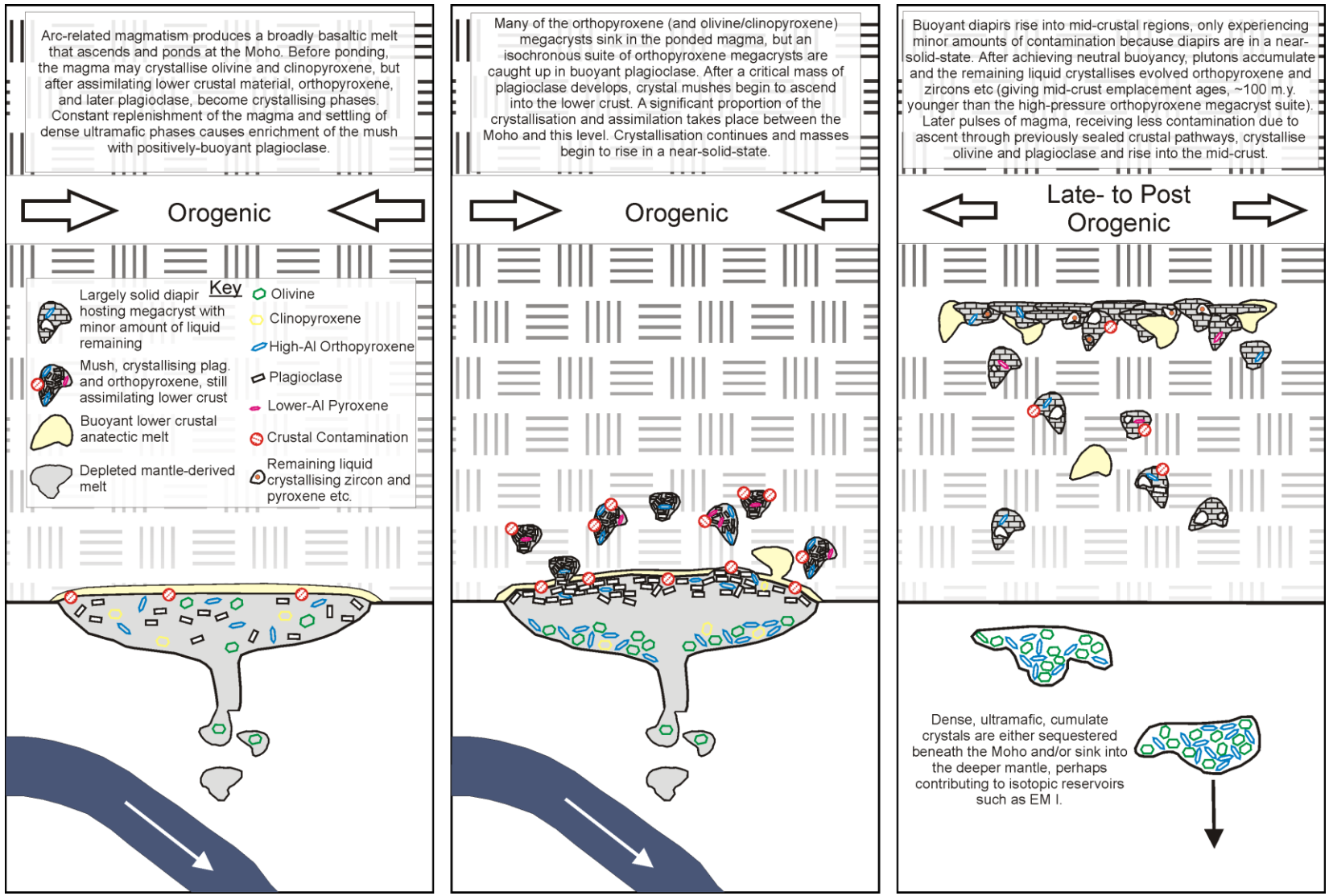

Figure 4.17 A revised petrogenetic model for the petrogenesis of Proterozoic massif-type anorthosites.

5 Insights into the Final Stages of Proterozoic Anorthosite Crystallisation in the Mealy Mountains Intrusive Suite

The Mealy Mountains Intrusive Suite (MMIS; 1650-1630 Ma) is one of several classic Proterozoic anorthosite-bearing complexes in the Grenville Province of eastern North America, although it is unique in that it is the sole anorthositic intrusion of Labradorian (1805-1770 Ma) age in the province (Emslie 1976). Large coalesced, intrusive complexes like the MMIS, temporally restricted to the Proterozoic eon, are known as Proterozoic anorthosite massifs. The anorthositic rocks in these massifs consist predominantly of plagioclase (An_{45-65}) and minor mafic minerals such as orthopyroxene, olivine and clinopyroxene and Fe-Ti oxides (Ashwal 1993). Associated with these plagioclase-rich intrusions are equally voluminous batholiths of granite and mangerite/monzonite, smaller bodies of mafic cumulates and minor amounts of a suite of Fe-Ti-P-rich dioritic ferrodiorites/jotunites-monzonorites and oxide-apatite-gabbronorites (Morse 1982; Owens & Dymek 1992; Dymek & Owens 2001). When considered in conjunction with the anorthositic rocks, these samples constitute the Proterozoic massif-type anorthosite suite (Ashwal 1993). Proterozoic anorthosites and their related rocks have puzzled petrologists for decades with ongoing debate surrounding their tectonic setting, source, emplacement mechanisms and parental liquids. Among the many contentious issues regarding Proterozoic anorthosites, the nature of the residual liquids of anorthosite crystallisation is uncertain (Dymek & Owens 2001). A wide range of associated Fe-Ti-P-rich rock types like diorite, ferrodiorites, monzonorite, jotunite, oxide-apatite-rich gabbronorites and Fe-Ti-oxide ore deposits have been considered the residual liquids of Proterozoic anorthosite magmas (Ashwal 1982; Duchesne 1984; Dymek & Owens 2001; Heinonen et al. 2010; McLelland et al. 1994; Mitchell et al. 1996; Morse 1982; Owens & Dymek 1992; Vander Auwera et al. 1998;). Numerous mutually-exclusive hypotheses regarding their origin have been proposed (Owens & Dymek 1992), including suggestions that these rocks represent parental magmas of the anorthosites (Demaiffe & Hertogen 1981), lower crustal partial melts (Emslie 1978), transitional differentiates between anorthosite and mangerite (de Waard & Romey, 1969), fractionates or cumulates of mangeritic magmas (Emslie, 1975b) or immiscible liquids (Philpotts, 1981; Powell et al., 1982) and residual liquids (Ashwal 1982; McLelland et al. 1994; Mitchell et al. 1996; Morse 1982).

The MMIS is host to intriguing pods, or segregations, previously described as graphic granites (Emslie, 1976). These 1-5 m graphic, pegmatitic pods were reported to contain central areas of red graphic granite surrounded by coarse pyroxene and oxide-rich material. I describe the petrology, geochemistry and age of these pods and show that the compositions are highly variable, ranging from monzogranite through monzodiorite/monzonorites to oxide-apatite-rich ferrodiorites. I propose and test the hypothesis that these pods are extremely fractionated compositions representing *in situ* residual liquids of Proterozoic massif-type anorthosites and that they provide insight into the final stages of crystallisation in the anorthosite system. Based on the range of pod-like, residual liquid segregations preserved *in situ* in the MMIS, I then suggest that the rock types purported to represent

residual liquids in anorthosites (Fe-Ti-P-rich dioritic ferrodiorites/jotunites-monzonorites and oxide-apatite-gabbronorites) are indeed all residual liquids created by slight variations in magma composition and extreme, isolated differentiation.

5.1 Geologic Setting

The Mealy Mountains Intrusive Suite (MMIS; Figure 5.1), which forms part of a deep-level, thrust-stacked block in the exterior thrust belt of the Grenville Province, known as the Mealy Mountains Terrane, is the largest complex of its type in the northeastern sector of the Grenville Province in Labrador (Emslie 1976). The MMIS lies ~100 km southeast of the Grenville Front and has been emplaced into relatively juvenile and immature, pre-Labradorian (1800-1770 Ma) and early-Labradorian (1710-1655 Ma) ortho- and paragneisses that make up a significant portion of the NE sector of the Grenville Province (Emslie & Hegner 1993; Gower et al. 2008b). The pre-Labradorian (1800-1710 Ma) crust was constructed during intrusion of granitoid magma into earlier supracrustal assemblages (between 1805 and 1770 Ma) that themselves were deposited after ~ 1800 Ma from immature, local sources (Gower et al. 2008b; Gower & Krogh 2002). Early-Labradorian crust, recognised in deformed and metamorphosed gneisses (e.g. nebulitic granodiorite; 1709 Ma), as well as strongly foliated calc-alkaline granitoids (1680-1650 Ma), formed mostly between 1710 and 1655 Ma in what is interpreted to be an island arc above southward-subducting oceanic crust off the southern margin of Laurentia (present-day coordinates; Gower & Krogh 2002; Gower & Krogh 2003; Gower et al. 2008b). This calc-alkaline magmatism and island arc formation was outboard of pre-Labradorian Laurentia (Gower & Krogh 2002). A well-constrained period of deformation and metamorphism between 1665 and 1655 Ma likely marked the subsequent accretion of this outboard arc to the Laurentian continent. Subsequent convergence on the margin of Laurentia between 1665-1655 Ma initiated what has been referred to as Trans-Labradorian magmatism (Gower & Krogh, 2002; Gower & Krogh, 2003). Magmatism in this mid-Labradorian period manifests itself as three distinct, but intimately linked, suites that include the dominantly alkali-calcic granitoids of the Trans-Labrador batholith (1654-1646 Ma), coeval supracrustal units and trimodal anorthositic, mafic and monzogranitic magmatism (1650-1625 Ma) that includes the Mealy Mountains Intrusive Suite (Figure 5.1; Gower et al. 2008b; Kerr 1989). The main anorthositic members of the MMIS are divided into the south-western, leucotroctolite-dominant Kenemich massif and the north-eastern, leuconorite-dominant Etaugalet massif. These massifs exist along with a group of rock types typified by pyroxene quartz monzonites, but include a complete spectrum of rock types from diorite to granite (Figure 5.1; Ashwal et al. 1986, Emslie & Bonardi 1979, 1983; Gower 2010a; Gower 2010b; Gower & Nunn, 2010; Gower & Erdmer, 2010). Although no direct ages for the two major anorthosite massifs that make up the MMIS exist, one U-Pb zircon age from an isolated intrusion of the MMIS (south of the area shown in Figure 5.1), known as the Crooks Lake Intrusion, has yielded an emplacement age of 1632 ± 3 Ma (Gower & Krogh 2002; Gower et al. 2008b). This age corresponds with geochronological results from monzonites associated with the MMIS that yield ages between 1642 ± 4 and 1635 ± 2 Ma. The age span for the MMIS has therefore been estimated between 1650 - 1630 Ma (Gower & Krogh 2002; Gower et al. 2008b; James et al. 2000).

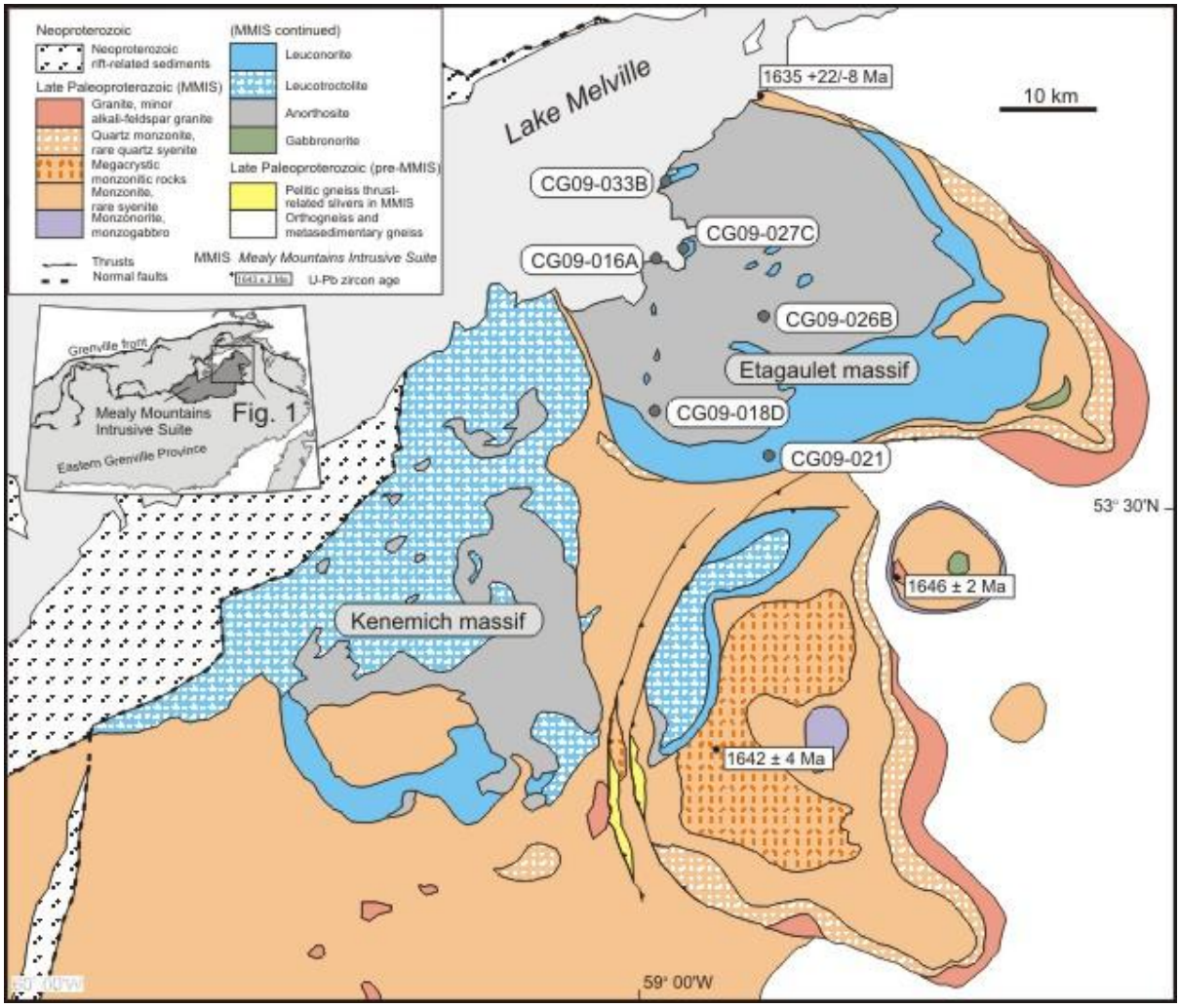

Figure 5.1 Geologic setting of the Mealy Mountains Intrusive Suite showing sampling location of pegmatitic pods (and one anorthosite; CG09-21). Ages indicated by small black circles show previous geochronological measurements performed on felsic members of the MMIS and reported in Gower et al. (2008b).

5.2 Pod Petrography and Mineral Chemistry

Red-brown, pegmatitic, irregular to sub-rounded, pod-like segregations (0.5-5 m across) are typically hosted by coarse-grained (up to 10 cm) leuconorites, and are representative of the pegmatoidal patches originally described in the MMIS by Emslie (1976; Figure 5.2). Rare occurrences also include those hosted by olivine-bearing anorthosite. Field observations of the MMIS in this study and by earlier workers show that the pegmatitic pods may be restricted to the leuconorite-dominant Etaugalet massif (Figure 5.1). Only one chemically and mineralogically distinct pegmatitic pod has been observed in an olivine-bearing anorthositic rock type of the Etaugalet massif. All leuconorite-hosted pods show extensive feldspar alteration that hinders identification of feldspar and textural relationships. Electron microprobe analyses are crucial in unravelling the crystallisation and replacement sequences shown by the feldspars and in characterising the general mineral makeup of the pods, and have therefore been presented alongside the pod petrography in this section along with a separate section dealing with feldspar alteration (Appendix A, B, C and F). Pods were sampled for geochronology together with some host anorthosites, but sample CG09-021 was the only processed anorthositic

sample that yielded a viable zircon population for geochronology and consists of subhedral plagioclase (0.3-1 cm), showing slight recrystallisation and annealing, with very minor, intercumulus magnetite.

5.2.1 Leuconorite-Hosted Pods

Several varieties of pods are observed in the leuconoritic and orthopyroxene-bearing anorthositic samples. Accumulations of randomly oriented 15-36 cm long, fresh, randomly oriented euhedral plagioclase crystals with interstitial orthopyroxene and magnetite, in addition to a pinkish, highly albitised material constitutes the most "anorthositic" pod (CG09-027C; 57.7 % SiO_2 26.8 % Al_2O_3 6.15 % Na_2O) observed in the MMIS (Figure 5.2a, b; 5.3a, 5.4; Appendix A, B, F). The albitised material is surrounded by fresh plagioclase crystals and is situated adjacent to intercumulus sub-calcic augite and magnetite. Fresh plagioclase shows An_{45}, at the low-end, but typical of Proterozoic anorthosites ($An_{\sim 45\text{-}65}$). Microscopic symplectic intergrowths of plagioclase ($An_{45.9}$) and diopside (Wo:En:Fs – 46:32:22) occur on the edges of larger clinopyroxene grains, while myrmekitic (quartz-plagioclase) intergrowths are observed on the boundaries of fresh plagioclase grains and the pinkish, highly altered, albitic material (Figure 5.5d). The remaining three pods hosted by leuconorites all show ubiquitous development of macroscopic, graphic intergrowths between, either plagioclase and quartz (CG09-016A; Figure 5.3f), or potassic feldspar and quartz (CG09-018D and 26B; Figure 5.3 b,c,e). The first of these pods (CG09-016A) is a large (2 m wide) pod characterised by intergrowths of quartz and red, variably hematised and albitised plagioclase (Figure 5.2c-e; Figure 5.3f). Remnant albite twinning is recognisable in several domains, indicating that quartz is intergrown with what was originally plagioclase. These "unaltered" domains show plagioclase compositions of $An_{0\text{-}1}$ indicating that severe albitisation has affected original, intermediate plagioclase compositions. The red-stained feldspars have up to 0.75 wt% FeO_T and $An_{\sim 1}$ suggesting that most of this pod has experienced hematisation (as tiny Fe-Ti oxide inclusions typical of Proterozoic anorthosite plagioclase) in addition to extreme albitisation. Altered clinopyroxene, together with Fe-Ti oxide, forms a minor proportion of the assemblage. Macroscopic symplectic intergrowths of apatite and magnetite/ilmenite are also observed (Figure 5.3d).

Two circular pods (CG09-018D, 26B) display the most prominent graphic intergrowths of quartz and K-feldspar as well as much more diverse mineral makeup (Figure 5.2f, 5.3b). Pod CG09-018D displays large (2-3 cm), rounded crystals of albitised plagioclase, as well as large, euhedral ~20 cm plagioclase megacrysts, surrounded by graphic intergrowths of quartz and albitised K-feldspar (Figure 5.3b). Both plagioclase and orthoclase occur as primary phases in this sample, but K-feldspar is also observed as a magmatic replacement product of plagioclase, as discussed in the subsequent section on feldspar replacement textures. Although this K-feldspar is extensively albitised, fresh domains show perthitic texture with albitic exsolution lamellae ($An_{17\text{-}19}$; Figure 5.4). These ~ 4 um wide lamellae are fairly abundant, forming 20-30% of the perthite. Primary plagioclase ($An_{\sim 15\text{-}25}$) is found as isolated remnants within the albitised K-feldspar and is occasionally preserved adjacent to quartz (Figure 5.4). Altered orthopyroxene (alteration product unidentified) and large (~1 cm) crystals of adjoining magnetite and ilmenite are observed along with euhedral zircon crystals, commonly included within plagioclase, and minor euhedral apatite crystals (Figure 5.5a). Pod CG09-026B shows extreme development of graphic intergrowths between quartz and K-feldspar in some areas, but on the whole presents similar mineral makeup to CG09-018D, except that no apatite is observed and smaller amounts of zircon are seen (Figure 5.3c, e).

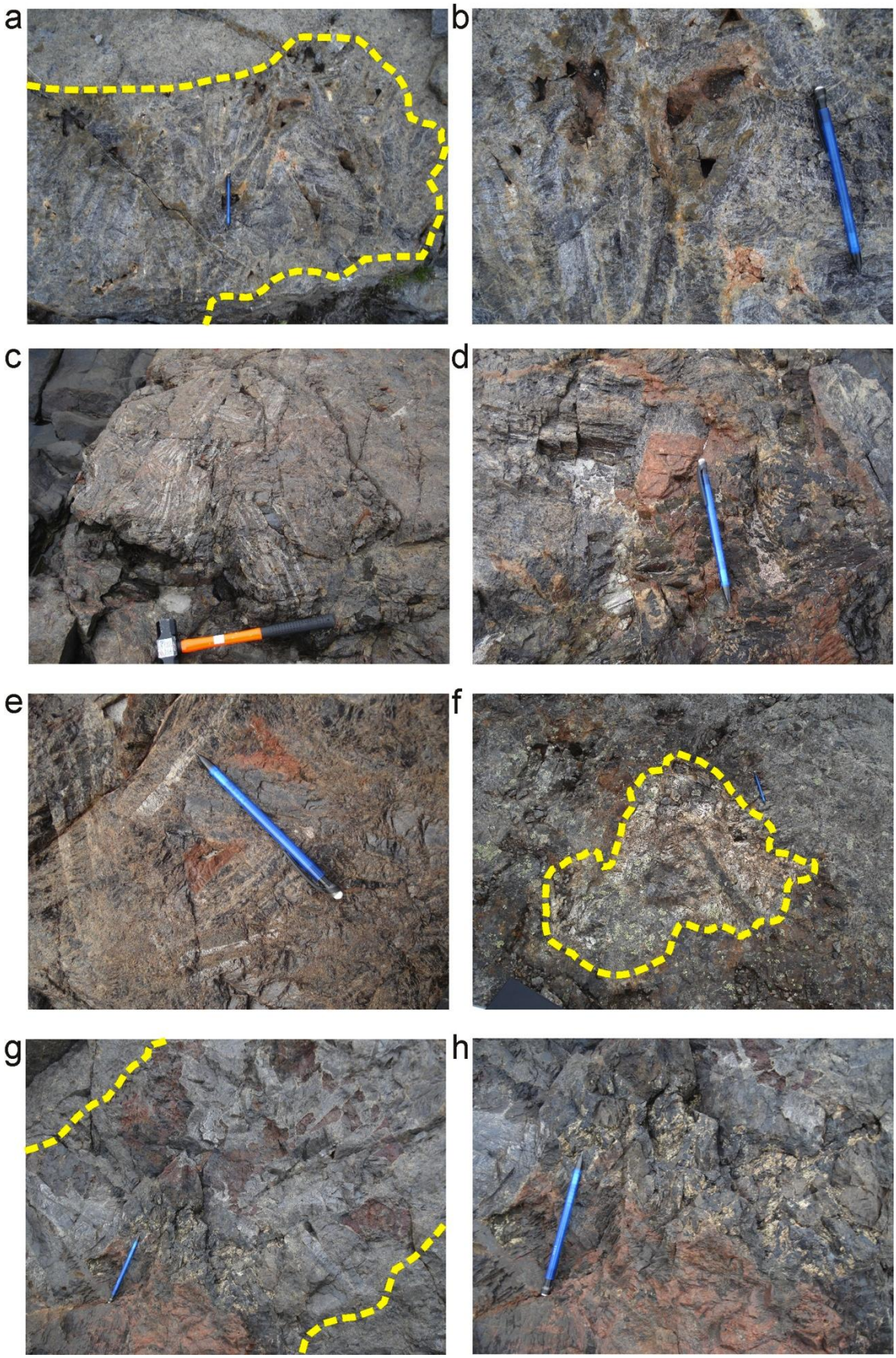
a
b
c
d
e
f
g
h

Figure 5.2 (previous page): a-b. Irregular pods (CG09-027C) of pegmatitic (~15 cm) plagioclase crystals hosted by coarse-grained (~2-4 cm) anorthosite. Interstitial areas within the pods are filled with altered pyroxenes and pinkish albitic alteration material. This pod most resembles the host anorthosites. c-e. Pod CG0916A (hosted by leuconorite) consisting of large (20 cm) plagioclase crystals showing variable stages of alteration (fresh = grey, alteration = red/brown). In d, intergrowths of Fe-Ti oxide are observed intergrown with apatite (see also Fig 3d). f. Irregular pod (CG0918D) with large (~50 cm) plagioclase crystals and graphic intergrowth of quartz and K-feldspar forming an Fe-rich quartz-monzodiorite composition. g-h. Pod CG0933B, hosted by olivine-bearing anorthosite. Pod consists of large, dark, pyroxene crystals with interstitial altered feldspar and intergrowths of Fe-Ti oxide and apatite (h; see also Fig 6a).

Only minor plagioclase (<10%) is observed in samples from CG09-026B, but CG09-018D shows a higher modal abundance of plagioclase. This fresh plagioclase has An contents between 15 and 25. The accurate estimation of modal proportions of plagioclase and K-feldspar is made difficult by the pegmatitic nature of the samples, but I have attempted to estimate these proportions using normative calculations in Section 5.3. Quartz in both of these pods is fresh and shows many fluid inclusions trails.

In all four of the aforementioned pods, abundant microscopic, myrmekitic intergrowths of quartz and plagioclase form at the interface between quartz and albitised K-feldspar of the graphic intergrowths (Figure 5.5a-c). Plagioclase in these myrmekitic intergrowths has a broadly oligioclase-andesine composition (An_{23-34}, Figure 5.4). These myrmekitic intergrowths either form bulging, plumose structures or occur as thin films at the interface between macroscopic graphic intergrowths of potassic feldspar and quartz. In general, these myrmekitic intergrowths are very irregular and do not radiate from any particular point, but form at a high angle to the adjacent potassic feldspar and quartz. In areas where bulbous, plumose myrmekite develops, the structure radiates outwards from the graphic quartz intergrowths. On the boundaries between minerals involved in the graphic textures, where myrmekite is not developed, quartz of the graphic intergrowths is rimmed by plagioclase ($An_{\sim 19}$) that is successively surrounded by albitised K-feldspar.

5.2.2 Pod Hosted by Olivine-Bearing Anorthosite

A distinct, mafic pod (CG09-033B; 39.6 % SiO_2, 24.1 % FeO, 7.6 % MgO), found within an olivine-bearing leucogabbroic sample of the Etaugalet massif, shows macroscopic intergrowths of apatite and magnetite/ilmenite together with large crystals of inverted pigeonite, plagioclase and lesser amounts of K-feldspar (Figure 5.2g, h, 5.6a, b, c; Appendix A, B, F). K-feldspar displays the characteristic red-stained colour common to the other pods, but the K-feldspar observed microscopically shows no albitisation or hematisation, although it does host an exsolved plagioclase component. These lamellae are near sub-micron sized (1-2 microns wide), making estimation of the proportions very difficult, but made up approximately 25-40 % of the perthite. In contrast to the perthitic feldspars in the aforementioned pods, the exsolution lamellae are significantly more calcic (An_{50}), but equally abundant. The large pyroxenes show a red-bronze weathered colour but are generally unaltered (Figure 5.2g, h). Inverted pigeonite shows extensive, blebby and regular exsolution lamellae (Figure 5.6b, c). K-feldspar grains are commonly surrounded by plagioclase-orthopyroxene symplectites that are in turn in contact with inverted pigeonite and apatite grains (Figure 5.6c, d). Plagioclase in these symplectic relationships is labradoritic ($An_{\sim 49}$), while the intergrown pyroxene is an intermediate

orthopyroxene (Wo:En: Fs – 1.4:52-54:44-46). No olivine or quartz were observed in any of the samples taken from this pod.

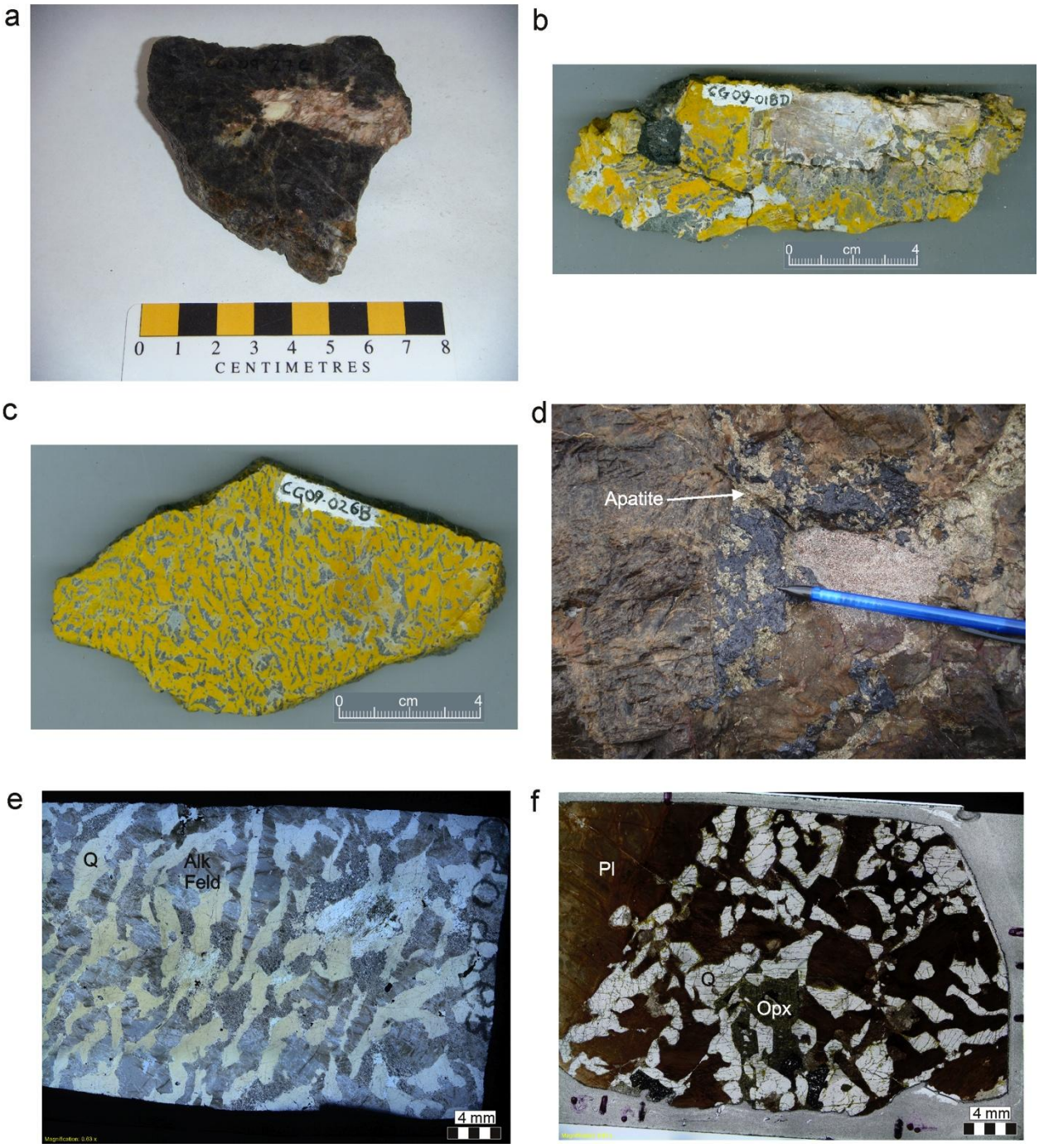

Figure 5.3 a. Pinkish albitic alteration material interstitial to coare-grained, euhedral to subhedral plagioclase grains and minor magnetite from the most 'anorthositic' pod (CG09-027C). b. Cobaltinitrate-stained hand sample from pod CG09-018D showing the presence of K-bearing phases and large plagioclase crystals surrounded by symplectic intergrowths of quartz and K-feldspar. c. Extensive development of graphic quartz-K-feldspar intergrowths in pod CG09-026B. d. Fe-Ti oxide-apatite (light green colour) symplectites in the pod hosted by an olivine-bearing anorthosite (CG09-033B). e-f. Crossed-polarised (e) and plane-polarised (f) view of extensive symplectic intergrowths of K-feldspar (e) or plagioclase (f) and quartz in pods CG09-026B and CG09-016A, respectively.

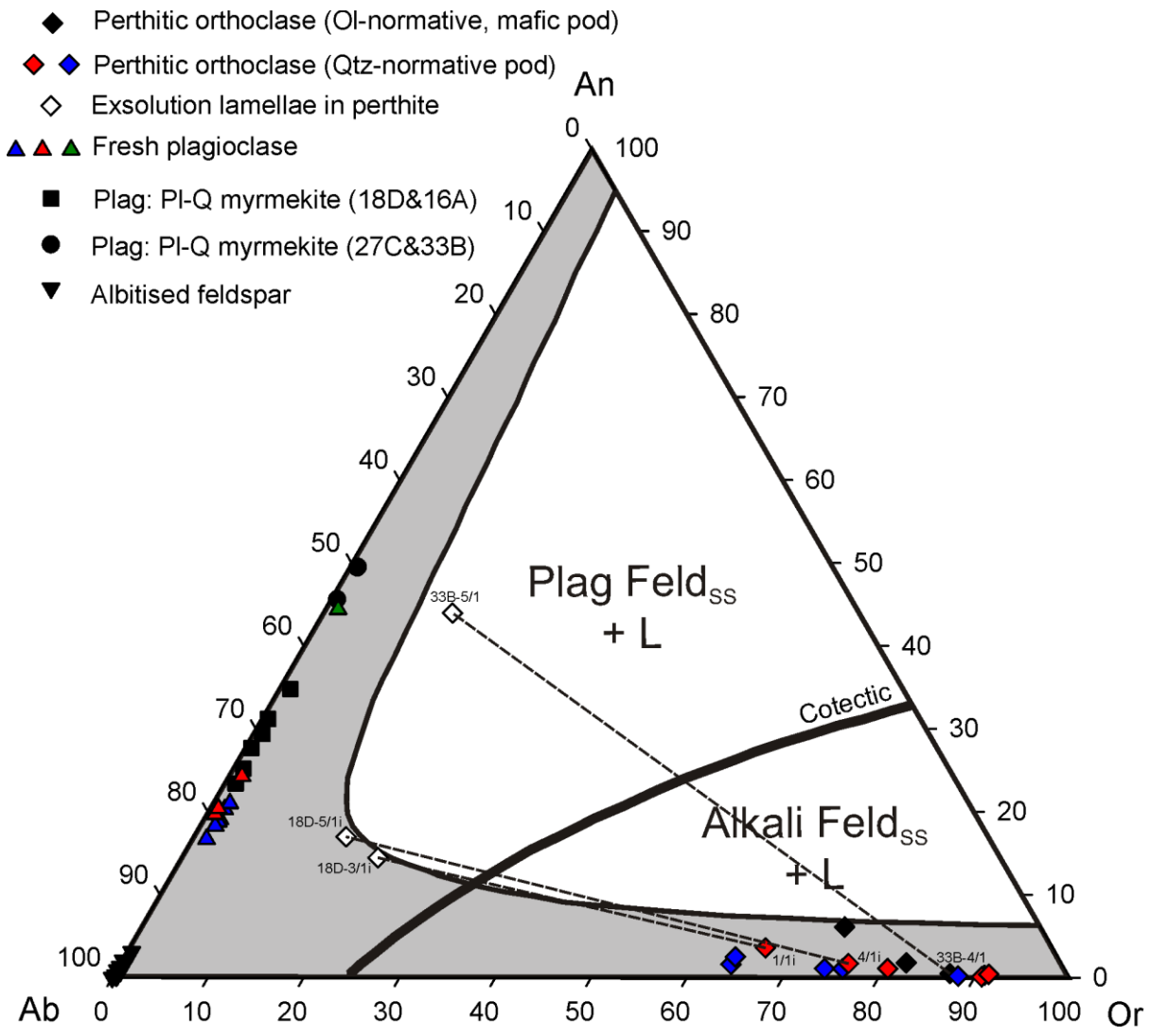

Figure 5.4 Or-An-Ab ternary diagram illustrating feldspar compositions observed in the pods, determined using EMPA. Tie-lines join host orthoclase compositions and plagioclase exsolution lamellae observed in several pods. These exsolution lamellae are less than 4 um wide and are abundant in the feldspar, with an estimated ratio of 70:30 for host and lamellae, respectively (See Fig. 7d). Care was taken in ensuring that the orthoclase analyses were free of exsolution lamellae except for one point (black diamond falling on solvus). Data presented in Appendix F-1.

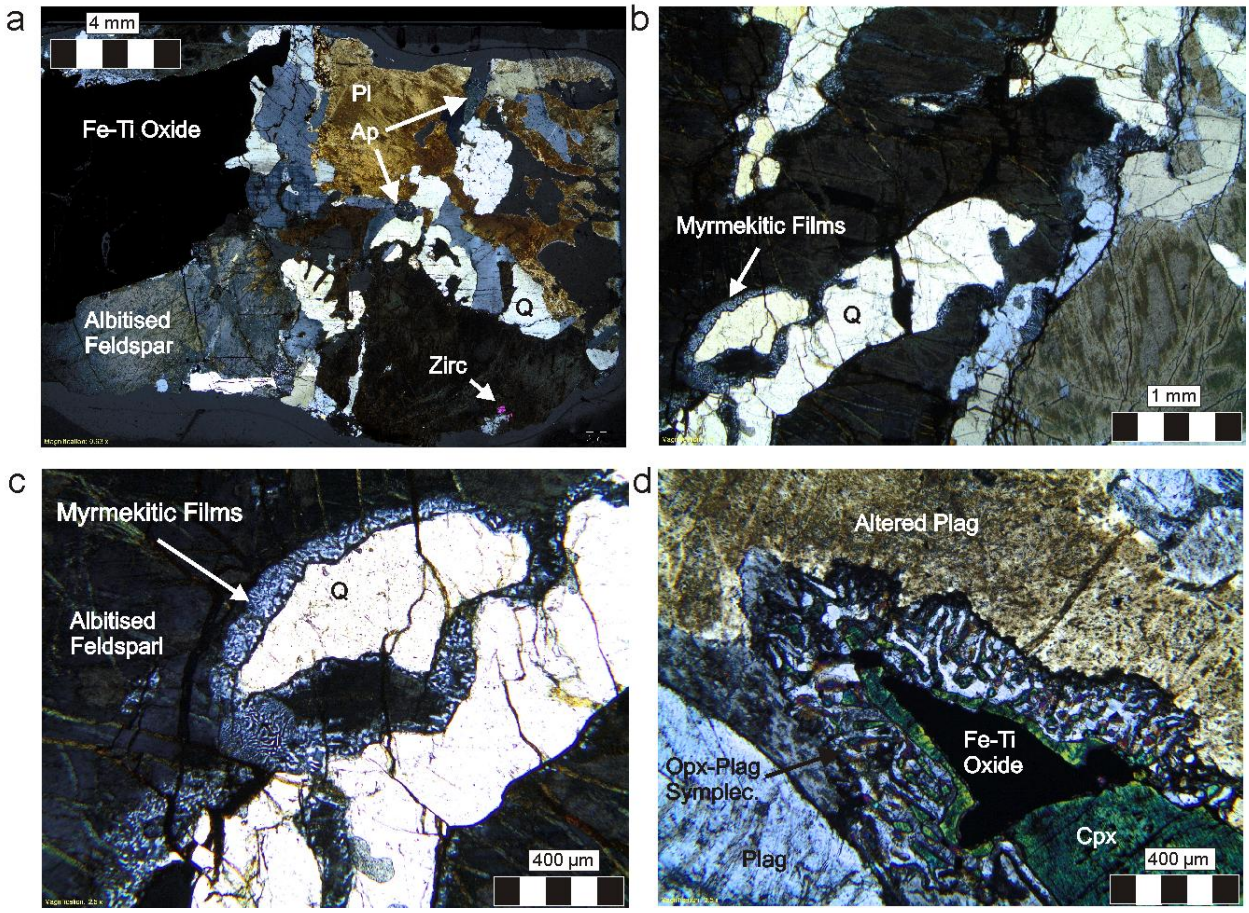

Figure 5.5 a. Apatite, zircon and Fe-Ti oxides in combination with a graphic quartz-orthoclase intergrowth in sample CG09-018D. b-c. Development of microscopic films and plumose structures of myrmekite at the interface between quartz and K-feldspar phases of a graphic intergrowth (CG0918D). d. Similar microscopic symplectites, in this case developed between plagioclase and clinopyroxene in pod CG09-027C.

5.2.3 Replacement Features of the Pods

The alteration or replacement of feldspar in several of the documented pods is extensive and in many places obscures the primary mineral composition and textures. Cobaltinitrate staining was used during sample preparation to identify K-rich phases. Pods CG09-018D and 26B (Figure 5.3b,c) show extensive yellow staining, indicating the presence of K-rich phases. Microscopically, the phases that show yellow staining are variably altered to a cloudy, brown material while the fresh areas have optical properties suggesting that they are untwinned feldspar crystals. Electron microprobe analyses of both the fresh and altered domains reveal that this feldspar is a typical K-feldspar (orthoclase) with microscopic blebby exsolution of an albitic feldspar (An_{19-17}; lamellae are no more than 3 micron wide). In several areas of CG09-018D and 26B, K-feldspar also replaces adjacent oligoclasic plagioclase (An_{18-26}, Figure 5.7a-c). In this case, the replacive K-feldspar tends to have higher Or contents (±90) than primary K-feldspar, although a spectrum of Or contents is observed in each pod. Isolated plagioclase, surrounded by fresh and albitised potassic feldspar remnants, is observed in both CG09-018D and 26B and support the notion that replacement of plagioclase by K-feldspar has occurred. This potassic replacement of plagioclase has only been observed in these two pods – the most chemically and minerlogically evolved pods.

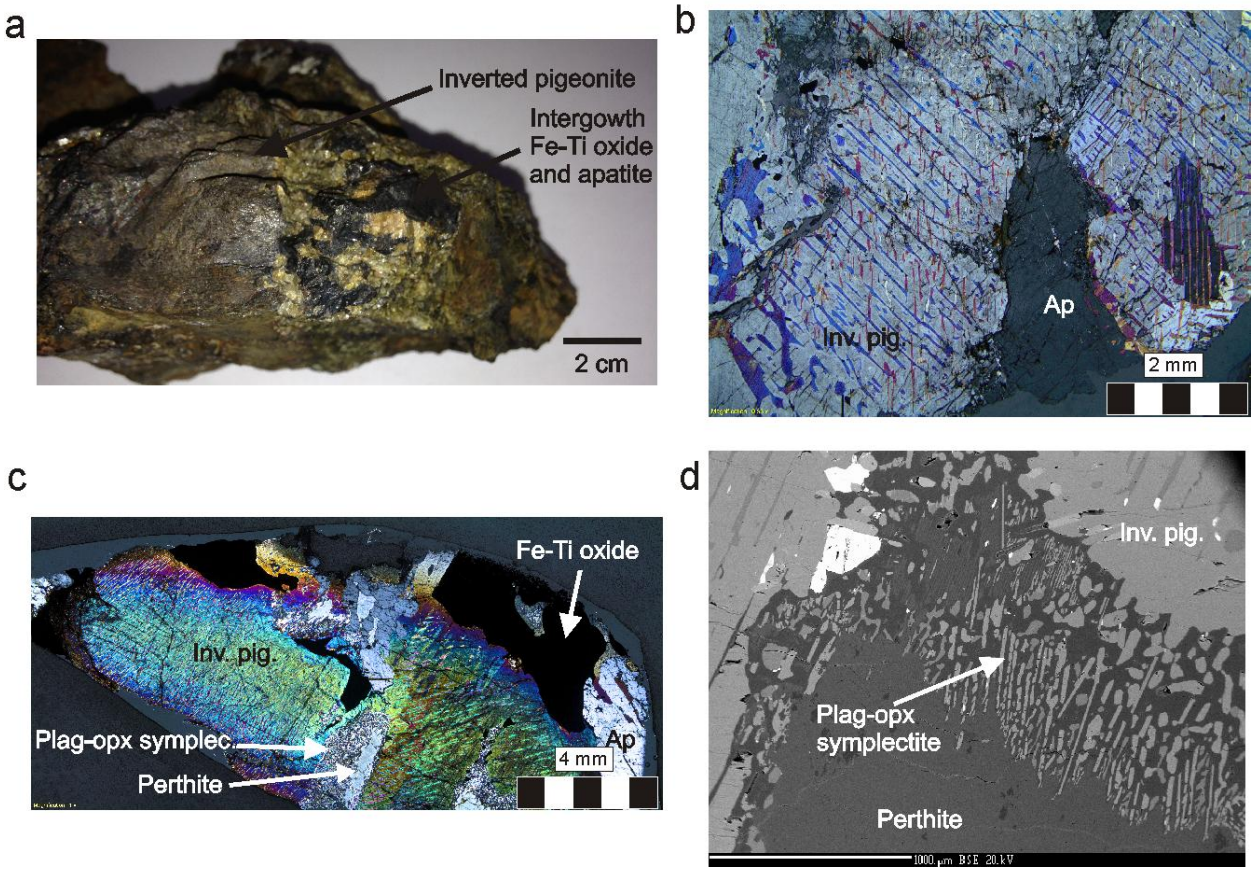

Figure 5.6 Petrography of the only observed pod hosted by leucotroctolites. a. Intergrowths of apatite and Fe-Ti oxide adjacent to a large crystal of pyroxene (inverted pigeonite). b. Blebby and lamellar inverted pigeonite surrounding apatite crystal viewed under cross-polarised light. c. Microphotograph of a slightly thick thin-section of sample CG0933B in cross-polarised light showing apatite, Fe-Ti oxide, inverted pigeonite and plagioclase-orthopyroxene symplectites radiating from a corroded plagioclase grain, magnified in d. d. SEM image of plagioclase-orthopyroxene symplectites emanating from a perthite grain.

Alteration of this perthitic feldspar produces pure albite (An_{0-4}) that appears cloudy and brown microscopically (Figure 5.7a,d). Extensive albitisation and hematisation (producing the red-brown staining) of plagioclase feldspar is observed in CG09-027C, 16A and 33B, and although albitisation of K-feldspar is common in CG09-018D and 26B, no hematisation is observed in these pods. Restriction of these unique alteration/replacement processes to the pods and not the host anorthosites indicates that these processes are not related to pervasive, low-temperature fluid circulation throughout the anorthosite intrusion, but must be related to the unique chemistry of, and processes operating in, the pods.

5.3 Pod Compositions

As the pod petrography suggests, the compositions of the pods hosted by orthopyroxene- and olivine-bearing anorthosites are different (Appendix A, B, C, F). The pods hosted by leuconorites have SiO_2 contents ranging between ~57 and 75 wt%, high Al_2O_3 contents (~11-27 wt%) and very low MgO concentrations (<2 wt%).

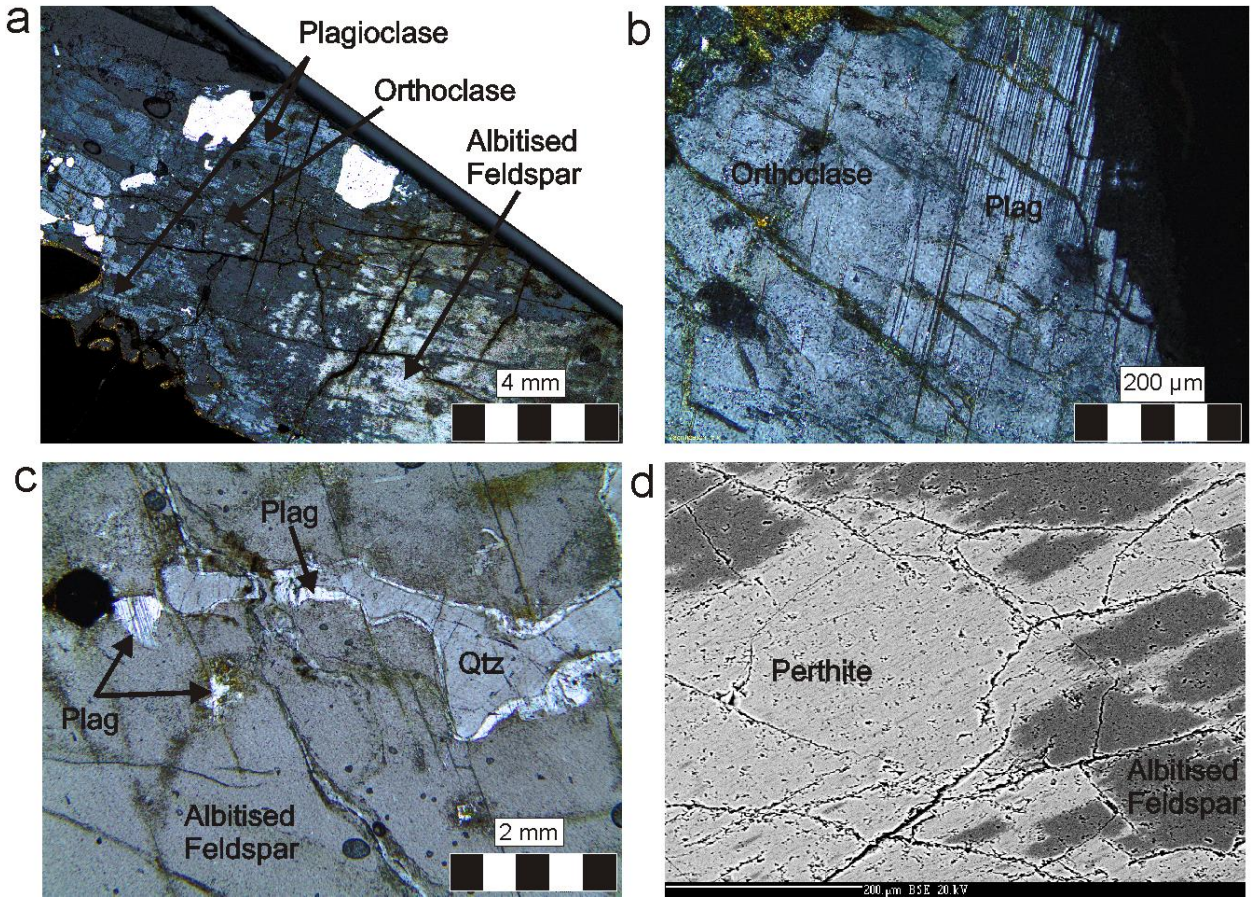

Figure 5.7 a. Crossed-polarised view of primary plagioclase (An_{15-25}) showing albite twinning, replaced by darker orthoclase later altered to albite (An_{0-5}). Black grain is Fe-Ti-oxide while white grains are quartz. b. A plagioclase grain (albite twinning) situated adjacent to an extinct quartz grain and surrounded by orthoclase (crossed-polars). c. An intergrowth of quartz, rimmed by plagioclase that is surrounded by albitised orthoclase. Remnant domains of plagioclase are observed indicating that orthoclase is a replacement phase after plagioclase. This orthoclase is subsequently altered to albite, potentially by late-stage magmatic fluids. d. SEM image of perthite (intergrown graphically with quartz) altering to albite. Lamellae of abundant ~4 um wide plagioclase visible in perthite.

FeO and TiO_2 are generally low, although one pod with significant amounts of magnetite-ilmenite shows elevated FeO (13.04 wt%) and TiO_2 (3.33 wt%). In contrast, the only sampled and observed pod in an olivine-bearing anorthosite is significantly more mafic (SiO_2: 39.55 wt%, MgO: 7.63 wt%, FeO: 24.08 wt%, TiO_2: 6.05 wt%). The significant proportion of magnetite-ilmenite and apatite in this pod is evident in the elevated FeO, TiO_2 and P_2O_5 (1.28 wt%) concentrations. The whole-rock data produce reasonable normative mineral composition and based on this normative proportion, these pods classify as a range of rock types, from monzogranite through quartz-monzodiorite and monzodiorite to Fe-P-rich gabbronorite (Table 5.1; Streckeisen, 1976).

A progressive enrichment in REE concentration is evident among the pods (Figure 5.8). The pods hosted by pyroxene-bearing rocks that most closely resemble the anorthositic hosts (CG09-027C, 16A) show only minor REE enrichments and similar positive Eu anomalies (Eu/Eu* = 4.75 vs. 4.81 average for leuconorite hosts). Large prominent negative Eu anomalies (Eu/Eu* = 0.12-0.53) and abundant REE, and particularly LREE,

enrichment (up to ~1000x chondrite) relative to the host leuconorites characterise pods CG09-026B and 18D. $[La/Sm]_N$ averages 5.56 in the pyroxene-anorthosite hosted pods, but is noticeably different in the pod hosted by an olivine-bearing rock,with a value of 1.67.

Table 5.1 Normative mineral composition of five pods from the MMIS

	Hosted by leuconorite				Hosted by olivine-bearing anorthosite
	CG09-16A	CG09-18D	CG09-26B	CG09-27C	CG09-33B
Quartz (Q)		11.80	32.70	0.29	
Corundum (C)	3.96		1.06	0.85	
Orthoclase (Or)	13.12	9.28	37.11	5.32	9.69
Albite (Ab)	60.16	39.77	21.58	52.04	15.15
Anorthite (An)	19.57	5.94	3.62	40.59	10.67
Nepheline (Ne)					
Diopside (Di)		4.59			8.51
Hypersthene (Hy)	2.30	19.82	3.26	1.46	7.54
Olivine (Ol)	0.29				29.52
Magnetite (Mt)	0.14	2.33	0.26	0.13	4.31
Ilmenite (Il)	0.21	6.33	0.25	0.25	11.49
Apatite (Ap)	0.12	0.14	0.07	0.14	2.97
Q		17.67	34.42	0.30	
K	14.13	13.89	39.06	5.41	27.30
P	85.87	68.44	26.52	94.29	72.70
	Monzodiorite	Quartz monzodiorite	Monzogranite	Anorthosite	Olivine gabbronorite

The pods are similar isotopically, with values ranging between $\varepsilon_{Nd,\ 1640\ Ma}$ = +2.19 and 2.48 (Figure 5.9). The higher ε_{Nd} values of this range overlap with the compositions of the host leuconorites. A noticeable trend in the isotopic composition of the anorthositic samples is observed, however. True anorthosites (>90 % plagioclase) display the highest ε_{Nd} isotopic compositions, while olivine-bearing, followed by orthopyroxene-bearing samples are progressively less depleted (lower ε_{Nd}). Hornblende-biotite granites from the MMIS have far lower ε_{Nd} compositions between 0.3 and -0.5 (Hegner et al. 2010).

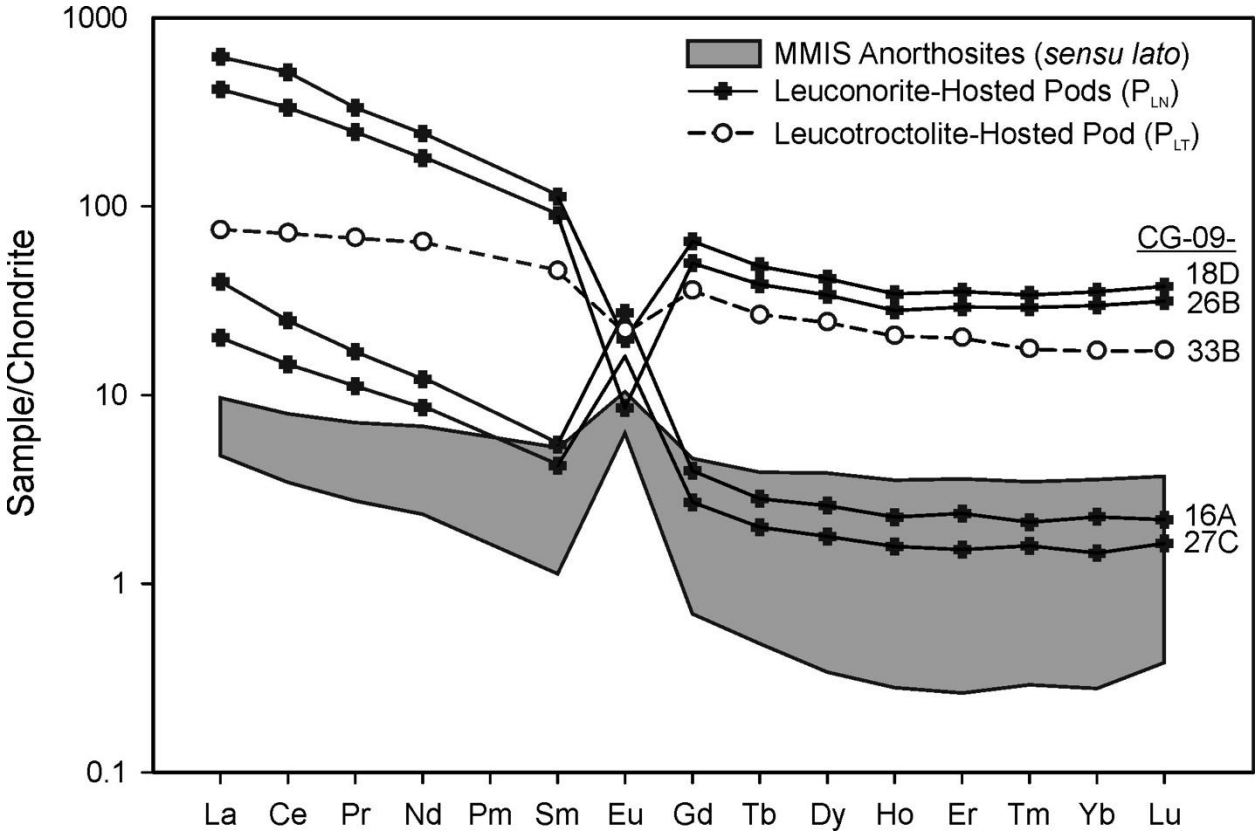

Figure 5.8 Chondrite-normalised (Anders and Grevesse, 1989) rare earth element diagram comparing the composition of the pods and host anorthosites. A spectrum of REE enrichment is observed in the pods, from very similar to the host anorthosite, to 1000x chondrite enrichment, along with negative Eu anomalies in the most evolved pods.

5.4 U-Pb Geochronology

The coarse-grained and evolved nature of the pegmatitic pods suggests that these compositions had the potential to have crystallised either zircon or baddeleyite as accessory phases, as had been demonstrated in other AMCG massif-type anorthosites (Emslie et al., 1994; Hamilton et al., 1994; Hamilton, 2008). Indeed, macroscopic crystals of needle-like, acicular zircon were easily recovered from two of the graphic pods developed within leuconoritic hosts, CG09-018BD and CG09-026B. In addition to these, from samples collected from well-exposed outcrops along the shore of Etaugalet Bay, zircon was separated from a third leuconorite-hosted pegmatitic pod, CG09-016A, as well as from the pod enclosed in olivine-bearing anorthosite, CG09-033B (Figure 5.1). Zircon from graphic pods occurring in samples CG09-016A, -26B and -33B is present as irregular, colourless or pale yellow-brown, clear to slightly clouded, typically large but broken or cracked grains or shards. Despite strong chemical abrasion pre-treatment, analysed single or two-grain fractions from these samples tend to be relatively discordant (approximately 1-5%; Appendix F-2, Figures 5.10a-c). Clouded zircons commonly show more elevated levels of total common Pb and are likely retain radiation damaged and altered domains. Uranium concentrations in zircon from graphic pod CG09-026B are notably elevated (up to 2000 ppm), in concert with the higher overall abundances of incompatible elements in the bulk analysis of this pod – particularly for U, Th, Rb and the REE.

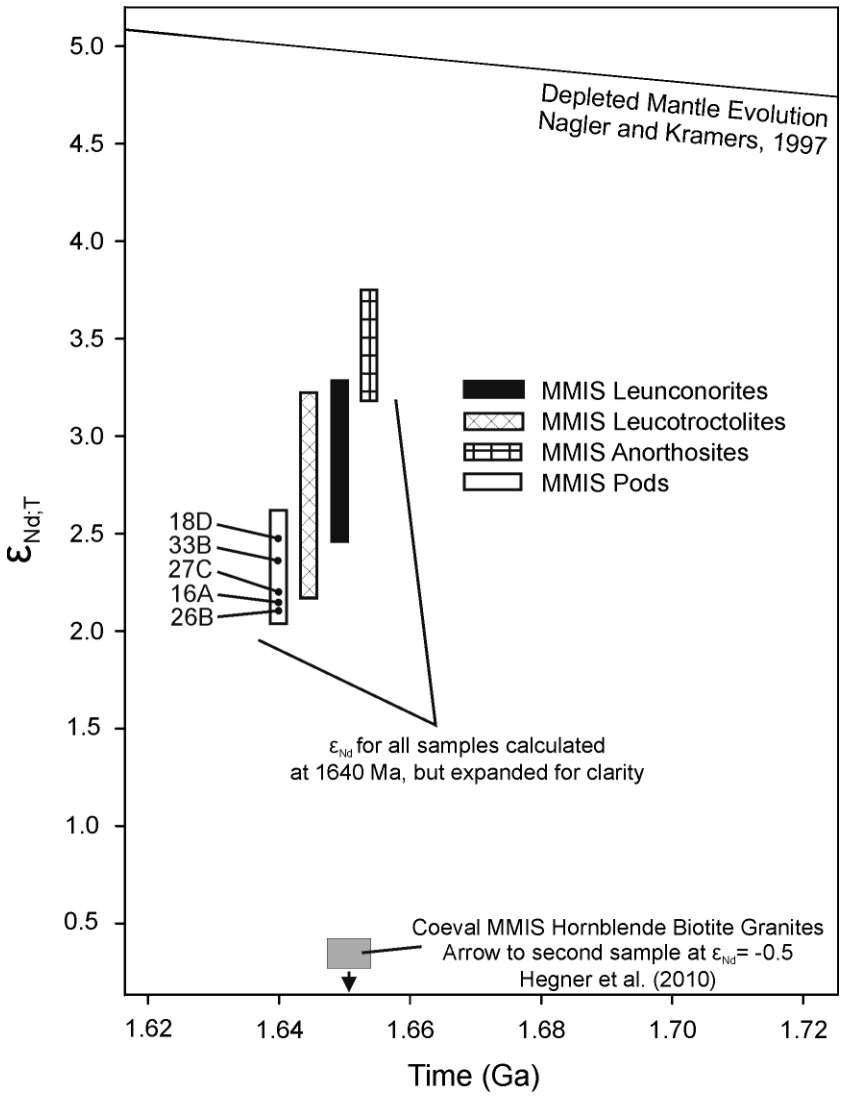

Figure 5.9 When compared to the host anorthosites, the pegmatitic pods show the least radiogenic or lowest isotopic compositions ($\varepsilon_{Nd;\,T}$), slightly overlapping with leuconorites and leucotroctolites of the MMIS. Isotopic compositions are all calculated at 1.65 Ga, but are expanded for clarity. A decrease in $\varepsilon_{Nd;\,T}$ with progressive increase in silica content is noted in the anorthosites, leucotroctolites and leuconorites. Coeval granites of the MMIS plot at lower ε_{Nd} compositions and are not comparable with the late-stage pods which are geochemically most similar to the most contaminated host rocks. Isotopic data for pods and anorthosites are provided in Appendix C.

Despite the dispersion of Pb/U isotopic ratios, the data describe well-fitted colinear trends controlled by Pb-loss effects during Grenvillian metamorphism, and yield upper intercept ages of 1654 ± 8 Ma (CG09-016A), 1647 ± 6 Ma (CG09-026B), and 1638 ± 6 Ma (Figure 5.10a-c).

Zircons recovered from graphic pod CG09-018D (in a leuconorite host) and from leuconorite wholerock CG09-021 are of distinctly better quality than in the other pods. Most crystals are colourless to pale yellow in colour, and are generally water-clear; in sample 18D, they are especially well-formed, prismatic and euhedral. Analysed single zircon grains from sample 18D are mostly near-concordant, and four points regress to yield an upper intercept age of 1632.8 ± 1.8 Ma (Appendix F-2, Figure 5.10d), with little to no evidence for Proterozoic Pb-loss. Results for five zircon fractions from sample 21 are all colinear, suggesting an igneous crystallisation age

of 1628.0 ± 3.5 Ma. A lower intercept age of 1119 ± 38 Ma suggests modest Pb-loss effects during early Grenvillian reheating (Figure 5.10e).

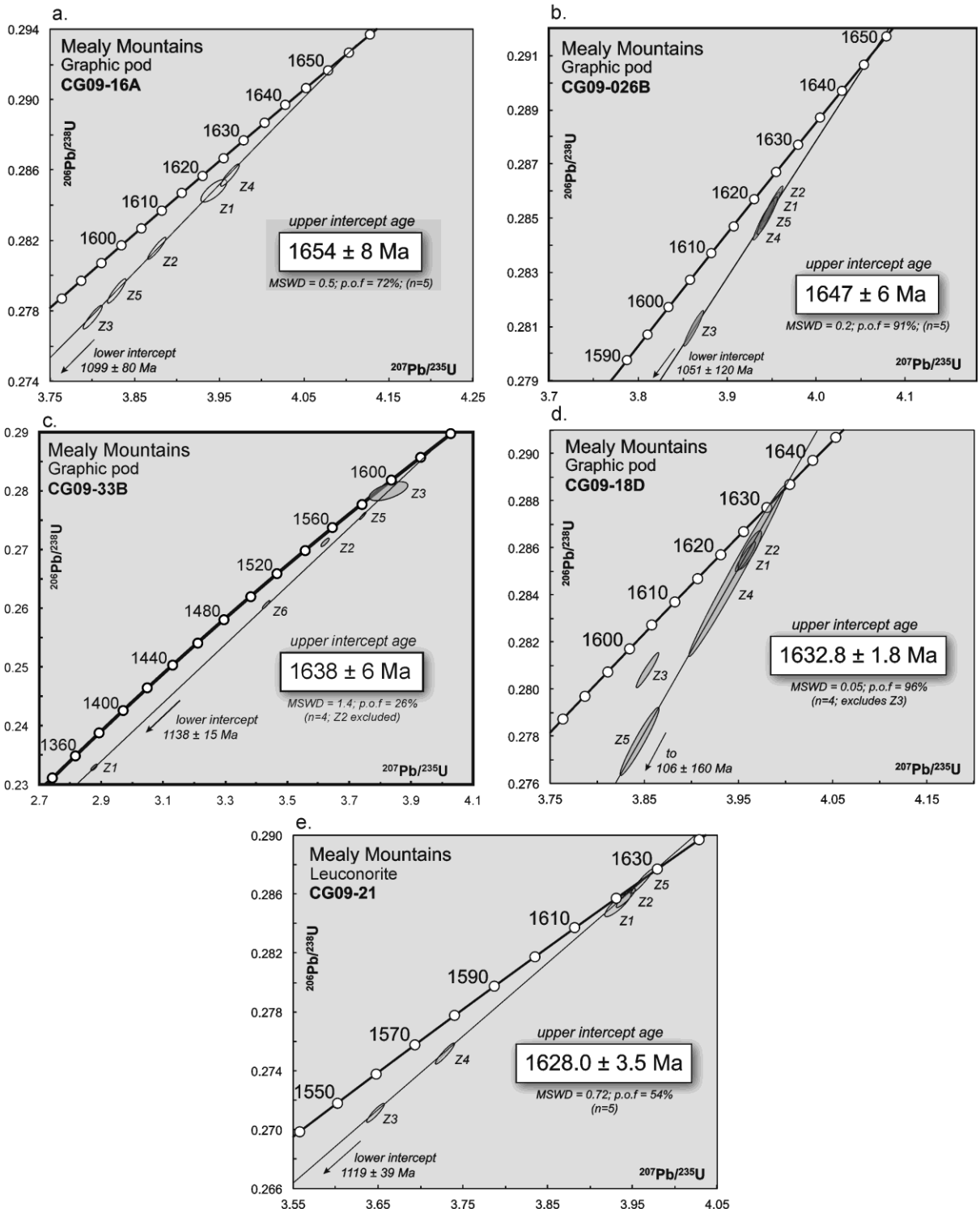

Figure 5.10 U-Pb zircon geochronology for the four pegmatitic pods and one anorthosite from the MMIS. Although extending the emplacement ages for the MMIS to between 1654 to 1628 Ma, the ages produced agree well with previous geochronological determinations from felsic members of the MMIS (Gower et al. 2008b).

The U-Pb crystallisation ages reported here for the pegmatitic pods and for the leuconorite are in good agreement with previously published ages (~1650-1630 Ma) for Mealy Mountains Intrusive Suite magmas (Emslie & Hunt 1990; Gower et al. 2008; James et al. 2000). With one exception, however, the span of intrusive ages for MMIS has been based on a half-dozen U-Pb determinations on monzonitic and quartz monzodioritic compositions; a single age of 1632 ± 3 Ma was determined through analyses of zircon and baddeleyite from a pegmatitic patch enclosed within the Crooks Lake anorthosite (not shown on Figure 5.1; Gower et al. 2008b). The new U-Pb data presented in this work expand the total range of MMIS magmatism slightly from 1654 to 1628 Ma (not including associated errors), but, importantly, confirm that the ages of basic plutonism essentially mimics that of felsic intrusive activity, a characteristic typical of other AMCG complexes (Emslie et al. 1994; Hamilton et al. 1994).

5.5 Discussion

The pod-like geometry of the rock types discussed here is indicative of crystallisation of residual liquids trapped in a viscous crystal mush. In addition, the extreme incompatible element enrichment in several of the pods, the presence of significant proportions of minerals like zircon and apatite, along with concomitant enrichments in P_2O_5, suggests that these pods may represent highly fractionated liquids. The interpretation of the unique set of symplectic textures observed in these pods provides further insight into the processes in operation in these final stages of crystallisation and is discussed below.

5.5.1 Graphic Intergrowths

Graphic intergrowths of quartz with albitised and hematised plagioclase (CG09-016A) as well as potassic feldspar (CG09-026B and 18D) provide important constraints on the processes involved in the crystallisation of these pods. These intergrowths are indicative of simultaneous crystallisation of the two phases, controlled by contrasting rates of diffusion (particularly of Al and Si) and growth in a melt adjacent to the developing intergrowth (Vernon 2004). Eutectic crystallisation is also thought to play a role in developing this texture, although may not be a determining factor. Graphic intergrowths between quartz and both plagioclase and/or orthoclase are developed in these pods. The Si-rich pods (CG09-026B and 18D), at first glance, show quartz intergrown with K-feldspar, but on closer inspection, primary plagioclase grains are found included within orthoclase, commonly displaying reaction relationships. These reaction relationships, discussed below, in addition to extensive albitic alteration of the orthoclase, make discerning the original extent of plagioclase in these intergrowths very difficult. Plagioclase has been reported as a nucleus on which orthoclase grows in graphic intergrowths (Hughes 1972) and this is the likely scenario in the pods, given the relatively low proportion of normative plagioclase in the pods. In pod CG09-016A, graphic intergrowths of quartz and plagioclase are observed, while CG09-033B presents macroscopic symplectic integrowths of apatite and magnetite.

The similarity of macroscopic, pegmatitic textures in all of these graphic pods points to the operation of similar kinetic processes in most of the pods, but significantly different chemistries of the trapped residual liquids to produce the variation in mineralogies involved in the intergowths. I interpret these textures, commonly ascribed to simultaneous, eutectic crystallisation, as evidence that these pods represent the final crystallisation products of anorthositic magmas, trapped by virtue of the viscous, surrounding felsic mushes.

5.5.2 Potassic Replacement of Plagioclase

In pods where significant felsic, graphic intergrowths are noted (CG09-016A, 18D, 26B), many examples of replacement of plagioclase by K-feldspar are observed. This unusual texture is overprinted by albitizstion of plagioclase, although several areas remain where both the plagioclase and orthoclase are fresh. The fact that this potassic replacement is only observed in the pods with the most evolved mineral makeup and chemistry (not in CG09-016A, 27C or the host anorthosites) indicates that the replacive process is associated with unique conditions developed in these pods. Albitic alteration is ubiquitous to all the pods and commonly causes intense red staining of the altered feldspar. It is likely that this saussuritisation is due to the effects of low temperature fluids.

Low-temperature, fluid alteration of plagioclase to K-feldspar has been reported in several igneous settings (Larsson et al. 2002; Morad et al. 2010), but the replacement of plagioclase by K-feldspar can also be related to a high-temperature, peritectic reaction relationship between plagioclase and a potassium-rich fluid (Cox et al. 1979). Low temperature metasomatic alteration of plagioclase to K-feldspar occurs at temperatures below 350 °C and consequently these phases should not show exsolution. The observation of perthitic textures in the potassic feldspar indicates that this K-feldspar is a high-temperature phase. Furthermore, one would expect potassic alteration due to low temperature fluid circulation to permeate all the late-stage pods, like the pervasive albitisation, and cause alteration of the plagioclase therein. Potassic replacement of plagioclase is only observed in the most silicic and evolved pods, suggesting that higher-temperature magmatic processes specific to these pods created these replacive textures, rather than low-temperature metasomatic processes.

Experimental phase relations in the Or-An-Ab system reveal that under certain pressure and temperature conditions, crystallisation of K-feldspar, evolving to more sodic compositions, will eventually cause the liquid to react with plagioclase, driving the liquid off the cotectic and into the stability field of K-feldspar solid solution (Cox et al., 1979). This results in a peritectic reaction between plagioclase feldspar and a K-rich liquid, producing K-feldspar and Na-Ca rich fluids. The pods showing potassic replacement of plagioclase have extremely evolved primary plagioclase compositions (An_{15-25}; Figure 5.4), as expected for geochemically and mineralogically evolved pods. Using the estimated proportions of lamellae and host, bulk K-feldspar would have a composition close to the ternary cotectic (Figure 5.4 and 5.11). With continued crystallisation, the K-feldspar composition would reach, and cross the cotectic (Figure 5.11; Alk1 to Alk2). The crystallisation of this evolved K-feldspar phase would drive the liquid off the cotectic (bold arrow from L2), into the field of plagioclase instability, causing a peritectic reaction between K-rich fluid and primary albitic plagioclase. This liquid vector would travel parallel, or slightly down temperature, relative to isotherms in this system. The compositions I observe in these pods support the notion that magmatic plagioclase replacement is likely to occur, especially given extreme differentiation.

Where the perthitic feldspar is not albitised, a fresh appearance and the presence of exsolution lamellae indicate that it could also be a primary magmatic phase in addition to a magmatic replacement product. In fact, the peritectic phase equilibria described above require that primary K-feldspar crystallised, driving the potassic feldspar composition over the cotectic composition. Discerning and estimating the abundance of primary versus replacive magmatic K-feldspar is challenging and makes classification of the pods difficult. Assuming the K-

feldspar replacement and later albitisation processes are isochemical, closed-system processes as suggested by the restriction of replacement effects in the pods, the bulk rock chemical analyses should provide reasonable estimates of the true chemistry of the pods, as discussed in subsequent sections.

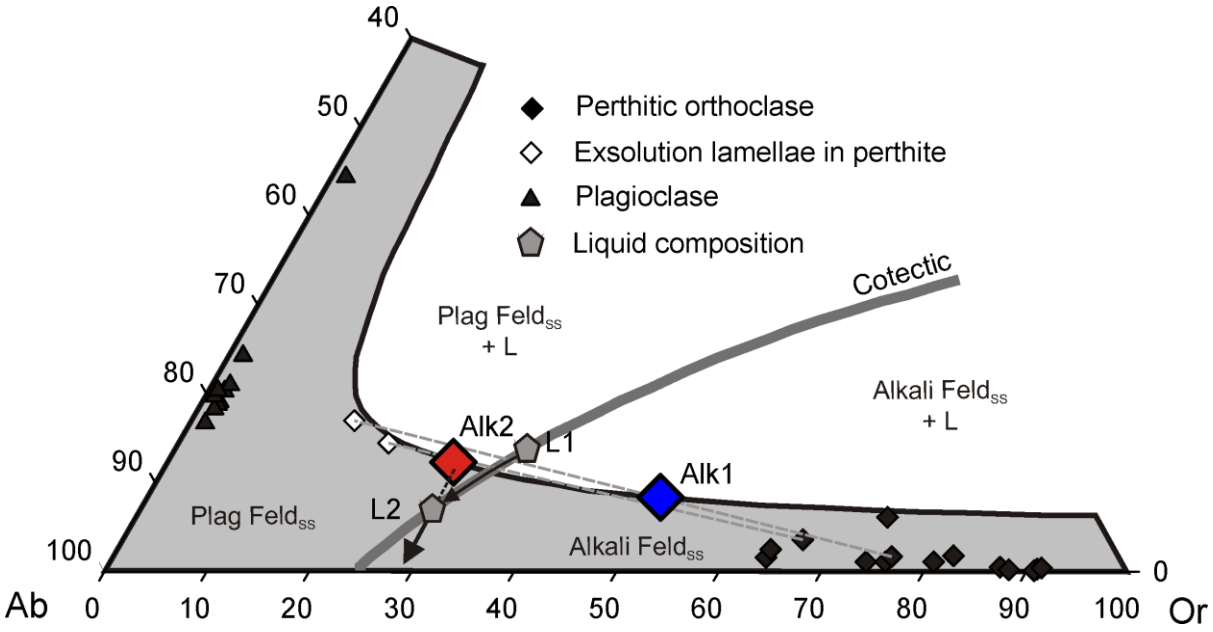

Figure 5.11 Development of peritectic phase equilibria due to extreme differentiation in pod-like structures. With continued differentiation, alkali feldspar compositions move across the cotectic (Alk1 to Alk 2) and force the evolving liquid off the cotectic, causing instability in plagioclase phases and reaction with the K-rich liquid to form K-feldspar.

5.6 Myrmekitic Intergrowths

Although myrmekitic intergrowths of calcic plagioclase (An_{62-92}) and quartz on interfaces of cumulus plagioclase have been noted in anorthosites from the St-Urbain massif (Quebec; Dymek & Schiffries 1987), the calcic nature of the plagioclase component distinguishes these symplectites from those observed in the MMIS pods. It is therefore likely that a different process causes formation of these myrmekitic textures. The calcic myrmekitic intergrowths identified by Dymek & Schiffries (1987) were ascribed to corrosive reaction between a magmatically-derived, high-temperature aqueous fluid and cumulate plagioclase crystals, a process referred to as steam corrosion.

The predominant myrmekitic intergrowths observed in the present study consist of sodic plagioclase (An_{17-25}) and quartz, which form between graphic K-feldspar and quartz intergrowths. These 100-400 um-wide films of myrmekite therefore represent true myrmekite, defined as worm-like intergrowths of sodic plagioclase and quartz in contact with potassic feldspar (Phillips 1974). Several different hypotheses relating to the origin of myrmekite have been proposed, ranging from simultaneous crystallisation of plagioclase and quartz, products of various replacement reactions, and hypotheses based on exsolution, such as the exsolution vacancy and exsolution silica-pump models (see review in Phillips 1974; Castle & Lindsley 1993). The most consistent and convincing arguments for the development of myrmekitic intergrowths are described in the models dealing with exsolution of ternary feldspars. During exsolution of a hypersolvus feldspar, excess silica generated by either a hypothetical, high-silica Schwantke molecule ($CaAl_2Si_6O_{16}$; Phillips 1974) or pumping of silica from a reservoir

into the exsolving plagioclase, grows simultaneously with an exsolving feldspar, forming the myrmekitic texture (Phillips 1974). In both of these exsolution scenarios, plagioclase feldspar components and quartz diffuse away from the exsolving K-feldspar and crystallise simultaneously on the edges of the K-feldspar grains to form the observed myrmekites. Observation of myrmekitic textures at the interface between perthite and quartz intergrowths provides the necessary silica-reservoir and supports the notion that these myrmekites formed by diffusion of the necessary components from the perthite. Although these noteworthy myrmekites do not directly support a residual liquid origin for the pods, the relationship to evolved and exsolved ternary feldspars indicates that these pods were late-stage features.

Microscopic orthopyroxene-plagioclase symplectites found between K-feldspar and inverted pigeonite grains in the Fe-rich, Si-poor pod (Figure 5.6c and d; CG09-033) hosted by olivine-bearing anorthosite, show strong resemblance to late-stage replacive 'fish-hook' symplectites described by Holness et al. (2011) in the Skaergaard Intrusion. The formation of these replacive symplectites in the Skaergaard intrusion is related to primocryst reaction with hydrous melt during the late stages of solidification of the intrusion (Holness et al. 2011). Similar processes may have operated in these pods as reactive, late stage fluids alter grain boundary zones. Although no hydrous minerals are observed in these pods, pods from other anorthositic massifs do contain hydrous minerals, such as biotite (pers. comm. C.F. Gower, 2013).

In the context of the pod geochemistry, unusual late-stage textures, the pegmatitic nature of these pods and the severe alteration present, it is clear that these pods represent highly fractionated, late-stage segregations trapped within a viscous crystal mush. Myrmekitic intergrowths between different mineral pairs in all pods may point to an effect of reactive, late-stage fluids in these pods. Trace element modelling of the chemical evolution of the proposed residual liquids of Proterozoic anorthosite magmas presented by McLelland et al. (1994), produces a trend of increasing REE enrichment with transition from positive Eu anomalies in the relatively 'primitive' residual liquids to negative Eu anomalies in the most evolved liquids (Figure 5.12). Three of the sampled pods have REE concentrations that plot within the modelled geochemical evolution of an anorthositic residual liquid. The remaining two pods, displaying the most pronounced graphic, quartz-K-feldspar intergrowths, show similar patterns to the most evolved liquids (negative Eu anomalies, extreme LREE enrichment, concave upwards HREE patterns) but are slightly more enriched than these model liquids.

The very dramatic geochemical, mineralogical and textural differences in the compositions of the pods hosted by orthopyroxene and olivine-bearing anorthosites indicate that the character of the original magmas had an influence on the residual liquids produced. The extent of contamination may also have played a role in differentiating the magmatic compositions of the olivine- vs. orthopyroxene-bearing magmas. Proterozoic anorthosite massifs are considered to be constructed from multiple pulses of crystal-rich magma (Ashwal and Twist 1992). The MMIS could have also been constructed from two or more pulses of magma that are manifest in the two geographically and petrologically distinct massifs: the leucotroctolite-dominant Kenemich massif and leuconorite-dominant Etaugalet massif. Isotopic analyses in this thesis show that the anorthositic and leucotroctolitic samples have higher ε_{Nd} compositions, whilst the samples with higher silica content, i.e. leuconorites, are more evolved. The occurrence of the silica-rich pods in the latter rock types may therefore be expected, whilst the relatively silica-poor magmas differentiate to more mafic, Fe-rich residual liquids as I observe in the sole pod hosted by an olivine-bearing anorthosite. This suggests that compositional differences in

intruding magma mushes may lead to slightly different liquid lines of descent and ultimately, significantly different residual liquids. Further support for the crystallisation of the residual liquids from compositionally different magmas is observed in the different $[La/Sm]_N$ in the pods hosted by pyroxene vs olivine-bearing anorthosite.

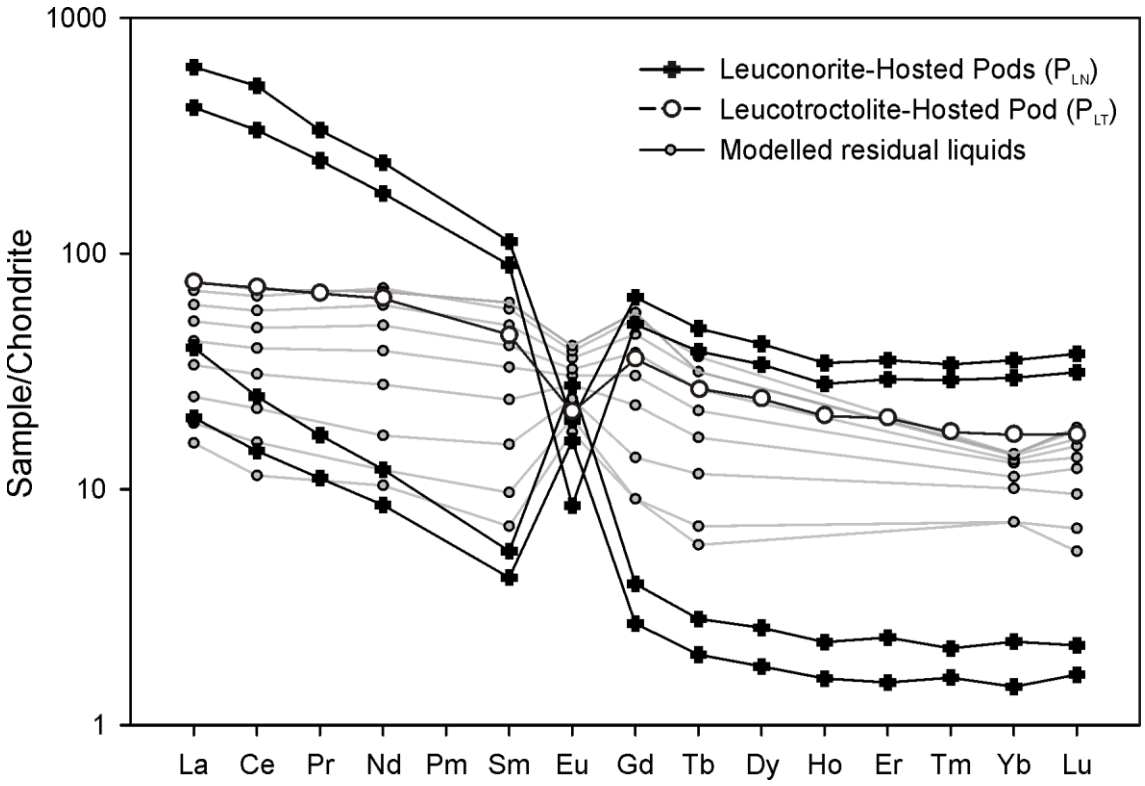

Figure 5.12 Chondrite-normalizsd REE (Anders and Grevesse, 1989) diagram showing the close similarity between modelled residual liquids of anorthositic magmas and the pegmatitic pod compositions. Two of the most mineralogically evolved pods show increased enrichment and display similar pattens with more prominent negative Eu anomalies. The $[La/Sm]_N$ in the pod hosted by leuconorite is noticeably different to the $[La/Sm]_N$ of the modelled residual liquid as well as the pod hosted by an olivine-bearing anorthosite. Light grey patterns with filled circles represent residual liquid concentrations calculated by mass-balance fractionation models in (McLelland et al. 1994).

This fundamental difference is corroborated by U (and Th) concentration data in zircon for the pod hosted by olivine-bearing anorthosite, with low U concentration (<100 ppm U on average) relative to the highly U and Th enriched pods (up to 2000 ppm U) hosted by leuconorites (Appendix F-2). In any event, the character of the residual liquids of Proterozoic anorthosites appear to diverge, on Si- and Fe-enrichment trends, depending on the composition of the magma from which they crystallise; i.e. the residual liquids of relatively silica-rich leuconoritic crystal mushes will form dioritic/jotunitic, and in extreme cases silicic, residual liquids, while the residual liquids of the olivine mushes will form oxide-, apatite-rich gabbronoritic compositions. These observations and interpretations explain the origin of both these rock types in the anorthositic suite.

I ascribe the differing character of the initial magmas to different degrees of crustal contamination during mush ascent, whereby certain magma volumes experience higher degrees of contamination during ascent (and go on to form leuconorites), while other magmas experience less contamination, perhaps because the crustal pathways

have been sealed or preconditioned by anatexis of the earlier magma pulses (and go on to form leucotroctolites). Leucotroctolites have, in many massif-type anorthosites, been observed to show more depleted isotopic signatures than orthopyroxene-bearing anorthosites (Frost et al. 2010; Gleißner et al. 2011; Heinonen et al. 2010a) corroborating the hypothesis that variable contamination during ascent affects the composition of various pulses of magma and ultimately the residual liquids.

A range of rock types, from oxide-apatite-rich gabbro through monzodiorites to monzogranite, have been observed in the pods found in the MMIS. This extreme variation in mineral makeup and chemistry suggests that these pods represent segregations of residual liquid in isolated pockets that evolved to very different compositions. The fundamental difference in chemistry between the pod found in an olivine-bearing lithologic unit and those in the orthopyroxene-bearing anorthosites suggests that the normative magma composition may play an important role in the type of residual liquid observed. Although in many FTP-rich diorite occurrences, the mafic minerals of the host or associated anorthositic rocks is not noted, FTP dikes and pods in the Laramie Anorthosite Complex are associated with the olivine-bearing Poe Mountain massif and have not been reported in association with the pyroxene-bearing, olivine-absent Chugwater and Snow Creek massifs (Mitchell et al. 1996; Frost et al. 2010). This relationship, which must be confirmed in other massifs, suggests a genetic link between olivine-normative magmas and the Fe-enriched, dioritic pods. I propose that olivine-normative magmas, after crystallising vast amounts of plagioclase and olivine, will tend to produce relatively mafic, oxide-rich pods with Fe-enrichment trends similar to the Fe-rich diorites and oxide-apatite gabbronorites observed as residual liquids in many Proterozoic anorthosites. Quartz-normative magmas will produce relatively felsic residual liquids with Si-enrichment trends effectively producing residual liquids such as quartz diorites and monzonorites/jotunites. The wide range in composition of the residual pods in the MMIS shows that extensive, isolated differentiation can produce a spectrum of compositions. I suggest that the range of rock types identified as residual liquids in different anorthosite massifs around the world (monzonorites, jotunite, diorites and oxide-rich gabbronorites) are all, therefore, residual liquids. These observations lead to the proposal that the rock types commonly suggested to represent residual liquids of Proterozoic anorthosite crystallisation are in fact all residual liquids formed from magmas of slightly different compositions and from liquids at differing degrees of differentiation. In other massifs, these rock types occur as dykes and plutons, and occasionally as pods within the anorthosites, but in essence represent residual liquids that have been mobilised and accumulated from similar pod-like structures. Such a range of residual liquids is possible if isolated pods mix during mobilisation or simply evolve in isolation.

Although pods with essentially granitic composition are observed in the MMIS, caution must be excercised before proposing that the extensive, coeval granitic suites associated with Proterozoic anorthosites represent the residual liquids of anorthosite crystallisation (Frost & Frost 2013). Various isotopic and trace element arguments against consanguinity have been proposed (Morse 1982; Ashwal 1993) and the isotopic compositions of the silica-rich pods observed in the MMIS are different to that of the contemporaneous hornblende-biotite granites of the MMIS, further supporting this claim (Figure 5.9; Hegner et al. 2010). The huge volume of associated granites in typical anorthosite suites would be difficult to produce by accumulating such small segregations of highly differentiated, silica-rich material as observed in some of the pods in the MMIS.

5.7 Conclusions

The occurrences of pegmatitic, ferrodioritic to monzogranitic pods or segregations in the Proterozoic Mealy Mountains Intrusive Suite, in combination with conspicuous symplectic and myrmekitic textures, evolved minerals and geochemistry, indicate that these rock types represent the *in situ* crystallisation products of the last remaining liquid in the differentiation of anorthositic magma mushes. With these results I propose that the nature of the residual liquids of Proterozoic anorthosite magmas can vary dramatically depending on geochemical differences in successive magma pulses and by mixing of mobilised, independently-evolved segregations of residual liquids. This process could explain why so many varied rock types associated with Proterozoic anorthosites have been suggested as residual liquids: these rock types all represent residual liquids resulting from varying degrees of differentiation, subsequent mobilisation, mixing and final solidification as plutons or dykes.

6 A Summary – Probing the Petrogenesis of Proterozoic Anorthosites

Coalesced batholithic intrusions, dominated by plagioclase-rich compositions and known as Proterozoic anorthosites are, as the name suggests, restricted to the Proterozoic eon. This temporal restriction (between 1.8 and 1.1 Ga) and many other aspects of anorthosite petrogenesis remain enigmatic, despite decades of research and conjecture. Among these issues, the tectonic setting, source, emplacement mechanisms and hyperfeldspathic compositions are all unresolved issues hampering solution of the ultimate scientific question: what mechanisms were responsible for producing massive volumes of plagioclase-rich magmas over a relatively restricted period of Earth's history? The inherent cumulate nature of these rocks and variable isotopic signatures have hampered progress in unravelling the petrogenesis of the intrusions. In particular, crustal isotopic signatures have led to competing hypotheses proposing that either a mafic, lower crust or depleted mantle may be sources of the magma. Until this issue is resolved, little consensus on the other aspects of Proterozoic petrogenesis, particularly the tectonic setting and temporal restriction, can be achieved. Ultimately, this contribution aims to strip away the effects of crustal contamination and investigate, using high-pressure pyroxene megacrysts, whole-rock anorthosite and internal mineral compositions, the magmatic processes operating from the deep magma sources to final emplacement in the mid-crust.

High-Al megacrysts from the Mealy Mountains Intrusive Suite (MMIS), Nain Plutonic Suite (NPS) and the Rogaland Anorthosite Province (RAP) represent some of the deepest and most primitive, comagmatic components of these classic anorthosite suites. Given this unique provenance, radiogenic isotope analysis offers a means of investigating the early magmatic processes operating close to the source of these magmas. Sr- and Nd-isotopic compositions of megacrysts from the MMIS and RAP suites, which intruded through juvenile, immature crust, are offset from, but track, depleted mantle evolution. Qualitatively this points to magma derivation from the depleted mantle, followed by lower crustal assimilation. Predictably, megacrysts from the NPS, where the likely crustal contaminants are old and evolved, show more evolved, negative ε_{Nd} isotopic compositions. Using lower crustal compositions (where available), EC-AFC modelling of a depleted mantle-derived melt is able to reproduce the isotopic compositions observed in the megacryst suites as well as the host anorthosites. Therefore, using more realistic models that balance thermal and chemical components quantitatively indicates that depleted mantle is the source for Proterozoic anorthosites. However, the increased complexities of the models require that more assumptions have to be made regarding chemical and thermal parameters in scenarios where there are fewer constraints on these parameters. This inevitably means that less favourable conditions are required to reproduce the required compositions. These issues highlight the complexities involved in Proterozoic anorthosite petrogenesis, but where parameters are well constrained, models indicate the derivation of the melts from melting of the depleted mantle is plausible and likely, given the other lines of evidence presented in this thesis.

Sm-Nd geochronology for subsets of high-Al megacrysts show that these phases crystallised 110-130 m.y. before host anorthosite emplacement at mid- to upper-crustal levels. I show through time-integrated AFC

modelling that these ages, obtained from isochronous arrays of megacrysts, are not the result of initial variations in the isotopic composition of the magma forming the megacrysts, but represent true crystallisation ages. These results indicate that the magmatic system producing these megacrysts is long-lived. Although many different tectonic settings have been proposed for the formation of Proterozoic anorthosites, the geochronological constraints presented in this thesis place limits on the types of settings that can reasonably be expected to form these intrusives. Commonly proposed rift or anorogenic settings, particularly in continental settings, are unlikely to produce the geographically-localised magmatism for such long periods without initiating continental break-up or opening oceanic basins. The long magmatic timescales also suggest that the late- to post-orogenic magmatism in convergent settings cannot fully explain the formation of anorthosites, as magma-forming mechanisms in these scenarios are relatively short-lived (10-30 m.y.). The only setting, therefore, capable of delivering sufficient, geographically-focused quantities of magma (and heat) to the base of the crust on 100 m.y. timescales is an Andean-arc setting. Ascribing anorthosite petrogenesis to this tectonic setting reconciles observed features of these massifs, such as long, linear arrays of anorthosites (e.g. Grenville Province, Eastern Ghats Belt) and metamorphic overprinting during eventual Himalayan-style continent-continent collision.

Proterozoic anorthosites, consisting of over 80 % plagioclase and derived from a broadly basaltic magma, are missing a significant mafic component (30-40 %). In a similar manner, the continental crust, that is thought to be derived from basaltic magmas in arc environments, but has bulk SiO_2 contents of 60 wt %, is also missing a mafic component. The mechanisms producing this compositional discrepancy are poorly understood, mainly because any evidence for potential processes remains trapped at upper mantle to lower crustal depths. Proterozoic anorthosites are therefore useful proxies for this continental crust paradox and are particularly insightful because the viscous, plagioclase-rich magmas entrain samples of differentiation - high-pressure mafic megacrysts from Moho depths – where major crustal differentiation is thought to occur. As described above, the isotopic composition of these megacrysts shows that they formed in a fractionating magma that received minor lower crustal contamination and/or little compositionally-distinct magmatic recharge or contamination, in ponding magma at the Moho. MELTS modelling, using likely parental magma compositions for the anorthosites, illustrates that mafic phases, similar to these megacrysts, would sink in both the magma and surrounding mantle. These observations and models show that mafic cumulate formation and sequestration at the Moho is a significant mechanism of crustal differentiation in crust-forming environments, contributing to the mass balance problem observed for bulk crustal compositions. It is vital that this mechanism of crustal differentiation be given important consideration in future models dealing with the continental crust paradox, recycling with the Earth and compositional evolution of Earth's crust.

Analysis of high-pressure megacrysts, whole-rock anorthosite compositions and internal mineral phases provides important information regarding processes operating throughout the polybaric petrogenetic history of Proterozoic massif-type anorthosites. Megacrysts from different crustal terranes consistently plot at the upper end of the anorthosite Nd-isotopic spectrum and still preserve the dramatic differences in isotopic geochemistry that characterise the anorthositic suites from different crustal terranes. This overlap indicates that lower crustal assimilation in the anorthositic magmas plays an important role in developing the isotopic signature of the magmas that initially crystallise the megacrysts, but that also go on to crystallise the anorthosites at shallower crustal levels. Given the polybaric petrogenesis of Proterozoic anorthosites and the need to develop significant

amounts of plagioclase at Moho depths (to facilitate magma ascent to upper crustal levels) one would expect plagioclase to be more isotopically primitive than intercumulus orthopyroxene from the anorthosites. Analysis of isotopic disequilibrium indicates that this is not always the case and that on average, orthopyroxene is more primitive than plagioclase for a given time-integrated whole-rock reference value. I suggest that these counter-intuitive internal isotopic compositions result from a significant proportion of crystallisation occurring at lower crustal levels, before the magmas had the opportunity to ascend through more evolved crustal material. This assertion implies that these very crystal-rich mushes (~ >50 % crystallinity), which formed at lower crustal levels, rose diapirically as immobile, incredibly viscous fluids. The rise of effectively solid-state diapirs does occur and has been modelled numerically. Many of the fabrics developed in these models compare favourably with the deformation and strain observed in some Proterozoic anorthosite massifs.

The final stages of anorthosite petrogenesis have also attracted controversy in the past with considerable debate surrounding the composition of residual liquids in this system. Several rock types intimately associated with the anorthosites have been proposed, including Fe-Ti-P-rich samples like diorite, ferrodiorites, monzonorite, jotunite and oxide-apatite-rich gabbronorites. Mineralogically and geochemically diverse pegmatitic pods or segregations preserved *in situ* within the anorthosites of the Mealy Mountains Intrusive Suite display a unique set of textures, including graphic intergrowths, magmatic and fluid replacement features, as well as replacive/exsolution myrmekitic intergrowths. Along with significant geochemical enrichment of incompatible elements (10-1000 times chrondrite) and derivitive minerals (e.g. apatite, zircon), the location and textures observed in the pods suggest that these pods are late-stage, fluid-bearing residual liquids of the anorthosites. Using observed mineral composition and normative calculations; these pods show a range of rock types from monzogranite through quartz-monzodiorite and monzodiorite to Fe-P-rich gabbronorite. Significant petrologic and geochemical differences between pods preserved in orthopyroxene vs. olivine-bearing anorthosites suggest that the original magma composition and degree of crustal contamination influence the composition of the residual liquid. Isolation and/or mixing of these chemically diverse residual compositions could also accentuate the diversity observed in residual liquid compositions. I infer that the residual liquids observed in other anorthosite massifs as plutons and dykes, represent residual magmas in anorthosites that were mobilised and accumulated from similar pod-like segregations. This process could explain why so many varied rock types associated with Proterozoic anorthosites have been suggested as residual liquids: these rock types all represent residual liquids resulting from varying degrees of differentiation, subsequent mobilisation, mixing and final solidification as plutons or dykes.

Crustal contamination has been shown to play an important role in developing the chemical signatures observed in Proterozoic anorthosites. Models of anorthosite genesis have postulated where this contamination may take place, but detailed isotopic work in this thesis shows that the most significant contamination occurs while the magmas are ponded at the Moho and assimilating lower-crustal material. Lower-crustal contamination is therefore a crucial process in the petrogenesis of these magmas and may be as important for magmas generated in other settings. Although the traces of this contaminant are apparent in isotopic data and mineral makeup, even in juvenile terranes, care must be taken in making assertions regarding the petrogenesis of the anorthosites using simplified models and modelling techniques (e.g. traditional AFC models). Based on evidence presented in this thesis, the Proterozoic anorthosite system involves the interplay of many different igneous processes occurring

at a range of depths and so any model hoping to realistically describe the petrogenesis needs to carefully tease apart these polybaric processes.

In this thesis, I also provide new and compelling evidence showing that Proterozoic anorthosites are derived from melting of the depleted mantle in convergent, Andean-arc settings. Assumptions of upper crustal contamination and simple AFC modelling have led previous researchers to argue against depleted mantle derivation, but these assumptions prove to be too simplistic in what, from the evidence presented herein, is a complex, multi-faceted, polybaric petrogenetic history. Recognising and stripping away the effects of significant lower-crustal contamination as well as polybaric AFC, through energy-constrained AFC modelling, allows a much clearer view of the depleted mantle source. This, together with long magmatic histories, indicates that these anorthosites must have formed in convergent arc settings – the only settings able to supply the base of the crust with sufficient, geographically-localised magma and heat for over 100 million years. However, this long-lived Proterozoic magmatic system contrasts with recent research suggesting that the duration of magma ascent from the Moho to surface (35 km; Irazú volcano, Costa Rica) is on the order of months to years (Ruprecht & Plank 2013).

The 100 m.y. timescales observed in these anorthosite systems, together with correlations of regional magmatic arc activity and orogenic decline/collapse, do however make sense when considered alongside the evidence for significant magmatic differentiation at Moho/lower crustal levels and ascent of positively buoyant, high-crystallinity (> 50 %), super-saturated plagioclase diapirs. Long periods of magma ponding, recharge and lower-crustal assimilation may be vital aspects required for the development the plagioclase-rich assemblages observed in Proterozoic anorthosite massifs. Magma ponding and recharge would not only facilitate the mechanical accumulation of buoyant plagioclase and possibly the remelting or resorption of plagioclase, but the associated lower crustal anatexis may also promote the development of hyper-feldspathic magmas (Wiebe 1990). The ascent of high-crystallinity diapirs may, in itself, play a role in the long timescales observed in Proterozoic anorthosite massifs. Although I have observed that the onset of anorthositic magmatism coincides with orogenic activity in two of the three regions investigated, mid-crustal anorthosite emplacement coincides with the waning stages of orogeny and orogenic collapse. Therefore, although I argue that Proterozoic anorthosites are products of Andean-arc-type magmatism, the extensional stress regimes often associated with the waning stages of orogeny may be crucial in allowing these extremely viscous magma/bodies to rise as immobile diapirs from the lower crust to mid-crustal levels. Contrasting timescales for magmatism in the Proterozoic (this study) compared with some modern-day arc volcanoes (Ruprecht & Plank 2013) hints at non-uniformitarian processes at work in the subduction regime over time and/or suggests that there may be a continuum of magma ascent rates in arcs with Proterozoic anorthosite ascent rates representing the slowest end of the spectrum.

The ultimate frontier in Proterozoic anorthosite research now lies in understanding the temporal restriction of these intrusive rocks. The assertion that these massifs formed in Andean-arc settings dictates that either similar anorthosites are forming today, or subduction mechanisms, for a large part of the Proterozoic, favoured the production of large volumes of plagioclase with intermediate An contents. The absence of any modern-day "Proterozoic-type" anorthosites argues against a uniformitarian hypothesis, although we should continue to explore for them in the roots of young Andean arcs. The occurrence of anorthosite xenoliths, albeit of different

compositions, in arc volcanics (Ashwal 1993) suggests that these rock types are being formed in the deep roots of arcs today, but that characteristics, like water content, pressure and subduction-style, may be different – an inherently non-uniformitarian view. These questions highlight how understanding this final frontier in anorthosite petrology promises to shed new light on hitherto unknown aspects of Earths crust formation and geodynamic evolution in the Proterozoic eon.

7 References

Amelin, Y., Li, C. & Valeyev, O., 2000. Nd-Pb-Sr Isotope Systematics of Crustal Assimilation in the Voisey's Bay and Mushuau Intrusions, Labrador, Canada. *Economic Geology*, **95**, pp. 815-830.

Anders, E. & Grevesse, N., 1989. Abundances of the elements: Meteoritic and solar. *Geochimica et Cosmochimica Acta*, **53**, pp. 197-214.

Andersen, T. & Griffin, W.L., 2004. Lu–Hf and U–Pb isotope systematics of zircons from the Storgangen intrusion, Rogaland Intrusive Complex, SW Norway: implications for the composition and evolution of Precambrian lower crust in the Baltic Shield. *Lithos*, **73**, pp. 271-288.

Anderson, A.T., Jr, 1966. Mineralogy of the Labrieville anorthosite, Quebec. *Am. Mineral*, **51**, pp. 1671-1711.

Artemieva, I., 2011. *The Lithosphere: An Interdisciplinary Approach* (Cambridge Univ Press)

Ashwal, L., 1982. Mineralogy of mafic and Fe-Ti oxide-rich differentiates of the Marcy anorthosite massif, Adirondacks, New York. *American Mineralogist*, **67**, pp. 14-27.

Ashwal, L., 1993. *Anorthosites* (Springer-Verlag, 1993)

Ashwal, L.D., 2004. Origin of Anorthosites: Petrological and Tectonic Considerations. *AGU Spring Meeting Abstracts*, **#V51E-04**.

Ashwal, L.D., 2010. The Temporality of Anorthosites. *Canadian Mineralogist*, **48**, pp. 711-728.

Ashwal, L.D. & Seifert, K.E., 1980. Rare-earth-element geochemistry of anorthosite and related rocks from the Adirondacks, New York, and other massif-type complexes: Summary. *Geological Society of America Bulletin*, **91**, pp. 105.

Ashwal, L.D., Twist, D., 1994. The Kunene complex, Angola/Namibia: a composite massif-type anorthosite complex. *Geological Magazine*, **131**, pp. 579-591.

Ashwal, L.D. & Wiebe, R.A., 1989. Isotopic disequilibrium in the internal Sm-Nd and Rb-Sr systematics of Proterozoic anorthosites. EOS **70**: 486.

Ashwal, L.D. & Wooden, J.L., 1983. Isotopic evidence from the eastern Canadian shield for geochemical discontinuity in the Proterozoic mantle. *Nature*, **306**, pp. 679-680.

Ashwal, L.D. & Wooden, J.L., 1989. River Valley pluton, Ontario: A late-Archean/early-Proterozoic anorthositic intrusion in the Grenville Province. *Geochimica et Cosmochimica Acta*, **53**, pp. 633-641.

Ashwal, L., Wooden, J. & Emslie, R., 1986. Sr, Nd and Pb isotopes in Proterozoic intrusives astride the Grenville Front in Labrador: Implications for crustal contamination and basement mapping. *Geochimica et Cosmochimica Acta*, **50**, pp. 2571-2585.

Bédard, J.H., 2001. Parental magmas of the Nain Plutonic Suite anorthosites and mafic cumulates: a trace element modelling approach. *Contributions to Mineralogy and Petrology*, **141**, pp. 747-771.

Bingen, B., et al., 2005. Timing of continental building in the Sveconorwegian orogen, SW Scandinavia. *Norwegian Journal of Geology*, **85**, pp. 87-116.

Bédard, J.H., 2010. Parental magmas of Grenville Province massif-type anorthosites, and conjectures about why massif anorthosites are restricted to the Proterozoic. *In*: Earth and Environmental Science Transactions of the Royal Society of Edinburgh, **100,** pp. 77-103.

Berg, J.H., 1969. Petrology of anorthosites of the Bitterroot Range, Montana. *In:* Isachsen, Y.W. (eds), *Origin of anorthosite and related rocks*, **Memoir 18**, New York State Museum and Science Service, pp. 387-398.

Berg, J.H., 1977. Regional Geobarometry in the Contact Aureoles of the Anorthositic Nain Complex, Labrador. *Journal of Petrology*, **18**, pp. 399-430.

Bertrand, J.-M., Van Kranendonk, M., Hanmer, S., Roddick, C., (1990). Structural and metamorphic geochronology of the Torngat Orogen in the North River - Nutak transect area, Labrador: Preliminary results of U-Pb dating. *Geoscience Canada*, **17**, pp. 297-301.

Bingen, B., Nordgulen, Ø., Viola, G., 2008. A four-phase model for the Sveconorwegian orogeny, SW Scandinavia. *Norwegian Journal of Geology*, **88**, pp. 43-72.

Bogdanova, S.V., et al., 2008. The East European Craton (Baltica) before and during the assembly of Rodinia. *Precambrian Research*, **160**, pp. 23-45.

Bohlen, S. & Essene, E., 1978. Igneous pyroxenes from metamorphosed anorthosite massifs. *Contributions to Mineralogy and Petrology*, **65**, pp. 433-442.

Bohrson, W.A & Spera, F., 2001. Energy-Constrained Open-System Magmatic Processes II: Application of Energy-Constrained Assimilation-Fractional Crystallization (EC-AFC) Model to Magmatic Systems. *Journal of Petrology*, **42**, pp. 1019-1041.

Bohrson, W.A. & Spera, F., 2003. Energy-constrained open-system magmatic processes IV: Geochemical, thermal and mass consequences of energy-constrained recharge, assimilation and fractional crystallization (EC-RAFC). *Geochemistry Geophysics Geosystems*, **4**.

Bowen, N.L., 1917. The Problem of Anorthosites. *The Journal of Geology*, **25**, pp. 209-243.

Bowen, N.L., 1928. The evolution of the igneous rocks. Dover, New York, 332 p.

Bridgewater, D. & Windley, B.F., (1973). Anorthosites, post-orogenic granites, acid volcanic rocks and crustal development in the North Atlantic Shield during the mid-Proterozoic. *Geological Society of South Africa Special Publication*, **3**, pp. 307-317.

Buddington, A.F., 1939. Adirondack igneous rocks and their metamorphism. *Geological Society of America Memoir*, **7**, 343 p.

Bussy, F., Wardle, R.J., Krogh, T.E., 1995. Late Labradorian metamorphism and anorthosite-granitoid intrusion, Cape Caribou River Allochthon, Grenville Province, Labrador; evidence from U-Pb geochronology. *Canadian Journal of Earth Sciences*, **32**, pp. 1411-1425.

Carlson, R.W. et al., 2006. A comparison of Siberian meimechites and kimberlites: Implications for the source of high-Mg alkalic magmas and flood basalts. *Geochemistry Geophysics Geosystems*, **7**.

Castle, R.O. & Lindsley, D.H., 1993. An exsolution silica-pump model for the origin of myrmekite. *Contributions to Mineralogy and Petrology*, **115**, pp. 58-65.

Charlier, B., Duchesne, J.-C., Vander Auwera, J., 2006. Magma chamber processes in the Tellnes ilmenite deposit (Rogaland Anorthosite Province, SW Norway) and the formation of Fe-Ti ores in massif-type anorthosites. *Chemical Geology*, **234**, pp. 264-290.

Charlier, B. et al., 2010. Polybaric Fractional Crystallization of High-alumina Basalt Parental Magmas in the Egersund-Ogna Massif-type Anorthosite (Rogaland, SW Norway) Constrained by Plagioclase and High-alumina Orthopyroxene Megacrysts. *Journal of Petrology*, **51**, pp. 2515-2546.

Clemens, J.D. & Mawer, C.K., 1992. Granitic magma transport by fracture propagation. *Tectonophysics*, **204**, pp. 339-360.

Conrad, W.K. & Kay, R.W., 1984. Ultramafic and Mafic Inclusions from Adak Island: Crystallization History, and Implications for the Nature of Primary Magmas and Crustal Evolution in the Aleutian Arc. *Journal of Petrology*, **25**, pp. 88-125.

Corrigan, D. & Hanmer, S., 1997. Anorthosites and related granitoids in the Grenville orogen: A product of convective thinning of the lithosphere? *Geology*, **25**, pp. 61-64.

Cox, K.G., Bell, J.D. & Pankhurst, R.J., 1979. *The Interpretation of Igneous Rocks* 1st Ed, (Hyman, London, 1979).

Cruden, A.R., 1990. Flow and fabric development during the diapiric rise of magma. *Journal of Geology*, **98**, pp. 681-698.

Davidson, J.P., Tepley III, F.J., 1997. Recharge in Volcanic Systems: Evidence from Isotope Profiles of Phenocrysts. *Science* **275**, 826-829

Davidson, J.P et al., 2005a. Mineral isochrons and isotopic fingerprinting: Pitfalls and promises. *Geology*, **33**, pp. 29-32.

Davidson, J.P., Hora, J.M., Garrison, J.M., Dungann, M.A., 2005b. Crustal forensics in arc magmas. *Journal of Volcanology and Geothermal Research*, **140**, pp. 157-170.

Davidson, J.P., Morgan, D.J. & Charlier, B.L.A., 2007a. Isotopic microsampling of magmatic rocks. *Elements*, **3**, pp. 253-259.

Davidson, J.P., Morgan, D.J., Charlier, B.L.A., et al., 2007b. Microsampling and Isotopic Analysis of Igneous Rocks: Implications for the Study of Magmatic Systems. *Annual Review of Earth and Planetary Sciences*, **35**, pp. 273–311.

DeCelles, P.G. et al., 2009. Cyclicity in Cordilleran orogenic systems. *Nature Geoscience*, **2**, pp. 251-257.

del Potro, R., Diez, M., Blundy, J., Camacho, A.G., Gottsmann, J., 2013. Diapiric ascent of silicic magma beneath the Bolivian Altiplano. *Geophysical Research Letters*, **40**, pp. 2044-2048.

Demaiffe, D. & Hertogen, J., 1981. Rare-Earth Element Geochemistry and Strontium Isotopic Composition of a Massif-Type Anorthositic-Charnockitic Body - the Hidra-Massif (Rogaland, SW Norway). *Geochimica et Cosmochimica Acta*, **45**, pp. 1545–1561.

DePaolo, D., 1981. Trace element and isotopic effects of combined wallrock assimilation and fractional crystallization. *Earth and Planetary Science Letters*, **53**, pp. 189-202.

DePaolo, D., Wasserburg, G.J., 1976. Inferences about magma sources and mantle structure from variations of $^{143}Nd/^{144}Nd$. *Geophysical Research Letters*, **3**, pp. 743-746.

de Waard, D. & Romey, W.D., 1969. Chemical and petrologic trends in the anorthosite-charnockite series of the Snowy Mountain massif, Adirondack Highlands. *American Mineralogist*, **54**, pp. 529-538.

Downes, H. & Dupuy, C., 1990. Crustal evolution of the Hercynian belt of Western Europe: Evidence from lower-crustal granulitic xenoliths (French Massif Central). *Chemical Geology*, **79**, pp. 195-218.

Drueppel, K., Franke, H., Brandt. S., 2008. High-grade metamorphism and partial melting of granuite facies para- and orthogneisses surrounding the Rogaland Complex, Norway. *In:* International Geological Congress, **33**, Oslo.

Ducea, M., 2001. The California arc: Thick granitic batholiths, eclogitic residues, lithospheric-scale thrusting, and magmatic flare-ups. *GSA today*, **11**, pp. 4-10.

Duchesne, J.-C., 1984. Massif anorthosites: another partisan review. *In:* Feldspars and Feldspathoids, *NATO*

ASI, pp. 411-433.

Duchesne, J.-C., 1985. The Rogaland anorthosites: facts and speculations. *In:* Tobi, A.C., Touret, J.L.R. (eds) The deep Proterozoic crust in the North Atlantic Provinces. *NATO ASI*, Ser C, 158. Reidel, Dordrecht, pp. 449-476.

Duchesne, J.-C., 2001. Anorthosites: the lower crustal connection. *EUROPROBE*, 1-4 November 2011, St Petersburg.

Duchesne, J.-C. et al., 1999. The crustal tongue melting model and the origin of massive anorthosites. *Terra Nova*, **11**, pp. 100-105.

Dymek, R. & Gromet, L., 1984. Nature and origin of orthopyroxene megacrysts from the St-Urbain anorthosite massif, Quebec. *The Canadian Mineralogist*, **22**, pp. 297-326.

Dymek, R. & Owens, B., 2001. Petrogenesis of apatite-rich rocks (nelsonites and oxide-apatite gabbronorites) associated with massif anorthosites. *Economic Geology and the Bulletin of the Society of Economic Geologists*, **96**, pp. 797-815.

Dymek & Schiffries, C.M., 1987. Calcic myrmekite: Possible evidence for the involvement of water during the evolution of andesine anorthosite from St-Urbain, Quebec. *Canadian Mineralogist*, **25**, pp. 291-319.

Elsaesser, L., Drueppel, K., Gerdes, A., 2008. Metamorphic evolution of saphirine-granulites from Rogaland, Norway: evidence from in-situ LA-ICPMS geochronology of mineral reactions combined with calculated P-T-x phase diagrams. *In:* International Geological Congress, **33**, Oslo.

Emslie, R.F., 1975a. Pyroxene megacrysts from anorthositic rocks: New clues to the sources and evolution of the parent magmas. *Canadian Mineralogist*, **13**, pp. 138-145.

Emslie, R.F., 1975b. Major rock units of the Morin Complex, Southwestern Quebec. *Geological Survey of Canada Paper*, **74-48**, 37 p.

Emslie, R.F., 1976. Mealy Mountains complex, Grenville Province, southern Labrador. *In:* Current Research, Part A. *Geological Survey of Canada Paper*, **76-1A**, pp. 165-170.

Emslie, R.F., 1978. Anorthosite massifs, rapakivi granites, and late proterozoic rifting of north America. *Precambrian Research*, **7**, pp. 61-98.

Emslie, R.F. & Bonardi, M., 1979. Anorthositic massifs and associated rocks of the Mealy Mountains Complex, Grenville Province, southern Labrador. *GACMAC 1979.*

Emslie, R.F., 1980. Geology and petrology of the Harp Lake Complex, Central Labrador: an example of Elsonian magmatism. *Geological Survey of Canada Bulletin*, **293**, 136 p.

Emslie, R.F., 1983. Igneous and tectonothermal evolution, Mealy Mountains, Labrador. *GACMAC 1983.*

Emslie, R.F., 1985. Proterozoic Anorthosite Massifs. *In*: A. C. Tobi & J. L. R. Touret, (eds.) Dordrecht: Springer Netherlands, pp. 39–60.

Emslie, R.F., 1990. Ages and Petrogenetic Significance of Igneous Mangerite-Charnockite Suites Associated with Massif Anorthosites, Grenville Province. *The Journal of Geology*, **98**, pp. 213-231.

Emslie, R., Hamilton, M. & Theriault, R., 1994. Petrogenesis of a Mid-Proterozoic Anorthosite-Mangerite-Charnockite-Granite (AMCG) Complex: Isotopic and Chemical Evidence from the Nain Plutonic Suite. *The Journal of Geology*, **102**, pp. 539-558.

Emslie, R.F. & Hegner, E., 1993. Reconnaissance isotopic geochemistry of anorthosite mangerite-charnockite-granite (AMCG) complexes, Grenville Province, Canada. *Chemical Geology*, **106**, pp. 279-298.

Emslie, R.F. & Hunt, P.A., 1990. Ages and petrogenetic significance of igneous mangerite-charnockite suites associated with massif anorthosites, Grenville Province. *Journal of Geology*, **98**, pp. 213-232.

Emslie, R.F. & Loveridge, W.D., 1992. Fluorite-bearing early and middle proterozoic granites, Okak Bay area, labrador: Geochronology, geochemistry and petrogenesis. *Lithos*, **28**, pp. 87-109.

Emslie, R.F., Loveridge, W.D., Stevens, R.D., Sullivan, R.W., 1983. Igneous and tectonothermal evolution, Mealy Mountains, Labrador. *Geological Association of Canada Program Abstracts*, **8**, A-20.

Ersoy, Y. & Helvacı, C., 2010. FC-AFC-FCA and mixing modeler: A Microsoft® Excel© spreadsheet program for modeling geochemical differentiation of magma by crystal fractionation. *Computers and Geosciences*, **36**, pp. 383-390.

Faure, G., & Mensing, T.M., 2005. Isotopes: Principles and Applications. 3rd Ed. John Wiley and Sons.

Fram, M. & Longhi, J., 1992. Phase-Equilibria of Dikes Associated with Proterozoic Anorthosite Complexes. *American Mineralogist*, **77**, pp. 605-616.

Frost, C.D. & Frost, B.R., 2013. Proterozoic ferroan feldspathic magmatism. *Precambrian Research*, **228**, pp. 151-163.

Frost, C.D. et al., 2010. Geochemical and Isotopic Evolution of the Anorthositic Plutons of the Laramie Anorthosite Complex: Explanations for Variations in Silica Activity and Oxygen Fugacity of Massif Anorthosites. *Canadian Mineralogist*, **48**, pp. 925-946.

Ghiorso, M.S. & Sack, R.O., 1995. Chemical mass transfer in magmatic processes IV. A revised and internally consistent thermodynamic model for the interpolation and extrapolation of liquid-solid equilibria in magmatic systems at elevated temperatures and pressures. *Contributions to Mineralogy and Petrology*, **119**, pp. 197-212.

Gleißner, P., 2011, Petrogenesis of anorthosites of the Mesoproterozoic Kunene Intrusive Complex, NW Namibia: evidence from stable and radiogenic isotope and lithophile and highly siderophile trace element composition. *PhD Dissertation*, Technischen Universität Berlin.

Gleißner, P., Drueppel, K. & Romer, R.L., 2011. The role of crustal contamination in massif-type anorthosites, new evidence from Sr-Nd-Pb isotopic composition of the Kunene Intrusive Complex, NW Namibia. *Precambrian Research*, **185**, pp.18–36.

Gower, C.F., 1996. The evolution of the Grenville Province in eastern Labrador, Canada. *In:* Precambrian Crustal Evolution in the North Atlantic Region, Brewer, T.S., (Ed). *Geological Society Special Publication*, **112**, pp. 197-218.

Gower, C.F., 2010a. Geology of the English River area (NTS sheets 13G/09, 10, 15 and 16), southeastern Labrador. Geological Survey, Mines Branch, Department of Natural Resources, Government of Newfoundland and Labrador, Map 2010-10, Open File 013G/0055.

Gower, C.F., 2010b. Geology of the Southeast Mealy Mountains area (NTS sheets 13G/01, 02, 07 and 08), southeastern Labrador. Geological Survey, Mines Branch, Department of Natural Resources, Government of Newfoundland and Labrador, Map 2010-14, Open File 013G/0057.

Gower, C.F. and Erdmer, P., 2010: Geology of the Lake Melville area (NTS sheets 13G/11, 12, 13 and 14), southeastern Labrador. Geological Survey, Mines Branch, Department of Natural Resources, Government of Newfoundland and Labrador, Map 2010-09, Open File 013G/0054.

Gower, C.F., Kamo, S. & Krogh, T.E., 2008a. Indentor tectonism in the eastern Grenville Province. *Precambrian Research*, **167**, pp. 201-212.

Gower, C.F., Kamo, S.L., Kwok, K., et al., 2008b. Proterozoic southward accretion and Grenvillian orogenesis in the interior Grenville Province in eastern Labrador: Evidence from U-Pb geochronological investigations. *Precambrian Research*, **165**, pp. 61-95.

Gower, C.F. & Krogh, T.E., 2002. A U–Pb geochronological review of the Proterozoic history of the eastern Grenville Province. *Canadian Journal of Earth Sciences*, **39**, pp. 795-829.

Gower, C.F., Krogh, T.E., 2003. A geochronological review of the pre-Labradorian and Labradorian geological history of the eastern Grenville Province. *Ministère des Ressources naturelles*, Québec, DV 2003-3

Gower, C.F. & Nunn, G.A.G., 2010: Geology of the Kenemich River area (NTS sheets 13G/03, 04, 05 and 06), southeastern Labrador. Geological Survey, Mines Branch, Department of Natural Resources, Government of Newfoundland and Labrador, Map 2010-13, Open File 013G/0056.

Gower, C.F., Schärer, U., Heaman, L.M., 1992. The Labradorian Orogeny in the Grenville Province, eastern Labrador. *Canadian Journal of Earth Sciences*, **29**, pp. 1944-1957.

Gutscher, M.-A. et al., 2000. Can slab melting be caused by flat subduction? *Geology*, **28**, pp. 535-538.

Hamilton M. A., Emslie R. F., and Roddick J. C. 1994. Detailed emplacement chronology of basic magmas of the mid-Proterozoic Nain Plutonic Suite, Labrador 8th ICOG, USGS Circular 1107, 124.

Hamilton, M.A. 2008. Geochronological synopsis of the Nain Plutonic Suite, Labrador: Age variations, patterns of AMCG magmatism, and Gardar connections revisited. GAC-MAC Annual Meeting 2008.

Hamilton, W.B. 1981. Crustal evolution by arc magmatism. *In:* Moorbath, S., Windley, BF (Eds) The origin and evolution of Earth's continental crust. *Philosophical Transactions of the Royal Society of London*, **301**, pp. 279-291.

Hegner, E. et al., 2010. Sources of the Mealy Mountains and Atikonak River Anorthosite-Granitoid Complexes, Grenville Province, Canada. *Canadian Mineralogist*, **48**, pp. 787-808.

Heinonen, A. et al., 2010. Formation and fractionation of high-Al tholeiitic magmas in the Ahvenisto Rapakivi Granite Massif-type anorthosite complex, SE Finland. *The Canadian Mineralogist*, **48**, pp. 969-990.

Heinonen, J.S., Carlson, R.W. & Luttinen, A.V., 2010. Isotopic (Sr, Nd, Pb, and Os) composition of highly magnesian dikes of Vestfjella, western Dronning Maud Land, Antarctica: A key to the origins of the Jurassic Karoo large igneous province? *Chemical Geology*, **277**, pp. 227-244.

Hervé, F. et al., 2007. The South Patagonian batholith: 150 my of granite magmatism on a plate margin. *Lithos*, **97**, pp. 373-394.

Hoffman, P., 1989. Speculations on Laurentia's first gigayear (2.0 to 1.0 Ga). *Geology*, **17**, pp. 135-138.

Holness, M.B. et al., 2011. Silicate Liquid Immiscibility within the Crystal Mush: Late-stage Magmatic Microstructures in the Skaergaard Intrusion, East Greenland. *Journal of Petrology*, **52**, pp. 175-222.

Hughes, C.J., 1972. Note on the Variability of Granophyric Texture. *Geological Society of America Bulletin*, **83**, pp. 2419-2422.

Icenhower, J., Dymek, R. & Weaver, B., 1998. Evidence for an enriched mantle source for jotunite (orthopyroxene monzodiorite) associated with the St. Urbain anorthosite, Quebec. *Lithos*, **42**, pp. 191-212.

Jaffey, A.H., Flynn, K.F., Glendenin, L.E., Bentley, W.C. and Essling, A.M. 1971. Precision measurement of half-lives and specific activities of ^{235}U and ^{238}U. *Physical Review*, **4**, pp. 1889-1906.

Jagoutz, O. et al., 2006. Lower continental crust formation through focused flow in km-scale melt conduits: The zoned ultramafic bodies of the Chilas Complex in the Kohistan island arc (NW Pakistan). *Earth and Planetary Science Letters*, **242**, pp. 320-342.

Jagoutz, O. et al., 2011. The roles of flux- and decompression melting and their respective fractionation lines for continental crust formation: Evidence from the Kohistan arc. *Earth and Planetary Science Letters*, **303**, pp. 25-36.

Jagoutz, O. & Schmidt, M.W., 2012. The formation and bulk composition of modern juvenile continental crust: The Kohistan arc. *Chemical Geology*, **298-299**, pp. 79-96.

James, D.T., & Connelly, J.N., 1995. Geology of the Paleoproterozoic Blueberry Lake Group, Grenville Province, western Labrador. *In:* Current Research. Department of Natural Resources, Geological Survey Branch, **95-1**, pp. 25-36.

Jull, M. & Keleman, P.B., 2001. On the conditions for lower crustal convective instability. *Journal of Geophysical Research*, **106**, pp. 6423-6446.

Kay, R.W. & Kay, S.M, 1991. Creation and desctruction of lower continental crust. *Geologische Rundschau*, **80**, pp. 259-278.

Kay, R.W. & Kay, S.M., 1993. Delamination and delamination magmatism. *Tectonophysics*, **219**, pp. 177-189.

Kerr, A., 1989. Geochemistry of the Trans-Labrador granitoid belt, Canada. A quantitative comparative study of a Proterozoic batholith and possible Phanerozoic counterparts. *Precambrian Research*, **45**, pp. 1-17.

Krogh, T.E. 1973. A low contamination method for hydrothermal decomposition of zircon and extraction of U and Pb for isotopic age determinations. Geochimica et Cosmochimica Acta, **37**, pp. 485-494.

Kushiro, I. & Fuji, T., 1977. Floatation of plagioclase in magma at high pressures and its bearing on the origin of anorthosite. Procedings of the Japanese Academy of Science, **53**, pp. 262-266

Kushiro, I., 1980. Viscosity, density, and structure of silicate melts at high pressures, and their petrological applications. *In:* Hargraves R.B. (ed.) Physics of magmatic processes. Princeton University Press, Princeton, NJ, p. 93-120.

Larsson, D. et al., 2002. Hydrothermal alteration of plagioclase and growth of secondary feldspar in the Hengill Volcanic Centre, SW Iceland. *Journal of volcanology and geothermal research*, **114**, pp. 275-290.

Le Roux, A.P., Späth, A. & Zartman, R.E., 2001. Lithospheric thickness beneath the southern Kenya Rift: implications from basalt geochemistry. *Contributions to Mineralogy and Petrology*, **142**, pp. 89-106

Lee, C.-T.A., Cheng, X. & Horodyskyj, U., 2006. The development and refinement of continental arcs by primary basaltic magmatism, garnet pyroxenite accumulation, basaltic recharge and delamination: insights from the Sierra Nevada, California. *Contributions to Mineralogy and Petrology*, **151**, pp. 222-242.

Longhi, J., 2005. A mantle or mafic crustal source for Proterozoic anorthosites? *Lithos*, **83**, pp. 183-198.

Longhi, J. & Ashwal, L.D., 1985. Two stage models for lunar and terrestrial anorthosites: petrogenesis without a magma ocean. *Procedings of the Fifteenth Lunar and Planetary Science Conference, Journal of Geophysical Research*, **90**, C571-C584.

Longhi, J. et al., 1993. Pressure Effects, Kinetics, and Rheology of Anorthositic and Related Magmas. *American Mineralogist*, 78, pp. 1016-1030.

Longhi, J., Vander Auwera, J. & Fram, M., 1999. Some Phase Equilibrium Constraints on the Origin of Proterozoic (Massif) Anorthosites and Related Rocks. *Journal of Petrology*, **40**, pp. 339-362.

Ludwig, K.R. 2003. User's manual for Isoplot 3.00 a geochronological toolkit for Excel. Berkeley Geochronological Center Special Publication 4, 71 p.

Maji, A.K., Patra, A. & Ghosh, P., 2010. An overview on geochemistry of Proterozoic massif-type anorthosites and associated rocks. *Journal of Earth System Science*, **119**, pp. 861-878.

Marsh, B.D., 1981. On the crystallinity, probability of occurrence, and rheology of lava and magma. *Contributions to Mineralogy and Petrology*, **78**, pp. 85-98.

Martignole, J. & Schrijver, K., 1970. Tectonic setting and evolution of the Morin anorthosite, Grenville

Province, Quebec. *Bulletin of the Geoogical Society of Finland*, **42**, pp. 165-209.

Martignole, J., Machado, N. & Nantel, S., 1993. Timing of Intrusion and Deformation of the Rivière-Pentecôte Anorthosite (Grenville Province). *The Journal of Geology*, **101**, pp. 652-658.

Mattinson, J. 2005. Zircon U-Pb chemical abrasion (CA-TIMS) method: Combined annealing and multi-step partial dissolution analysis for improved precision and accuracy of zircon ages. *Chemical Geology*, **220**, pp. 47-66.

McLelland, J., Ashwal, L. & Moore, L., 1994. Composition and petrogenesis of oxide-, apatite-rich gabbronorites associated with Proterozoic anorthosite massifs: examples from the Adirondack Mountains, New York. *Contributions to Mineralogy and Petrology*, **116**, pp. 225-238.

McLelland, J., Daly, S., McLelland, J.M., 1996. The Grenville Orogenic Cycle (ca. 1350 – 1000 Ma): An Adirondack perspective. *Tectonophysics*, **265**, pp. 1-28.

McLelland, J.M. et al., 2010. Late- to Post-Tectonic Setting of Some Major Proterozoic Anorthosite - Mangerite - Charnockite - Granite (AMCG) Suites. *Canadian Mineralogist*, **48**, pp. 729-750.

Menuge, J.F., 1988. The petrogenesis of massif anorthosites: a Nd and Sr isotopic investigation of the Proterozoic of Rogaland/Vest-Agder, SW Norway. *Contributions to Mineralogy and Petrology*, **98**, pp. 363-373.

Miller, C.F. et al., 2011. Growth of plutons by incremental emplacement of sheets in crystal-rich host: Evidence from Miocene intrusions of the Colorado River region, Nevada, USA. *Tectonophysics*, **500**, pp. 65-77.

Mitchell, J. et al., 1996. The geochemical evolution of anorthosite residual magmas in the Laramie Anorthosite Complex, Wyoming. *Journal of Petrology*, **37**, pp. 637-660.

Mitchell, J., Scoates, J. & Frost, C., 1995. High-Al Gabbros in the Laramie Anorthosite Complex, Wyoming - Implications for the Composition of Melts Parental to Proterozoic Anorthosite. *Contributions to Mineralogy and Petrology*, **119**, pp. 166-180.

Moore, J.M., Thompson, P., 1980. The Flinton Group: A late Precambrian metasedimentary sequence in the Grenville Province of eastern Ontario. *Canadian Journal of Earth Sciences*, **17**, pp. 1685-1707.

Morad, S. et al., 2010. Hydrothermal alteration of plagioclase in granitic rocks from Proterozoic basement of SE Sweden. *Geological Journal*, **45**, pp. 105-116.

Morse, S.A., 1969. Layered intrusions and anorthosite genesis. *In:* Isachsen, Y.W. (eds), *Origin of anorthosite and related rocks*, **Memoir 18**, New York State Museum and Science Service, pp. 175-188.

Morse, S.A., 1975. Plagioclase Lamellae in Hypersthene, Tikkoatokhakh Bay, Labrador. *Earth and Planetary Science Letters*, **26**, pp. 331-336.

Morse, S.A., 1976. Plagioclase composition and anorthosite classification. *In:* The Nain anorthosite project, Labrador: field report 1975, Morse, S.A. (Ed). University Mass. Amherst Department Geol. Geog Contrib **26**, pp. 51-57.

Morse, S.A., 1982. A partisan review of Proterozoic anorthosites. *The American Mineralogist*, **67**, pp. 1087-1100.

Morse, S.A., 1991. Basaltic magma from the crust is not a free option. *EOS Transactions of the American Geophysical Union*, **72**, p. 161.

Möller, C. et al., 2013. A non-collisional, accretionary Sveconorwegian orogen - Comment. *Terra Nova*, doi:10.1111/ter.12029.

Müntener, O. & Kelemen, P.B., 2001. The role of H2O during crystallisation of primitive arc magmas under

uppermost mantle conditions and genesis of igneous pyroxenites: an experimental study. *Contributions to Mineralogy and Petrology*, **141**, pp. 643-658.

Müntener, O. & Ulmer, P., 2006. Experimentally derived high-pressure cumulates from hydrous arc magmas and consequences for the seismic velocity structure of lower arc crust. *Geophysical Research Letters*, **33**, pp. L21308.

Myers, J.S., Voordouw, R.J. & Tettelaar, T.A., 2008. Proterozoic anorthosite-granite Nain batholith: structure and intrusion processes in an active lithosphere-scale fault zone, northern Labrador. *Canadian Journal of Earth Sciences*, **45**, pp. 909-934.

Nägler, Th.F., & Kramers, J.D., 1998. Nd idotopic evidence of the upper mantle during the Precambrian: models, data and the uncertainty of both. *Precambrian Research*, **91**, pp. 233-252.

Olson, K., 1992. The Petrology and Geochemistry of Mafic Igneous Rocks in the Anorthosite-Bearing Adirondack Highlands, New York. *Journal of Petrology*, **33**, pp. 471-502.

Othman, D.B., Polvé, M. & Allègre, C.J., 1984. Nd—Sr isotopic composition of granulites and constraints on the evolution of the lower continental crust. *Nature*, **307**, pp. 510-515.

Owens, B. & Dymek, R., 1995. Significance of Pyroxene Megacrysts for Massif Anorthosite Petrogenesis - Constraints From the Labrieville, Quebec, Pluton. *American Mineralogist*, **80**, pp.144-161.

Owens, B.E.Dymek, 1992. Fe-Ti-P-rich rocks and massif anorthosite; problems of interpretation illustrated from the Labrieville and St-Urbain plutons, Quebec. *The Canadian Mineralogist*, **30**, pp.163-190.

Palme, H. & O'Neill, H.S.C., 2003. Cosmochemical estimates of mantle composition. *Treatise on Geochemistry*, **2**, pp. 1-38.

Peck, W. & Valley, J., 2000. Large crustal input to high delta O-18 anorthosite massifs of the southern Grenville Province: new evidence from the Morin Complex, Quebec. *Contributions to Mineralogy and Petrology*, **139**, pp. 402-417.

Peck, W.H. et al., 2010. Oxygen Isotopes in the Grenville and Nain AMCG Suites: Regional Aspects of the Crustal Component in Massif Anorthosites. *The Canadian Mineralogist*, **48**, pp. 763-786.

Petford, N., Kerr, R.C., Lister, J.R., 1993. Dyke transport model for transport of granitoid magmas. *Geology*, **21**, pp. 845-848.

Phillips, E.R., 1974. Myrmekite — one hundred years later. *Lithos*, **7**, pp. 181-194.

Philippe, S., Wardle, R.J., Schärer, U., 1993. Labradorian and Grenvillian crustal evolution of the Goose Bay region, Labrador: new U-Pb geochronological constraints. *Canadian Journal of Earth Sciences*, **30**, pp. 2315-2327.

Philpotts, A.R., 1966. Origin of the anorthosite-mangerite rocks in S. Quebec. *Journal of Petrology*, **7**, pp. 1-64.

Philpotts, A.R., 1969. Parental magma of the anorthosite-mangerite suite. *In:* Isachsen, Y.W. (eds), *Origin of anorthosite and related rocks*, **Memoir 18**, New York State Museum and Science Service, pp. 207-212.

Philpotts, A.R., 1981. A model for the generation of massif-type anorthosites. *Canadian Mineralogist*, **19**, pp. 233-253.

Prevec, S.A., Ashwal, L.D., Mkaza, M.S., 2005. Mineral disequilibrium in the Merensky Reef, western Bushveld Complex, South Africa: new Sm-Nd isotopic evidence. *Contributions to Mineralogy and Petrology*, **149**, pp. 306-315.

Powell, J.A., Gromet, L.P., Dymek, R.F., 1982. Quartz monzodiorite and oxide-apatite-rich norites marginal to the Saint-Urbain anorthosite massif: products of liquid immiscibility? *Transactions of the American Geophysical Union*, **63**, pp. 456.

Ramos, F.C., Wolff, J.A., Tollstrup, D.L., 2005. Sr isotope disequilibrium in Columbia River flood basalts: Evidence for rapid shallow-level open-system processes. *Geology*, **33**, pp. 457-460.

Ramsey, J.G., 1989. Emplacement kinetics of a granite diapir: the Chindamora batholith, Zimbabwe. *Journal of Structural Geology*, **11**, pp. 191-209.

Rehkämper, M., Hofmann, A., 1997. Recycled ocean crust and sediment in Indian Ocean MORB, *Earth Planetary Science Letters*, **147**, pp. 93-106.

Richards, M., Contreras-Reyes, E., Lithgow-Bertelloni, C., Ghiorso, M., Stixrude, L., 2013. Petrological interpretation of deep crustal intrusive bodies beneath oceanic hotspot provinces. *Geochemistry, Geophysics, Geosystems*, **14**, DOI: 10.1029/2012GC004448

Rivers, T., 1997. Lithotectonic elements of the Grenville Province: Review and tectonic implications. *Precambrian Research* **86**, pp. 117-154

Rivers, T., & Corrigan, D., (2000). Convergent margin on southeatern Laurentia during the Mesoporoterozoic: tectonic impications. *Canadian Journal of Earth Science*, **37**, pp. 359-383.

Robins, B., Wilson, R. & Thjomoe, P., 2008. Magma Geopark - The Rogaland Anorthosite Province. *33 IGC Excursion,* **26,** pp.1–94.

Royse, K. & Park, R., 2000. Emplacement of the Nain anorthosite: diapiric versus conduit ascent. *Canadian Journal of Earth Sciences*, **37**, pp. 1195-1207.

Rudnick, R., 1995. Making continental crust, *Nature* **378**, pp. 571-578.

Rudnick, R., & Gao, S., 2003. Composition of the Continental Crust, *Treatise on Geochemistry* **3**, 1-64.

Ruprecht, P. & Plank, T., 2013. Feeding andesitic eruptions with a high-speed connection from the mantle. *Nature*, **500**, pp. 68-72.

Ryan, B. 1990. Preliminary geological map of the Nain Plutonic Suite and surrounding rocks (Nain-Nutak, NTS 14 S.W.), scale 1:500,000. Geological Survey Branch, Department of Mines and Energy, St. John's, Newfoundland, Map 90-44.

Ryan, B., 2000. The Nain-Churchill boundary and the Nain Plutonic Suite: A regional perspective on the geologic setting of the Voisey's Bay Ni-Cu-Co deposit. *Economic Geology*, **95**, pp. 703-724.

Sauer, S. et al., 2013. Zircon Lu–Hf isotopes in high-alumina orthopyroxene megacrysts from the Neoproterozoic Rogaland Anorthosite Province, SW Norway: A window into the Sveconorwegian lower crust. *Geophysical Research Abstracts*, **15** (EGU2013-13958).

Schärer, U., Wilmart, E. & Duchesne, J., 1996. The short duration and anorogenic character of anorthosite magmatism: U-Pb dating of the Rogaland complex, Norway. *Earth and Planetary Science Letters*, **139**, pp. 335-350.

Schiellerup, H. et al., 2000. Re-Os isotopic evidence for a lower crustal origin of massif-type anorthosites. *Nature*, **405**, pp. 781-784.

Schmeling, H., Cruden, A.R., Marquart, G., 1988. Finite deformation in and around a fluid sphere moving through a viscous medium: implications for diapiric ascent. *Tectonophysics*, **17**, pp. 227-231.

Schmidt, M.E., & Grunder, A.L., 2010. Deep Mafic Roots to Arc Volcanoes: Mafic Recharge and Differentiation of Basaltic Andesite at North Sister Volcano, Oregon Cascades. *Journal of Petrology*, **52**, pp. 603-641.

Scoates, J. & Frost, C., 1996. A strontium and neodymium isotopic investigation of the Laramie anorthosites, Wyoming, USA: Implications for magma chamber processes and the evolution of magma conduits in

Proterozoic anorthosites. *Geochimica et Cosmochimica Acta*, **60**, pp. 95-107.

Scoates, J.S. & Chamberlain, K.R., 1997. Orogenic to Post-Orogenic Origin for the 1.76 Ga Horse Creek Anorthosite Complex, Wyoming, Usa. *The Journal of Geology*, **105**, pp. 331-344.

Simmons, G., 1964. Gravity survey and geological interpretation, northern New York. *Geological Society of America Bulletin*, **75**, pp.81-98.

Slagstad, T. et al., 2013. A non-collisional, accretionary Sveconorwegian orogen - Reply. *Terra Nova*, doi: 10.1111/ter.12028.

Slagstad, T. et al., 2012. A non-collisional, accretionary Sveconorwegian orogen. *Terra Nova*, doi: 10.1111/ter.12001.

Spera, F. & Bohrson, W., 2001. Energy-constrained open-system magmatic processes I: General model and energy-constrained assimilation and fractional crystallization (EC-AFC) formulation. *Journal of Petrology*, **42**, pp. 999-1018.

Spera, F. & Bohrson, W., 2002. Energy-constrained open-system magmatic processes III. Energy-Constrained Recharge, Assimilation, and Fractional Crystallization (EC-RAFC). *Geochemistry Geophysics Geosystems*, **3**.

Spera, F. & Bohrson, W., 2004. Open-System Magma Chamber Evolution: an Energy-constrained Geochemical Model Incorporating the Effects of Concurrent Eruption, Recharge, Variable Assimilation and Fractional Crystallization (EC-E'RA FC). *Journal of Petrology*, **45**, pp. 2459-2480.

Streckeisen, A., 1976. To each plutonic rock its proper name. *Earth Science Reviews*, **12**, pp. 1-33.

Tatsumi, Y., 2000. Continental crust formation by crustal delamination in subduction zones and complementary accumulation of the enriched mantle I component in the mantle. *Geochemistry Geophysics Geosystems*, **1**.

Tatsumi, Y., 2005. The subduction factory: How it operates in the evolving Earth. *GSA today*, **15**, p. 4-10.

Taylor Jr., H.P., 1980. The effects of assimilation of country rocks by magmas on $^{18}O/^{16}O$ and $^{87}Sr/^{86}Sr$ systematics in igneous rocks. *Earth and Planetary Science Letters*, **47**, pp. 243-254.

Taylor, S. et al., 1984. A Lower Crustal Origin for Massif-Type Anorthosites. *Nature*, **311**, pp. 372-374.

Todt, W. et al., 1996. Earth Processes: Reading the Isotopic Code. *Earth Processes: Reading the Isotopic Code*.

Tollo, R.P., Corriveau, L., McLelland, J., and Bartholomew, M.J., (2004). Proterozoic tectonic evolution of the Grenville Orogen in North America: An Introduction, *In:* Tollo, R.P., Corriveau, L., McLelland, J., and Bartholomew, M.J., eds., Proterozoic tectonic evolution of the Grenville Orogen in North America: Boulder Colorado, *Geological Society of America Memoir*, **197**, pp. 1-18.

Valley, J. & O'Neil, J.R., 1982. Oxygen isotope evidence for shallow emplacement of Adirondack anorthosite. *Nature*, **300**, pp. 497-500.

Vander Auwera, J. et al., 2011. Sveconorwegian massif-type anorthosites and related granitoids result from post-collisional melting of a continental arc root. *Earth Science Reviews*, **107**, pp. 375-397.

Vander Auwera, J., Longhi, J. & Duchesne, J., 1998. A liquid line of descent of the jotunite (Hypersthene monzodiorite) suite. *Journal of Petrology*, **39**, pp. 439-468.

Van Kranendonk, M.J., 1996. Tectonic evolution of the Paleoproterozoic Torngat orogen: Evidence from pressure-temperature-time-deformation paths in the North River map area, Labrador. *Tectonics*, **15**, pp. 843-869.

Vernon, R.H., 2004. *A Practical Guide to Rock Microstructure.* 1st Ed, Cambridge University Press.

Vigneresse, J.L., 2005. The specific case of the Mid-Proterozoic rapakivi granites and associated suite within the context of the Columbia supercontinent. *Precambrian Research*, **137**, pp. 1-34.

Weinberg, R.F. & Podladchikov, Y., 1994. Diapiric ascent of magmas through power law crust and mantle. *Journal of Geophysical Research*, **99**, pp. 9543-9559.

Weinberg, R.F. & Podladchikov, Y.Y., 1995. The rise of solid-state diapirs. *Journal of Structural Geology*, **17**, pp. 1183-1195.

Westphal, M., Schumacher, J.C., Boschert, S., (2003). High-temperature metamorphism and the role of magmatic heat sources at the Rogaland Anorthosite Complex in Southwestern Norway. *Journal of Petrology*, **44**, pp. 1145-1162.

Wiebe, R.A., 1978. Anorthosite and related plutonism southern Nain complex, Labrador. *Canadian Journal of Earth Science*, **15**, pp. 1326-1340.

Wiebe, R.A., 1986. Lower crustal cumulate nodules in Proterozoic dikes of the Nain Complex: Evidence for the origin of Proterozoic anorthosites. *Journal of Petrology*, **27**, pp. 1253-1275.

Wiebe, R.A., 1990. Evidence for Unusually Feldspathic Liquids in the Nain Complex, Labrador. *American Mineralogist*, **75**, pp. 1–12.

Wilson, A.H., 2012. A Chill Sequence to the Bushveld Complex: Insight into the First Stage of Emplacement and Implications for the Parental Magmas. *Journal of Petrology*, **53**, pp. 1123-1168.

Xue, S. & Morse, S.A., 1993. Geochemistry of the nain massif anorthosite, labrador: Magma diversity in five intrusions. *Geochimica et Cosmochimica Acta*, **57**, pp. 3925-3948.

Yang, S.-H. et al., 2013. Strontium isotope disequilibrium of plagioclase in the Upper Critical Zone of the Bushveld Complex: evidence for mixing of crystal slurries. *Contributions to Mineralogy and Petrology*, doi: 10.1007/s00410-013-0903-4.

Zajacz, Z. et al., 2007. Evolution of Mafic Alkaline Melts Crystallized in the Uppermost Lithospheric Mantle: a Melt Inclusion Study of Olivine-Clinopyroxenite Xenoliths, Northern Hungary. *Journal of Petrology*, **48**, pp. 853-883.

Appendices

Appendix A: Major Element Data

Appendix B: Trace Element Data

Appendix C: Sr, Nd and Pb Whole-Rock Isotope Data

Appendix D: Sr, Nd and Pb Mineral Isotope Data

Appendix E: Crustal Reference Isotopic Data

Appendix F-1: EMPA Pod Data

Appendix F-2 Pod Geochronology Data

Appendix A

Mealy Mountains Intrusive Suite

Anorthosites																
	SiO2	Al2O3	Fe2O3	FeO	MnO	MgO	CaO	Na2O	K2O	TiO2	P2O5	Cr2O3	NiO	TOTAL	LOI	Mg #
CG.09.17	54.01	22.53	0.61	4.87	0.08	4.8	7.9	4.19	0.65	0.33	0.03	0.02	0.01	100.02	0.56	46.69
CG.09.18A	45.03	15.78	2.03	16.43	0.2	5.67	7	2.64	0.84	4.28	0.08	0.07	0	100.06	-0.58	23.50
CG.09.20A	53.36	23.84	0.47	3.8	0.07	4.56	8.65	3.84	0.68	0.21	0.04	0.02	0.01	99.55	0.09	51.64
CG.09.26A	53.06	24.78	0.51	4.08	0.07	4.17	9.56	3.48	0.53	0.32	0.03	0.02	0.01	100.62	0.07	47.60
CG.09.27A	53.79	23.89	0.52	4.18	0.06	1.98	8.09	4.89	0.57	0.83	0.06	0.01	0.01	98.87	0.27	29.64
CG.09.30	50.73	26.76	0.59	4.72	0.04	1.04	9.95	4.21	0.66	0.94	0.06	0.07	0.01	99.77	0.22	16.38
CG.09.32A	52.83	23.65	0.68	5.45	0.07	2.87	8.41	4.09	0.99	0.95	0.07	0.02	0.01	100.09	0.22	31.89
CG.09.32B	54.11	26.66	0.3	2.41	0.03	0.58	9.27	4.71	1.09	0.59	0.07	0.01	0	99.83	0.35	17.63
CG.09.33A	52.15	23.94	0.65	5.19	0.07	4.3	8.49	4.01	1.01	0.18	0.04	0.01	0.01	100.05	0.04	42.41
CG.09.34	50.7	24.49	0.59	4.77	0.07	4.86	9.31	3.71	0.69	0.15	0.04	0.01	0.01	99.4	0.03	47.55
CG.09.43	51.05	23.83	0.76	6.16	0.08	3.27	8.65	4.11	0.9	0.92	0.07	0.02	0.01	99.83	0.05	32.09
CG.09.44	51.98	25.11	0.57	4.6	0.06	2.94	9.3	4.1	0.82	0.53	0.08	0.02	0.01	100.12	0.42	36.25
Orthopyroxene Megacrysts																
CG.09.18B	50.32	5.51	2.05	16.58	0.3	22.83	1.79	0.14	0.04	0.56	0.03	0.11	0.03	100.3	-1.05	55.07
CG-09-20B	49.03	5.87	2.08	16.81	0.32	22.94	1.83	0.09	0.03	0.54	0.02	0.11	0.04	99.68	-0.86	54.84
CG-09-26C	50.07	6.39	1.52	12.27	0.24	26.88	1.85	0.02	-0.02	0.26	0.01	0.13	0.04	99.67	-0.7	66.09
CG-09-33C	41.27	2.98	3.16	25.55	0.39	23.77	1.62	0.26	0.15	0.69	0.06	0.01	0.05	99.95	-1.83	45.29
GMB-09-02	49.99	5.45	1.98	16.02	0.29	23.71	1.86	-0.04	0.01	0.4	0.01	0.13	0.03	99.84	-1.08	56.84
EC-75-138																
EC-75-227	51.1	5.48	1.7	16	0.35	23	1.83	0.1	0.06	0.55	0.02	-	-	100.28		56.51
BR-03-284B	48.94	4.94	2.6	21	0.34	19.05	1.96	0.43	0.01	0.67	0.02	0.04	0.02	100.01	-1.25	44.67
BR-03-283	49	5.72	2.27	18.33	0.29	19.57	2.06	1	0.16	0.76	0.05	0.09	0.02	99.32	-1.14	48.72
Plagioclase Megacrysts																
CG-09-16C	55.33	26.05	0.16	1.27	0.02	0.65	8.65	6.7	0.39	0.11	0.04	0	0	99.34	0.63	31.25
CG.09.18C	55.42	27.78	0.08	0.64	0.01	0.06	9.84	4.89	1.09	0.1	0.03	0	0	99.94	0.48	7.69
CG-09-20C	53.96	27.74	0.1	0.78	0.01	0.38	10.48	5.15	1.02	0.11	0.05	0	0	99.78	0.37	30.16
CG-09-27B	55.98	26.74	0.09	0.74	0.01	0.1	8.93	5.73	1.17	0.15	0.06	0	0	99.71	0.39	10.75
Graphic Pods																
CG-09-16A	59.63	25.23	0.1	0.8	0.04	0.57	4.01	7.11	2.22	0.11	0.05	0	0	99.87	1.95	38.78
CG-09-18D	59.65	11.61	1.61	13.04	0.17	1.91	2.35	4.7	1.57	3.33	0.06	0.01	0	100	0.09	11.53
CG-09-26B	74.74	13.38	0.18	1.5	0.01	0.34	0.77	2.55	6.28	0.13	0.03	0	0	99.92	0.55	16.83
CG-09-27C	57.75	26.82	0.09	0.75	0.01	0.14	8.26	6.15	0.9	0.13	0.06	0	0	101.05	0.41	14.29
CG-09-33B	39.55	8.63	2.97	24.08	0.34	7.63	5.87	1.79	1.64	6.05	1.28	0.03	0.02	99.89	-0.82	22.00

Appendix A

Nain Plutonic Suite																
Orthopyroxene Megacrysts																
	SiO2	Al2O3	Fe2O3	FeO	MnO	MgO	CaO	Na2O	K2O	TiO2	P2O5	Cr2O3	NiO	TOTAL	LOI	Mg #
BR-03-69B	50.13	5.22	2.32	18.73	0.29	20.98	1.65	0.28	0.02	0.722	0.03	0.088	0.022	100.48	-0.87	49.92
BR-03-108	50.63	5.43	2.08	16.81	0.27	22.03	1.66	0.07	0.03	0.664	0.01	0.112	0.02	99.8	-0.71	53.84
BR-03-112	48.56	4.5	2.87	23.24	0.38	16.74	1.96	0.52	0.05	0.658	0.02	0.043	0.012	99.56	-1.55	39.07
BR-03-283	50.07	5.82	2.28	18.44	0.29	19.75	2.05	1.11	0.16	0.765	0.05	0.083	0.014	100.86	-0.94	48.80
BR-03-284B	49.42	4.94	2.54	20.56	0.32	18.78	1.88	0.62	0.05	0.661	0.02	0.032	0.018	99.85	-1.14	44.84
BR-03-475	50.77	5.66	2.21	17.85	0.3	19.13	2.34	0.44	0.03	0.591	0.02	0.049	0.021	99.39	-1.04	48.81
BR-04-169	50.57	5.6	2.23	18.03	0.29	19.97	1.79	0.6	0.11	0.658	0.06	0.081	0.021	100	-0.79	49.64
BR-04-170B	50.3	5.99	2.16	17.48	0.28	21.57	1.45	0.1	0	0.687	0.01	0.089	0.021	100.15	-0.66	52.34
BR-99-34A	50.63	5.8	1.89	15.3	0.27	23.68	1.5	0.12	0.01	0.597	0.02	0.147	0.028	99.99	-0.34	57.94
NA4563	49.4	4.49	2.62	21.2	0.33	18.83	1.79	0.24	0.03	0.824	0.08	0.062	0.015	99.92	-1.29	44.15
Rogaland Anorthosite Province																
Orthopyroxene Megacrysts																
	SiO2	Al2O3	Fe2O3	FeO	MnO	MgO	CaO	Na2O	K2O	TiO2	P2O5	Cr2O3	NiO	TOTAL	LOI	Mg #
GMB-11-01	50.9	6.92	1.55	12.5	0.21	25.25	1.63	0.08	0.02	0.35	0.02	0.12	0.05	99.59	-0.03	64.25
GMB-11-02	50.75	7.3	1.56	12.62	0.2	25.07	1.64	0.08	0.02	0.35	0.02	0.12	0.04	99.76	0.3	63.87
GMB-11-04	52.56	3.88	1.79	14.51	0.28	24.02	2.21	0.13	0	0.33	0.02	0.14	0.03	99.9	0.72	59.57
GMB-11-05	51.96	2.85	2.17	17.58	0.33	22.5	1.94	0.07	0.02	0.49	0.01	0.09	0.03	100.04	-0.98	53.25
GMB-11-14	51.34	4.78	2.29	18.51	0.28	20.45	1.49	0.37	0.04	0.61	0.02	0.07	0.03	100.27	-1.04	49.58
GMB-11-16	51.15	3.6	2.42	19.6	0.29	21.05	1.28	0.13	0.01	0.58	0.02	0.06	0.03	100.21	-1.24	48.87
GMB-11-18	50.59	8.35	1.55	12.54	0.19	24.9	1.44	0.13	0	0.38	0.02	0.12	0.03	100.22	-0.36	63.86
GMB-11-19	49.94	8.66	1.49	12.04	0.19	25.48	1.44	0.09	-0.01	0.36	0.01	0.15	0.05	99.88	-0.46	65.32
GMB-11-21	50.44	7.92	1.55	12.56	0.2	24.86	1.71	0.11	-0.01	0.39	0.01	0.11	0.03	99.87	-0.13	63.79
GMB-11-26	51.4	4.64	1.76	14.32	0.28	24.5	1.91	0.19	0.08	0.48	0.02	0.13	0.04	99.77	-0.34	60.37
GMB-11-27	52.38	4.18	1.65	13.34	0.26	25.27	1.85	0.1	-0.01	0.36	0.01	0.17	0.04	99.6	-0.61	62.77
GMB-11-28	50.33	8.16	1.44	11.65	0.19	25.89	1.44	0.08	0	0.34	0.01	0.14	0.05	99.7	-0.28	66.42
GMB-11-32	50.57	7.65	1.84	14.93	0.25	22.13	2.11	0.33	0.01	0.7	0.03	0.13	0.04	100.72	-0.55	56.89
GMB-11-33	50.1	8.43	1.57	12.65	0.2	24.77	1.5	0.08	0	0.37	0.01	0.13	0.04	99.84	-0.42	63.53
GMB-11-34	50.42	8.63	1.48	11.97	0.19	25.52	1.45	0.09	-0.01	0.36	0.01	0.13	0.04	100.27	-0.48	65.49
GMB-11-36	50.48	8.28	1.5	12.09	0.19	25.32	1.53	0.08	0.04	0.35	0.01	0.11	0.04	100.01	-0.25	65.07
GMB-11-37	49.45	7.52	1.9	15.41	0.24	23.18	1.71	0.2	-0.01	0.57	0.02	0.15	0.05	100.38	-0.88	57.25
GMB-11-39	49.76	7.2	1.91	15.45	0.25	22.63	1.88	0.22	0.01	0.68	0.03	0.09	0.04	100.16	-0.64	56.59

Appendix B

Mealy Mountains Intrusive Suite																															
Anorthosites	7Li	45Sc	51V	52Cr	59Co	60Ni	63Cu	66Zn	85Rb	88Sr	89Y	90Zr	93Nb	137Ba	139La	140Ce	141Pr	144Nd	152Sm	153Eu	160Gd	159Tb	163Dy	165Ho	166Er	169Tm	174Yb	175Lu	178Hf	181Ta	208Pb	232Th	238U
	CG.09.17	13.440	11.7	77.09	162.1	26.55	61.83	9.80	51.47	3.086	636.3	1.946	3.61	0.197	550.8	2.497	4.39	0.499	1.998	0.341	0.764	0.349	0.054	0.344	0.074	0.232	0.038	0.263	0.045	0.131	0.025	1.947	0.040	0.019
	CG.09.18A	4.038	26.0	537.90	395.6	58.97	44.59	-29.28	200.80	5.858	406.1	8.030	21.66	3.565	504.6	4.305	9.03	1.189	5.650	1.363	0.927	1.520	0.235	1.518	0.314	0.901	0.131	0.883	0.136	0.748	0.165	2.103	0.217	0.061
	CG.09.20A	7.869	10.8	55.16	149.2	22.79	58.75	12.03	35.42	2.507	833.9	2.148	7.06	0.170	489.6	2.085	4.01	0.494	2.153	0.385	0.531	0.407	0.060	0.382	0.082	0.249	0.036	0.253	0.040	0.210	0.018	1.123	0.049	0.016
	CG.09.26A	4.661	9.9	62.23	122.7	21.35	40.16	6.26	43.87	3.444	732.4	2.072	2.64	0.077	341.1	2.129	3.91	0.458	1.930	0.337	0.610	0.353	0.053	0.351	0.079	0.242	0.037	0.275	0.043	0.127	0.009	1.311	0.018	0.006
	CG.09.27A	4.749	5.6	118.20	10.5	17.53	30.12	3.58	45.82	2.751	676.5	2.190	3.87	0.764	415.0	4.047	7.33	0.838	3.482	0.587	1.013	0.523	0.070	0.420	0.086	0.238	0.035	0.231	0.036	0.129	0.040	2.431	0.137	0.036
	CG.09.30	5.948	2.6	162.70	482.1	20.18	61.30	10.66	52.09	2.829	1088.0	1.734	5.01	0.620	559.6	2.499	4.81	0.604	2.682	0.493	0.711	0.456	0.063	0.354	0.067	0.183	0.025	0.151	0.021	0.155	0.035	1.243	0.030	0.021
	CG.09.32A	4.273	7.7	181.20	135.5	26.33	51.57	14.37	52.36	5.446	641.7	2.603	7.42	0.726	558.9	3.915	7.28	0.854	3.534	0.619	0.873	0.580	0.082	0.504	0.103	0.289	0.042	0.280	0.046	0.240	0.047	2.280	0.156	0.049
	CG.09.32B	6.569	2.4	83.33	51.7	6.97	12.26	b.d.l	23.44	5.199	825.8	2.016	6.45	0.771	603.9	4.168	7.81	0.903	3.735	0.619	0.921	0.540	0.073	0.396	0.078	0.209	0.030	0.185	0.029	0.191	0.043	2.461	0.189	0.059
	CG.09.33A	11.260	1.7	17.33	16.1	36.27	72.11	3.85	45.69	4.839	691.6	0.650	1.42	0.151	592.3	2.820	4.84	0.532	2.040	0.291	0.855	0.228	0.029	0.134	0.025	0.066	0.011	0.069	0.014	0.045	0.016	1.784	0.043	0.015
	CG.09.34	5.916	2.0	11.59	8.8	32.86	77.58	0.85	41.42	3.200	993.6	1.044	3.53	0.296	512.9	2.390	4.60	0.563	2.407	0.385	0.640	0.322	0.039	0.204	0.039	0.109	0.017	0.109	0.018	0.088	0.021	1.178	0.025	0.013
	CG.09.43	3.416	5.0	114.90	72.1	29.52	52.15	17.94	55.43	3.512	889.5	2.245	10.73	0.540	683.6	3.007	5.92	0.747	3.353	0.635	0.813	0.593	0.079	0.453	0.085	0.241	0.032	0.213	0.034	0.281	0.030	1.461	0.049	0.020
	CG.09.44	4.365	2.8	61.13	86.4	24.31	57.44	2.81	51.74	2.760	1049.0	1.826	5.88	0.331	702.2	3.109	6.04	0.757	3.363	0.607	0.786	0.519	0.067	0.364	0.071	0.185	0.024	0.159	0.025	0.157	0.020	1.423	0.036	0.016
Orthopyroxene Megacrysts																																	
	CG.09.18B	1.741	37.1	186.90	654.7	84.10	195.10	< 0.05 ppb	164	0.717	8.2	5.406	9.55	0.187	15.7	0.548	1.33	0.190	1.011	0.344	0.121	0.533	0.099	0.775	0.186	0.640	0.104	0.791	0.135	0.314	0.008	0.380	0.073	0.025
	CG.09.20B	2.697	48.0	236.50	682.2	104.45	257.45	25.0	159	0.489	8.1	5.256	8.58	0.066	14.7	0.233	0.61	0.105	0.655	0.289	0.104	0.491	0.094	0.747	0.179	0.621	0.101	0.766	0.131	0.293	0.003	0.342	0.028	0.012
	CG.09.26C	0.978	30.1	134.00	595.0	64.41	207.10	< 0.05 ppb	90.5	0.036	1.4	2.839	3.02	0.049	0.4	0.053	0.15	0.022	0.143	0.084	0.037	0.177	0.041	0.366	0.096	0.357	0.062	0.489	0.087	0.133	0.001	0.194	0.003	0.002
	CG.09.33C	8.060	18.6	99.51	47.5	147.60	264.90	< 0.05 ppb	243	1.655	54.2	4.873	10.64	0.724	71.0	1.068	2.28	0.307	1.495	0.417	0.136	0.541	0.095	0.714	0.166	0.572	0.093	0.705	0.122	0.314	0.029	0.540	0.109	0.024
	GMB.09.02	1.731	48.1	226.50	863.6	98.27	230.30	< 0.05 ppb	169	1.338	2.3	6.299	10.64	0.319	5.8	0.821	2.22	0.280	1.343	0.416	0.083	0.585	0.112	0.894	0.216	0.750	0.124	0.957	0.163	0.366	0.012	0.356	0.185	0.059
	EC-75-138	0.807	38.6	188.00	740.7	86.33	277.40	1.835*	97.5	0.187	1.8	2.181	2.65	0.027	2.9	0.036	0.12	0.019	0.118	0.076	0.034	0.154	0.036	0.311	0.082	0.283	0.050	0.391	0.067	0.134	< d.l.	0.313	0.005	0.008
	EC-75-227	0.750	47.2	221.00	488.0	91.80	175.00	3.23*	144	0.150	3.0	4.160	6.58	0.040	3.4	0.140	0.45	0.080	0.450	0.220	0.080	0.370	0.080	0.620	0.160	0.530	0.090	0.710	0.120	0.270	< d.l.	0.340	0.010	0.010
*Data from University of Cape Town ICPMS Lab																																	
Plagioclase Megacrysts																																	
	CG.09.16C	13.640	< 0.14 ppb	1.98	0.7	5.76	6.35	2.72	18.3	1.641	706.5	0.698	1.89	0.218	149.3	4.040	6.78	0.703	2.635	0.372	1.312	0.250	0.030	0.141	0.025	0.072	0.009	0.062	0.009	0.039	0.007	2.881	0.072	0.016
	CG.09.18C	3.455	< 0.14 ppb	2.97	1.3	1.40	3.03	0.72	5.32	3.505	0.1	0.455	0.77	0.066	667.6	1.934	3.44	0.397	1.654	0.306	0.681	0.178	0.020	0.091	0.016	0.041	0.006	0.027	0.004	0.018	0.003	1.398	0.011	0.007
	CG.09.20C	10.220	1.2	3.50	1.4	3.15	10.53	3.84	5.80	4.789	934.5	1.214	7.67	0.390	645.3	3.140	6.05	0.706	2.962	0.557	0.842	0.389	0.046	0.241	0.042	0.111	0.013	0.079	0.011	0.169	0.017	1.775	0.133	0.039
	CG.09.27B	5.894	0.3	3.07	0.5	1.17	0.30	0.32	11.4	5.962	776.7	1.502	5.02	0.623	948.3	4.410	7.84	0.858	3.426	0.623	1.396	0.426	0.052	0.283	0.051	0.146	0.019	0.124	0.018	0.104	0.024	3.273	0.163	0.043
Graphic Granite Pods																																	
	CG.09.16A	10.648	-	1.48	1.2	0.94	0.60	0.68	21.66	14.680	505.3	5.974	20.40	2.637	1345.0	17.775	28.10	2.834	10.049	1.413	2.684	1.309	0.175	1.016	0.200	0.588	0.081	0.556	0.081	0.487	0.102	18.960	0.856	0.308
	CG.09.18D	1.044	23.7	86.35	10.5	24.39	16.61	b.d.l.	173.60	65.735	52.6	74.180	316.95	58.600	95.4	276.050	583.10	55.690	201.150	29.075	1.906	21.525	2.897	16.310	3.048	8.851	1.275	8.743	1.379	10.350	2.785	41.865	31.705	2.560
	CG.09.26B	2.839	0.2	0.78	1.4	2.45	3.68	5.47	26.32	507.050	32.4	59.840	171.50	37.120	126.9	185.800	378.80	41.390	149.150	23.090	0.833	16.495	2.321	13.340	2.488	7.331	1.096	7.366	1.154	6.177	2.261	57.695	44.825	7.645
	CG.09.27C	3.761	-	2.14	0.4	0.90	-0.59	0.86	16.69	4.533	760.5	3.432	24.21	1.861	885.7	8.956	16.53	1.858	7.095	1.088	1.558	0.894	0.124	0.699	0.139	0.385	0.058	0.365	0.059	0.602	0.094	4.588	1.012	0.229
	CG.09.33B	3.841	39.4	336.50	84.1	88.81	125.75	52.84	306.15	34.755	144.6	47.215	35.41	15.175	555.7	33.585	81.43	11.290	53.295	11.675	2.065	11.745	1.614	9.530	1.816	5.025	0.661	4.223	0.633	1.510	0.670	6.870	1.027	0.328
Nain Plutonic Suite																																	
	7Li	45Sc	51V	52Cr	59Co	60Ni	63Cu	66Zn	85Rb	88Sr	89Y	90Zr	93Nb	137Ba	139La	140Ce	141Pr	144Nd	152Sm	153Eu	160Gd	159Tb	163Dy	165Ho	166Er	169Tm	174Yb	175Lu	178Hf	181Ta	208Pb	232Th	238U
	BR-04-18	3.677	15.58	93.96	113.9	37.31	44.85	0.953	104.80	2.512	514.3	5.931	21.22	1.331	472.0	6.267	13.26	1.676	7.196	1.436	0.959	1.398	0.204	1.192	0.239	0.684	0.103	0.638	0.106	0.574	0.038	1.825	0.125	0.035
	BR-04-125	2.776	4.49	30.56	74.7	21.43	34.98	2.161	43.43	0.721	585.3	0.994	2.26	0.058	249.7	1.804	3.05	0.324	1.230	0.214	0.531	0.190	0.030	0.189	0.042	0.118	0.022	0.133	0.024	0.071	b.d.l	1.263	0.014	0.011
	BR-00-328	5.885	14.10	56.56	46.2	17.50	25.90	13.43	32.79	1.386	691.5	4.521	15.52	0.476	278.4	3.686	7.77	0.980	4.413	0.964	0.845	1.022	0.146	0.895	0.176	0.507	0.070	0.443	0.065	0.412	b.d.l	1.696	0.090	0.021
	BR-97-237C	6.566	9.33	79.07	51.4	19.34	23.66	15.61	53.17	1.319	601.8	7.361	17.55	1.768	305.4	7.987	16.54	2.013	8.474	1.684	1.029	1.727	0.244	1.466	0.290	0.793	0.110	0.694	0.103	0.546	0.052	2.699	0.264	0.037
	BR-99-83	5.287	16.77	114.80	289.5	44.88	75.79	0.609	78.20	1.673	372.0	2.679	5.77	0.245	134.2	1.766	3.16	0.364	1.467	0.299	0.585	0.375	0.065	0.453	0.107	0.342	0.057	0.393	0.070	0.178	b.d.l	1.813	0.027	0.026
	BR-99-159	2.822	11.30	80.95	234.2	33.17	81.97	0.263	45.78	1.278	399.2	2.398	5.98	0.132	116.7	1.789	3.43	0.413	1.669	0.338	0.401	0.365	0.057	0.399	0.089	0.295	0.047	0.327	0.053	0.195	0.007	0.842	0.019	0.003
	BR-99-221	7.073	15.97	99.61	125.2	36.79	45.37	b.d.l	85.47	2.045	468.3	5.339	13.41	2.598	261.6	5.229	10.61	1.299	5.349	1.063	0.838	1.075	0.158	1.019	0.203	0.619	0.092	0.628	0.099	0.430	0.106	1.967	0.142	0.019
	EP-97-150	8.471	2.77	73.22	10.9	9.90	3.07	1.886	38.09	3.310	554.6	5.514	8.87	3.396	340.4	9.518	18.26	2.244	9.457	1.708	2.023	1.623	0.207	1.132	0.209	0.570	0.074	0.450	0.067	0.234	0.149	3.500	0.227	0.047
	DJ-03-64	5.432	11.26	62.08	117.5	35.93	56.02	8.517	88.05	0.649	577.6	3.640	6.24	0.447	308.4	4.854	9.14	1.088	4.464	0.803	0.817	0.769	0.109	0.689	0.140	0.434	0.061	0.436	0.067	0.229	b.d.l	2.112	0.002	b.d.l
	GMB-09-01	4.176	5.07	38.21	162.9	21.11	40.26	0.251	40.07	0.712	510.3	1.625	4.58	0.197	165.7	2.041	3.74	0.441	1.759	0.320	0.557	0.319	0.045	0.293	0.058	0.186	0.027	0.198	0.030	0.141	b.d.l	1.225	0.028	0.018
	GM-97-83	7.030	14.95	44.08	8.9	11.11	0.91	0.057	93.04	4.761	544.7	14.910	18.77	6.660	696.0	15.150	31.54	3.987	17.900	3.689	2.879	3.691	0.510	3.043	0.586	1.650	0.223	1.499	0.228	0.653	0.264	4.837	0.509	0.084
Orthopyroxene Megacrysts																																	
	BR-03-69B	1.483	32.97	32.97	455.0	54.62	90.14	2.892	101.15	0.593	6.1	5.934	16.80	0.522	9.1	1.474	2.81	0.488	2.114	0.538	0.108	0.656	0.115	0.846	0.185	0.555	0.094	0.654	0.107	0.537	0.024	0.591	0.126	0.461
	BR-03-108	1.157	33.06	33.06	695.7	88.01	141.77	2.287	153.31	0.663	8.2	5.419	18.67	0.610	6.3	1.603	3.67	0.454	1.986	0.475	0.102	0.568	0.096	0.742	0.167	0.506	0.091	0.658	0.109	0.580	0.015	0.685	0.059	0.025
	BR-03-112	1.946	39.48	39.48	286.3	77.77	62.66	4.749	286.70	1.132	25.4	17.923	45.54	0.713	41.6	2.699	5.47	0.780	3.831	1.348	0.298	1.800	0.362	2.658	0.589	1.748	0.301	2.045	0.331	1.493	0.053	1.014	0.026	0.008
	BR-03-283	3.731	35.94	35.94	592.3	87.28	98.57	5.724	195.68	1.228	20.4	11.827	34.59	1.369	20.1	9.674	19.47	2.399	9.118	1.780	0.213	1.966	0.305	1.882	0.384	1.087	0.171	1.161	0.178	0.946	0.058	2.145	0.281	0.068
	BR-03-284B	0.929	36.11	36.11	187.5	95.80	114.33	6.51	205.06	0.338	8.9	7.532	26.66	0.335	8.5	0.686	1.50	0.228	1.225	0.456	0.121	0.662	0.135	1.022	0.236	0.707	0.119	0.854	0.138	0.846	0.010	1.274	0.063	0.010
Wits Earth Lab	BR-03-475	1.703	36.45	36.45	328.9	88.93	152.08	2.998	177.48	0.203	64.3	5.526	17.17	0.200	23.9	0.820	1.61	0.237	1.209	0.368	0.150	0.482	0.092	0.736	0.175	0.543	0.098	0.723	0.123	0.638	0.003	0.652	0.016	0.040
	BR-04-169	3.118	35.09	35.09	418.1	58.69	96.47	3.435	111.39	2.583	18.5	14.951	28.86	2.576	20.0	6.470	8.73	1.381	5.588	1.314	0.278	1.636	0.305	2.147	0.482	1.435	0.243	1.633	0.260	0.954	0.132	0.927	0.164	0.595
	BR-04-170B	2.221	34.28	34.28	560.9	91.82	140.93	4.996	150.85	0.122	4.5	6.513	26.70	0.154	5.2	1.018	2.64	0.347	1.558	0.467	0.085	0.601	0.115	0.897	0.204	0.613	0.105	0.736	0.115	0.653	0.000	0.831	0.026	0.022
	BR-99-34A	0.839	28.97	28.97	911.7	93.63	212.58	2.774	123.27	0.235	12.7	5.277	25.79	0.280	6.1	0.747	1.65	0.241	1.217	0.388	0.096	0.509	0.095	0.721	0.165	0.498	0.084	0.630	0.106	0.743	0.012	0.508	0.033	0.047
	NA4563																																	
Orthopyroxene Megacrysts																																	
	BR03-284B	1.214	34.24	213	180	103	115	7.78	249	0.32	8.12	6.16	23.3	0.26	8.69	0.57	1.35	0.21	1.09	0.43	0.13	0.74	0.15	1.07	0.24	0.75	0.12	0.83	0.13	0.75	< d.l.	0.78	0.03	0.01
	BR03-283	3.932	33.77	246	530	95.4	94.8	7.36	261	1.07	18.8	9.36	28.2	1.11	19.0	8.26	17.8	1.99	7.62	1.58	0.21	1.71	0.28	1.79	0.36	1.07	0.16	1.07	0.16	0.81	< d.l.	2.00	0.26	0.06
	NA4563	2.430	34.26	194	340	89.3	90.4	6.27	281	0.52	11.0	9.12	21.2	0.66	12.1	2.08	5.34	0.79	3.90	1.11	0.18	1.33	0.23	1.56	0.33	1.04	0.16	1.12	0.17	0.74	< d.l.	0.70	0.19	0.04
	BR99-34A	1.081	33.04	229	893	97.9	217	5.03	160	0.23	11.9	4.53	22.1	0.21	5.89	0.64	1.50	0.20	1.00	0.37	0.10	0.57	0.10	0.76	0.17	0.56	0.09	0.68	0.11	0.68	< d.l.	0.96	0.03	0.01
UCT Lab	BR03-69B	2.084	33.21	241	542	101	138	5.07	230	0.97	6.65	6.11	22.3	0.59	12.3	1.61	4.07	0.54	2.42	0.68	0.14	0.87	0.15	1.09	0.24	0.74	0.11	0.79	0.13	0.82	0.06	0.99	0.23	0.22
	BR03-108	1.786	33.59	237	678	89.5	134	3.77	202	0.67	7.57	5.30	16.6	0.50	6.62	1.42	3.49	0.42	1.77	0.53	0.12	0.66	0.13	0.87	0.20	0.66	0.11	0.76	0.13	0.57	< d.l.	0.46	0.08	0.05
	BR03-112	2.309	35.30	181	266	81.9	55.8	6.23	357	1.11	23.2	14.2	37.5	0.58	39.5	2.41	5.01	0.69	3.47	1.27	0.28	1.84	0.35	2.53	0.55	1.74	0.27	1.90	0.30	1.31	< d.l.	0.49	0.03	0.02
	BR04-169	3.646	32.84	221	479	93.7	124	4.23	217	3.59	18.6	13.6	30.1	2.28	26.0	6.29	11.9	1.37	5.58	1.40	0.30	1.78	0.33	2.37	0.52	1.63	0.25	1.75	0.28	1.03	0.06	0.79	0.19	0.05
	BR04-170B	2.319	31.57	243	537	95.1	137	5.80	180	0.11	4.20	5.69	23.0	0.13	5.29	0.83	2.40	0.30	1.38	0.46	0.08	0.64	0.13	0.93	0.21	0.69	0.11	0.75	0.12	0.60	< d.l.	1.36	0.03	0.03
	BR03-475	2.569	32.97	217	310	90.2	145	4.87	208	0.17	60.2	4.77	13.9	0.17	24.3	0.70	1.54	0.23	1.12	0.39	0.15	0.53	0.10	0.76	0.18	0.61	0.10	0.76	0.13	0.58	< d.l.	0.36	0.02	0.01
Rogaland Anorthosite Province																																	
Orthopyroxene Megacrysts	7Li	45Sc	51V	52Cr	59Co	60Ni	63Cu	66Zn	85Rb	88Sr	89Y	90Zr	93Nb	137Ba	139La	140Ce	141Pr	144Nd	152Sm	153Eu	160Gd	159Tb	163Dy	165Ho	166Er	169Tm	174Yb	175Lu	178Hf	181Ta	208Pb	232Th	238U
	GMB-11-01	1.810	27.2	206.92	726.4	95.39	313.29	6.759	91.78	0.336	20.9	2.898	6.26	0.053	11.5	0.139	0.23	0.032	0.267	0.129	0.052	0.210	0.045	0.380	0.092	0.304	0.054	0.405	0.063	0.255	0.009	0.555	0.010	0.008
	GMB-11-02	2.244	21.2	212.16	490.0	54.25	184.13	5.127	53.86	0.447	46.3	2.756	19.06	0.707	8.2	0.091	0.19	0.032	0.271	0.142	0.050	0.238	0.049	0.390	0.088	0.281	0.050	0.356	0.054	0.546	0.048	0.487	0.025	0.025
	GMB-11-04	2.301	43.4	183.59	862.6	94.96	222.14	4.791	115.02	0.153	23.5	4.637	10.75	0.123	3.0	0.100	0.28	0.059	0.418	0.202	0.059	0.336	0.072	0.599	0.148	0.502	0.087	0.679	0.117	0.331	0.010	0.482	0.157	0.068
	GMB-11-05	1.147	50.1	229.23	536.5	111.66	203.94	4.649	143.10	0.390	2.2	6.229	8.24	0.119	8.1	0.202	0.55	0.092	0.581	0.250	0.072	0.430	0.099	0.781	0.201	0.676	0.119	0.937	0.166	0.295	0.008	0.514	0.081	0.035
	GMB-11-14	1.683	28.3	251.83	320.3	56.87	173.96	8.127	117.96	0.433	27.7	8.209	21.21	0.948	13.5	1.047	2.76	0.428	2.253	0.747	0.205	0.999	0.177	1.240	0.275	0.813	0.127	0.894	0.146	0.652	0.062	0.705	0.033	0.027
	GMB-11-16	3.610	36.3	269.80	395.7	113.71	252.79	5.222	197.07	0.346	12.4	7.406	17.90	0.207	5.9	0.213	0.41	0.074	0.610	0.381	0.070	0.650	0.134	1.043	0.248	0.755	0.123	0.925	0.151	0.526	0.013	3.721	0.038	0.022
	GMB-11-18	2.906	26.0	243.03	778.9	102.28	197.08	4.838	94.24	0.220	13.1	3.767	12.16	0.314	1.9	0.111	0.21	0.032	0.297	0.159	0.048	0.294	0.068	0.532	0.126	0.403	0.066	0.479	0.073	0.353	0.023	0.493	0.080	0.038
	GMB-11-19	1.286	22.6	240.56	954.2	103.72	336.86	4.297	93.39	0.112	12.8	3.013	8.53	0.173	1.5	0.129	0.27	0.051	0.363	0.170	0.045	0.268	0.056	0.433	0.097	0.322	0.050	0.372	0.055	0.271	0.009	0.741	0.056	0.040
	GMB-11-21	2.445	23.8	240.38	727.6	104.04	192.86	5.949	96.01	0.048	10.0	2.857	7.97	0.093	1.2	0.061	0.20	0.037	0.266	0.139	0.048	0.243	0.047	0.417	0.096	0.306	0.049	0.364	0.052	0.311	0.009	0.295	0.013	0.013
	GMB-11-26	1.146	45.4	226.16	899.0	106.89	342.25	10.097	114.19	2.920	11.3	8.570	26.03	0.385	12.9	1.053	2.19	0.320	1.639	0.568	0.139	0.832	0.163	1.189	0.287	0.904	0.148	1.078	0.183	0.769	0.019	0.703	0.234	0.111
	GMB-11-27	1.113	37.1	201.05	738.8	62.28	197.44	5.036	65.11	0.453	5.0	3.631	13.03	0.509	2.5	0.509	1.49	0.260	1.180	0.300	0.049	0.382	0.069	0.501	0.121	0.394	0.070	0.525	0.093	0.402	0.038	0.846	0.157	0.085
	GMB-11-28	1.155	19.2	206.62	822.4	99.21	343.36	3.461	78.65	0.273	4.5	2.125	5.08	0.054	3.7	0.075	0.16	0.030	0.188	0.101	0.041	0.171	0.036	0.291	0.069	0.225	0.037	0.282	0.044	0.223	0.009	0.380	0.006	0.005
ICPMS Data from WITS Earth Lab																																	
	GMB-11-36	2.383	23.6	223.90	754.1	100.10	279.30	3.780	83.87	0.604	40.3	2.693	5.98	0.180	20.

Appendix B

ICPMS Data from UCT Lab	GMB11-01	1.61	22.6	219	754	95.2	321	8.35	106	0.31	19.9	2.04	5.97	0.04	5.19	0.05	0.15	0.03	0.15	0.09	0.04	0.17	0.04	0.30	0.08	0.26	0.05	0.36	0.06	0.25		0.12	0.02	0.01
	GMB11-02	1.80	23.0	218	739	95.0	286	6.07	107	0.45	47.8	2.16	8.58	0.08	3.06	0.05	0.19	0.03	0.17	0.10	0.04	0.19	0.04	0.34	0.08	0.27	0.05	0.34	0.06	0.27		0.12	0.02	0.01
	GMB11-04	4.26	38.3	186	859	89.6	215	7.54	136	0.27	22.7	4.08	10.1	0.10	3.00	0.09	0.26	0.06	0.38	0.20	0.06	0.33	0.07	0.62	0.15	0.52	0.09	0.70	0.12	0.32		0.23	0.18	0.06
	GMB11-05	0.72	43.3	221	483	105	198	6.46	164	0.50	1.96	3.97	7.38	0.09	3.84	0.11	0.41	0.06	0.36	0.16	0.05	0.30	0.07	0.56	0.15	0.51	0.09	0.71	0.12	0.29		0.14	0.06	0.03
	GMB11-14	1.50	22.5	238	398	102	247	10.6	247	0.55	32.0	7.27	13.6	0.25	13.43	1.11	2.90	0.41	2.04	0.71	0.19	0.98	0.17	1.24	0.27	0.83	0.13	0.92	0.15	0.45		0.41	0.03	0.02
	GMB11-16	3.04	26.3	249	350	108	244	6.98	229	0.53	11.3	5.27	18.1	0.16	4.39	0.15	0.39	0.06	0.45	0.31	0.06	0.55	0.11	0.84	0.19	0.63	0.10	0.75	0.12	0.53		2.99	0.03	0.02
	GMB11-18	1.66	22.5	225	714	94.8	185	6.00	90.0	0.34	12.8	2.60	11.2	0.24	0.80	0.05	0.19	0.03	0.19	0.11	0.04	0.22	0.05	0.40	0.10	0.32	0.05	0.39	0.06	0.34		0.16	0.05	0.03
	GMB11-19	0.98	23.1	230	868	96.2	322	5.88	93.3	0.19	11.9	2.33	8.19	0.19	0.65	0.10	0.29	0.08	0.27	0.15	0.08	0.25	0.09	0.41	0.13	0.32	0.08	0.38	0.09	0.31		0.43	0.10	0.11
	GMB11-26	1.18	39.1	213	818	97.9	327	12.8	113	3.35	10.5	5.91	25.0	0.34	9.43	0.67	1.89	0.27	1.23	0.43	0.13	0.66	0.14	0.95	0.23	0.75	0.13	0.89	0.15	0.77		0.38	0.24	0.13
	GMB11-27	2.56	46.2	219	1082	96.5	276	9.64	142	0.20	4.75	4.44	7.04	0.09	2.19	0.67	2.03	0.31	1.41	0.37	0.07	0.47	0.10	0.69	0.17	0.58	0.09	0.72	0.12	0.23		0.58	0.24	0.11
	GMB11-28	1.47	20.4	215	794	95.5	347	4.90	96.4	0.23	4.25	1.58	5.08	0.05	2.23	0.03	0.09	0.02	0.12	0.08	0.04	0.15	0.04	0.25	0.06	0.20	0.03	0.24	0.04	0.23		0.05	0.01	0.01
	GMB11-32	2.61	30.2	226	826	102	287	15.2	155	0.16	60.0	3.98	11.0	0.13	7.57	0.24	0.56	0.08	0.44	0.20	0.11	0.37	0.08	0.58	0.14	0.49	0.07	0.60	0.09	0.44		0.34	0.03	0.01
	GMB11-33	1.45	22.9	230	758	97.4	302	5.40	110	0.23	13.6	2.94	12.3	0.11	1.57	0.19	0.66	0.09	0.49	0.20	0.05	0.30	0.06	0.47	0.10	0.36	0.05	0.41	0.06	0.34		0.21	0.03	0.02
	GMB11-34	0.99	21.0	227	799	95.8	272	6.41	136	0.10	6.38	1.71	5.59	0.05	1.09	0.04	0.12	0.02	0.12	0.07	0.03	0.14	0.03	0.26	0.06	0.22	0.03	0.27	0.04	0.26		0.41	0.01	0.01
	GMB11-36	2.09	21.4	222	679	95.8	280	6.59	124	0.51	39.0	1.85	5.78	0.15	10.2	0.07	0.22	0.03	0.19	0.09	0.03	0.17	0.04	0.28	0.07	0.23	0.03	0.28	0.04	0.23		0.23	0.03	0.03
	GMB11-37	0.82	30.7	239	909	104	346	5.56	153	0.10	2.86	3.81	8.92	0.02	0.60	0.04	0.18	0.04	0.28	0.15	0.06	0.32	0.07	0.56	0.14	0.49	0.07	0.62	0.09	0.39		0.08	0.01	0.004
	GMB11-39	1.89	34.7	262	494	113	345	6.49	168	0.35	22.9	4.78	13.5	0.14	5.34	0.39	1.03	0.16	0.81	0.29	0.13	0.53	0.11	0.79	0.18	0.59	0.10	0.71	0.12	0.49		0.38	0.05	0.02

Appendix C

Rb-Sr		LN = leuconorite; LT = leucotroctolite			Pink Fill = Calculated Value									
Sample	Rock Type	Rb (mol)	Std Error	Sr (ppm)	Sr (mol)	Std Error	$^{87}Rb/^{86}Sr$	2σ	$^{87}Sr/^{86}Sr$	2σ	I_{Sr} at	2σ	I_{Sr} at	2σ
MMIS WR			2σ			2σ					1640		1765	
CG-09-15	LN	2.01E-09	4.01E-12	502.10	8.98E-08	1.80E-10	0.022340	0.000090	0.703697	0.000004	0.703181	0.000006	0.703141	0.000006
CG-09-17	LN	8.34E-10	1.67E-12	705.05	7.83E-08	1.57E-10	0.010644	0.000043	0.703507	0.000004	0.703261	0.000005	0.703242	0.000005
CG-09-18A	LN	2.48E-09	4.96E-12	401.07	6.18E-08	1.24E-10	0.040136	0.000161	0.704038	0.000003	0.703110	0.000007	0.703038	0.000007
CG-09-20A	LN	8.01E-10	1.60E-12	861.86	1.11E-07	2.21E-10	0.007235	0.000029	0.702743	0.000004	0.702576	0.000005	0.702563	0.000005
CG-09-26A	LN	1.31E-09	2.62E-12	758.76	1.16E-07	2.31E-10	0.011313	0.000045	0.702940	0.000004	0.702678	0.000005	0.702658	0.000005
CG-09-27A	LN	8.01E-10	1.60E-12	726.93	8.68E-08	1.74E-10	0.009234	0.000037	0.703738	0.000004	0.703525	0.000004	0.703508	0.000004
CG-09-29	A	6.26E-10	1.25E-12	1225.48	1.43E-07	2.86E-10	0.004383	0.000018	0.702640	0.000004	0.702538	0.000005	0.702530	0.000005
CG-09-30	A	8.66E-10	1.73E-12	1115.23	1.50E-07	3.00E-10	0.005768	0.000023	0.702693	0.000004	0.702559	0.000004	0.702549	0.000004
CG-09-32A	LN	1.75E-09	3.51E-12	660.43	7.71E-08	1.54E-10	0.022747	0.000091	0.703732	0.000004	0.703205	0.000006	0.703165	0.000006
CG-09-32B	LN	1.70E-09	3.40E-12	872.70	1.04E-07	2.09E-10	0.016272	0.000065	0.703355	0.000003	0.702978	0.000005	0.702949	0.000005
CG-09-33A	LT	1.68E-09	3.37E-12	706.73	9.13E-08	1.83E-10	0.018450	0.000074	0.703477	0.000004	0.703050	0.000005	0.703017	0.000005
CG-09-34	LT	8.85E-10	1.77E-12	1041.46	1.15E-07	2.29E-10	0.007723	0.000031	0.702734	0.000004	0.702555	0.000004	0.702541	0.000004
CG-09-43	LT	9.79E-10	1.96E-12	909.43	9.75E-08	1.95E-10	0.010044	0.000040	0.702894	0.000004	0.702662	0.000004	0.702644	0.000004
CG-09-44	A	1.10E-09	2.21E-12	1031.19	1.79E-07	3.59E-10	0.006158	0.000025	0.702735	0.000004	0.702592	0.000004	0.702581	0.000004
CG-09-20A Rep	LN	7.41E-10	1.48E-12	877.02	1.04E-07	2.08E-10	0.007125	0.000029	0.702747	0.000003	0.702582	0.000004	0.702569	0.000004
CG-09-26A Rep	LN	1.23E-09	2.46E-12	754.94	1.07E-07	2.14E-10	0.011517	0.000046	0.702952	0.000004	0.702686	0.000005	0.702665	0.000005
											1640		1765	
CG-09-18B	Opy megaxl	6.78E-10	1.36E-12	7.4421	2.69E-09	5.39E-12	0.251460	0.001008	0.708527	0.000005	0.702707	0.000029	0.702258	0.000029
CG-09-20B	Opy megaxl	4.41E-10	8.82E-13	7.0009	2.38E-09	4.76E-12	0.185299	0.000743	0.705393	0.000006	0.701105	0.000023	0.700774	0.000023
CG-09-26C	Opy megaxl	3.96E-11	7.93E-14	1.1111	4.41E-10	8.82E-13	0.089927	0.000360	0.705099	0.000007	0.703018	0.000016	0.702858	0.000016
CG-09-33C (T2)	Opy megaxl	1.65E-09	3.30E-12	56.5670	2.02E-08	4.04E-11	0.081797	0.000328	0.704429	0.000005	0.702536	0.000013	0.702390	0.000013
GMB-09-02	Opy megaxl	8.81E-10	1.76E-12	2.2100	5.23E-10	1.05E-12	1.685157	0.006754	0.738997	0.000007	0.700000	0.000163	0.696991	0.000163
EC-75-138	Opy megaxl	-		-	-	-	-	-	-	-	-	-	-	-
EC-75-138 Rep	Opy megaxl	1.86E-10	3.71E-13	1.9542	6.99E-10	1.40E-12	0.265511	0.001064	0.706553	0.000011	0.700409	0.000035	0.699935	0.000035
CG-09-26C Rep	Opy megaxl	3.68E-11	7.36E-14		4.57E-10	9.13E-13	0.080632	0.000323	0.705018	0.000006	0.703152	0.000013	0.703008	0.000013
CG-09-16C	Plag megaxl	5.12E-10	1.02E-12	712.33	8.39E-08	1.68E-10	0.006103	0.000024	0.703601	0.000003	0.703460	0.000004	0.703449	0.000004
CG-09-18C	Plag megaxl	1.25E-09	2.49E-12	1124.60	1.40E-07	2.79E-10	0.008926	0.000036	0.702829	0.000003	0.702622	0.000004	0.702607	0.000004
CG-09-20C	Plag megaxl	1.52E-09	3.04E-12	942.27	1.10E-07	2.20E-10	0.013828	0.000055	0.702995	0.000004	0.702675	0.000005	0.702650	0.000005
CG-09-27B	Plag megaxl	1.99E-09	3.97E-12	776.82	9.61E-08	1.92E-10	0.020669	0.000083	0.703995	0.000004	0.703517	0.000006	0.703480	0.000006
CG-09-16A	Peg pod	5.25E-09	1.05E-11		5.63E-08	1.13E-10	0.093231	0.000374	0.705502	0.000004	0.703344	0.000012	0.703178	0.000012
CG-09-18D	Peg pod	2.33E-08	4.66E-11		6.24E-09	1.25E-11	3.734908	0.014970	0.795901	0.000004	0.709469	0.000350	0.702800	0.000350
CG-09-26B	Peg pod	2.09E-07	4.18E-10		3.94E-09	7.88E-12	53.032697	0.212556	1.722747	0.000006	0.495480	0.004925	0.400781	0.004925
CG-09-27C	Peg pod	1.80E-09	3.61E-12		8.50E-08	1.70E-10	0.021213	0.000085	0.704236	0.000004	0.703745	0.000006	0.703707	0.000006
CG-09-33B	Peg pod	1.24E-08	2.48E-11		1.73E-08	3.46E-11	0.716036	0.002870	0.720027	0.000004	0.703457	0.000070	0.702178	0.000070
CG-09-26B Rep	Peg pod	8.70E-09	1.74E-11		3.86E-09	7.72E-12	2.254368	0.009036	1.722626	0.000006	1.670456	0.000215	1.666431	0.000215
NPS WR											1363		1311	
GMB-09-01	LN	2.73E-10	5.45E-13	572.09	6.80E-09	1.36E-11	0.040066	0.000161	0.704022	0.000009	0.703253	0.000012	0.703283	0.000012
BR-04-18	LN	1.16E-09	2.32E-12	533.39	7.59E-09	1.52E-11	0.152730	0.000612	0.706020	0.000004	0.703088	0.000015	0.703201	0.000015
DJ-03-64	LN	2.39E-10	4.79E-13	588.96	7.55E-08	1.51E-10	0.003168	0.000013	0.705902	0.000008	0.705841	0.000008	0.705843	0.000008
BR-99-83	LN	5.76E-10	1.15E-12	383.12	4.69E-08	9.38E-11	0.012274	0.000049	0.704864	0.000004	0.704628	0.000005	0.704637	0.000004
GM-97-83	LN	1.78E-09	3.55E-12	564.82	6.76E-08	1.35E-10	0.026286	0.000105	0.707604	0.000009	0.707099	0.000011	0.707119	0.000011
BR-04-125	LN	3.76E-10	7.52E-13	697.18	9.59E-09	1.92E-11	0.039208	0.000157	0.705018	0.000010	0.704265	0.000013	0.704294	0.000013
EP-97-150	LN	1.30E-09	2.59E-12	605.38	7.11E-08	1.42E-10	0.018234	0.000073	0.706547	0.000008	0.706197	0.000009	0.706210	0.000009
BR-99-159	LN	5.19E-10	1.04E-12	418.36	5.01E-08	1.00E-10	0.010357	0.000042	0.704351	0.000010	0.704152	0.000010	0.704159	0.000010
BR-99-221	LN	9.93E-10	1.99E-12	502.26	7.19E-08	1.44E-10	0.013810	0.000055	0.705586	0.000009	0.705321	0.000011	0.705331	0.000011
BR-00-328	LN	5.20E-10	1.04E-12	745.07	9.12E-08	1.82E-10	0.005703	0.000023	0.704921	0.000008	0.704812	0.000009	0.704816	0.000009
EP-97-232	LN	4.18E-10	8.36E-13	554.35	6.97E-08	1.39E-10	0.006001	0.000024	0.705979	0.000004	0.705864	0.000004	0.705869	0.000004
BR-99-237C	LN	5.03E-10	1.01E-12	623.07	8.05E-08	1.61E-10	0.006252	0.000025	0.705865	0.000009	0.705745	0.000010	0.705750	0.000010
GM-09-01 Rep	LN	2.72E-10	5.44E-13	588.78	7.05E-08	1.41E-10	0.003861	0.000015	0.704477	0.000008	0.704403	0.000009	0.704405	0.000009
BR-00-328 Rep	LN	4.91E-10	9.82E-13	707.11	8.28E-08	1.66E-10	0.005927	0.000024	0.704923	0.000004	0.704809	0.000004	0.704814	0.000004
											1444		1311	
BR-03-284B	Opy megaxl	3.01E-10	6.02E-13	7.8985	2.73E-09	5.45E-12	0.110524	0.000443	0.705963	0.000004	0.703714	0.000013	0.703923	0.000012
BR-03-283	Opy megaxl	4.06E-10	8.12E-13	18.5257	2.47E-09	4.93E-12	0.164774	0.000660	0.705692	0.000009	0.702339	0.000023	0.702651	0.000022
NA4563	Opy megaxl	5.41E-10	1.08E-12	10.6611	3.73E-09	7.46E-12	0.145179	0.000582	0.706573	0.000004	0.703619	0.000016	0.703893	0.000015
BR-03-69B	Opy megaxl	8.12E-10	1.62E-12	6.4179	2.18E-09	4.36E-12	0.372285	0.001492	0.708766	0.000004	0.701191	0.000034	0.701895	0.000032
BR-03-108	Opy megaxl	6.21E-10	1.24E-12	7.4784	2.58E-09	5.16E-12	0.240693	0.000965	0.708984	0.000004	0.704086	0.000024	0.704541	0.000022
BR-03-112	Opy megaxl	1.13E-09	2.26E-12	23.3950	7.99E-09	1.60E-11	0.141411	0.000567	0.705378	0.000004	0.702500	0.000015	0.702768	0.000014
BR-03-475	Opy megaxl													
BR-04-169	Opy megaxl	4.04E-09	8.08E-12		6.44E-09	1.29E-11	0.627047	0.002513	0.712878	0.000004	0.700118	0.000055	0.701304	0.000050
BR-04-170	Opy megaxl	8.93E-11	1.79E-13	4.0894	1.41E-09	2.82E-12	0.063454	0.000254	0.706660	0.000004	0.705369	0.000009	0.705489	0.000008
BR-99-34A	Opy megaxl	2.17E-10	4.33E-13	11.5676	4.19E-09	8.38E-12	0.051745	0.000207	0.704685	0.000004	0.703632	0.000008	0.703730	0.000008
BR-03-284B Rep	Opy megaxl	3.01E-10	6.03E-13	8.0409	2.80E-09	5.60E-12	0.107655	0.000431	0.705949	0.000004	0.703758	0.000013	0.703962	0.000012
RAP WR											930		1041	
GMB-11-01	Opy megaxl	2.07E-10	4.15E-13	19.9396	6.76E-09	1.35E-11	0.030704	0.000123	0.704919	0.000004	0.704518	0.000005	0.704470	0.000006
GMB-11-02	Opy megaxl	3.21E-10	6.43E-13	48.4740	1.64E-08	3.28E-11	0.019568	0.000078	0.704617	0.000005	0.704361	0.000006	0.704331	0.000006
GMB-11-04	Opy megaxl	1.31E-10	2.63E-13	23.0156	7.80E-09	1.56E-11	0.016833	0.000067	0.705126	0.000004	0.704906	0.000005	0.704880	0.000005
GMB-11-14	Opy megaxl	3.85E-10	7.69E-13	31.8518	1.08E-08	2.16E-11	0.035582	0.000143	0.705032	0.000004	0.704568	0.000006	0.704512	0.000006
GMB-11-18	Opy megaxl	1.58E-10	3.16E-13	12.8746	4.41E-09	8.83E-12	0.035766	0.000143	0.706460	0.000004	0.705993	0.000006	0.705937	0.000006
GMB-11-19	Opy megaxl	9.46E-11	1.89E-13	12.0245	4.09E-09	8.18E-12	0.023137	0.000093	0.704766	0.000004	0.704464	0.000005	0.704427	0.000005
GMB-11-21	Opy megaxl	5.05E-11	1.01E-13	9.8702	3.35E-09	6.70E-12	0.015065	0.000060	0.704587	0.000004	0.704390	0.000005	0.704367	0.000005
GMB-11-26	Opy megaxl	3.32E-09	6.63E-12	11.0831	3.74E-09	7.48E-12	0.887264	0.003556	0.714792	0.000004	0.703206	0.000050	0.701813	0.000056
GMB-11-28	Opy megaxl													
GMB-11-33	Opy megaxl	2.05E-10	4.10E-13	13.7151	4.66E-09	9.31E-12	0.044030	0.000176	0.704511	0.000004	0.703936	0.000007	0.703867	0.000007
GMB-11-36	Opy megaxl	4.76E-10	9.51E-13	39.4110	1.33E-08	2.67E-11	0.035683	0.000143	0.704278	0.000004	0.703812	0.000006	0.703756	0.000006
GMB-11-37	Opy megaxl													
GMB-11-39	Opy megaxl	2.54E-10	5.09E-13	22.5640	7.74E-09	1.55E-11	0.032896	0.000132	0.705829	0.000004	0.705399	0.000006	0.705347	0.000006
GMB-11-28 Rep	Opy megaxl	2.08E-10	4.17E-13	4.3069	1.51E-09	3.03E-12	0.137704	0.000552	0.706199	0.000011	0.704401	0.000018	0.704185	0.000019

Appendix C

Sm-Nd		LN = leuconorite; LT = leucotroctolite			Pink Fill = Calculated Value																	
Sample	Rock Type	Sm (ppm)	Sm (mol)	Std Error	Nd (ppm)	Nd (mol)	Std Error	$^{147}Sm/^{144}Nd$	2σ	$^{143}Nd/^{144}Nd$	2σ	I_{Nd} at		I_{Nd} at		$\varepsilon_{Nd\ at}$	2σ	$\varepsilon_{Nd\ at}$	2σ	$\varepsilon_{Nd\ at}$	2σ
MMIS WR				2σ			2σ					1640		1765		1640		1765		0	
CG-09-15	LN	0.4934	7.55E-11	1.51E-13	2.6156	6.86E-10	1.37E-12	0.110159	0.000442	0.511845	0.000004	0.510657	0.000009	0.510566	0.000009	2.74	0.17	4.14	0.18	-15.47	0.08
CG-09-17	LN	0.3879	3.65E-11	7.31E-14	2.2683	3.69E-10	7.38E-13	0.098936	0.000397	0.511703	0.000004	0.510636	0.000008	0.510554	0.000009	2.33	0.16	3.92	0.17	-18.24	0.08
CG-09-18A	LN	1.2293	1.61E-10	3.21E-13	5.2076	1.18E-09	2.35E-12	0.136576	0.000547	0.512134	0.000002	0.510661	0.000008	0.510548	0.000009	2.82	0.16	3.80	0.17	-9.83	0.05
CG-09-20A	LN	0.3985	4.34E-11	8.68E-14	2.1614	4.07E-10	8.13E-13	0.106657	0.000427	0.511824	0.000003	0.510674	0.000007	0.510586	0.000008	3.07	0.14	4.53	0.15	-15.88	0.05
CG-09-26A	LN	0.3545	4.58E-11	9.16E-14	1.9746	4.41E-10	8.82E-13	0.103878	0.000416	0.511776	0.000002	0.510656	0.000007	0.510570	0.000007	2.73	0.13	4.23	0.14	-16.81	0.05
CG-09-27A	LN	0.6203	6.27E-11	1.25E-13	3.6286	6.34E-10	1.27E-12	0.098904	0.000396	0.511710	0.000002	0.510644	0.000007	0.510562	0.000007	2.48	0.13	4.07	0.13	-18.10	0.04
CG-09-29	A	0.3531	3.46E-11	6.93E-14	2.1302	3.64E-10	7.27E-13	0.095232	0.000382	0.511728	0.000002	0.510702	0.000006	0.510623	0.000006	3.62	0.12	5.26	0.13	-17.74	0.04
CG-09-30	A	0.4854	5.54E-11	1.11E-13	2.6530	5.23E-10	1.05E-12	0.105850	0.000424	0.511827	0.000002	0.510686	0.000007	0.510598	0.000007	3.31	0.13	4.78	0.14	-15.82	0.04
CG-09-32A	LN	0.6430	6.37E-11	1.27E-13	3.6238	6.20E-10	1.24E-12	0.102746	0.000412	0.511760	0.000002	0.510652	0.000006	0.510567	0.000006	2.64	0.12	4.16	0.12	-17.14	0.03
CG-09-32B	LN	0.6439	6.54E-11	1.31E-13	3.8281	6.71E-10	1.34E-12	0.097398	0.000390	0.511704	0.000002	0.510654	0.000006	0.510574	0.000007	2.69	0.12	4.29	0.13	-18.21	0.04
CG-09-33A	LT	0.2867	3.14E-11	6.28E-14	2.0015	3.79E-10	7.58E-13	0.082943	0.000332	0.511544	0.000004	0.510650	0.000008	0.510581	0.000008	2.61	0.15	4.45	0.16	-21.33	0.08
CG-09-34	LT	0.4614	4.30E-11	8.60E-14	2.8323	4.56E-10	9.13E-13	0.094241	0.000378	0.511686	0.000002	0.510670	0.000006	0.510592	0.000007	3.00	0.12	4.66	0.13	-18.56	0.04
CG-09-43	LT	0.6141	5.58E-11	1.12E-13	3.2768	5.14E-10	1.03E-12	0.108426	0.000435	0.511845	0.000004	0.510676	0.000009	0.510586	0.000009	3.11	0.17	4.54	0.18	-15.47	0.08
CG-09-44	A	0.6231	9.18E-11	1.84E-13	3.5905	9.14E-10	1.83E-12	0.100408	0.000402	0.511772	0.000002	0.510690	0.000006	0.510607	0.000006	3.38	0.12	4.94	0.12	-16.89	0.03
CG-09-20A Rep	LN	0.4135	4.18E-11	8.35E-14	2.2091	3.84E-10	7.67E-13	0.108861	0.000436	0.511840	0.000002	0.510666	0.000006	0.510576	0.000007	2.93	0.12	4.35	0.13	-15.56	0.03
CG-09-26A Rep	LN	0.3452	4.16E-11	8.33E-14	1.9202	3.98E-10	7.96E-13	0.104559	0.000419	0.511781	0.000002	0.510653	0.000007	0.510567	0.000007	2.67	0.14	4.16	0.14	-16.72	0.05
CG-09-18B	Opy megaxl	0.3400	1.05E-10	2.10E-13	1.0039	5.33E-10	1.07E-12	0.196940	0.000789	0.512810	0.000002	0.510686	0.000010	0.510523	0.000011	3.31	0.20	3.31	0.22	3.35	0.04
CG-09-20B	Opy megaxl	0.2872	8.32E-11	1.66E-13	0.6576	3.28E-10	6.55E-13	0.253947	0.001018	0.513460	0.000002	0.510722	0.000013	0.510512	0.000014	4.02	0.26	3.09	0.27	16.04	0.04
CG-09-26C	Opy megaxl	0.1094	3.70E-11	7.39E-14	0.2031	1.18E-10	2.36E-13	0.313160	0.001255	0.514149	0.000007	0.510772	0.000020	0.510513	0.000021	4.99	0.40	3.11	0.42	29.47	0.13
CG-09-33C (T2)	Opy megaxl	0.4212	1.29E-10	2.58E-13	1.5438	8.08E-10	1.62E-12	0.160025	0.000641	0.512376	0.000002	0.510650	0.000009	0.510518	0.000009	2.61	0.18	3.21	0.19	-5.12	0.04
GMB-09-02	Opy megaxl	0.4450	9.00E-11	1.80E-13	1.4883	5.17E-10	1.03E-12	0.173865	0.000697	0.512529	0.000002	0.510655	0.000010	0.510511	0.000010	2.70	0.19	3.07	0.20	-2.12	0.04
EC-75-138	Opy megaxl	0.1068	3.22E-11	6.45E-14	0.1872	9.61E-11	1.92E-13	0.335320	0.001344	0.514415	0.000010	0.510799	0.000024	0.510522	0.000025	5.53	0.47	3.28	0.49	34.66	0.19
CG-09-26C Rep	Opy megaxl		3.77E-11	7.53E-14	0.1993	1.20E-10	2.39E-13	0.314664	0.001261	0.514155	0.000006	0.510762	0.000019	0.510502	0.000020	4.80	0.38	2.90	0.40	29.60	0.11
												Isochron Initial		0.510516	0.000016			3.17	0.31		
CG-09-16C	Plag megaxl		3.51E-11	7.02E-14	2.5907	4.47E-10	8.94E-13	0.078540	0.000315	0.511472	0.000002	0.510625	0.000006	0.510560	0.000006	2.12	0.11	4.04	0.12	-22.74	0.04
CG-09-18C	Plag megaxl		2.47E-11	4.95E-14	1.5870	2.88E-10	5.77E-13	0.085773	0.000344	0.511584	0.000003	0.510659	0.000006	0.510588	0.000007	2.79	0.12	4.59	0.13	-20.56	0.05
CG-09-20C	Plag megaxl		4.80E-11	9.60E-14	2.8769	4.97E-10	9.93E-13	0.096665	0.000387	0.511696	0.000002	0.510654	0.000006	0.510574	0.000006	2.68	0.12	4.30	0.12	-18.38	0.03
CG-09-27B	Plag megaxl		5.63E-11	1.13E-13	3.3923	6.15E-10	1.23E-12	0.091531	0.000367	0.511613	0.000002	0.510626	0.000006	0.510550	0.000006	2.14	0.11	3.84	0.12	-19.99	0.03
CG-09-16A	Peg pod		1.56E-10	3.12E-13	10.39451493	1.76E-09	3.52E-12	0.088678	0.000355	0.511585	0.000003	0.510629	0.000006	0.510556	0.000007	2.20	0.13	3.95	0.13	-20.53	0.05
CG-09-18D	Peg pod		2.73E-09	5.46E-12	177.8680318	3.15E-08	6.29E-11	0.086845	0.000348	0.511580	0.000003	0.510643	0.000006	0.510572	0.000007	2.48	0.13	4.26	0.13	-20.64	0.05
CG-09-26B	Peg pod		2.19E-09	4.39E-12	144.4346757	2.44E-08	4.87E-11	0.089978	0.000361	0.511599	0.000009	0.510629	0.000013	0.510555	0.000013	2.19	0.25	3.92	0.25	-20.26	0.17
CG-09-27C	Peg pod		1.05E-10	2.09E-13	6.743387151	1.13E-09	2.26E-12	0.092381	0.000370	0.511627	0.000006	0.510631	0.000010	0.510555	0.000010	2.23	0.19	3.93	0.20	-19.72	0.11
CG-09-33B	Peg pod		1.26E-09	2.53E-12	55.54016654	1.01E-08	2.02E-11	0.125054	0.000501	0.511987	0.000003	0.510639	0.000009	0.510535	0.000009	2.38	0.17	3.55	0.18	-12.70	0.06
CG-09-26B Rep	Peg pod		2.26E-09	4.53E-12	148.7774055	2.50E-08	5.00E-11	0.090476	0.000363	0.511613	0.000010	0.510637	0.000014	0.510562	0.000014	2.36	0.28	4.08	0.28	-20.00	0.20
NPS WR												1363		1444		1363		1444		0	
GMB-09-01	LN	0.3258	3.29E-11	6.57E-14	1.7808	3.10E-10	6.20E-13	0.105942	0.000425	0.511491	0.000002	0.510543	0.000006	0.510486	0.000006	-6.54	0.12	-5.59	0.12	-22.37	0.05
BR-04-18	LN	1.6615	2.01E-10	4.03E-13	8.4512	1.76E-09	3.52E-12	0.114232	0.000458	0.511819	0.000002	0.510797	0.000006	0.510736	0.000006	-1.57	0.12	-0.71	0.12	-15.97	0.04
DJ-03-64	LN	0.7994	8.73E-11	1.75E-13	4.4183	8.30E-10	1.66E-12	0.105126	0.000421	0.511398	0.000004	0.510457	0.000008	0.510401	0.000008	-8.22	0.15	-7.26	0.16	-24.19	0.08
BR-99-83	LN	0.3017	3.14E-11	6.28E-14	1.4922	2.68E-10	5.35E-13	0.117325	0.000470	0.511582	0.000002	0.510531	0.000007	0.510469	0.000007	-6.76	0.13	-5.93	0.13	-20.60	0.05
GM-97-83	LN	3.1230	3.19E-10	6.38E-13	18.8644	3.33E-09	6.65E-12	0.095862	0.000384	0.511618	0.000004	0.510760	0.000007	0.510709	0.000008	-2.28	0.14	-1.23	0.15	-19.89	0.08
BR-04-125	LN	0.2457	2.87E-11	5.74E-14	1.5452	3.11E-10	6.23E-13	0.092064	0.000369	0.511298	0.000003	0.510474	0.000007	0.510425	0.000007	-7.89	0.13	-6.79	0.13	-26.14	0.06
EP-97-150	LN	1.9344	1.93E-10	3.87E-13	10.7441	1.85E-09	3.70E-12	0.104608	0.000419	0.511411	0.000003	0.510475	0.000007	0.510419	0.000007	-7.87	0.13	-6.91	0.14	-23.93	0.06
BR-99-159	LN	0.3706	3.77E-11	7.53E-14	1.8869	3.31E-10	6.62E-13	0.113718	0.000456	0.511621	0.000005	0.510602	0.000009	0.510542	0.000009	-5.37	0.17	-4.50	0.17	-19.85	0.09
BR-99-221	LN	1.1577	1.41E-10	2.81E-13	5.8701	1.23E-09	2.46E-12	0.114198	0.000458	0.511512	0.000002	0.510490	0.000006	0.510429	0.000007	-7.58	0.13	-6.72	0.13	-21.96	0.05
BR-00-328	LN	1.1526	1.20E-10	2.40E-13	5.2475	9.41E-10	1.88E-12	0.127618	0.000511	0.511586	0.000003	0.510443	0.000007	0.510375	0.000008	-8.49	0.14	-7.76	0.15	-20.52	0.05
EP-97-232	LN	0.5225	5.59E-11	1.12E-13	2.8913	5.33E-10	1.07E-12	0.105006	0.000421	0.511445	0.000002	0.510505	0.000006	0.510448	0.000006	-7.28	0.11	-6.33	0.12	-23.28	0.04
BR-99-237C	LN	1.7529	1.93E-10	3.85E-13	8.8498	1.67E-09	3.35E-12	0.115086	0.000461	0.511493	0.000003	0.510462	0.000007	0.510401	0.000007	-8.11	0.13	-7.26	0.14	-22.34	0.05
GM-09-01 Rep	LN	0.3293	3.34E-11	6.69E-14	1.7990	3.15E-10	6.31E-13	0.105981	0.000425	0.511496	0.000004	0.510547	0.000008	0.510490	0.000008	-6.46	0.15	-5.51	0.15	-22.28	0.07
BR-00-328 Rep	LN	1.0001	9.98E-11	2.00E-13	4.6164	7.92E-10	1.58E-12	0.125979	0.000505	0.511582	0.000002	0.510454	0.000007	0.510387	0.000007	-8.27	0.13	-7.53	0.14	-20.60	0.04
BR-03-284B	Opy megaxl	0.47681	1.40E-10	2.80E-13	1.1856	5.99E-10	1.20E-12	0.233408	0.000936	0.512840	0.000002	0.510750	0.000011	0.510625	0.000011	-2.48	0.21	-2.87	0.22	3.94	0.05
BR-03-283	Opy megaxl	1.71308	1.94E-10	3.88E-13	8.2232	1.60E-09	3.21E-12	0.120901	0.000485	0.511764	0.000002	0.510681	0.000006	0.510617	0.000007	-3.82	0.12	-3.03	0.13	-17.05	0.04
NA4563	Opy megaxl	1.16503	3.46E-10	6.93E-13	4.1260	2.11E-09	4.23E-12	0.163869	0.000657	0.512210	0.000002	0.510742	0.000008	0.510655	0.000008	-2.63	0.15	-2.29	0.16	-8.36	0.04

Appendix C

BR-03-69B	Opy megaxl	0.71600	2.07E-10	4.14E-13	2.6180	1.30E-09	2.61E-12	0.158717	0.000636	0.512131	0.000002	0.510710	0.000008	0.510625	0.000008	-3.26	0.15	-2.86	0.16	-9.88	0.04
BR-03-108	Opy megaxl	0.61136	1.79E-10	3.59E-13	2.2356	1.13E-09	2.26E-12	0.158709	0.000636	0.512071	0.000003	0.510650	0.000009	0.510565	0.000009	-4.43	0.17	-4.04	0.18	-11.05	0.06
BR-03-112	Opy megaxl	1.31896	3.83E-10	7.66E-13	3.6990	1.85E-09	3.70E-12	0.206886	0.000829	0.512561	0.000002	0.510708	0.000010	0.510598	0.000010	-3.30	0.19	-3.41	0.20	-1.51	0.04
BR-03-475	Opy megaxl	0.37760	1.16E-10	2.32E-13	1.1901	6.23E-10	1.25E-12	0.186082	0.000746	0.512156	0.000003	0.510490	0.000009	0.510390	0.000010	-7.58	0.18	-7.47	0.19	-9.40	0.05
BR-04-169	Opy megaxl	1.73701	5.01E-10	1.00E-12	7.0498	3.50E-09	7.01E-12	0.142957	0.000573	0.511960	0.000002	0.510680	0.000007	0.510604	0.000007	-3.84	0.14	-3.28	0.14	-13.22	0.04
BR-04-170	Opy megaxl	0.53867	1.58E-10	3.15E-13	1.6774	8.46E-10	1.69E-12	0.186324	0.000747	0.512420	0.000002	0.510752	0.000009	0.510652	0.000009	-2.45	0.17	-2.34	0.18	-4.25	0.04
BR-99-34A	Opy megaxl	0.44506	1.37E-10	2.74E-13	1.2551	6.66E-10	1.33E-12	0.205742	0.000825	0.512510	0.000002	0.510667	0.000009	0.510557	0.000010	-4.10	0.18	-4.19	0.19	-2.50	0.04
BR-03-284B Rep	Opy megaxl	0.48302	1.43E-10	2.86E-13	1.2021	6.13E-10	1.23E-12	0.233197	0.000935	0.512839	0.000002	0.510751	0.000011	0.510626	0.000011	-2.47	0.21	-2.85	0.22	3.91	0.05
										Isochron Initial		0.510610	0.000130					-3.16	2.55		
RAP												930		1041		930		1041		0	
GMB-11-01	Opy megaxl	0.1450	4.17E-11	8.34E-14	0.2834	1.41E-10	2.81E-13	0.296534	0.001189	0.513516	0.000004	0.511707	0.000011	0.511490	0.000012	5.26	0.22	3.84	0.23	17.13	0.07
GMB-11-02	Opy megaxl	0.1659	4.77E-11	9.54E-14	0.3075	1.53E-10	3.05E-13	0.312633	0.001253	0.513645	0.000004	0.511738	0.000012	0.511509	0.000013	5.86	0.24	4.20	0.25	19.64	0.09
GMB-11-04	Opy megaxl	0.2515	7.24E-11	1.45E-13	0.4933	2.45E-10	4.90E-13	0.295472	0.001184	0.513364	0.000004	0.511561	0.000011	0.511345	0.000012	2.41	0.22	1.00	0.24	14.16	0.08
GMB-11-14	Opy megaxl	0.8719	2.51E-10	5.03E-13	2.6773	1.33E-09	2.66E-12	0.188733	0.000756	0.512725	0.000002	0.511574	0.000007	0.511436	0.000008	2.66	0.14	2.77	0.15	1.71	0.05
GMB-11-18	Opy megaxl	0.1621	4.72E-11	9.44E-14	0.2937	1.48E-10	2.95E-13	0.319964	0.001282	0.513727	0.000004	0.511775	0.000012	0.511541	0.000013	6.59	0.23	4.83	0.24	21.24	0.07
GMB-11-19	Opy megaxl		5.21E-11	1.04E-13	0.3667	1.83E-10	3.65E-13	0.284851	0.001142	0.513488	0.000004	0.511750	0.000010	0.511542	0.000011	6.10	0.20	4.84	0.22	16.58	0.07
GMB-11-21	Opy megaxl		4.49E-11	8.98E-14	0.2908	1.45E-10	2.89E-13	0.310469	0.001244	0.513640	0.000009	0.511746	0.000017	0.511519	0.000018	6.02	0.33	4.40	0.35	19.55	0.18
GMB-11-26	Opy megaxl		1.66E-10	3.33E-13	1.7622	8.72E-10	1.74E-12	0.190921	0.000765	0.512821	0.000004	0.511656	0.000008	0.511517	0.000009	4.26	0.17	4.35	0.18	3.57	0.07
GMB-11-28	Opy megaxl	0.1168	3.37E-11	6.74E-14	0.1996	9.94E-11	1.99E-13	0.339090	0.001359	0.513856	0.000008	0.511788	0.000016	0.511540	0.000017	6.84	0.31	4.80	0.33	23.77	0.15
GMB-11-33	Opy megaxl	0.2910	8.39E-11	1.68E-13	0.7342	3.65E-10	7.30E-13	0.229702	0.000921	0.513109	0.000005	0.511708	0.000010	0.511540	0.000011	5.28	0.20	4.81	0.22	9.20	0.09
GMB-11-36	Opy megaxl	0.1391	4.00E-11	7.99E-14	0.2943	1.46E-10	2.92E-13	0.274073	0.001098	0.513417	0.000006	0.511745	0.000013	0.511544	0.000014	6.00	0.25	4.89	0.27	15.19	0.12
GMB-11-37	Opy megaxl	0.2259	6.51E-11	1.30E-13	0.3952	1.96E-10	3.93E-13	0.331328	0.001328	0.513660	0.000005	0.511639	0.000013	0.511397	0.000014	3.93	0.26	2.01	0.28	19.94	0.10
GMB-11-39	Opy megaxl	0.3703	1.08E-10	2.16E-13	0.9986	5.02E-10	1.00E-12	0.214959	0.000862	0.512903	0.000003	0.511592	0.000009	0.511435	0.000009	3.01	0.17	2.75	0.18	5.18	0.07
										Isochron Initial		0.511541	0.000031					4.83	0.61		

Appendix C

U-Th-Pb		LN = leuconorite; LT = leucotroctolite					Pink Fill = Calculated Value																				
Sample	Rock Type	U	%RSD	2σ	Th	%RSD	2σ	Pb	%RSD	2σ	$^{238}U/^{204}Pb$	2σ	$^{235}U/^{204}Pb$	2σ	$^{232}Th/^{204}Pb$	2σ	$^{206}Pb/^{204}Pb$	2σ	$^{206}Pb/^{204}Pb$ at	2σ	$^{207}Pb/^{204}Pb$	2σ	$^{207}Pb/^{204}Pb$ at	2σ	$^{208}Pb/^{204}Pb$	2σ	$^{208}Pb/^{204}Pb$ at	2σ
MMIS WR																			1640				1640				1640	
CG-09-15	LN	-	-	-	-	-	-	-	-	-	-	-	-	-	-	-	-	-	-	-	-	-	-	-	-	-	-	-
CG-09-17	LN	0.02	7.36	0.0029	0.04	1.86	0.0015	1.9500	0.84	0.0328	0.6048	0.1010	0.0044	0.0007	1.2498	0.0688	16.1586	0.001236	16.1586	0.0012	15.3486	0.0015	15.3486	0.0015	35.7202	0.0043	35.7202	0.0043
CG-09-18A	LN	0.06	4.6	0.0055	0.22	3.08	0.0136	2.1000	0.59	0.0248	1.7091	0.1797	0.0124	0.0013	6.4750	0.4815	16.5889	0.001078	16.5889	0.0011	15.3891	0.0011	15.3891	0.0011	36.2319	0.0038	36.2319	0.0038
CG-09-20A	LN	0.02	2.68	0.0011	0.05	0.31	0.0003	1.0566		0.0021	1.1157	0.0622	0.0081	0.0005	2.8820	0.0238	16.1521	0.0007	16.1521	0.0007	15.3216	0.0005	15.3216	0.0005	35.7206	0.0017	35.7206	0.0017
CG-09-26A	LN	-	-	-	-	-	-	-	-	-	-	-	-	-	-	-	-	-	-	-	-	-	-	-	-	-	-	-
CG-09-27A	LN	-	-	-	-	-	-	-	-	-	-	-	-	-	-	-	-	-	-	-	-	-	-	-	-	-	-	-
CG-09-29	A	-	-	-	-	-	-	-	-	-	-	-	-	-	-	-	-	-	-	-	-	-	-	-	-	-	-	-
CG-09-30	A	0.02	5.66	0.0023	0.03	2.88	0.0017	1.2400	3.29	0.0816	0.9488	0.1819	0.0069	0.0013	1.4706	0.1944	16.0933	0.000956	16.0933	0.0010	15.3209	0.0012	15.3209	0.0012	35.6504	0.0034	35.6504	0.0034
CG-09-32A	LN	0.05	2.07	0.0021	0.16	2.09	0.0067	2.2800	0.9	0.0410	1.3060	0.0791	0.0095	0.0006	4.3183	0.2632	16.4544	0.000752	16.4544	0.0008	15.3767	0.0009	15.3767	0.0009	36.0754	0.0026	36.0754	0.0026
CG-09-32B	LN	0.06	3	0.0036	0.19	0.75	0.0029	2.4600	0.95	0.0467	1.4658	0.1181	0.0106	0.0009	4.7960	0.1666	16.7539	0.000888	16.7539	0.0009	15.4130	0.0009	15.4130	0.0009	36.3681	0.0028	36.3681	0.0028
CG-09-33A	LT	0.02	16.17	0.0065	0.04	2.44	0.0020	1.7800	1.59	0.0566	0.6628	0.2432	0.0048	0.0018	1.3698	0.1141	16.1632	0.000748	16.1632	0.0007	15.3499	0.0008	15.3499	0.0008	35.7414	0.0026	35.7414	0.0026
CG-09-34	LT	0.01	10.43	0.0021	0.03	8.65	0.0052	1.1800	0.66	0.0156	0.5000	0.1124	0.0036	0.0008	1.5499	0.2926	16.1792	0.00089	16.1792	0.0009	15.3300	0.0012	15.3300	0.0012	35.7534	0.0035	35.7534	0.0035
CG-09-43	LT	0.02	7.5	0.0030	0.05	2.17	0.0022	1.4600	0.37	0.0108	0.8087	0.1283	0.0059	0.0009	2.0890	0.1071	16.2326	0.000752	16.2326	0.0008	15.3398	0.0010	15.3398	0.0010	35.7319	0.0029	35.7319	0.0029
CG-09-44	A	0.02	8.68	0.0035	0.04	6.57	0.0053	1.4327		0.0029	0.8195	0.1442	0.0059	0.0010	1.6936	0.2264	16.0616	0.0004	16.0616	0.0004	15.3049	0.0004	15.3049	0.0004	35.5593	0.0011	35.5593	0.0011
CG-09-20A Rep	LN	-	-	-	-	-	-	-	-	-	-	-	-	-	-	-	-	-	-	-	-	-	-	-	-	-	-	-
CG-09-26A Rep	LN	-	-	-	-	-	-	-	-	-	-	-	-	-	-	-	-	-	-	-	-	-	-	-	-	-	-	-
																			1765				1765				1765	
CG-09-18B	*Opy megaxl*	0.03	1.53	0.0009	0.07	0.96	0.0013	0.3442		0.0007	5.3655	0.1755	0.0389	0.0013	12.9359	0.2753	17.5160	0.0007	17.5160	0.0007	15.5102	0.0006	15.5102	0.0006	37.1960	0.0017	37.1960	0.0017
CG-09-20B	*Opy megaxl*	0.01	6.01	0.0012	0.03	2.48	0.0015	0.2914		0.0006	2.0465	0.2506	0.0148	0.0018	6.3436	0.3281	16.5806	0.0003	16.5806	0.0003	15.3853	0.0003	15.3853	0.0003	36.0365	0.0009	36.0365	0.0009
CG-09-26C	Opy megaxl	0.002	17.1	0.0007	0.003	6.264	0.0004	0.2202		0.0004	0.5494	0.1894	0.0040	0.0014	0.8514	0.1086	16.8905	0.0004	16.8905	0.0004	15.4868	0.0004	15.4868	0.0004	36.6097	0.0011	36.6097	0.0011
CG-09-33C (T2)	*Opy megaxl*	0.02	2.8	0.0011	0.11	0.76	0.0017	0.5530		0.0011	2.2495	0.1308	0.0163	0.0009	12.7835	0.2208	17.7471	0.0004	17.7471	0.0004	15.5314	0.0005	15.5314	0.0005	37.6893	0.0016	37.6893	0.0016
GMB-09-02	*Opy megaxl*	0.06	2.22	0.0027	0.19	0.74	0.0028	0.3062		0.0006	12.9663	0.6034	0.0940	0.0044	42.4256	0.7159	19.9430	0.0008	19.9430	0.0008	15.7396	0.0006	15.7396	0.0006	39.8800	0.0017	39.8800	0.0017
EC-75-138	*Opy megaxl*	0.008	12.7	0.0020	0.005	15.1	0.0015	0.3684		0.0007	1.3728	0.3522	0.0100	0.0026	0.8865	0.2701	18.4565	0.0005	18.4565	0.0005	15.6520	0.0005	15.6520	0.0005	38.0418	0.0014	38.0418	0.0014
CG-09-26C Rep	Opy megaxl	-	-	-	-	-	-	-	-	-	-	-	-	-	-	-	-	-	-	-	-	-	-	-	-	-	-	-
CG-09-16C	Plag megaxl	-	-	-	-	-	-	-	-	-	-	-	-	-	-	-	-	-	-	-	-	-	-	-	-	-	-	-
CG-09-18C	Plag megaxl	-	-	-	-	-	-	-	-	-	-	-	-	-	-	-	-	-	-	-	-	-	-	-	-	-	-	-
CG-09-20C	Plag megaxl	-	-	-	-	-	-	-	-	-	-	-	-	-	-	-	-	-	-	-	-	-	-	-	-	-	-	-
CG-09-27B	Plag megaxl	-	-	-	-	-	-	-	-	-	-	-	-	-	-	-	-	-	-	-	-	-	-	-	-	-	-	-
CG-09-16A	Peg pod	-	-	-	-	-	-	-	-	-	-	-	-	-	-	-	-	-	-	-	-	-	-	-	-	-	-	-
CG-09-18D	Peg pod	-	-	-	-	-	-	-	-	-	-	-	-	-	-	-	-	-	-	-	-	-	-	-	-	-	-	-
CG-09-26B	Peg pod	-	-	-	-	-	-	-	-	-	-	-	-	-	-	-	-	-	-	-	-	-	-	-	-	-	-	-
CG-09-27C	Peg pod	-	-	-	-	-	-	-	-	-	-	-	-	-	-	-	-	-	-	-	-	-	-	-	-	-	-	-
CG-09-33B	Peg pod	-	-	-	-	-	-	-	-	-	-	-	-	-	-	-	-	-	-	-	-	-	-	-	-	-	-	-
CG-09-26B Rep	Peg pod	-	-	-	-	-	-	-	-	-	-	-	-	-	-	-	-	-	-	-	-	-	-	-	-	-	-	-
NPS WR																			1363				1363				1363	
GMB-09-01	LN	0.018	11.39	0.0041	0.028	11.11	0.0062	1.2250	1.683	0.0412	0.8373	0.2266	0.0061	0.0016	1.3458	0.3565	14.9915	0.0010	14.9915	0.0010	14.8814	0.0011	14.8814	0.0011	35.0518	0.0032	35.0518	0.0032
BR-04-18	LN	0.035	21.41	0.0150	0.125	2.757	0.0069	1.8250	0.035	0.0013	1.1016	0.4729	0.0080	0.0034	4.0651	0.2274	15.1629	0.0008	15.1629	0.0008	14.9965	0.0009	14.9965	0.0009	35.2946	0.0027	35.2946	0.0027
DJ-03-64	LN																15.2581	0.0020			15.0655	0.0026			35.2077	0.0069		
BR-99-83	LN	0.026	29.7	0.0154	0.027	10.54	0.0057	1.8130	1.79	0.0649	0.8532	0.5574	0.0062	0.0040	0.9155	0.2342	16.3357	0.0008	16.3357	0.0008	15.2194	0.0009	15.2194	0.0009	36.2835	0.0024	36.2835	0.0024
GM-97-83	LN	0.084	0.513	0.0009	0.509	2.101	0.0214	4.8370	0.982	0.0950	1.0272	0.0314	0.0074	0.0002	6.4315	0.4050	15.9089	0.0009	15.9089	0.0009	15.2760	0.0010	15.2760	0.0010	36.2496	0.0030	36.2496	0.0030
BR-04-125	LN	0.011	34.07	0.0075	0.014	6.728	0.0019	0.0140	6.728	0.0019	45.4049	42.8157	0.3293	0.3105	59.7100	18.5737	15.4108	0.0009	15.4108	0.0009	15.0938	0.0011	15.0938	0.0011	35.3537	0.0032	35.3537	0.0032
EP-97-150	LN	0.047	4.358	0.0041	0.227	4.729	0.0215	3.5000	6.769	0.4738	0.7798	0.2008	0.0057	0.0015	3.8914	1.0354	15.5175	0.0010	15.5175	0.0010	15.0693	0.0012	15.0693	0.0012	35.5960	0.0039	35.5960	0.0039
BR-99-159	LN	0.003	194.7	0.0117	0.019	7.119	0.0027	0.8420	0.226	0.0038	0.2090	0.8186	0.0015	0.0059	1.3678	0.2020	15.8502	0.0012	15.8502	0.0012	15.1645	0.0013	15.1645	0.0013	35.8559	0.0028	35.8559	0.0028
BR-99-221	LN	0.019	21.11	0.0080	0.142	0.196	0.0006	1.9670	0.657	0.0258	0.5582	0.2463	0.0040	0.0018	4.3103	0.0749	15.3446	0.0012	15.3446	0.0012	15.0327	0.0014	15.0327	0.0014	35.4768	0.0040	35.4768	0.0040
BR-00-328	LN	0.021	16.54	0.0069	0.09	6.751	0.0122	0.0900	6.751	0.0122	13.4766	7.2592	0.0977	0.0526	59.6780	18.6371	15.3734	0.0009	15.3734	0.0009	15.0266	0.0011	15.0266	0.0011	35.4218	0.0033	35.4218	0.0033
EP-97-232	LN																15.8923	0.0007			15.2026	0.0009			35.9798	0.0027		
BR-99-237C	LN	0.037	8.543	0.0063	0.264	0.517	0.0027	2.6990	3.489	0.1883	0.7987	0.2067	0.0058	0.0015	5.8881	0.5077	15.4563	0.0010	15.4563	0.0010	15.0960	0.0012	15.0960	0.0012	35.8494	0.0035	35.8494	0.0035
GM-09-01 Rep	LN	-	-	-	-	-	-	-	-	-	-	-	-	-	-	-	-	-	-	-	-	-	-	-	-	-	-	-
BR-00-328 Rep	LN	-	-	-	-	-	-	-	-	-	-	-	-	-	-	-	-	-	-	-	-	-	-	-	-	-	-	-
																			1444				1444				1444	
BR-03-284B	Opy megaxl	0.01	6.87	0.0014	0.03	2.09	0.0013	0.7405		0.0015	0.8222	0.1149	0.0060	0.0008	2.5486	0.1120	17.1093	0.0008	17.1093	0.0008	15.4566	0.0007	15.4566	0.0007	36.8836	0.0018	36.8836	0.0018
BR-03-283	Opy megaxl	0.06	6.11	0.0073	0.26	1.66	0.0086	1.7586		0.0035	2.0269	0.2523	0.0147	0.0018	9.0754	0.3203	16.2443	0.0004	16.2443	0.0004	15.2354	0.0004	15.2354	0.0004	36.2575	0.0011	36.2575	0.0011
NA4563	Opy megaxl	0.04	6.47	0.0052	0.19	0.34	0.0013	0.6173		0.0012	4.0342	0.5316	0.0293	0.0039	19.7997	0.1764	17.4787	0.0015	17.4787	0.0015	15.3778	0.0014	15.3778	0.0014	38.1755	0.0036	38.1755	0.0036
BR-03-69B	Opy megaxl	0.22	5.36	0.0236	0.23	2.56	0.0118	0.2436		0.0005	56.5352	6.1906	0.4100	0.0449	61.0708	3.2602	17.6685	0.0013	17.6685	0.0013	15.2870	0.0011	15.2870	0.0011	38.4609	0.0029	38.4609	0.0029
BR-03-108	Opy megaxl	0.05	5	0.0050	0.08	3.72	0.0060	0.2716		0.0005	10.8854	1.1132	0.0789	0.0081	17.9959	1.3787	16.0694	0.0008	16.0694	0.0008	15.0787	0.0008	15.0787	0.0008	36.2702	0.0021	36.2702	0.0021
BR-03-112	Opy megaxl	0.02	2.23	0.0009	0.03	4.47	0.0027	0.4052		0.0008	2.8353	0.1325	0.0206	0.0010	4.3943	0.4026	15.2282	0.0005	15.2282	0.0005	15.0492	0.0006	15.0492	0.0006	35.1788	0.0014	35.1788	0.0014
BR-03-475	Opy megaxl	-	-	-	-	-	-	-	-	-	-	-	-	-	-	-	-	-	-	-	-	-	-	-	-	-	-	-
BR-04-169	Opy megaxl	-	-	-	-	-	-	-	-	-	-	-	-	-	-	-	-	-	-	-	-	-	-	-	-	-	-	-
BR-04-170	Opy megaxl	0.03	4.83	0.0029	0.03	6.54	0.0039	0.4967		0.0010	3.5778	0.3536	0.0259	0.0026	3.6968	0.4920	16.3172	0.0004	16.3172	0.0004	15.0699	0.0004	15.0699	0.0004	36.1529	0.0009	36.1529	0.0009
BR-99-34A	Opy megaxl	-	-	-	-	-	-	-	-	-	-	-	-	-	-	-	-	-	-	-	-	-	-	-	-	-	-	-
BR-03-284B Rep	Opy megaxl	-	-	-	-	-	-	-	-	-	-	-	-	-	-	-	-	-	-	-	-	-	-	-	-	-	-	-
RAP																			1041				1041				1041	
GMB-11-01	Opy megaxl	0.01	6.25	0.0013	0.02	8.45	0.0034	0.1059		0.0002	5.8749	0.7480	0.0426	0.0054	12.1407	2.0812	17.9849	0.0010	17.9849	0.0010	15.5414	0.0010	15.5414	0.0010	37.4766	0.0027	37.4766	0.0027
GMB-11-02	Opy megaxl	0.01	15.5	0.0031	0.02	6.21	0.0025	0.1182		0.0002	5.3538	1.6749	0.0388	0.0121	11.0637	1.4011	18.5694	0.0031	18.5694	0.0031	15.5891	0.0025	15.5891	0.0025	38.0929	0.0064	38.0929	0.0064
GMB-11-04	Opy megaxl	0.06	3.89	0.0047	0.18	1.77	0.0064	0.2218		0.0004	17.7401	1.4191	0.1287	0.0103	54.9904	2.0626	19.5835	0.0006	19.5835	0.0006	15.6453	0.0005	15.6453	0.0005	39.6565	0.0014	39.6565	0.0014
GMB-11-14	Opy megaxl	0.02	4.84	0.0019	0.03	3.28	0.0020	0.3937		0.0008	3.1464	0.3116	0.0228	0.0023	4.8766	0.3305	17.9089	0.0006	17.9089	0.0006	15.5328	0.0005	15.5328	0.0005	37.2237	0.0013	37.2237	0.0013
GMB-11-18	Opy megaxl	0.03	5.2	0.0031	0.05	2.42	0.0024	0.1329		0.0003	15.0296	1.5976	0.1090	0.0116	25.8824	1.3092	20.5390	0.0015	20.5390	0.0015	15.7298	0.0012	15.7298	0.0012	39.8044	0.0032	39.8044	0.0032
GMB-11-19	Opy megaxl	0.11	7.88	0.0173	0.1	3.97	0.0079	0.3490		0.0007	20.2245	3.2352	0.1467	0.0235	18.9974	1.5503	19.1312	0.0006	19.1312	0.0006	15.6345	0.0006	15.6345	0.0006	38.4750	0.0017	38.4750	0.0017
GMB-11-21	Opy megaxl	0.01		0.0000	0.013		0.0000	0.0484		0.0001	13.3451	0.0281	0.0968	0.0002	17.9256	0.0377	19.9381	0.0019	19.9381	0.0019	15.6601	0.0016	15.6601	0.0016	38.1759	0.0040	38.1759	0.0040
GMB-11-26	Opy megaxl	0.13	4.22	0.0110	0.24	2.45	0.0118	0.3802		0.0008	22.9795	1.9906	0.1667	0.0144	43.8347	2.2422	20.9807	0.0009	20.9807	0.0009	15.7587	0.0007	15.7587	0.0007	40.0260	0.0020	40.0260	0.0020
GMB-11-28	Opy megaxl	0.01	4.66	0.0009	0.01	4.87	0.0010	0.0288		0.0001	21.9472	2.1003	0.1592	0.0152	22.6771	2.2657	18.7923	0.0052	18.7923	0.0052	15.6075	0.0045	15.6075	0.0045	37.8053	0.0109	37.8053	0.0109
GMB-11-33	Opy megaxl	0.02	4.4	0.0018	0.03	5.09	0.0031	0.2277		0.0005	5.5011	0.4966	0.0399	0.0036	8.5261	0.8875	18.2590	0.0011	18.2590	0.0011	15.5560	0.0012	15.5560	0.0012	37.6521	0.0034	37.6521	0.0034
GMB-11-36	Opy megaxl	0.03	3.82	0.0023	0.03	3.88	0.0023	0.1983		0.0004	9.6953	0.7620	0.0703	0.0055	10.0178	0.7994	19.3122	0.0005	19.3122	0.0005	15.6390	0.0005	15.6390	0.0005	38.2003	0.0015	38.2003	0.0015
GMB-11-37	Opy megaxl	0.004	11	0.0009	0.01	13.7	0.0027	0.0469		0.0001	5.3867	1.1990	0.0391	0.0087	13.9146	3.8501	18.5584	0.0020	18.5584	0.0020	15.5797	0.0017	15.5797	0.0017	37.9118	0.0043	37.9118	0.0043
GMB-11-39	Opy megaxl	0.02	4.33	0.0017	0.05	4.45	0.0045	0.2745		0.0005	4.6164	0.4100	0.0335	0.0030	11.9248	1.0877	18.5503	0.0004	18.5503	0.0004	15.5856	0.0004	15.5856	0.0004	38.1895	0.0012	38.1895	0.0012

Appendix D

Rb-Sr Mineral													
Sample	Rb (mol)	Std Error	Sr (ppm)	Sr (mol)	Std Error	$^{87}Rb/^{86}Sr$	2σ	$^{87}Sr/^{86}Sr$	2σ	I_{Sr} at	2σ	I_{Sr} at	2σ
MMIS Plag		2σ			2σ	mol				1640		1630	
CG-09-15 Pl	1.20E-09	2.40E-12	804.965	9.54E-08	1.91E-10	0.012602	0.000051	0.703493	0.000004	0.703201	0.000005	0.703203	0.000005
CG-09-17 Pl	4.70E-10	9.39E-13	873.175	7.76E-08	1.55E-10	0.006054	0.000024	0.703361	0.000004	0.703221	0.000004	0.703222	0.000004
CG-09-18A Pl	2.70E-09	5.40E-12	776.552	7.54E-08	1.51E-10	0.035789	0.000143	0.703967	0.000004	0.703138	0.000007	0.703143	0.000007
CG-09-20A Pl	1.86E-10	3.72E-13	1096.617	1.01E-07	2.02E-10	0.001846	0.000007	0.702647	0.000004	0.702604	0.000004	0.702604	0.000004
CG-09-26A Pl	3.54E-10	7.08E-13	919.347	5.89E-08	1.18E-10	0.006007	0.000024	0.702851	0.000004	0.702712	0.000004	0.702713	0.000004
CG-09-30 Pl	6.66E-10	1.33E-12	1209.472	1.49E-07	2.98E-10	0.004471	0.000018	0.702657	0.000004	0.702553	0.000005	0.702554	0.000005
CG-09-32A Pl	1.36E-09	2.72E-12	791.665	8.37E-08	1.67E-10	0.016235	0.000065	0.703621	0.000004	0.703245	0.000006	0.703248	0.000005
CG-09-33A Pl	-	-	856.157	1.12E-07	2.24E-10	-	-	0.703421	0.000004	-	-	-	-
CG-09-34 Pl	1.34E-09	2.68E-12	1190.014	1.41E-07	2.81E-10	0.009516	0.000038	0.702748	0.000004	0.702527	0.000004	0.702529	0.000004
CG-09-43 Pl	7.20E-10	1.44E-12	1076.361	1.23E-07	2.45E-10	0.005875	0.000024	0.702803	0.000004	0.702667	0.000005	0.702668	0.000005
CG-09-44 Pl	7.68E-10	1.54E-12	1199.450	1.40E-07	2.79E-10	0.005507	0.000022	0.702730	0.000004	0.702602	0.000005	0.702603	0.000005
CG-09-20A Pl Rep	2.55E-10	5.10E-13	1099.257	1.28E-07	2.56E-10	0.001992	0.000008	0.702647	0.000004	0.702600	0.000004	0.702601	0.000004
MMIS Opy/Mag													
CG-09-15 Opy	2.59E-10	5.18E-13	3.038	1.10E-09	2.20E-12	0.235480	0.000944	0.708585	0.000005	0.703135	0.000027	0.703169	0.000027
CG-09-15 Mag	-	-	8.146	3.24E-09	6.48E-12	-	-	0.708941	0.000010	-	-	-	-
CG-09-17 Opy	3.08E-10	6.17E-13	8.675	3.07E-09	6.15E-12	0.100369	0.000402	0.706569	0.000007	0.704247	0.000016	0.704261	0.000016
CG-09-18A Opy	6.56E-11	1.31E-13	-	1.80E-09	3.61E-12	0.036353	0.000146	0.704128	-	0.703287	-	0.703292	#VALUE!
CG-09-20A Opy	3.90E-10	7.80E-13	10.098	3.51E-09	7.01E-12	0.111213	0.000446	0.704703	0.000005	0.702129	0.000016	0.702145	0.000016
CG-09-26A Opy	1.57E-09	3.14E-12	8.682	3.00E-09	5.99E-12	0.525014	0.002104	0.711462	0.000004	0.699313	0.000053	0.699388	0.000053
CG-09-30 Mag	-	-	16.397	5.68E-09	1.14E-11	-	-	0.704941	0.000008	-	-	-	-
CG-09-32A Opy	4.94E-10	9.88E-13	9.223	2.83E-09	5.65E-12	0.174915	0.000701	0.707129	0.000007	0.703082	0.000023	0.703106	0.000023
CG-09-43 Mag	3.36E-10	6.72E-13	27.951	9.56E-09	1.91E-11	0.035156	0.000141	0.703179	0.000010	0.702365	0.000013	0.702370	0.000013
CG-09-44 Mag	-	-	29.850	3.87E-09	7.74E-12	-	-	0.703324	0.000010	-	-	-	-
NPS Plag										1444		1311	
GMB-09-01 Pl	3.73E-10	7.46E-13	716.6643	9.71E-08	1.94E-10	0.003841	0.000015	0.704458	0.000004	0.704380	0.000004	0.704387	0.000004
BR-04-18 Pl	1.44E-09	2.87E-12	911.7017	1.20E-07	2.40E-10	0.011959	0.000048	0.7056765	0.000004	0.705433	0.000005	0.705456	0.000005
BR-99-83 Pl	2.86E-10	5.73E-13	643.7453	7.44E-08	1.49E-10	0.003850	0.000015	0.704701	0.000005	0.704623	0.000005	0.704630	0.000005
BR-04-125 Pl	2.54E-10	5.08E-13	878.9405	9.04E-08	1.81E-10	0.002810	0.000011	0.705394	0.000005	0.705337	0.000005	0.705342	0.000005
EP-97-150 Pl		0.00E+00	634.4974	7.14E-08	1.43E-10	0.000000	0.000000	0.706421	0.000004	0.706421	0.000004	0.706421	0.000004
BR-99-159 Pl	2.92E-10	5.85E-13	623.8013	7.52E-08	1.50E-10	0.003885	0.000016	0.704217	0.000004	0.704137	0.000004	0.704145	0.000004
JS-97-215 Pl	4.21E-10	8.41E-13	717.0442	8.95E-08	1.79E-10	0.004700	0.000019	0.706818	0.000004	0.706722	0.000004	0.706731	0.000004
BR-99-221 Pl	6.59E-10	1.32E-12	771.0659	8.98E-08	1.80E-10	0.007343	0.000029	0.705443	0.000004	0.705294	0.000005	0.705308	0.000005
EP-97-232 Pl	2.70E-10	5.41E-13	663.9233	7.54E-08	1.51E-10	0.003585	0.000014	0.705942	0.000003	0.705869	0.000004	0.705876	0.000004
BR-97-237C Pl	2.79E-10	5.58E-13	758.7868	8.30E-08	1.66E-10	0.003365	0.000013	0.705807	0.000004	0.705739	0.000004	0.705745	0.000004
BR-03-284B Pl	-	-	-	-	-	-	-	-	-	-	-	-	-
NPS Opy													
GMB-09-01 Opy	1.15E-10	2.30E-13	4.0638	1.32E-09	2.63E-12	0.087440	0.000350	0.708073	0.000019	0.706294	0.000027	0.706459	0.000027
BR-04-18 Opy	1.04E-10	2.08E-13	3.7615	1.12E-09	2.25E-12	0.092331	0.000370	0.707735	0.000005	0.705856	0.000014	0.706031	0.000013
BR-99-83 Opy	2.15E-10	4.30E-13	2.1628	7.57E-10	1.51E-12	0.283965	0.001138	0.710485	0.000007	0.704707	0.000033	0.705244	0.000033
BR-04-125 Opy	1.86E-10	3.72E-13	2.8200	9.63E-10	1.93E-12	0.193008	0.000774	0.707454	0.000017	0.703527	0.000035	0.703892	0.000034
EP-97-150 Opy	-	-	13.4492	4.30E-09	8.59E-12	-	-	0.710397	0.000006	-	-	-	-
BR-99-159 Opy	1.79E-10	3.58E-13	4.7985	1.64E-09	3.28E-12	0.109386	0.000438	0.707790	0.000006	0.705564	0.000016	0.705771	0.000016
JS-97-215 Opy	1.84E-10	3.68E-13	9.9631	3.67E-09	7.35E-12	0.050054	0.000201	0.708187	0.000007	0.707168	0.000011	0.707263	0.000011
BR-99-221 Opy	1.71E-10	3.42E-13	4.0700	1.43E-09	2.85E-12	0.119712	0.000480	0.709033	0.000007	0.706597	0.000018	0.706823	0.000018
EP-97-232 Opy	1.18E-10	2.35E-13	3.1840	1.08E-09	2.15E-12	0.109142	0.000437	0.707740	0.000006	0.705520	0.000016	0.705726	0.000016
BR-97-237C Opy	2.16E-10	4.32E-13	4.5760	1.59E-09	3.18E-12	0.135936	0.000545	0.708101	0.000006	0.705335	0.000019	0.705592	0.000019
BR-03-284B Opy													
GMB-11-28 Pl	-	-	66.2316	3.30E-09	6.59E-12	-	-	0.707619	0.000011	-	-	-	-
GMB-11-28 Opy	-	-	1.7443	6.89E-10	1.38E-12	-	-	0.706318	0.000005	-	-	-	-
BR-03-284B Opy													
BR-03-284B Pl													

Appendix D

Sm-Nd Mineral Sample	Sm (ppm)	Sm (mol)	Std Error	Nd (ppm)	Nd (mol)	Std Error	$^{147}Sm/^{144}Nd$	2σ	$^{143}Nd/^{144}Nd$	2σ	I_{Nd} at	2σ	I_{Nd} at		$\varepsilon_{Nd\ at}$	2σ	$\varepsilon_{Nd\ at}$	2σ
MMIS Plag			2σ			2σ					1640		1765		1640		1765	
CG-09-15 Pl	0.310304	3.10E-11	6.19E-14	2.6636	4.62E-10	9.24E-13	0.066972	0.000268	0.511380	0.000004	0.510657	0.000007	0.510602	0.000007	2.75	0.13	4.86	0.13
CG-09-17 Pl	0.268762	2.05E-11	4.11E-14	2.0597	2.68E-10	5.36E-13	0.076655	0.000307	0.511448	0.000002	0.510621	0.000006	0.510558	0.000006	2.04	0.11	3.98	0.12
CG-09-18A Pl	0.378612	3.16E-11	6.33E-14	3.1459	4.48E-10	8.95E-13	0.070701	0.000283	0.511408	0.000016	0.510646	0.000019	0.510588	0.000019	2.53	0.38	4.57	0.38
CG-09-20A Pl	0.406012	3.21E-11	6.42E-14	2.6340	3.55E-10	7.09E-13	0.090550	0.000363	0.511630	0.000002	0.510654	0.000006	0.510579	0.000006	2.68	0.12	4.40	0.13
CG-09-26A Pl	0.345670	1.91E-11	3.81E-14	2.2187	2.08E-10	4.16E-13	0.091524	0.000367	0.511626	0.000004	0.510640	0.000008	0.510564	0.000008	2.40	0.15	4.11	0.16
CG-09-30 Pl	0.950347	9.86E-11	1.97E-13	4.9350	8.91E-10	1.78E-12	0.110704	0.000444	0.511909	0.000002	0.510715	0.000007	0.510623	0.000008	3.88	0.14	5.27	0.15
CG-09-32A Pl	0.374548	3.34E-11	6.67E-14	3.0051	4.65E-10	9.31E-13	0.071650	0.000287	0.511440	0.000003	0.510667	0.000006	0.510608	0.000007	2.94	0.13	4.97	0.13
CG-09-33A Pl	0.298235	3.29E-11	6.59E-14	2.3506	4.51E-10	9.03E-13	0.072950	0.000292	0.511454	0.000004	0.510668	0.000007	0.510607	0.000007	2.95	0.13	4.96	0.14
CG-09-34 Pl	0.551018	5.48E-11	1.10E-13	3.5486	6.14E-10	1.23E-12	0.089264	0.000358	0.511654	0.000003	0.510692	0.000007	0.510618	0.000007	3.43	0.14	5.17	0.14
CG-09-43 Pl	0.428040	4.10E-11	8.21E-14	3.1176	5.20E-10	1.04E-12	0.078928	0.000316	0.511539	0.000003	0.510688	0.000007	0.510623	0.000007	3.35	0.13	5.26	0.14
CG-09-44 Pl	0.384276	3.77E-11	7.53E-14	2.9324	5.00E-10	9.99E-13	0.075347	0.000302	0.511491	0.000003	0.510679	0.000006	0.510616	0.000006	3.17	0.12	5.13	0.12
CG-09-20A Pl Rep	0.422808	4.15E-11	8.29E-14	2.7927	4.76E-10	9.53E-13	0.087049	0.000349	0.511625	0.000003	0.510686	0.000006	0.510614	0.000007	3.31	0.12	5.09	0.13
MMIS Opy/Mag																		
CG-09-15 Opy	0.456725	1.40E-10	2.80E-13	1.0868	5.76E-10	1.15E-12	0.242494	0.000972	0.513345	0.000004	0.510731	0.000014	0.510530	0.000015	4.18	0.28	3.44	0.30
CG-09-15 Mag	0.039565	1.33E-11	2.65E-14	0.2350	1.37E-10	2.74E-13	0.096766	0.000388	0.511923	0.000011	0.510879	0.000015	0.510799	0.000016	7.10	0.30	8.72	0.31
CG-09-17 Opy	0.367133	1.10E-10	2.20E-13	0.9823	5.10E-10	1.02E-12	0.215662	0.000864	0.512992	0.000005	0.510667	0.000014	0.510488	0.000015	2.93	0.28	2.63	0.29
CG-09-18A Opy	-	5.16E-10	1.03E-12	14.9147	2.77E-09	5.54E-12	0.186090	0.000746	0.512709	0.000003	0.510702	0.000011	0.510549	0.000012	3.63	0.21	3.81	0.23
CG-09-20A Opy	0.384082	1.14E-10	2.28E-13	0.7229	3.68E-10	7.35E-13	0.310434	0.001244	0.514099	0.000005	0.510752	0.000019	0.510495	0.000020	4.60	0.37	2.76	0.39
CG-09-26A Opy	-	9.35E-11	1.87E-13	0.5822	2.94E-10	5.89E-13	0.317490	0.001273	0.513970	0.000003	0.510546	0.000017	0.510284	0.000018	0.57	0.34	-1.39	0.36
CG-09-30 Mag	0.069027	2.05E-11	4.09E-14	0.2807	1.42E-10	2.85E-13	0.143703	0.000576	0.512298	0.000013	0.510748	0.000019	0.510629	0.000020	4.53	0.38	5.39	0.39
CG-09-32A Opy	0.712609	1.87E-10	3.74E-13	1.9341	8.68E-10	1.74E-12	0.215281	0.000863	0.512949	0.000004	0.510628	0.000013	0.510450	0.000014	2.17	0.26	1.87	0.27
CG-09-43 Mag	0.046946	1.37E-11	2.75E-14	0.2246	1.13E-10	2.25E-13	0.122066	0.000489	0.512002	0.000027	0.510686	0.000032	0.510585	0.000033	3.31	0.64	4.52	0.64
CG-09-44 Mag	0.088504	9.67E-12	1.93E-14	0.3515	6.68E-11	1.34E-13	0.144706	0.000580	0.512284	0.000006	0.510723	0.000012	0.510604	0.000013	4.04	0.24	4.89	0.25
NPS Plag											1363		1289		1363		1289	
GMB-09-01 Pl	0.291386	3.38E-11	6.75E-14	2.1658	4.30E-10	8.60E-13	0.078562	0.000315	0.511239	0.000004	0.510536	0.000006	0.510574	0.000006	-6.67	0.13	-7.80	0.12
BR-04-18 Pl	0.726855	8.20E-11	1.64E-13	5.6631	1.09E-09	2.19E-12	0.074981	0.000301	0.511144	0.000003	0.510473	0.000006	0.510510	0.000006	-7.90	0.12	-9.06	0.11
BR-99-83 Pl	0.244313	2.42E-11	4.83E-14	1.9451	3.29E-10	6.58E-13	0.073375	0.000294	0.511200	0.000004	0.510543	0.000007	0.510578	0.000006	-6.54	0.13	-7.72	0.13
BR-04-125 Pl	0.177827	1.54E-11	3.08E-14	1.6106	2.43E-10	4.85E-13	0.063484	0.000254	0.511040	0.000003	0.510471	0.000005	0.510502	0.000005	-7.94	0.10	-9.21	0.10
EP-97-150 Pl	2.099422	1.99E-10	3.98E-13	12.1035	1.99E-09	3.99E-12	0.099681	0.000400	0.511398	0.000004	0.510506	0.000007	0.510554	0.000007	-7.26	0.15	-8.19	0.14
BR-99-159 Pl	0.369953	3.82E-11	7.64E-14	2.5218	4.46E-10	8.91E-13	0.085702	0.000343	0.511365	0.000004	0.510597	0.000007	0.510639	0.000007	-5.47	0.13	-6.53	0.13
JS-97-215 Pl	0.304954	3.21E-11	6.42E-14	2.5474	4.66E-10	9.32E-13	0.068830	0.000276	0.511056	0.000003	0.510440	0.000006	0.510474	0.000006	-8.55	0.11	-9.77	0.11
BR-99-221 Pl	0.411280	4.10E-11	8.20E-14	3.9981	6.82E-10	1.36E-12	0.060095	0.000241	0.511024	0.000003	0.510486	0.000005	0.510516	0.000005	-7.65	0.10	-8.95	0.10
EP-97-232 Pl	0.338293	3.29E-11	6.58E-14	2.5954	4.32E-10	8.64E-13	0.076147	0.000305	0.511199	0.000003	0.510517	0.000006	0.510555	0.000005	-7.03	0.11	-8.18	0.11
BR-97-237C Pl	1.818289	1.67E-10	3.35E-13	10.9531	1.75E-09	3.51E-12	0.095432	0.000382	0.511343	0.000003	0.510489	0.000006	0.510535	0.000006	-7.60	0.12	-8.56	0.12
BR-03-284B Pl		1.67E-10	3.33E-13		1.78E-09	3.55E-12	0.093895	0.000376	0.511608	0.000005	0.510767	0.000009	0.510813	0.000008	-2.15	0.17	-3.13	0.16
NPS Opy																		
GMB-09-01 Opy	0.262364	7.22E-11	1.44E-13	7.4136	3.52E-10	7.03E-13	0.205196	0.000822	0.512410	0.000005	0.510572	0.000012	0.510673	0.000012	-5.96	0.24	-5.88	0.23
BR-04-18 Opy	0.836111	2.12E-10	4.25E-13	2.6377	1.16E-09	2.31E-12	0.183796	0.000737	0.512168	0.000004	0.510522	0.000011	0.510612	0.000010	-6.94	0.21	-7.06	0.20
BR-99-83 Opy	0.241133	7.18E-11	1.44E-13	0.5207	2.67E-10	5.34E-13	0.268535	0.001076	0.512984	0.000005	0.510579	0.000015	0.510711	0.000014	-5.82	0.28	-5.13	0.27
BR-04-125 Opy	0.202838	5.93E-11	1.19E-13	0.5231	2.62E-10	5.23E-13	0.226417	0.000907	0.512523	0.000004	0.510496	0.000012	0.510607	0.000011	-7.45	0.23	-7.17	0.22
EP-97-150 Opy	-	-	-	-	-	-	-	-	-	-	-	-	-	-	-	-	-	-
BR-99-159 Opy	0.374722	1.09E-10	2.17E-13	0.7293	3.65E-10	7.30E-13	0.297933	0.001194	0.513312	0.000003	0.510644	0.000014	0.510789	0.000014	-4.56	0.28	-3.59	0.27
JS-97-215 Opy	1.178557	3.72E-10	7.45E-13	3.4682	1.87E-09	3.75E-12	0.198556	0.000796	0.512214	0.000003	0.510436	0.000010	0.510533	0.000010	-8.62	0.20	-8.60	0.19
BR-99-221 Opy	1.109407	3.31E-10	6.61E-13	3.5519	1.83E-09	3.65E-12	0.181105	0.000726	0.512134	0.000003	0.510512	0.000009	0.510601	0.000009	-7.13	0.18	-7.28	0.17
EP-97-232 Opy	0.496018	1.43E-10	2.85E-13	1.1838	5.87E-10	1.17E-12	0.242941	0.000974	0.512735	0.000003	0.510560	0.000012	0.510678	0.000011	-6.21	0.23	-5.76	0.22
BR-97-237C Opy	0.610963	1.81E-10	3.63E-13	1.5639	7.96E-10	1.59E-12	0.228125	0.000914	0.512540	0.000004	0.510498	0.000012	0.510609	0.000012	-7.42	0.24	-7.12	0.23
BR-03-284B Opy		8.08E-11	1.62E-13		1.47E-10	2.94E-13	0.550419	0.002206	0.515650	0.000004	0.510722	0.000024	0.510991	0.000023	-3.03	0.47	0.35	0.45
											930		1340		930			
GMB-11-28 Pl	0.409810	1.72E-11	3.43E-14	1.7410	1.27E-10	2.54E-13	0.135272	0.000542	0.512584	0.000004	0.511759	0.000007	-	-	6.28	0.14		
GMB-11-28 Opy	0.089653	2.98E-11	5.96E-14	0.1155	6.68E-11	1.34E-13	0.446101	0.001788	0.514563	0.000006	0.511841	0.000017	-	-	7.89	0.33		
BR-03-284B Opy	-	8.08E-11	1.62E-13	-	1.47E-10	2.94E-13	0.550419	0.002206	0.515650	0.000004	-	-	0.510806	0.000024	-1.98	0.46		
BR-03-284B Pl	-	1.67E-10	3.33E-13	-	1.78E-09	3.55E-12	0.093895	0.000376	0.511608	0.000005	-	-	0.510781	0.000008	-2.45	0.17		
															1340			

Appendix D

U-Th-Pb Mineral Sample	Pb	2σ	$^{206}Pb/^{204}Pb$	2σ	$^{207}Pb/^{204}Pb$	2σ	$^{208}Pb/^{204}Pb$	2σ
MMIS Plag								
CG-09-15 Pl	2.8120	0.005624	16.1031	0.0009	15.3349	0.0008	35.6446	0.0019
CG-09-17 Pl	2.3827	0.004765	15.0763	0.0012	15.2147	0.0011	34.3309	0.0028
CG-09-18A Pl	5.9458	0.011892	15.3087	0.0007	15.2714	0.0007	34.6404	0.0018
CG-09-20A Pl	1.1408	0.002282	16.0134	0.0009	15.2927	0.0009	35.5332	0.0021
CG-09-26A Pl	1.5226	0.003045	14.9611	0.0026	15.1877	0.0024	34.2141	0.0056
CG-09-30 Pl	1.2735	0.002547	16.5194	0.0016	15.3462	0.0014	35.9563	0.0034
CG-09-32A Pl	2.7754	0.005551	16.2561	0.0007	15.3591	0.0007	35.8406	0.0016
CG-09-33A Pl	3.4744	0.006949	16.3454	0.0008	15.3864	0.0007	35.9503	0.0017
CG-09-34 Pl	2.5656	0.005131	16.3843	0.0006	15.3923	0.0005	36.0088	0.0015
CG-09-43 Pl	1.5222	0.003044	15.9348	0.0010	15.2834	0.0010	35.4289	0.0022
CG-09-44 Pl	1.4875	0.002975	15.9043	0.0016	15.2735	0.0014	35.3907	0.0036
MMIS Opy/Mag								
CG-09-15 Opy	0.0631	0.000126	23.3582	0.0012	16.0411	0.0008	45.1943	0.0024
CG-09-15 Mag	0.0954	0.000191	21.5701	0.0007	15.7691	0.0004	39.5628	0.0009
CG-09-17 Opy	0.1262	0.000252	17.0249	0.0008	15.3934	0.0008	36.8318	0.0020
CG-09-18A Opy	2.2194	0.004439	17.2250	0.0004	15.5218	0.0004	37.2249	0.0010
CG-09-20A Opy	2.2194	0.004439	24.4981	0.0041	16.1970	0.0028	49.2197	0.0086
CG-09-26A Opy	0.0455	0.000091	20.5473	0.0013	15.7277	0.0010	40.7115	0.0026
CG-09-30 Mag	0.2746	0.000549	17.4753	0.0004	15.4981	0.0004	36.9860	0.0012
CG-09-32A Opy	0.6355	0.001271	17.3333	0.0005	15.5083	0.0004	37.3032	0.0011
CG-09-43 Mag	0.0814	0.000163	18.6996	0.0010	15.5552	0.0008	36.5733	0.0022
CG-09-44 Mag	0.0448	0.000090	19.2070	0.0027	15.6201	0.0022	37.4195	0.0056
NPS Plag								
GMB-09-01 Pl	0.9546	0.001909	14.3258	0.0004	14.6382	0.0004	34.4710	0.0012
BR-04-18 Pl	3.0397	0.006079	14.9026	0.0003	14.9426	0.0003	34.9707	0.0008
BR-99-83 Pl	1.2737	0.002547	14.8910	0.0004	14.8233	0.0004	34.9747	0.0012
BR-04-125 Pl	1.3495	0.002699	14.8597	0.0005	14.9214	0.0004	34.8092	0.0011
EP-97-150 Pl	3.5483	0.007097	15.3811	0.0005	15.0403	0.0005	35.4626	0.0015
BR-99-159 Pl	0.9122	0.001824	15.1260	0.0004	14.9637	0.0005	35.1767	0.0011
JS-97-215 Pl	2.3205	0.004641	14.8726	0.0006	14.8730	0.0007	34.9321	0.0015
BR-99-221 Pl	2.5649	0.005130	14.8480	0.0005	14.8820	0.0006	34.8951	0.0015
EP-97-232 Pl	1.8065	0.003613	15.3885	0.0003	15.1034	0.0003	35.4962	0.0006
BR-97-237C Pl	2.8960	0.005792	15.2718	0.0006	15.0392	0.0006	35.7346	0.0014
NPS Opy								
GMB-09-01 Opy	0.0596	0.000119	17.8917	0.0013	15.4143	0.0012	40.8252	0.0032
BR-04-18 Opy	0.1278	0.000256	17.4058	0.0005	15.3637	0.0004	38.5292	0.0011
BR-99-83 Opy	0.2873	0.000575	18.2906	0.0009	15.5579	0.0007	38.4569	0.0018
BR-04-125 Opy	0.0757	0.000151	17.6198	0.0008	15.4320	0.0008	38.6354	0.0019
EP-97-150 Opy	0.1940	0.000388	18.7782	0.0004	15.4031	0.0003	44.6575	0.0011
BR-99-159 Opy	0.1414	0.000283	17.9604	0.0005	15.5082	0.0004	38.3890	0.0010
JS-97-215 Opy	0.0709	0.000142	17.6076	0.0008	15.1968	0.0007	41.2880	0.0021
BR-99-221 Opy	0.0818	0.000164	18.7466	0.0009	15.4760	0.0008	45.8816	0.0023
EP-97-232 Opy	0.1404	0.000281	18.0491	0.0005	15.5074	0.0005	39.0069	0.0011
BR-97-237C Opy	0.0860	0.000172	18.7083	0.0010	15.5182	0.0008	42.2808	0.0021
GMB-11-28 Pl	0.1098	0.000220	18.0114	0.0117	15.5296	0.0040	37.4865	0.0125
GMB-11-28 Opy	0.0171	0.000034	19.8952	0.0038	15.7247	0.0020	38.9256	0.0054
BR-03-284B Opy								
BR-03-284B Pl								

Appendix E

Sample	Reference	Age (Ma)	Age (Ma)	Rb-Sr Rb (ppm)	%RSD	2σ	Sr (ppm)	%RSD	2σ	$^{87}Rb/^{86}Sr$	2σ	$^{87}Sr/^{86}Sr$	2σ	I_{Sr} at 1640	2σ	I_{Sr} at 1765	2σ
VN95-060; Granodioritic Gneiss		1640	1765	48	0.63	0.602910	401.3	1.490	11.958740	0.345123	0.015083	0.711790	0.000001	0.703803	0.000350	0.703187	0.000377
CG95-341; Quartzofeld. Gneiss	Work completed at University Cape Town in this study and coroborated by unpublished work C.F. Gower	1640	1765	123	0.66	1.623600	253.4	0.460	2.331280	1.408311	0.031839	0.736298	0.000001	0.703708	0.000738	0.701193	0.000795
CG95-096; Quartzofeld. Gneiss		1640	1765	123	0.77	1.889580	294.200	0.320	1.882880	1.209751	0.026543	0.733795	0.000001	0.705800	0.000615	0.703640	0.000663
CG-09-42; Hi-grade meta-sed gneiss		1640	1765	65	0.67	0.875422	259.05	0.50	2.590500	0.730824	0.017274	0.724115	0.000002	0.707202	0.000402	0.705897	0.000433
CG-09-19 B; Pyroxene granulite		1640	1765	4	1.27	0.113284	749.100	0.440	6.592080	0.017218	0.000594	0.703012	0.000002	0.702614	0.000015	0.702583	0.000017
75-33		1640	1765				1079.000			0.013000	-0.013000	0.702834		0.702533	-0.000301	0.70250994	-0.000324
75-101	Data from Hegner et al. (2010)	1640	1765				706.000			0.015900	-0.015900	0.703540		0.703172	-0.000368	0.70314365	-0.000396
75-113		1640	1765				802.000			0.011200	-0.011200	0.703134		0.702875	-0.000259	0.70285481	-0.000279
CHUR1; Augen Gneiss	Work completed at University Cape Town in this study and coroborated by unpublished work C.F. Gower	1363	1444	149	0.39	1.162200	122.000	0.410	1.000400	3.566634	0.057538	0.803361	0.000002	0.734897	0.001106	0.730787	0.001172
CHUR 2; Biotite-silli. Paragneiss		1363	1444	107	0.77	1.647800	133.000	0.250	0.665000	2.346009	0.048099	0.788296	0.000001	0.743262	0.000924	0.740559	0.000980
NAIN1; Migmatitic Gneiss		1363	1444	49	0.41	0.401800	465.000	0.340	3.162000	0.305146	0.004609	0.716589	0.000002	0.710732	0.000090	0.710380	0.000095
NAIN2; Migmatitic Gneiss		1363	1444	38	0.47	0.352500	767.000	0.380	5.829200	0.141477	0.002424	0.709172	0.000002	0.706457	0.000048	0.706294	0.000051
RAP R7.1		930	1041														
R7.4		930	1041														
R7.5		930	1041														
R7.12	Data from Menuge (1988)	930	1041														
R10.2		930	1041														
R10.3		930	1041														
R10.8		930	1041														
NOR Rog 65/75	Data from Ben-Othman (1984)	930	1041														
NOR Rog 39/73		930	1041														

Sample	Reference	Age (Ma)	Age (Ma)	Sm-Nd Sm (ppm)	Nd (ppm)	$^{147}Sm/^{144}Nd$	$^{143}Nd/^{144}Nd$	I_{Nd} at 1765	I_{Nd} at 1640	ε_{Nd} at 1765	ε_{Nd} at 1640
VN95-060; Granodioritic Gneiss		1640	1765	6.17	34.76	0.1073	0.511669	0.510423	0.510512	1.35	-0.09
CG95-341; Quartzofeld. Gneiss	Work completed at University Cape Town in this study and coroborated by unpublished work C.F. Gower	1640	1765	5.7	30.9	0.1115	0.511603	0.510309	0.510401	-0.90	-2.28
CG95-096; Quartzofeld. Gneiss		1640	1765	4.76	21.31	0.1350	0.511910	0.510342	0.510454	-0.23	-1.23
CG-09-42; Hi-grade meta-sed gneiss		1640	1765	5.85	37.3	0.0948	0.511570	0.510469	0.510547	2.25	0.60
CG-09-19 B; Pyroxene granulite		1640	1765	4.81	26.41	0.1101	0.511877	0.510599	0.510690	4.79	3.39
75-33		1640	1765		70.99	0.1030	0.511730	0.510534	0.510619	3.52	2.01
75-101	Data from Hegner et al. (2010)	1640	1765		16.16	0.1202	0.511853	0.510457	0.510557	2.02	0.78
75-113		1640	1765		3.541	0.1544	0.512187	0.510394	0.510522	0.79	0.10
CHUR1; Augen Gneiss	Work completed at University Cape Town in this study and coroborated by unpublished work C.F. Gower	1363	1444	8.854	50	0.1070	0.511421	0.510405	0.510463	-7.17	-8.10
CHUR 2; Biotite-silli. Paragneiss		1363	1444	6.771	41.27	0.0992	0.511228	0.510287	0.510340	-9.48	-10.50
NAIN1; Migmatitic Gneiss		1363	1444	1.827	12.84	0.0860	0.510451	0.509635	0.509681	-22.25	-23.40
NAIN2; Migmatitic Gneiss		1363	1444	8.772	55.84	0.0949	0.510758	0.509857	0.509908	-17.90	-18.96
RAP R7.1		930	1041	4.96	26.5	0.1130	0.512016	0.511244	0.511327	-0.98	-2.18
R7.4		930	1041	5.52	25.1	0.1329	0.512155	0.511247	0.511344	-0.92	-1.83
R7.5		930	1041	5.96	25.9	0.1391	0.512132	0.511182	0.511283	-2.20	-3.02
R7.12	Data from Menuge (1988)	930	1041	5.06	24.5	0.1246	0.512035	0.511184	0.511275	-2.16	-3.19
R10.2		930	1041	4.82	29.6	0.0987	0.511990	0.511316	0.511388	0.42	-0.98
R10.3		930	1041	5.24	30.8	0.1030	0.512013	0.511309	0.511385	0.30	-1.04
R10.8		930	1041	8.49	51.8	0.0992	0.512030	0.511352	0.511425	1.14	-0.26
NOR Rog 65/75	Data from Ben-Othman (1984)	930	1041	4.903	31.117	0.0953	0.511910	0.511259	0.511329	-0.69	-2.14
NOR Rog 39/73		930	1041	8.658	48.427	0.1081	0.511180	0.510442	0.510521	-16.68	-17.94

Sample	Reference	Age (Ma)	Age (Ma)	U-Th-Pb U	%RSD	2σ	Th	%RSD	2σ	Pb	%RSD	2σ	$^{238}U/^{204}Pb$	2σ	$^{235}U/^{204}Pb$	2σ	$^{232}Th/^{204}Pb$	2σ	$^{206}Pb/^{204}Pb$	2σ	$^{206}Pb/^{204}Pb$ at 1765	2σ	$^{207}Pb/^{204}Pb$	2σ	$^{207}Pb/^{204}Pb$ 1765	2σ	$^{208}Pb/^{204}Pb$	2σ	$^{208}Pb/^{204}Pb$ 1765	2σ
VN95-060; Granodioritic Gneiss		1640	1765	0.97			5.76			11.1			5.472	0.000337	0.040	2.44154E-06	33.574	0.0020656	17.7438	0.0009	16.020	0.000966	15.5167	0.0010	15.331	0.000985	38.1884	0.0026	35.125	0.002808
CG95-341; Quartzofeld. Gneiss	Work completed at University Cape Town in this study and coroborated by unpublished work C.F. Gower	1640	1765	1.75			16.15			29.82			3.641	0.000317	0.026	2.30082E-06	34.716	0.0030251	17.4576	0.0012	16.311	0.00131	15.5044	0.0013	15.381	0.001351	37.8162	0.0037	34.648	0.003976
CG95-096; Quartzofeld. Gneiss		1640	1765	1.96			15.28			31.58			3.851	0.000285	0.028	2.06862E-06	31.021	0.0022976	17.2161	0.0009	16.003	0.000982	15.4330	0.0011	15.302	0.00115	38.1402	0.0033	35.310	0.00349
CG-09-42; Hi-grade meta-sed gneiss		1640	1765	2.3			6.04			18.94			7.606	0.000515	0.055	3.73333E-06	20.638	0.0013968	18.6253	0.0011	16.230	0.001238	15.6215	0.0010	15.363	0.001043	37.2298	0.0028	35.347	0.002927
CG-09-19 B; Pyroxene granulite		1640	1765	0.01			0.02			1.3			0.454	3.44E-05	0.003	2.49786E-07	0.937	7.117E-05	16.2083	0.0010	16.065	0.000997	15.3632	0.0010	15.348	0.001031	35.6461	0.0032	35.561	0.003166
75-33		1640	1765																											
75-101	Data from Hegner et al. (2010)	1640	1765																											
75-113		1640	1765																											
CHUR1; Augen Gneiss	Work completed at University Cape Town in this study and coroborated by unpublished work C.F. Gower	1363	1444	1.38			22.6			31.6			2.745	0.000174	0.020	1.26011E-06	46.454	0.0029401	16.6496	0.0009	15.960	0.000955	15.4614	0.0010	15.399	0.001004	39.6105	0.0027	36.170	0.002918
CHUR 2; Biotite-silli. Paragneiss		1363	1444	1.45			16.9			24.3			3.691	0.000165	0.027	1.19731E-06	44.455	0.0019881	16.6201	0.0007	15.693	0.000752	15.4127	0.0008	15.328	0.000804	38.5370	0.0017	35.245	0.001847
NAIN1; Migmatitic Gneiss		1363	1444	0.16			2.49			14.7			0.606	3.2E-05	0.004	2.32189E-07	9.743	0.0005148	13.6727	0.0006	13.521	0.00061	14.5946	0.0007	14.581	0.000701	35.1274	0.0021	34.406	0.002138
NAIN2; Migmatitic Gneiss		1363	1444	0.12			1.41			10.7			0.618	5.82E-05	0.004	4.22041E-07	7.505	0.0007065	13.7488	0.0012	13.594	0.001218	14.5719	0.0014	14.558	0.001401	34.4436	0.0034	33.888	0.003452
RAP R7.1		930	1041																											
R7.4		930	1041																											
R7.5		930	1041																											
R7.12	Data from Menuge (1988)	930	1041																											
R10.2		930	1041																											
R10.3		930	1041																											
R10.8		930	1041																											
NOR Rog 65/75	Data from Ben-Othman (1984)	930	1041																											
NOR Rog 39/73		930	1041																											

Appendix F-1

	K-Feldspar																
	CG09-018D								CG09-026B					CG09-033B			
	10/1 .	12 / 1 .	13 / 1 .	16 / 1 .	1 / 1i	3/1i(es)	**4 / 1i**	5/1i(es)	5 / 1 .	6 / 1 .	7 / 1 .	5 / 1i	6 / 1i	1 / 1 .	4 / 1 .	**5/1 es**	**6 / 1 .**
SiO_2	64.55	64.36	64.69	64.59	64.27	63.57	65.46	62.88	64.66	65.25	67.03	64.45	65.48	63.97	65.12	57.05	64.16
TiO_2	0.01	0.00	0.03	0.27	0.06	0.00	0.05	0.02	0.04	0.00	0.01	0.01	0.00	0.03	0.05	0.00	0.04
Al_2O_3	17.94	17.86	17.80	18.12	18.41	20.87	18.55	20.93	18.14	18.15	17.59	17.68	17.96	18.09	18.30	25.71	19.35
FeO_T	0.03	0.02	0.04	0.28	0.06	0.03	0.04	0.07	0.04	0.05	0.22	0.04	0.03	0.02	0.02	0.38	0.07
MnO	0.01	0.00	0.01	0.02	0.00	0.01	0.01	0.01	0.00	0.00	0.00	0.00	0.00	0.00	0.01	0.00	0.00
MgO	0.01	0.00	0.00	0.00	0.01	0.01	0.00	0.00	0.00	0.00	0.06	0.03	0.01	0.00	0.00	0.20	0.00
CaO	0.04	0.02	0.08	0.22	0.72	3.12	0.35	3.45	0.23	0.33	0.47	0.03	0.06	0.36	0.11	9.24	1.27
Na_2O	1.14	1.01	0.88	2.01	3.36	7.97	2.52	7.65	2.78	3.84	3.57	1.28	0.98	1.79	1.39	4.97	2.34
K_2O	15.02	15.06	14.75	13.26	11.29	3.84	13.02	2.87	12.44	10.76	10.26	14.73	15.49	13.74	15.00	2.46	12.76
Cr_2O_3	0.01	0.00	0.00	0.00	0.00	0.00	0.00	0.00	0.00	0.00	0.00	0.01	0.00	0.00	0.01	0.00	0.00
Total	98.76	98.33	98.28	98.77	98.18	99.42	100.00	97.88	98.33	98.38	99.21	98.26	100.01	98.00	100.01	100.01	100.00
An	0.20	0.10	0.42	1.12	3.56	14.11	1.72	16.66	1.15	1.64	2.45	0.15	0.30	1.80	0.52	43.66	6.14
Ab	10.32	9.24	8.28	18.52	30.04	65.22	22.31	66.84	25.06	34.59	33.74	11.65	8.78	16.23	12.29	42.53	20.47
Or	89.48	90.66	91.30	80.36	66.41	20.67	75.97	16.50	73.79	63.77	63.80	88.20	90.92	81.97	87.19	13.81	73.39
An%	1.90	1.08	4.78	5.70	10.59	17.79	7.15	19.95	4.37	4.53	6.78	1.28	3.34	10.00	4.05	50.66	23.07

	Fresh Plagioclase Feldspar										Albitized Plagioclase									
	CG09-018D			CG09-026B						027C	CG09-016A				CG09-018D					027C
	1 / 1 .	3 / 1 .	4 / 1 .	1 / 1 .	2 / 1 .	3 / 1 .	***1 / 1 .***	2 / 1 .	4 / 1 .	7/1.	1 / 1 .	2 / 1 .	3 / 1 .	4 / 1 .	9 / 1 .	11 / 1 .	17 / 1 .	2 / 1i	6 / 1.	8 / 1 .
SiO_2	62.35	66.41	66.81	63.00	62.15	63.65	63.34	63.83	63.87	56.25	69.19	68.33	68.07	68.39	68.40	67.19	68.41	68.85	67.57	67.48
TiO_2	0.00	0.03	0.04	0.00	0.00	0.00	0.00	0.00	0.01	0.00	0.01	0.01	0.03	0.00	0.00	0.01	0.07	0.00	0.03	0.00
Al_2O_3	23.11	19.47	19.21	21.87	22.01	22.09	22.40	21.93	21.68	26.16	18.89	18.88	18.98	18.75	19.01	18.85	19.14	19.27	19.24	19.16
FeO_T	0.07	0.01	0.02	0.03	0.01	0.03	0.04	0.04	0.02	0.10	0.09	0.10	0.44	0.75	0.01	0.04	0.19	0.03	0.11	0.01
MnO	0.00	0.00	0.00	0.00	0.02	0.01	0.00	0.01	0.01	0.00	0.01	0.00	0.01	0.01	0.00	0.00	0.00	0.00	0.01	0.01
MgO	0.00	0.00	0.00	0.00	0.00	0.00	0.00	0.00	0.01	0.00	0.00	0.02	0.01	0.03	0.00	0.00	0.02	0.00	0.00	0.00
CaO	5.18	3.75	3.71	4.05	4.32	3.98	4.59	3.91	3.54	9.41	0.00	0.05	0.18	0.04	0.28	0.38	0.15	0.07	0.64	0.44
Na_2O	8.74	8.34	7.91	9.30	9.19	9.29	9.30	9.43	9.59	6.35	11.74	11.51	11.42	11.44	11.62	11.46	11.31	11.60	11.21	11.49
K_2O	0.24	0.14	0.13	0.31	0.29	0.29	0.32	0.28	0.27	0.26	0.00	0.04	0.03	0.08	0.04	0.09	0.08	0.03	0.09	0.02
Cr_2O_3	0.00	0.00	0.00	0.00	0.00	0.01	0.01	0.00	0.01	0.02	0.00	0.00	0.00	0.01	0.00	0.00	0.00	0.00	0.00	0.00
Total	99.69	98.15	97.83	98.56	97.99	99.35	100.00	99.43	99.01	98.55	99.93	98.94	99.17	99.50	99.36	98.02	99.37	99.85	98.90	98.61
An	24.34	19.73	20.41	19.06	20.29	18.83	21.05	18.35	16.69	44.36	0.00	0.24	0.86	0.19	1.31	1.79	0.72	0.33	3.04	2.07
Ab	74.32	79.40	78.74	79.20	78.09	79.54	77.20	80.09	81.80	54.18	100.00	99.53	98.97	99.35	98.47	97.70	98.82	99.50	96.45	97.82
Or	1.34	0.88	0.85	1.74	1.62	1.63	1.75	1.56	1.52	1.46	0.00	0.23	0.17	0.46	0.22	0.50	0.46	0.17	0.51	0.11
An%	24.67	19.90	20.58	19.40	20.62	19.14	21.42	18.64	16.94	45.02	0.00	0.24	0.86	0.19	1.31	1.80	0.73	0.33	3.06	2.07

	Plagioclase of Plagioclase-Quartz Myrmekite									Plag of Pl-Py Symplec	Py of Pl-Py Sympl				
	CG09-018D					016A	CG09-026B			027C	CG09-033B		027C	CG09-033B	
	7 / 1 .	14 / 1 .	11 / 1 i	13 / 1i	15 / 1i	5 / 1 .	***7 / 1 .***	8 / 1 .	10 / 1 .	4 / 1 .	7 / 1 .	14 / 1 .	3 / 1 .	8 / 1 .	15/1.	
SiO_2	59.14	61.43	60.94	60.58	60.72	59.42	63.83	63.43	63.83	56.51	55.47	55.35	51.47	50.95	50.83	
TiO_2	0.04	0.01	0.01	0.03	0.00	0.00	0.01	0.00	0.01	0.01	0.04	0.01	0.15	0.09	0.08	
Al_2O_3	25.18	22.69	23.18	23.56	24.13	24.58	22.33	22.06	22.89	26.90	27.06	26.99	1.23	1.11	1.35	
FeO_T	0.04	0.08	0.05	0.03	0.03	0.05	0.05	0.07	0.03	0.21	0.29	0.17	13.30	27.03	28.21	
MnO	0.00	0.02	0.01	0.00	0.00	0.01	0.00	0.00	0.00	0.00	0.02	0.00	0.54	0.57	0.62	
MgO	0.00	0.00	0.00	0.00	0.00	0.01	0.00	0.01	0.01	0.01	0.00	0.02	10.82	18.68	17.76	
CaO	5.88	5.00	5.92	6.10	6.55	7.24	4.16	4.16	4.37	9.59	10.89	10.48	22.66	0.68	0.67	
Na_2O	9.50	8.91	8.44	8.00	7.92	7.36	9.47	9.22	8.93	6.25	6.05	5.80	0.35	0.12	0.03	
K_2O	0.22	0.22	0.12	0.18	0.13	0.21	0.13	0.11	0.13	0.12	0.17	0.16	0.01	0.03	0.01	
Cr_2O_3	0.00	0.01	0.00	0.00	0.00	0.01	0.01	0.00	0.00	0.00	0.00	0.00	0.01	0.00	0.01	
Total	100.0	98.37	98.67	98.48	99.48	98.89	100.0	99.06	100.2	99.60	100.0	98.98	100.5	99.26	99.57	
An	25.19	23.38	27.75	29.34	31.14	34.79	19.38	19.83	21.13	45.57	49.41	49.51		1.42	1.41	Wo
Ab	73.69	75.40	71.58	69.63	68.13	64.01	79.88	79.54	78.13	53.75	49.69	49.59		54.41	52.13	En
Or	1.12	1.22	0.67	1.03	0.74	1.20	0.74	0.62	0.75	0.68	0.90	0.90		44.17	46.45	Fs
An%	25.48	23.67	27.93	29.64	31.37	35.22	19.52	19.96	21.29	45.88	49.86	49.96				

Bold, italicized samples wre recalculated to 100 % due to totals between 95 and 102 %
es: indicates exolution lamellae to aformentioned mineral

Appendix F-2

Fraction	Description	Weight (μg)	U (ppm)	Pb^T (pg)	Pb_C (pg)	Th/U	$^{206}Pb/^{204}Pb$	$^{206}Pb/^{238}U$	± 2σ	$^{207}Pb/^{235}U$	± 2σ	$^{207}Pb/^{206}Pb$	± 2σ	Ages (Ma) $^{206}Pb/^{238}U$	± 2σ	$^{207}Pb/^{235}U$	± 2σ	$^{207}Pb/^{206}Pb$	± 2σ	Disc. (%)
CG09-016A graphic pod																				
Z1	2 clr, cls shard frags	3.2	123	112.96	2.35	0.504	2884	0.284826	0.000528	3.94365	0.01245	0.100419	0.000212	1615.6	2.6	1622.7	2.6	1631.9	3.9	1.1
Z2	2 clr to sl cldy, cls shard frags	3.0	283	266.65	1.08	0.672	14182	0.281555	0.000502	3.87656	0.00878	0.099858	0.000090	1599.2	2.5	1608.8	1.8	1621.4	1.7	1.5
Z3	1 clr to sl cldy, cls shard frag	3.0	245	205.17	1.14	0.241	11504	0.277642	0.000545	3.80075	0.00917	0.099285	0.000099	1579.5	2.8	1592.9	1.9	1610.7	1.9	2.2
Z4	1 clr to sl cldy, cls irreg	1.2	430	129.28	0.63	0.419	12608	0.285717	0.000516	3.96307	0.00909	0.100600	0.000098	1620.1	2.6	1626.7	1.9	1635.2	1.8	1.3
Z5	1 cloudy grey, blocky	4.1	594	685.99	1.13	0.351	37754	0.279124	0.000563	3.82916	0.00901	0.099496	0.000096	1586.9	2.8	1598.9	1.9	1614.7	1.8	1.9
CG09-018D graphic pod																				
Z1	1 clr, euh, pyel, el, sq	2.9	295	274.99	0.81	0.565	19956	0.285623	0.000517	3.95528	0.00886	0.100435	0.000090	1619.6	2.6	1625.1	1.8	1632.1	1.7	0.9
Z2	1 clr, euh, pyel, flat needle	4.3	333	520.90	1.55	0.585	19683	0.285900	0.000672	3.96001	0.01013	0.100457	0.000127	1621.0	3.4	1626.0	2.1	1632.6	2.3	0.8
Z3	1 clr, euh, pyel, el, sq	5.6	395	599.41	1.18	0.535	30220	0.280802	0.000608	3.85170	0.00977	0.099484	0.000082	1595.4	3.1	1603.6	2.0	1614.4	1.5	1.3
Z4	1 clr, euh, pyel, sq needle frag	1.9	414	129.03	1.36	0.582	5593	0.285007	0.002963	3.94615	0.04151	0.100419	0.000152	1616.5	14.9	1623.2	8.5	1631.9	2.8	1.1
Z5	1 clr, euh, pyel, sq el frag	3.2	683	415.83	0.77	0.595	31578	0.277787	0.001184	3.84346	0.01690	0.100348	0.000123	1580.2	6.0	1601.9	3.5	1630.5	2.3	3.5
CG09-021 leuconorite																				
Z1	1 cls to pyel, irreg frag	5.8	195	346.95	4.55	1.204	3928	0.285284	0.000681	3.93059	0.01251	0.099926	0.000164	1617.9	3.4	1620.0	2.6	1622.7	3.1	0.3
Z2	1 cls to pyel, irreg frag	2.2	119	129.71	0.73	1.279	9034	0.285729	0.000537	3.94014	0.00943	0.100013	0.000106	1620.2	2.7	1622.0	1.9	1624.3	2.0	0.3
Z3	1 cls to pyel, irreg frag	3.1	187	186.93	0.75	1.120	12991	0.271141	0.000521	3.64528	0.00862	0.097506	0.000095	1546.6	2.6	1559.5	1.9	1577.0	1.8	2.2
Z4	1 cls to pyel, irreg shard frag	4.1	1280	472.73	0.55	1.571	41411	0.275169	0.000595	3.72699	0.00931	0.098233	0.000088	1567.0	3.0	1577.2	2.0	1590.9	1.7	1.7
Z5	1 cls to pyel, irreg shard frag	4.7	985	344.09	0.58	1.075	31032	0.286884	0.000672	3.95883	0.01063	0.100083	0.000084	1625.9	3.4	1625.8	2.2	1625.6	1.6	0.0
CG09-026B graphic pod																				
Z1	1 clr, cls, el shard frag	8.2	883	2106.07	5.00	0.394	25843	0.285296	0.000558	3.94943	0.00936	0.100401	0.000082	1618.0	2.8	1623.9	1.9	1631.5	1.5	0.9
Z2	2 clr, cls, el tips? frag	6.3	1331	1979.46	0.62	0.380	195088	0.285530	0.000542	3.95297	0.00912	0.100408	0.000077	1619.2	2.7	1624.6	1.9	1631.7	1.4	0.9
Z3	1 clr to sl cldy, cls frag	3.7	1680	1978.20	0.26	0.406	458449	0.280930	0.000537	3.86314	0.00895	0.099734	0.000077	1596.0	2.7	1606.0	1.9	1619.1	1.4	1.6
Z4	1 clr to sl cldy, cls el frag	5.0	2020	3005.20	2.83	0.390	65115	0.284921	0.000594	3.94242	0.00969	0.100354	0.000081	1616.1	3.0	1622.4	2.0	1630.7	1.5	1.0
Z5	1 clr to sl cldy, cls el frag	4.8	1965	3087.85	7.05	0.619	25505	0.285097	0.000565	3.94623	0.00938	0.100390	0.000087	1617.0	2.8	1623.2	1.9	1631.3	1.6	1.0
CG09-033B graphic pod																				
Z1	1 clr, cls, sq, frag, crks	5.3	128	99.07	1.39	0.674	4135	0.232896	0.000437	2.87634	0.00822	0.089573	0.000161	1349.7	2.3	1375.7	2.2	1416.4	3.4	5.2
Z2	1 clr, cls shard frag	4.5	40	34.77	0.40	0.445	5350	0.271233	0.000575	3.62415	0.01074	0.096909	0.000161	1547.1	2.9	1554.8	2.4	1565.5	3.1	1.3
Z3	1 clr to sl cldy, cls shard frag	3.9	110	34.75	3.94	0.729	519	0.279965	0.001335	3.82875	0.05117	0.099186	0.001102	1591.2	6.7	1598.8	10.8	1608.9	20.8	1.2
Z5	1 sl cldy, cls irreg, crks	7.1	42	83.16	0.36	0.365	14324	0.275786	0.000530	3.74615	0.00893	0.098517	0.000086	1570.1	2.7	1581.3	1.9	1596.2	1.6	1.8
Z6	1 clr to sl cldy, cls, irreg	3.2	38	34.08	0.27	0.777	7083	0.260644	0.000568	3.43408	0.00941	0.095557	0.000114	1493.1	2.9	1512.2	2.2	1539.1	2.3	3.3

Notes:

All analyzed fractions represent least magnetic, chemically-abraded zircon grains, free of cores or cracks unless stated otherwise.

Abbreviations: clr - clear; cls - colourless; sl cldy - slightly cloudy; yel - yellow; pyel - pale yellow; brn - brown; frag - fragment; irreg - irregular or anhedral; sq - square x-section; el - elongate

Pb^T is total amount (in picograms) of Pb.

Pb_C is total measured common Pb (in picograms) assuming the isotopic composition of laboratory blank: 206/204 - 18.221; 207/204 - 15.612; 208/204 - 39.360 (errors of 2%).

Pb/U atomic ratios are corrected for spike, fractionation, blank, and, where necessary, initial common Pb; 206Pb/204Pb is corrected for spike and fractionation.

Th/U is model value calculated from radiogenic 208Pb/206Pb ratio and 207Pb/206Pb age, assuming concordance.

Disc. (%) - per cent discordance for the given 207Pb/206Pb age.

Uranium decay constants are from Jaffey et al. (1971).